Deep Underground Neutrino Experiment (DUNE)

DRAFT Technical Design Report

Volume 4:

Dual-Phase Far Detector Module

Four chapters: High Voltage, Photon Detection,

TPC Electronics, and CISC

2nd draft for review by the LBNC

May 3, 2019

The DUNE Collaboration

DEEP UNDERGROUND NEUTRINO EXPERIMENT

Contents

Contents i

List of Figures vi

List of Tables ix

1 High Voltage 2

1.1 Scope . . . 2
1.2 Design Requirements . . . 5
1.3 ProtoDUNE-DP Experience . . . 8
1.3.1 Design . . . 8
1.3.2 Construction . . . 9
1.3.3 Assembly and Installation . . . 11
1.3.4 Pre-cool-down Commissioning Test . . . 13
1.3.5 Suggestions for future R&D . . . 13
1.4 HV System Design . . . 14
1.4.1 High Voltage Power Supply and Feedthrough . . . 16
1.4.2 High Voltage Extender and Voltage Degrader . . . 18
1.4.3 Cathode Plane . . . 18
1.4.4 Ground Grid . . . 22
1.4.5 Field Cage . . . 24
1.4.6 Electrical Interconnections . . . 29
1.4.7 HV Return and Monitoring Devices . . . 30
1.5 Quality Assurance and Quality Control . . . 30
1.5.1 Field Cage . . . 30
1.5.2 Electrical Interconnections and HV Divider . . . 31
1.5.3 Quality Control During Assembly and Installation . . . 32
1.6 Safety . . . 33
1.6.1 Production Safety . . . 33
1.6.2 Handling Safety . . . 34
1.7 Transport, Assembly, and Installation and Integration . . . 34
1.7.1 Transport and Handling . . . 34
1.7.2 Assembly . . . 35
1.7.3 Installation and Integration . . . 36
1.8 Design Validation and Verification Plan . . . 39
1.9 Interfaces . . . 40

1.9.1 Internal Cryogenics System . . . 40
1.9.2 Cryostat . . . 40
1.9.3 Charge Readout Plane . . . 41
1.9.4 Photon Detection System . . . 41
1.9.5 Cryogenics Instrumentation and Slow Control . . . 41
1.9.6 Calibration . . . 42
1.9.7 Technical Coordination . . . 42
1.10 Organization and Management . . . 42
1.10.1 HV Consortium Organization . . . 42
1.10.2 Planning Assumptions . . . 43
1.10.3 Risks . . . 44
1.10.4 High-level Cost and Schedule . . . 46
1.11 Appendix - Alternatives . . . 48
1.11.1 Calibration Laser Penetrations . . . 48
1.11.2 Individual Ground Grids on PDS PMTs . . . 48

2 TPC Electronics **49**
2.1 System Overview . . . 49
2.1.1 Introduction . . . 51
2.1.2 Design Considerations . . . 52
2.1.3 Scope . . . 55
2.2 System Design . . . 57
2.2.1 Cryogenic Analog Front-end Electronics . . . 58
2.2.2 Signal Feedthrough Chimneys . . . 61
2.2.3 Digital Advanced Mezzanine Card Electronics for Charge Readout . . . 63
2.2.4 Electronics for Light Readout . . . 65
2.2.5 Network-based μTCA Architecture . . . 68
2.2.6 Timing Distribution . . . 70
2.3 Production and Quality Assurance . . . 72
2.3.1 Charge Readout Electronics . . . 73
2.3.2 Light Readout Electronics . . . 74
2.3.3 Timing System and μTCA . . . 75
2.3.4 Signal Feedthrough Chimneys . . . 75
2.4 Transport and Handling . . . 76
2.5 Interfaces . . . 76
2.5.1 Electronics System to charge-readout plane (CRP) and Photon Detection Systems 77
2.5.2 Electronics System to DAQ System . . . 78
2.5.3 Electronics System to Cryostat and Cryogenics . . . 79
2.5.4 Electronics System to Slow Control System . . . 80
2.6 Installation, Integration, and Commissioning . . . 81
2.6.1 SFT Chimneys . . . 81
2.6.2 Digital μTCA Crates . . . 81
2.6.3 Integration within the DAQ . . . 82
2.6.4 Integration with the Photon Detection System . . . 82
2.6.5 Commissioning . . . 82
2.7 Risks . . . 82
2.8 Safety . . . 84

2.9 Organization and Management . . . 85
2.9.1 Consortium Organization . . . 85
2.9.2 Planning Assumptions . . . 85
2.9.3 Institutional Responsibilities . . . 85
2.9.4 High-level Cost and Schedule . . . 86

3 Photon Detection System 88
3.1 Physics Requirements and Goals . . . 88
3.1.1 Scientific Requirements . . . 89
3.1.2 Additional Scientific Opportunities . . . 91
3.2 Design Overview . . . 92
3.2.1 Scintillation Light Production in the DP Detector Module . . . 93
3.2.2 Detector Sub-systems and Layout . . . 94
3.2.3 Operational Modes . . . 96
3.2.4 Detector Design Specifications . . . 96
3.3 Photosensor System . . . 97
3.3.1 Photodetector Characterization . . . 98
3.3.2 High Voltage System . . . 100
3.3.3 Wavelength Shifting . . . 100
3.4 Mechanics . . . 101
3.4.1 PMT Support Structure . . . 101
3.4.2 Reflector/WLS Panel Assemblies . . . 102
3.5 Readout Electronics . . . 104
3.5.1 Photomultiplier High Voltage Dividers . . . 104
3.5.2 High Voltage and Signal Splitters . . . 105
3.5.3 Signal Readout . . . 107
3.6 Calibration System . . . 108
3.6.1 Calibration System Design . . . 108
3.7 Photon Detector Simulation . . . 110
3.7.1 Simulation Framework And Assumptions . . . 111
3.7.2 Expected Light Yields . . . 112
3.8 Validation with Data from Photon Detector System Prototypes . . . 113
3.8.1 Design Similarities and Differences Between Prototypes and Far Detector System 114
3.8.2 WA105 DP demonstrator Light Data Results and Simulation Validation . . . 116
3.8.3 Installation of the ProtoDUNE-DP Photon Detector System . . . 121
3.9 Baseline Design Validation and Projected Photon Detector Performance . . . 122
3.9.1 Event t_0 Reconstruction . . . 123
3.9.2 Supernova Burst Triggering . . . 125
3.9.3 Event Energy Reconstruction . . . 127
3.10 Quality Control and Quality Assurance . . . 130
3.10.1 Quality Control During Production and Assembly . . . 131
3.10.2 Quality Control at the Coating, Testing and Storage Facility . . . 132
3.10.3 Quality Control at the Underground Areas . . . 133
3.11 Interfaces . . . 133
3.12 Installation, Integration, and Commissioning . . . 135
3.12.1 Transport and Handling . . . 135
3.12.2 Coating, Testing and Storage Facility Operations . . . 136

3.12.3 Underground Installation and Integration . . . 137
3.12.4 Commissioning . . . 139
3.13 Risks . . . 140
3.13.1 Design and Construction Risks . . . 142
3.13.2 Risks During Installation . . . 143
3.13.3 Risks During Commissioning . . . 144
3.13.4 Risks During Operation . . . 144
3.14 Safety . . . 145
3.15 Project Management . . . 146
3.15.1 Consortium Organization . . . 147
3.15.2 Planning Assumptions . . . 148
3.15.3 Work Breakdown Structure and Institutional Responsibilities . . . 148
3.15.4 High Level Schedule . . . 149
3.15.5 High Level Cost of Baseline Design . . . 149
3.16 Appendix - Alternatives . . . 151
3.16.1 Individual Ground Grids . . . 151
3.16.2 Calibration System Alternatives . . . 151

4 Cryogenics Instrumentation and Slow Control 152
4.1 Introduction . . . 152
4.1.1 Scope . . . 155
4.1.2 Design Considerations . . . 156
4.1.3 Fluid Dynamics Simulation . . . 159
4.2 Cryogenic Instrumentation . . . 166
4.2.1 Purity Monitors . . . 167
4.2.2 Thermometers . . . 173
4.2.3 Liquid Level Monitoring . . . 182
4.2.4 Pressure Meters . . . 183
4.2.5 Gas Analyzers . . . 184
4.2.6 Cameras . . . 187
4.2.7 Cryogenic Instrumentation Test Facility . . . 191
4.2.8 Validation in ProtoDUNE . . . 192
4.3 Slow Controls . . . 193
4.3.1 Slow Controls Hardware . . . 193
4.3.2 Slow Controls Infrastructure . . . 195
4.3.3 Slow Controls Software . . . 195
4.3.4 Slow Controls Quantities . . . 196
4.3.5 Local Integration . . . 196
4.3.6 Validation in ProtoDUNE . . . 198
4.4 Organization and Management . . . 198
4.4.1 Institutional Responsibilities . . . 200
4.4.2 Cost and Labor . . . 202
4.4.3 Schedule . . . 203
4.4.4 Risks . . . 206
4.4.5 Interfaces . . . 206
4.4.6 Installation, Integration, and Commissioning . . . 210
4.4.7 Quality Control . . . 215

4.4.8 Safety 219

Glossary **221**

References **232**

List of Figures

1.1 DUNE DP detector module overview . . . 3
1.2 HV system for a DP detector module . . . 4
1.3 DP HV divider board . . . 9
1.4 Field cage parts . . . 10
1.5 DP FC installation process and inter-module connection . . . 12
1.6 HV power supply and feedthrough for a DP module . . . 17
1.7 DP HV feedthrough and extender . . . 19
1.8 A view of a ProtoDUNE-DP cathode module . . . 20
1.9 Deflection of the cathode truss . . . 21
1.10 ProtoDUNE-DP cathode field . . . 22
1.11 ProtoDUNE-DP cathode field 2D . . . 23
1.12 A single ground grid module . . . 24
1.13 FC elevation . . . 25
1.14 FC submodule view . . . 26
1.15 FC-cathode corner . . . 27
1.16 FC interconnections . . . 28
1.17 DP FC resistive sheath . . . 29
1.18 PDS reflector/WLS panel assembly for mounting onto FC . . . 37
1.19 FC super-module installation sequence for DP detector module . . . 38

2.1 Charge distributions from cosmic ray tracks . . . 50
2.2 Schematic layout of the dual-phase (DP) charge readout (CRO) subsystem . . . 51
2.3 Schematic layout of the DP light readout (LRO) subsystem . . . 52
2.4 Top corner view of DP module . . . 57
2.5 Cryogenic front-end (FE) ASIC properties . . . 59
2.6 Photo of an analog FE card mounted on the extraction blade . . . 59
2.7 Noise measurements in the WA105 DP demonstrator . . . 60
2.8 Details of the signal feedthrough chimney (SFT chimney) design . . . 62
2.9 Signal feedthrough chimney cold flange . . . 63
2.10 Block diagram of CRO advanced mezzanine card (AMC) . . . 64
2.11 Block diagram of LRO . . . 66
2.12 Photo of prototype LRO card . . . 66
2.13 CATIROC ASIC . . . 68
2.14 Instrumented μTCA crate from the WA105 DP demonstrator . . . 70
2.15 Picture of White Rabbit (WR) slave node card . . . 71
2.16 Architecture of WR network . . . 72

2.17 Overview of the configuration for quality control and calibration of CRO electronics system 73
2.18 Channel-to-channel gain uniformity measured on FE cards produced for ProtoDUNE-DP 74
2.19 Images of the WA105 DP demonstrator signal feedthrough (SFT) cold feedthrough . . . 77
2.20 Schematic illustration of the interface of DP time projection chamber (TPC) electronics to data acquisition (DAQ) . . . 78
2.21 Details of SFT chimney interface to the cryostat structure . . . 80

3.1 A sketch depicting the mechanism of light production in argon. . . . 93
3.2 The DP module (partly open) . . . 94
3.3 The sketch of the cryostat roof layout for DP photon detection system (PDS) penetrations. 95
3.4 Picture of the Hamamatsu R5912-MOD20 photomultiplier tube (PMT). . . . 98
3.5 Picture of the PMTs being installed in the testing vessel . . . 99
3.6 Sketch of the set up for PMT characterization tests. . . . 99
3.7 Sketches of the front (left) and side (right) views of the reflective foil/wavelength shifting (WLS) panel. . . . 101
3.8 Picture of the Hamamatsu R5912-MOD20 PMT fixed on the membrane floor of ProtoDUNE-DP. . . . 102
3.9 Sketches of the reflector/WLS panel assembly horizontal support bars. . . . 103
3.10 Sketches of the inside and outside views of a partial field cage (FC) submodule with a reflector/WLS panel assembly. . . . 104
3.11 Positive power supply and cathode grounding scheme. . . . 105
3.12 Generic splitter circuit diagram. . . . 106
3.13 Picture of the splitter box for ProtoDUNE-DP. . . . 106
3.14 single photoelectron (SPE) waveforms and amplitudes from the WA105 at different voltages. . . . 107
3.15 Sketch of the DUNE far detector (FD) PDS light calibration system. . . . 109
3.16 Picture of the light guide structure during the development phase and the schematics of the light way from the LED to the reference sensor. . . . 110
3.17 Expected 1D light yields in the full DP FD cryostat. . . . 113
3.18 Expected 2D light yield in the full DP FD cryostat. . . . 114
3.19 WA105 DP demonstrator PDS . . . 115
3.20 WA105 DP demonstrator schematic drawing . . . 117
3.21 WA105 DP demonstrator PMTs mean pedestal and RMS . . . 117
3.22 GAr and LAr scintillation profile in WA105 DP demonstrator . . . 118
3.23 Evolution of τ_{slow} as a function of time in WA105 DP demonstrator . . . 118
3.24 S2 light at different amplification field in WA105 DP demonstrator. . . . 119
3.25 Charge Collected in WA105 DP demonstrator vs Monte Carlo (MC) . . . 120
3.26 Charge Collected vs track-PMT shortest distance . . . 120
3.27 Installation of the ProtoDUNE-DP photon detector system. . . . 121
3.28 Optimization of t_0 candidate cluster spatial position reconstruction for nucleon decay (NDK) events. . . . 124
3.29 Nucleon decay t_0 reconstruction efficiency and purity. . . . 125
3.30 SN burst triggering assumptions. . . . 127
3.31 supernova neutrino burst (SNB) triggering efficiency for different cluster reconstruction parameters. . . . 128
3.32 SNB triggering efficiency for different WLS foil configurations. . . . 128
3.33 Average charge and amplitude per hit channel in beam neutrino interactions. . . . 129

3.34 Deposited energy and PDS-reconstructed energy for beam neutrino interactions. 130
3.35 Correlation between PDS-reconstructed energy and deposited energy for beam neutrino interactions. 131
3.36 An example transportation box to be used for all transport purposes i.e. from remote sites to the Coating, Testing and Storage Facility (CTSF) and from CTSF to SURF. . . 135
3.37 The layout of the CTSF. 136
3.38 Pictures of a single tetra-phenyl butadiene (TPB) coating station (courtesy of Wil Vollenberg, European Organization for Nuclear Research (CERN)-TE Department). 137
3.39 The schematic view of the installation sequence of a unit reflector/WLS panel assembly on the FC I-beams. 139

4.1 CISC subsystem chart 153
4.2 CFD example 163
4.3 Streamlines for LAr flow inside ProtoDUNE-SP 165
4.4 Comparison of ProtoDUNE-SP temperature data and CFD simulations 166
4.5 The ProtoDUNE-SP purity monitoring system 168
4.6 Measured electron lifetimes in the three purity monitors at ProtoDUNE-SP 169
4.7 Schematic diagram of the baseline purity monitor design 170
4.8 Block diagram of the purity monitor system. 171
4.9 Distribution of temperature sensors inside the cryostat 173
4.10 Temperature sensor resolution and reproducibility 175
4.11 ProtoDUNE-SP Static T-gradient results 175
4.12 Conceptual design of the static T-gradient monitor 176
4.13 Cryostat bolts and temperature sensor support 177
4.14 Principle of cross-calibration with dynamic T-gradient monitor 178
4.15 Temperature profile for dynamic T-Gradient with pumps-off 179
4.16 Dynamic T-gradient monitor overview 179
4.17 Sensor-cable assembly for dynamic T-gradient monitor 180
4.18 Arrays in gas phase 181
4.19 LAr level measurements 183
4.20 Photo of the pressure sensors installed on a flange in ProtoDUNE-SP 184
4.21 Photo of a gas analyzer switchyard valve assembly 185
4.22 Impurity levels during the pre-fill stages for 35 t prototype phase 1 186
4.23 O_2 just after the 35 t prototype was filled with LAr 187
4.24 A camera enclosure 189
4.25 Inspection camera design 190
4.26 Example schematic for LED chain 191
4.27 Slow controls connections and data 193
4.28 Rack monitoring box prototype for the SBND; based on MicroBooNE design 194
4.29 Diagram of the ProtoDUNE-SP control system topology 199
4.30 CISC consortium organization 200

List of Tables

1.1 Specifications for DP-HV . . . 6
1.2 high voltage (HV) System Components. Dimensions are given relative to the 60 m length (L), 12 m width (W), and 12 m height (H) of cryostat. . . . 14
1.3 DP HV system interface documents . . . 40
1.4 Participating institutes . . . 43
1.5 Risks for DP-FD-HV . . . 44
1.6 DP HV system cost summary . . . 46
1.7 DP HV system consortium schedule . . . 47

2.1 Specifications for DP-ELEC . . . 53
2.2 Key parameters for the TPC electronics system design . . . 56
2.3 Numbers for DP electronics components to procure . . . 56
2.4 Principal components and channel granularity of electronics system . . . 58
2.5 Main characteristics of analog-to-digital converter (ADC) AD9257 . . . 64
2.6 Main characteristics of ADC AD9249 . . . 67
2.7 Main characteristics of CATIROC. . . . 69
2.8 Bandwidth requirements per μTCA crate. . . . 69
2.9 TPC Electronics System Interface Links . . . 77
2.10 Risks for DP-FD-TPC . . . 82
2.11 Participating intitutions . . . 85
2.12 Milestones of the TPC electronics consortium . . . 86
2.13 DP TPC electronics system cost summary . . . 87

3.1 Specifications for DP-PDS . . . 96
3.2 Average light yields in the DUNE far detector (FD) geometry. . . . 112
3.3 WA105 DP demonstrator photomultiplier tubes (PMTs) configurations. . . . 115
3.4 DP photon detection system (PDS) interface documents . . . 133
3.5 Quantities related to the DP PDS installation. . . . 138
3.6 Risks for DP-FD-PDS . . . 140
3.7 Participating institutes . . . 147
3.8 DP photon detector (PD) Consortium Schedule . . . 149
3.9 DP PDS Cost Summary . . . 150

4.1 Specifications for DP-CISC . . . 157
4.2 Specifications for CISC subsystems . . . 160
4.3 Specifications for CISC subsystems. . . . 161

4.4 Specifications for CISC subsystems. 162
4.5 CFD parameters for ProtoDUNE 164
4.6 Slow controls quantities 197
4.7 CISC consortium institutions. 201
4.8 Institutional responsibilities in the CISC consortium 202
4.9 CISC cost 203
4.10 CISC labor 204
4.11 DP CISC schedule 205
4.12 CISC risks1 207
4.13 CISC risks2 208
4.14 CISC risks3 209
4.15 CISC system interface links 210

Chapter 1

High Voltage

A liquid argon time-projection chamber (LArTPC) requires an equipotential cathode plane at high voltage (HV) and a precisely regulated interior E field to drive the electrons from particle interactions to the sensor planes. For the DUNE dual-phase (DP) technology, this requires a horizontal cathode plane, held at a negative HV; a horizontal charge-readout plane (CRP) in the gas phase as described in Chapter **??**; and electrically and mechanically continuous horizontal field-shaping rings that surround the central active drift volume, providing a linear voltage gradient in the vertical direction, collectively called the field cage (FC). The DP HV system components are shown in Figure 1.1.

The HV consortium will provide a system that operates at the nominal voltage corresponding to the uniform 500 V/cm E field in the time projection chamber (TPC) drift volume. Mechanical and structural concerns are taken into account, together with the electrical design to meet the requirements.

1.1 Scope

The scope of the DP HV system, provided by the DUNE HV consortium includes selecting and procuring materials, as well as the fabrication, testing, delivery, and installation of the components needed to generate, distribute, and regulate the voltages that create a stable and precise E field within the DUNE DP module.

The DP HV system has the following components:

- −600 kV HVPS, cable, filters, and feedthrough;
- HV extender and voltage degrader;
- horizontal cathode plane (60 m long and 12 m wide) made of arrays of resistive elements

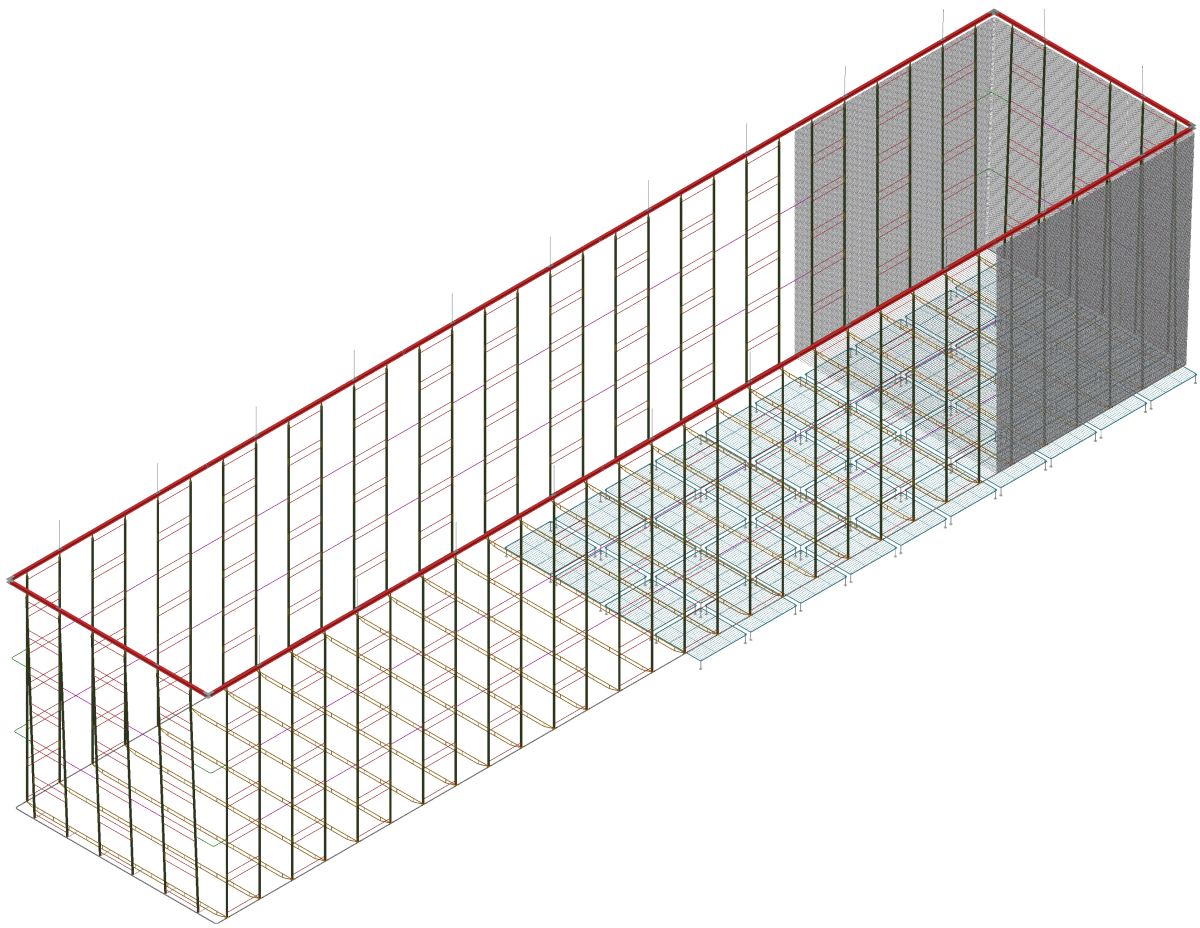

Figure 1.1: An isometric view of the DP HV system components. Most of the FC profiles are removed to emphasize the structural elements. The figure shows three completed FC super-modules, described in detail in Section 1.4.5, on the upper right, the structural members of the FC and cathode plane in the lower left, and half the ground grid modules on the bottom. The entire structure, except for the ground grid, which lies on the floor, is suspended under the cryostat ceiling by 24 cables and rods (Credit: BNL)

placed approximately 1.5 m above the bottom of the cryostat;

- ground planes (GPs) below the cathode to protect the photon detector (PD) array;
- vertical FC walls, 12 m tall surrounding the cathode and covering a total of 144 m circumference; and
- HV return feedthrough and resistor box.

The HV system consists of components both exterior and interior to the cryostat. The HVPS is external and will be mounted on top of the HV feedthrough, eliminating the need for the external HV cable. The voltage is fed directly to the feedthrough into the cryostat where it is distributed by interior components that form part of the TPC structure. The internal HV components, in fact, form a large fraction of the total internal structure of the TPC itself, and effectively bound the active volume of the detector module. Figure 1.2(a) is a schematic overview of the HV system (panels b-d show pictures of a few of the components from the WA105 DP demonstrator).

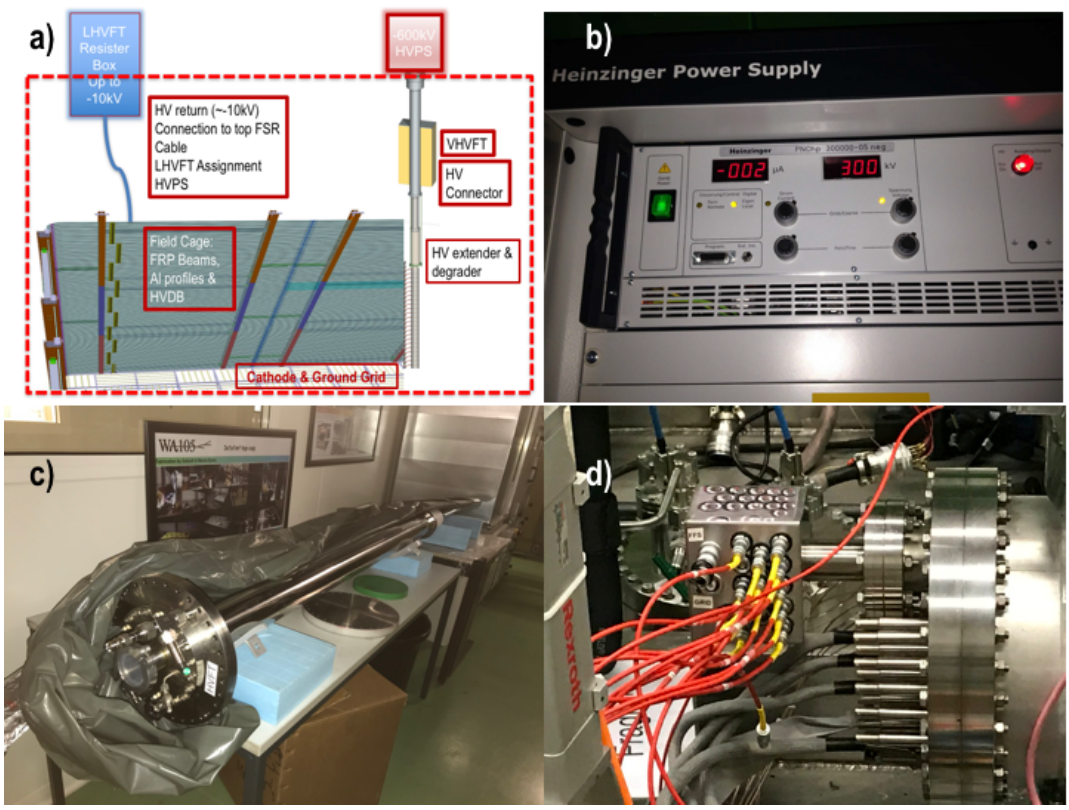

Figure 1.2: (a) Schematic overview of the HV system for a DP detector module, (b) photograph of the 300 kV Heinzinger power supply[1], (c) the HV feedthrough, and (d) the HV return connection. (All photographs from WA105 DP demonstrator.)

The system operates at the full range of voltages, −600 kV to ground, inside the TPC volume.

The SP and DP modules will use similar designs for some HV system components, in particular, some aspects of the FCs and their supporting beams. The DP versions are described in this chapter.

The design presented in this chapter is primarily based on the ProtoDUNE-DP, ProtoDUNE-SP, and WA105 DP demonstrator experiences. Scaling up from the size of these prototypes presents some challenges that the DUNE DP module is designed to meet, e.g.,

- generating and transmitting the 600 kV voltage safely to the cathode plane 12 m below the liquid level;
- safely dissipating all the energy stored (~ 3 kJ) in the TPC in the event of an HV discharge; and
- managing the dissimilar thermal contraction rates of the various component materials over the 60 m length of the TPC.

1.2 Design Requirements

The working principle of the LArTPC relies on applying a strong and very uniform E field. A number of detector performance parameters benefit from such an E field in ways that directly support the core components of the DUNE physics program. Some of these are examined in detail in technical design report (TDR) Volume 2, DUNE Physics. Here we set the context by presenting a qualitative description of the E field effects on physics.

Since free electron drift velocity in liquid argon (LAr) is a function of the E field, a uniform E field allows mapping along the drift direction using simple time versus position and enables precise and efficient 3D reconstruction. This allows, for example, establishing a well defined fiducial volume for reconstructing beam neutrino events in the DUNE DP module. A neutrino charge-parity symmetry violation (CPV) measurement, or a neutrino mass hierarchy test, compares normalized spectra for electron and muon neutrino and antineutrino interactions in the fiducial volume of the DUNE DP module, as projected from the near detector (ND). For this reason, fiducial volume characterization is critical.

Spectral information is necessary to separate charge parity (CP) and mass hierarchy (MH) effects, necessitating efficient track and shower reconstruction and good energy resolution. Toward these ends, higher E field strengths are generally better. More free charge is created at the ionization points because recombination decreases at higher fields, improving S/N and calorimetry. Drift times are reduced, resulting in less electron capture and better S/N, even under less than optimal LAr purity conditions. Spatial resolution improves as $\sqrt{t_{drift}}$-dependent diffusion effects decrease. Higher free charge production and lower electron capture give lower detection thresholds on components of electromagnetic showers, improving shower energy reconstruction. Lower detection thresholds also lead to higher detection efficiency for MeV-scale electron, photon, and neutron signatures of low-energy ν_e interactions from supernova neutrino burst (SNB) events. The decreased recombination affects highly ionizing particles, usually protons, more than minimum ionizing particles (MIPs). Less saturation of free charge production occurs, leading to better particle identification and more precise energy measurements. Lower recombination particularly helps proton-kaon separation by dE/dx, a key component of a search for $p \to K^+\nu$ baryon decay events.

However, apart from obvious technical limitations, the E field should not be raised beyond certain limits. For instance, while free charge production increases with E field, scintillation photon production decreases, resulting in fewer photons available for both triggering and establishing t_0. Two-track separation can degrade if drift velocity is increased while keeping the electronic waveform sampling frequency fixed. The distance between the TPC boundaries and the cryostat walls would likely need to be increased for very high E fields to prevent electrostatic discharge. This would, in turn, reduce the fraction of the LAr within the fiducial volume. The effects of the reduced number of photons is modest, and all effects are subsumed by technical challenges in delivering HV to the cryostat and maintaining highly stable HV surfaces for long-term operation. These challenges require developing non-commercial cryogenic HV feedthroughs, HV ripple-repression through custom HV RC circuits, careful construction and deployment of HV cables, redundant HV connections, high-precision monitoring, and best practices at all stages of design, installation, and operation.

Two decades of design and operational experience that began with ICARUS [2] have established that a 500 V/cm field is an appropriate trade-off value that can be realistically achieved using cost-effective design and construction methods. Achieving this design goal in the DUNE DP module will be challenging because of the 12 m drift distance, and the importance of overall detector optimization. The forthcoming test of ProtoDUNE-DP will likely run at the nominal HV of −300 kV applied on the cathode. Its successful operation will confirm that the DUNE DP module can operate at least at E=250 V/cm. However, it must be able to run at an E field of up to the nominal 500 V/cm (HV of −600 kV) to compensate for unexpectedly low-purity conditions that could arise over two decades of planned operation.

The 500 V/cm E field goal, combined with high LAr purity, a large S/N ratio, and a large CRP gain, will allow a wide range of possible operating points to optimize detector performance for maximum physics potential over two decades of stable conditions and very high live time. This value is therefore set as the goal. The value for minimal acceptable detector performance is 250 V/cm, assuming the purity and electronics specifications are achievable.

Unlike the single-phase (SP) case, in the DP detector space charge could distort the E field to a non-negligible degree because of the presence of the irreducible ^{39}Ar radioactive background that constantly produces positive ions in LAr and the long drift distance that prolongs their presence in the drift volume. Injections into LAr of positive ions produced by the electron multiplication in the large electron multiplier (LEM) amplification stage (up to a factor 20 at nominal LEM gain) could significantly enhance this effect. To reduce the overall space charge, it is necessary to keep the E field in the drift region as high as possible to drift the positive ions more quickly toward the cathode where they are neutralized. This underlines the importance of reaching the nominal value of 500 V/cm in the DP module despite the greater challenges.

The HV system is designed to meet the physics requirements of the DUNE experiment. This includes both physical requirements (e.g., an E field that allows robust event reconstruction) and operational requirements (e.g., avoiding over-complication that could compromise data collection efficiency). A collection of essential specifications for the HV system is shown in Table 1.1.

Table 1.1: Specifications for DP-HV

Label	Description	Specification (Goal)	Rationale	Validation
DP-FD-1	Minimum drift field	$> 250\,\mathrm{V/cm}$ ($> 500\,\mathrm{V/cm}$)	Lessens impacts of e^--Ar recombination, e^- lifetime, e^- diffusion and space charge.	ProtoDUNE
DP-FD-2	System noise	$< 2500\ e^-$ ($\sim 1000\ e^-$ (achieved in WA105))	Provides >5:1 S/N on induction planes for pattern recognition and two-track separation.	ProtoDUNE and simulation
DP-FD-3	Light yield	$> 1\,\mathrm{PE/MeV}$ (min), $> 3\,\mathrm{PE/MeV}$ (avg)	Corresponds to point where improvements in resolution with increasing light yield slow down significantly.	Simulated SN neutrinos in FD.
DP-FD-4	Time resolution	$< 1\,\mu\mathrm{s}$ ($< 100\,\mathrm{ns}$)	Enables 1 mm position resolution for 10 MeV SNB candidate events for instantaneous rate $< 1\,\mathrm{m^{-3}ms^{-1}}$.	
DP-FD-5	Liquid argon purity	$< 100\,\mathrm{ppt}$ ($< 30\,\mathrm{ppt}$)	Provides >5:1 S/N on induction planes for pattern recognition and two-track separation.	Purity monitors and cosmic ray tracks
DP-FD-11	Drift field uniformity due to HVS	$< 1\,\%$ throughout volume	High reconstruction efficiency.	
DP-FD-12	Cathode HV power supply ripple contribution to system noise	$< 100\,\mathrm{e^-}$	Maximize live time; maintain high S/N.	
DP-FD-17	Cathode resistivity	$> 1\,\mathrm{M\Omega/square}$ ($> 1\,\mathrm{G\Omega/square}$)	Detector damage prevention.	
DP-FD-24	Local electric fields	$< 30\,\mathrm{kV/cm}$	Maximize live time; maintain high S/N.	ProtoDUNE

DP-HV-1	Provide redundancy in HV distribution	$> num2$ HVDB chain (12 HVDB chains)	Ensure the HV connections to the detector	ProtoDUNE and calculations

1.3 ProtoDUNE-DP Experience

The ProtoDUNE-DP detector has a 6 m × 6 m × 6 m active volume. This enabled testing final detector components at scale, in particular the CRP, the cathode, and the ground grid, whose unit dimensions are 3 m (W) × 3 m (L). The FC, which surrounds the active volume, is made up of modules of dimensions 3 m (W) × 6 m (H); these are in turn made up of 3 m (W) × 2 m (H) submodules. The HV applied to the cathode is at maximum −300 kV to provide a 500 V/cm drift field to the 6 m drift length. The FC submodule assembly procedure and the subsequent installation procedure tested in the cryostat can be applied to the DUNE DP module with some minor changes to reflect the lessons learned from ProtoDUNE-DP.

The ProtoDUNE-DP detector is not yet in operation at the time of this writing, so we can only provide information on the air commissioning (see Section 1.3.4).

1.3.1 Design

The ProtoDUNE-DP FC submodules consist of two 15.2 cm (6 in) FRP I-beams connected by two 7.6 cm (3 in) FRP I-beam cross bars, to form a frame. The two 15.2 cm (6 in) I-beams have slots conforming to the shape of the aluminum profiles, into which they are inserted. Since the mechanical connections between the submodules use 10 cm-wide G10 plates exterior to the active volume as well as the (7.6 cm) I-beam cross bars, a large fraction of the insulators from the FRP frame structure is between the FC electrode and the cryostat membrane wall at ground.

The DUNE DP module FC submodule design has been changed such that all inter-submodule mechanical connections are inside the active volume, away from the cryostat walls, to reduce the potential for streamers, which were observed in ProtoDUNE-SP. Furthermore, to reduce the drift field distortion from surface charge accumulation, the cross bars are replaced with stainless steel tubes (see Section 1.4.5).

Two ProtoDUNE-DP design features raised significant concerns about the risk of discharging a large amount of stored energy toward the membrane wall or the floor: (1) the aluminum profile electrodes that form an electrically continuous field-shaping ring and that are interconnected with aluminum clips, and (2) the use of all stainless steel tubes in the cathode construction. A large discharge could seriously damage the cryostat wall, virtually disable detector operations and cause a significant safety hazard. To address these safety concerns, in the DUNE DP the metal profile clips are replaced with resistive sheaths, and the cathode modules are made of resistive tubes held

by metal trusses, as described in Sections 1.4.5 and 1.4.3, respectively.

The ProtoDUNE-DP resistive HV divider boards shown in Figure 1.3 a-c are designed to provide the desired voltage difference between two adjacent field-shaping rings. Most of these boards cover nine gaps. The two boards that connect the cathode to the FC cover eight gaps due to the total number of field-shaping rings. The design of the HV divider board implements ample redundancy. Each gap between the adjacent field-shaping rings has two 2 GΩ main resistors for the voltage drop and four varistors to accommodate up to 6 kV, twice the operation voltage, in case the final 600 kV HVPS becomes available. ProtoDUNE-DP uses two rows of HVDB for additional redundancy, taking advantage of the electrically continuous field-shaping rings. The board design will change slightly for the DUNE DP module to minimize the potential for a discharge between the solder balls on the back of the board, as shown in Figure 1.3c, that are exposed between the two adjacent field-shaping rings. In addition, since the operational voltage difference is 3 kV between the two adjacent profiles, the number of varistors will be reduced from four to two, significantly simplifying the design of the board and potentially eliminating the exposed solder balls.

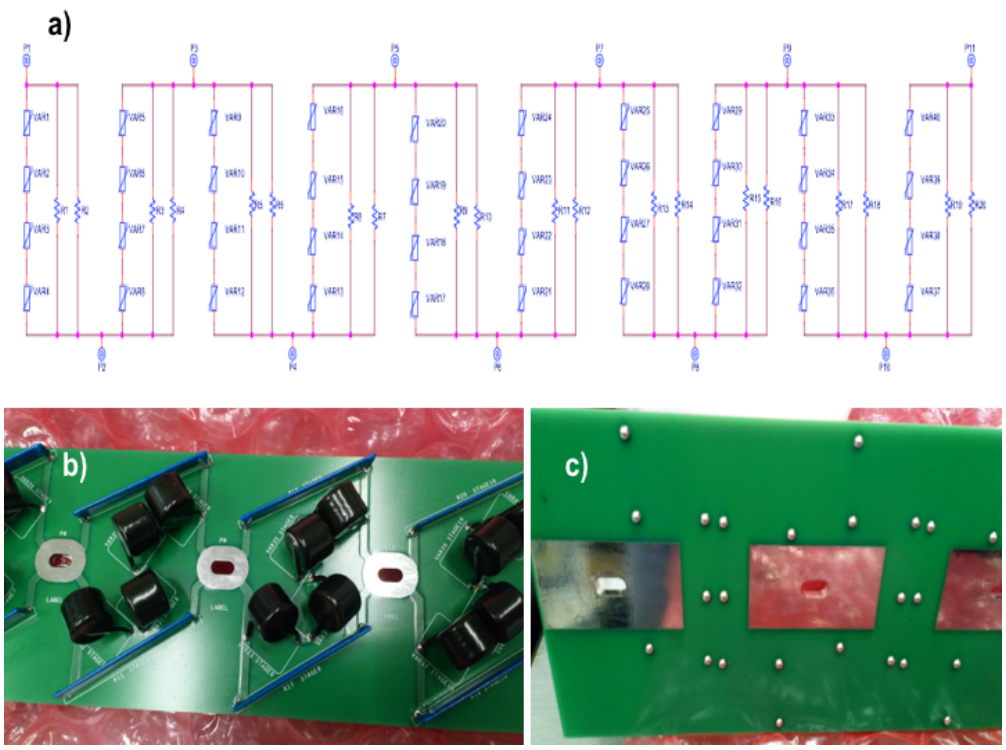

Figure 1.3: ProtoDUNE-DP HV divider board: (a) schematic circuit diagram, (b) photograph of the top of the board, and (c) photograph of the bottom of the board.

1.3.2 Construction

The ProtoDUNE-DP construction process worked out well, so the same process will be followed for the DUNE DP module. The vendor-machined FRP parts for the FC are processed at the factory to eliminate burrs and defects left on the parts for quality assurance (QA) and quality control (QC). These parts are then cleaned following a procedure using de-ionized water and

colorless Simple Green [2], and dried in a humidity-controlled storage room. Once the FRP I-beam parts are dried, the processed surfaces are covered with polyurethane varnish for further suppression of any remaining fiber on their edges. The parts are then brought to a humidity-controlled cleanroom (class $\sim$10,000), assembled as a frame to ensure mechanical fitness, then disassembled and packaged as a compact package of 0.2 m (W) $\times$ 0.2 m (H) $\times$ 2 m (L), and wrapped in plastic shrink wrap for storage before shipment. The design change makes it significantly easier to process and condition the FRP parts since the FRP I-beams no longer have slots conforming to the profiles, eliminating the time-consuming machining and cleaning process. In addition, the size of the package for each submodule will be considerably more compact than for the ProtoDUNE-DP FC submodules, since the width of the I-beams is 10.2 cm (4 in). Figure 1.4 shows the FC parts and connections for ProtoDUNE-DP.

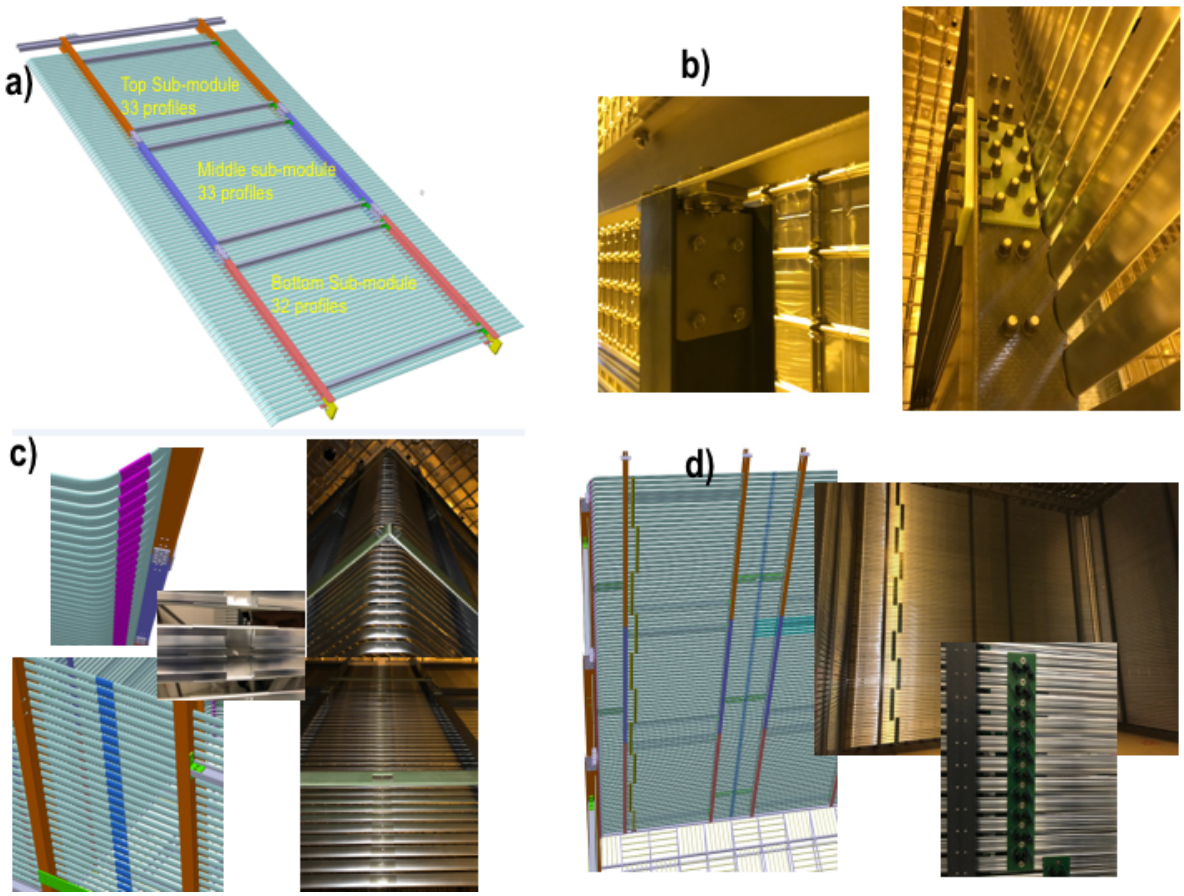

Figure 1.4: FC parts and connections for ProtoDUNE-DP: a. One 3 m (W) $\times$ 6 m (H) ProtoDUNE-DP FC module consisting of three 3 m (W) $\times$ 2 m (H) submodules. The DUNE DP module has a virtually identical structure except for the number of middle submodules (four) and the profile length (4 m instead of 3 m in ProtoDUNE-DP); b. A photograph of the top module connection to the stainless steel I-beam and an inter-submodule connection; c. Aluminum clip connections in the corner and in the straight sections. These clips will be replaced with resistive sheaths in DUNE DP module to increase the decay time in case of discharge; d. HV divider boards and their connections on ProtoDUNE-DP FC.

The resistor and varistor parts for the ProtoDUNE-DP HVDBs were tested in air while warm, in

[2] https://www.simplegreen.com

LN_2, and then again in air after warm up, to ensure the quality and resilience of the parts. Based on these measurements, parts were selected to ensure resistance values within 1% of the mean. The selected parts were shipped to the contractor to be mounted on the PCB with through holes allowing soldering on the back of the board. The boards with resistors mounted on them were then tested again for QC, twice in air and once in LN_2, unless any of the gaps failed the QC criteria, in which case the board was rejected and sent back to the manufacturer to replace the parts in the failed gap. The same QC process will be used for the DUNE DP module.

The ProtoDUNE-DP 3 m× 3 m cathode units were built out of stainless steel tubes welded together in a structure that ensures over 90% light transparency. To slow down energy release from an unexpected discharge in ProtoDUNE-DP, resistor boards were built to interconnect two neighboring cathode units. This resistor network, however, affected the input voltage to the HVDB row diagonally across the FC panel that accepts HVPS input. The bottom-most gap of the HVDB row was then modified to compensate for the voltage drop across the diagonal connection from the HV input. The DUNE DP module cathode will also implement resistors, as described in Section 1.4.3.

1.3.3 Assembly and Installation

The FC submodules were built in the cleanroom in front of the temporary construction opening (TCO) of the ProtoDUNE-DP cryostat. The assembly of each submodule, including inserting and securing the profiles onto the FRP frame took two people approximately two hours. When as many submodules were built as the cleanroom storage space allows, they were brought into the cryostat for installation. Installing each 6 m (H) × 3 m (W) full length module began with hanging the top submodule to a $\sim$ 3 m stainless steel I-beam attached to the stainless steel cable through feedthrough in the ceiling. The subsequent two submodules were then hung onto the top module successively. The whole installation process for a 6 m module took four people approximately an hour, with two people inside the cryostat connecting the modules while the other two were outside on top of the cryostat roof, operating the winches that raise the corresponding partial module as the successive submodules were attached.

This scheme requires two feedthrough holes per module, which makes the total number of FC installation feedthrough holes large. Figure 1.5 shows the two submodules connected and hanging from the two sets of stainless steel cables on the ceiling (left) and the inter-submodule connections (right).

A modified installation plan has been developed to dramatically reduce the number of feedthrough holes and reduce the parts needed for the FC modules, as described in Section 1.4.5.

The 3 m (L) × 3 m (W) ProtoDUNE-DP cathode and ground grid modules were preassembled outside of the cleanroom and brought into the cryostat for installation. The assembly and installation scheme for the DUNE DP cathode must also change because its structure and material composition will be modified so as to dramatically increase the time for energy release in order to protect the cryostat.

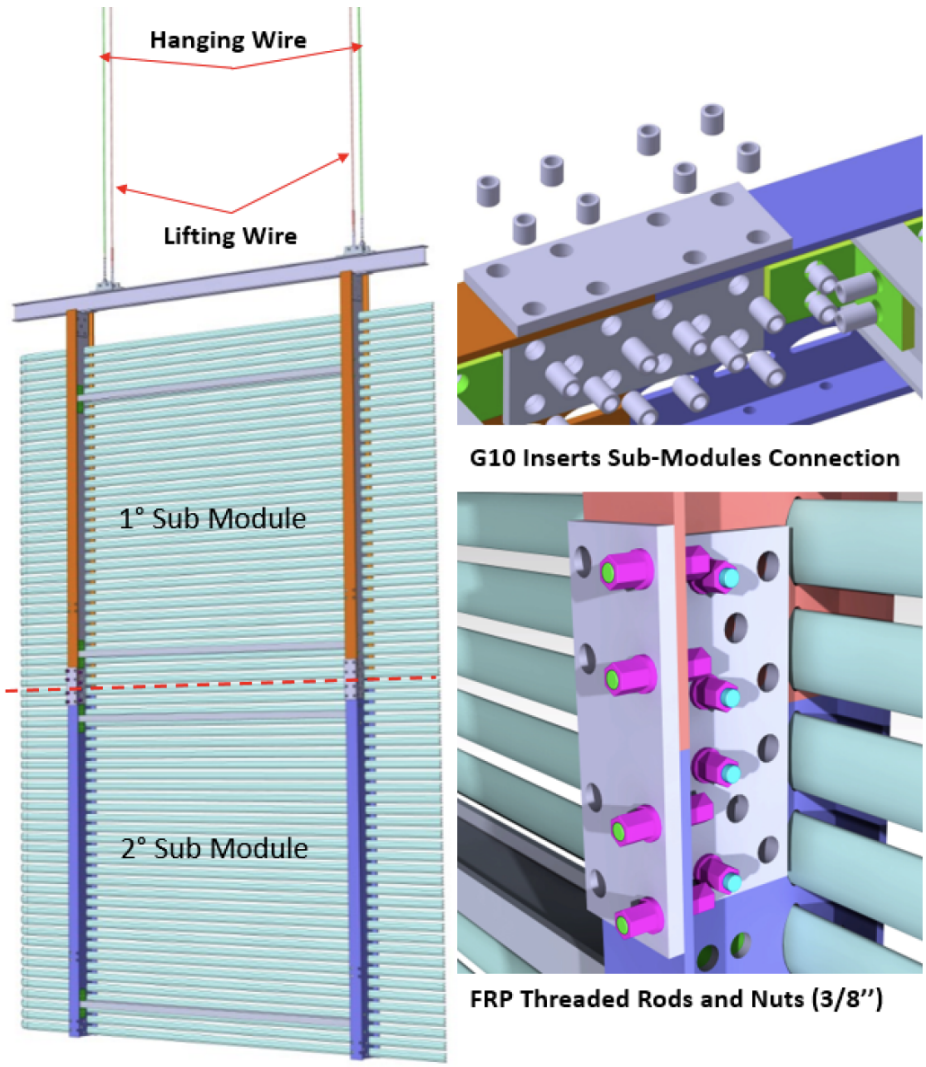

Figure 1.5: Left: Two submodules connected and hanging from the two sets of stainless steel cables on the ceiling. The lifting wires raise the module to its position as submodules are connected; the hanging wires keep the fully integrated module in its final position. Right: Inter-submodule connections. Each connection is made with two 1 cm thick G10 plates along the height of the I-beams and one 1 cm thick G10 plate on the flange.

1.3.4 Pre-cool-down Commissioning Test

To ensure the performance of the FC and to identify any issues well before the final installation of the detector pieces, the ProtoDUNE-DP FC was connected to a 150 kV power supply for an "air commissioning" test. The entire FC was fully installed and connected; slip nuts were used for inter-module connections to provide electrical continuity. As the electrical interconnections were made to each field-shaping ring, the resistance between the two neighboring rings was measured and compared to the expected values to verify the connection. The 150 kV HV was fed into the two middle field-shaping rings along the FC. This ensured a voltage difference between any two neighboring rings of 3 kV (the operational voltage) when the top-most and bottom-most rings were connected to the ground on the membrane wall.

An online wide-angle camera was placed on the floor at the corner where the HV was fed in to ensure any possible sparks could be seen. Current and voltage were carefully monitored and recorded to make sure any discharges could be observed and studied. When the HV was turned on for the first time, the current settled at about 50% higher than expected after the charge up. Voltage was left on for many hours to monitor the long-term behavior of the FC. The current continually increased to unexpectedly higher values several times through multiple power cycles. A systematic test revealed that the size of the current read back was directly proportional to the number of FC modules, independent of the magnitude of the current.

This result led to the hypothesis that current was flowing through a layer of water that formed on the surface of the FRP beams due to the ambient humidity.

Resistance measurements of a 50 cm long, 15.2 cm (6 in) wide I-beam sample piece were made in air at roughly the same humidity level and in LAr. The measurement in air was consistent with the ProtoDUNE-DP FC result, but in LAr the resistance showed expected values with virtually no surface current. Since this behavior was not observed in the ProtoDUNE-SP FC, which was under the similar humidity environment, we suspect that the FRP beams from different manufacturers may have different surface water adhesion properties. Thus, it may be necessary to study the FRP beam from the current manufacturer in further detail for the DP module FC.

1.3.5 Suggestions for future R&D

Based on experiences from construction, assembly, installation and the "air commissioning" of the high voltage system (HVS) at ProtoDUNE-DP, the following R&D items have been identified.

- FRP surface-water adhesion property,
- use of resistive sheath instead of aluminum clips,
- distance between two neighboring profiles,
- optimal resistance for delaying energy releases, and

- generating and transmitting 600 kV to the cathode safely in collaboration with Heinzinger.

1.4 HV System Design

The structural elements of the DUNE DP module cathode and FC resemble a rectangular wire basket (see Figure 1.1). The HV system components are summarized in Table 1.1. The vertical FC members are made of FRP beams and the horizontal members are made of stainless steel. The cathode (the bottom of the basket) consists of 15 pairs of 12 m long stainless steel trusses interconnected by stainless steel tubes at the bottom edges of the FC. Stainless steel I-beams support the FC from above; they are tied together to form a rigid rectangular frame.

Table 1.2: HV System Components. Dimensions are given relative to the 60 m length (L), 12 m width (W), and 12 m height (H) of cryostat.

Item	Arrangement	L	W	H	Components	Grand Total
HVPS	atop cryostat on feedthrough					1
HV feedthroughs						1
HV extender and voltage degrader	runs vertically down from feedthrough			12 m		1
HVDB row	runs vertically down each super-module					12
HVDBs	18 11-gap HVDBs and one 1-gap HVDBs per super-module					216 + 12
Degrader rings	installed on voltage degrader, 1 per field-shaping ring					199
HV return feedthroughs						1
Resistor box						1
Cathode modules	1 W × 15 L (horiz)	4 m	12 m	-	-	15
Cathode trusses	two per cathode module, run along cryostat width (horiz)		12 m			30
Ground grid modules	4 W × 20 L (horiz)	3 m	3 m			80

Resistive FRP rods in cathode	122 per cathode module, run along length (horiz), threaded through trusses					1,830
HV cable segments in bus	inside the cathode outer tubes					TBD
field-shaping rings		2×60 m	2×12 m			199
Profiles	33 (stacked) per FC submodule (34 on bottom submodules)	4 m				6,368 (straight) + 796 (90° bent)
FRP beams in FC	two per FC submodule	2 m	5 cm	10 cm		432
FC submodules	90 per long side, 18 per end (vert)		4 m	1.98 m	-	216
FC modules	15 L, three W (vert)		4 m	12 m	six stacked submodules	36
FC super-modules	five per long side, 1 per end (vert)		12 m	12 m	three adjacent FC modules	12

The DUNE DP cathode consists of an array of thin rods because it must be effectively transparent for scintillation light to reach the photomultiplier tubes (PMTs) below it. The basic mechanical and electrical element of the cathode plane is a 12 m long metal truss structure connecting the two FC super-modules opposite one another across the TPC volume. Two such trusses are linked (resistively) by two metal tubes at the ends, and 122 resistive rods (4 m long) are threaded across the trusses to form the cathode plane.

During cool-down, this top stainless steel frame, and all the stainless steel bracing bars between the FC FRP beams, as well as the entire cathode plane, shrink uniformly at the same CTE to ensure the walls of the FC move inward uniformly without additional stress.

The ProtoDUNE-SP operation revealed some instability in the HV system apparently related to surface charge build-up on the HVS insulating components. Based on this experience, the DUNE DP cathode and FC structure have been redesigned to eliminate all insulation surfaces outside of the active volume between the FC and the cryostat wall.

1.4.1 High Voltage Power Supply and Feedthrough

The HV delivery system consists of

- one HVPS,
- one HV cryogenic feedthrough, and
- one HV cryogenic extender,

as listed in Table 1.2. To ensure the nominal E field of 500 V/cm over the 12 m drift distance, an external HVPS must deliver −600 kV to the cathode through one HV cryogenic feedthrough, with a maximum current draw of 0.5 mA. At present, such a power supply does not exist, but Heinzinger, the industrial partner and leader in producing HVPSs, is committed to executing a vigorous R&D program toward this goal, relying on the following facts:

- 600 kV power supplies are feasible, scaling the present industrial technology although with significant development due to the doubling of the maximum delivered voltage with respect to the presently produced HVPSs.
- The same is possibly true for the HV cryogenics feedthrough, scaling to larger diameter and longer length than the present feedthrough prototypes for 300 kV delivery.
- The critical points of the HV distribution are then the cable and its connectors on the power supply and on the HV feedthrough.

A joint R&D program between DUNE and Heinzinger aims to eliminate cables and connectors, by building a power supply that can be mounted directly on the top of the HV feedthrough. A sample schematic and some details are shown in Figure 1.6.

Recent discussions with Heinzinger on the joint development of the "cable-less" −600 kV power supply, have led to a tentative schedule with three major steps, identified and proposed directly by Heinzinger:

- Assuming that the −300 kV power supply performs as expected in ProtoDUNE-DP, a workshop will be held at CERN or at Heinzinger in the summer of 2019 with the aim of finalizing a detailed plan for the design and the technical performance requirements of the −600 kV power supply. A dedicated Heinzinger R&D engineering team will take part to this workshop.
- The actual development phase of the −600 kV power supply could then start early in the second half of 2020 (due to other previous commitments within Heinzinger). At that time, the Heinzinger R&D team will be made fully available to work with high priority on the ultra-HV power supply project.
- The delivery of the −600 kV power supply unit (plus eventually a spare one) is expected to take place about 1.5 years from the start of the development phase (i.e., by the end of 2021).

This time estimate includes development and production phases. Its duration is motivated by the fact that the design of the HV cascade will be different in some points with respect to the present highest-voltage PS in production (−300 kV) and the construction will probably be more complex. The cascade of the −600 kV units will not be simply a straightforward upgrade of the −300 kV type and, during the development, several tests and material/design verification will be required. For instance, a new insulation layout scheme must be designed and the corresponding insulating material must be chosen and carefully tested. Also, other components and mechanical parts inside the cascade must be designed from scratch and then tested separately.

The schedule and actual cost of the project will be better understood after the 2019 summer workshop, when the design and the parameters of the unit will be finalized. Note that no intermediate prototyping is foreseen by Heinzinger because, at the moment, this is considered a special project with power supply unit(s) produced only for our purposes.

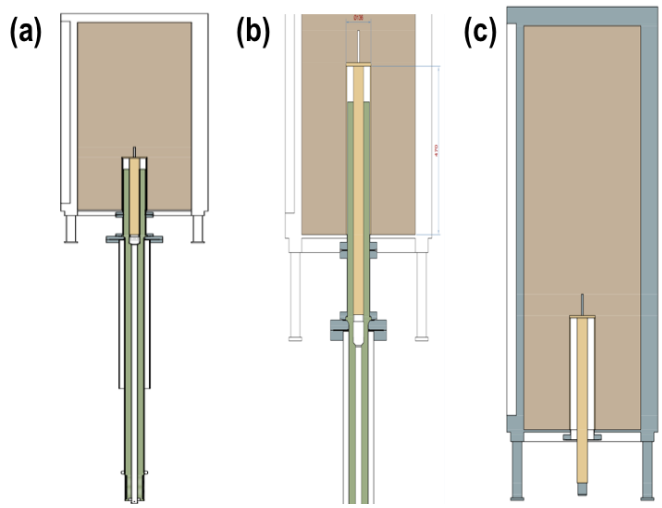

Figure 1.6: (a) Vertical cross section of the proposed HV power supply inserted over the 600 kV HV feedthrough for the DP detector module. (b) Insertion detail of the proposed HV power supply over the 600 kV HV feedthrough. The female add full name (HDPE) of the HV feedthrough is indicated in green. The male plug of the HVPS, shown inserted, is a metallic conductor inserted in an HDPE insulating tube (indicated in yellow). The gap between male and female is filled via a tube inside the HVPS (not indicated) by a silicone oil such as RHODORSIL 47 V1000. (c) Vertical cross section of the HVPS. The front panel is on the left.

Typical Heinzinger power supplies have ripples in the range of ∼30 kHz with an amplitude of $0.001\,\%\mathrm{V}_{\mathrm{nom}} \pm 50\,\mathrm{mV}$. A low-pass RC filter designed to reduce the voltage ripple could be integrated into the output of the power supply. It should be noted, however, that the required ripple suppression need not be as high as for the SP module because the DUNE DP module has more effective shielding of the anodic structure, performed by the extraction grid and by the CRP signal amplification stage.

The HV feedthrough is based on the same successful ICARUS design adopted in both ProtoDUNE-SP and ProtoDUNE-DP. In this design, the voltage is transmitted along a stainless steel center conductor on the warm exterior of the cryostat, where this conductor mates with a cable end. Inside the cryostat, the end of the center conductor has a spring-loaded tip that contacts a receptacle

cup mounted on the top of the HV extender, which is connected to the cathode plane 12 m below. The center conductor of the feedthrough is surrounded by UHMWPE.

To first order, the upper bound of operating voltage on a feedthrough is set by the maximum E field on the feedthrough. Increasing the insulator radius reduces the E field. For the target voltage, the feedthrough uses a UHMWPE cylinder of at least 15.2 cm (6 in) diameter. In the gas space and into at least 15.2 cm of the liquid, a tight-fitting stainless steel ground tube surrounds the insulator. The ground tube has a Conflat[3] flange of at least 25.4 cm (10 in) in diameter, welded on for attachment to the cryostat.

A prototype feedthrough[4] has been successfully tested up to −300 kV in pure argon in a dedicated setup; two similar prototypes are installed in ProtoDUNE-SP and ProtoDUNE-DP.

1.4.2 High Voltage Extender and Voltage Degrader

Since the HV must be guided from the top of the cryostat to the cathode (12 m below the LAr surface), an extension of the HV feedthrough is required, as shown in Figure 1.7 a, b, and c. The extender contains an inner conductor at −600 kV surrounded by an insulator. The extension runs the entire height of the drift volume, so metallic rings (degrader rings) are installed on the periphery of the extension close to the field-shaping ring. Each degrader ring is electrically connected to the field-shaping ring at the same height thus guaranteeing that the drift field in the LAr between the extender and the FC remains undistorted. As an alternative, equipping the extender with an independent voltage degrader is under evaluation. This would have the advantage of eliminating the large number of connecting strips to the FC profiles; on the other hand, it would require an independent path to ground.

1.4.3 Cathode Plane

The DUNE DP detector module's cathode plane forms the bottom of the 12 m (W) × 12.01 m (H) × 60 m drift volume and provides a constant potential surface at −600 kV. It receives its HV from the central conductor of the HV extender that carries the voltage from the power supply through the HV feedthrough.

The cathode plane consists of fifteen adjacent 4 m × 12 m modules to cover the 60 m length of the DUNE DP TPC. The cathode module design is based on the design used in ProtoDUNE-DP, with modifications to accommodate the 12 m span of the DUNE DP module and to implement features to electrically segment the cathode plane.

As shown in Figure 1.8, each cathode module is constructed from two 12 m long trusses made from thin-walled stainless steel tubes with approximately 50 mm outer diameter. They can either be prefabricated and transported underground like the large cryostat beams, or assembled in the

[3] Conflat™, `https://www.lesker.com/newweb/flanges/flanges_technicalnotes_conflat_1.cfm`.
[4] The prototype was manufactured by the company CINEL™ Strumenti Scientifici Srl.

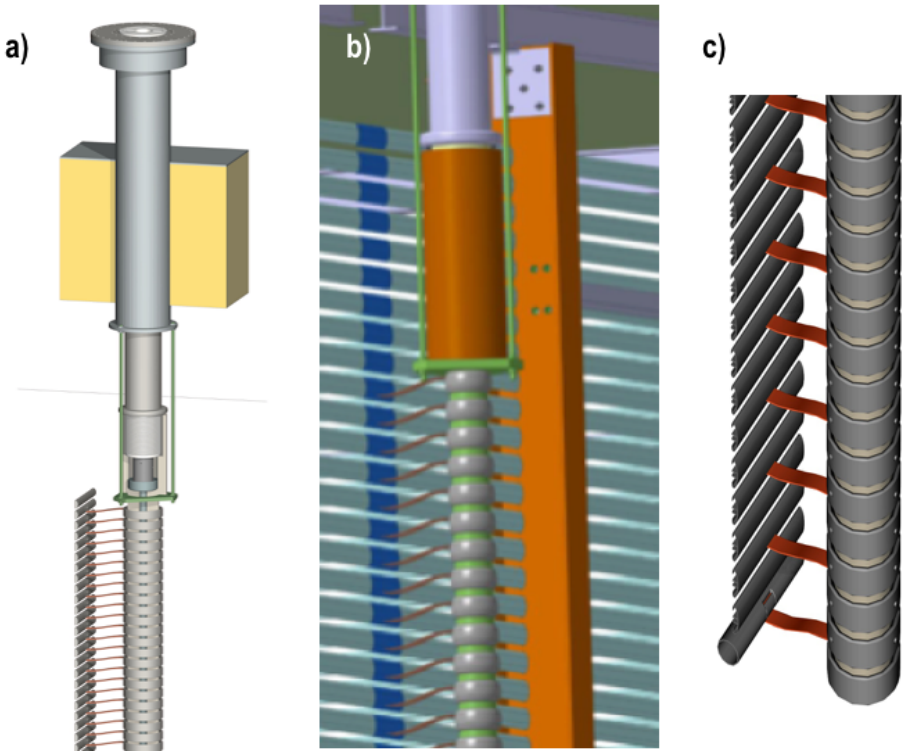

Figure 1.7: Sketches of HV feedthrough and HV extender-degrader: (a) Overview of the HV feedthrough, HV extender, and degrader chain; (b) details of the top portion of the HV extender and its connections to the field-shaping rings; (c) details of the HV extender and degrader connection to the bottom part of the FC, including the connection to the cathode plane.

underground cleanroom from sectional parts. The trusses are 2 m apart and are connected at both ends to stainless steel tubes ("outer tubes" in the figure) that run under the FC and form the outer edges of the cathode plane.

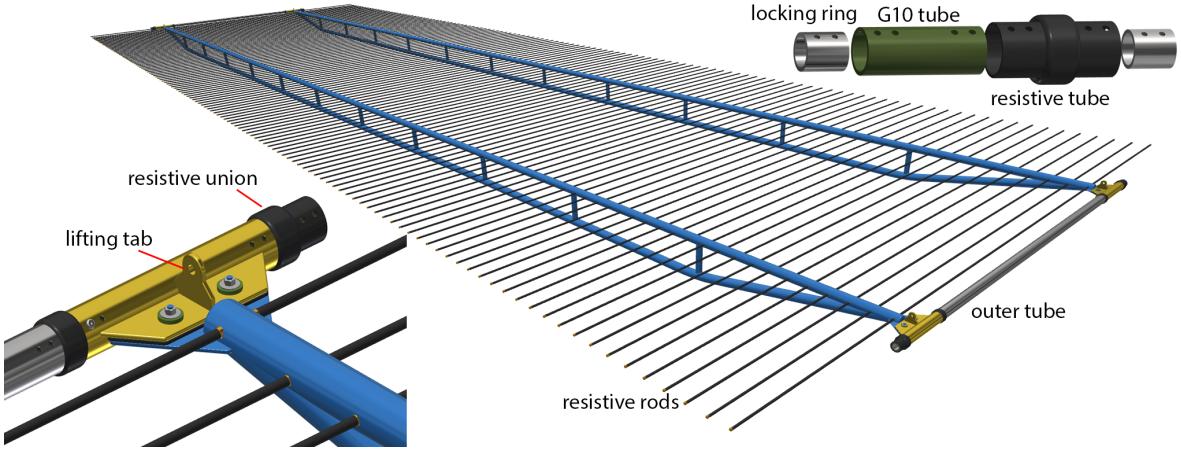

Figure 1.8: A view of a ProtoDUNE-DP cathode module: Construction uses a pair of stainless steel trusses as the framework with an array of coated FRP rods. The lower-left inset shows the details of the resistive interconnect and the lifting tab on the cathode truss structure. The upper-right inset is a detailed view of the components in a resistive union (Credit: BNL).

A total of 122 resistive rods of 10 mm diameter are installed at a 10 cm pitch through the holes in the straight upper tubes of the trusses, forming the effective cathode plane. The rods are made from extruded FRP and wrapped with a layer of the resistive DuPont Kapton XC film [5], also used in the SP cathode plane assemblies (CPAs). They have metal end caps to smooth out the sharp edges of the exposed resistive film and metal sleeves where they cross the trusses, so that they can be locked down with screws on the trusses.

Preliminary mechanical analysis of the design shows that the deflection of the structure is approximately 4 cm when warm and roughly 60% of that when in LAr (Figure 1.9). The cathode modules are suspended from the corresponding FRP I-beams on the FC super-modules along the two long sides of the detector module. Custom resistive unions, shown bottom left inset of Figure 1.8, provide the coupling between trusses and FC modules. Each is made from a resistive sleeve, a G10/FR4 stiffening tube, and two locking rings, as depicted in Figure 1.8, top-right inset.

An HV bus, made from HV cable segments, is threaded through the outer tube ring that is formed once the full set of cathode modules are in place to form a conductive ring that distributes the cathode bias voltage. The mounting plates (shown in gold in Figure 1.8) at both ends of a cathode truss are directly connected to the HV bus via metal rings inside the tube. These mounting plates are also connected to the FC resistive divider chains. Between the mounting plate and the truss, a layer of resistive sheet provides an additional barrier to energy transfer. The resistivity of this sheet will be chosen to ensure the ionization current from ^{39}Ar activity and the ion feedback from the LEM multiplication will not cause significant voltage drop on the cathode.

[5] http://www.dupont.com/content/dam/dupont/products-and-services/membranes-and-films/polyimde-films/documents/DEC-Kapton-summary-of-properties.pdf

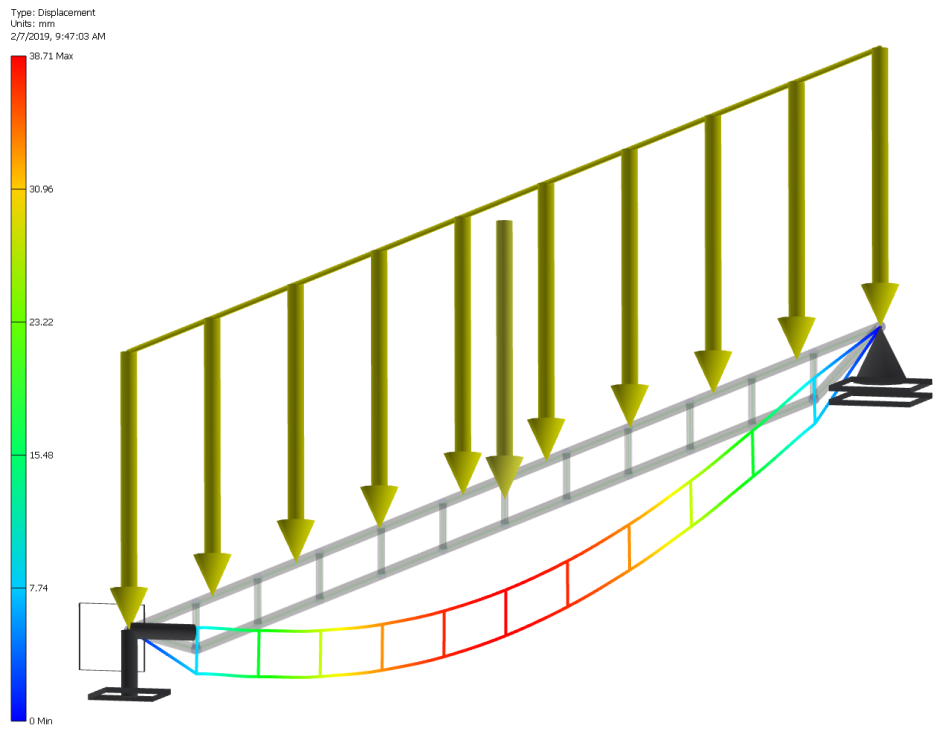

Figure 1.9: FEA of the cathode truss showing the deflection of the structure under its own weight and half the weight of the FRP resistive rods at room temperature. The deflection should reduce to approximately 60% once the structure is submerged in LAr (Credit: BNL).

The energy stored in the volume between the cathode plane and the ground grid (described in Section 1.4.4), which sits under the cathode and above the PDs, is estimated to be 1.7 kJ over the 12 m × 60 m area, based on the cathode voltage and the distance of 1 m between the cathode and the ground grid. The modular construction of the cathode minimizes potential damage to either or both components in the case of a sudden discharge from the cathode to the cryostat membrane. Along the 60 m length of the DUNE DP module, the trusses and their interconnecting metal tubes are coupled with highly resistive unions (on the order of GΩ), designed to restrict the flow of current from any potential discharge site.

Assuming that the 1.7 kJ of energy is stored evenly among the 15 cathode modules, each stores about 110 J. On a cathode module, each truss stores about an eighth of this energy (one quarter in total), while the resistive rods share the remaining three quarters. A worst-case discharge would come from a cathode truss, where ∼15 J is directly available to contribute, with the remaining 95 J arriving within a time constant of a few milliseconds. The energy transfer from other cathode and FC modules must pass through GΩs of resistive connections and therefore will have time constants on the order of a second.

Detailed calculations are in progress to determine the final shape and the size of the cathode and ground grid frames to limit the maximum E field to 30 kV cm^{-1} throughout the LAr volume (Figure 1.10) (see Table 1.1), and to correct the non-uniformity of drift field at the at the edges of the cathode (see Figure 1.11). Structural calculations must also verify the planarity of the cathode as it hangs on the FC supports. Values and voltage characteristics of the connecting resistors will also be defined based on the results of dedicated simulations of the cathode electrical model.

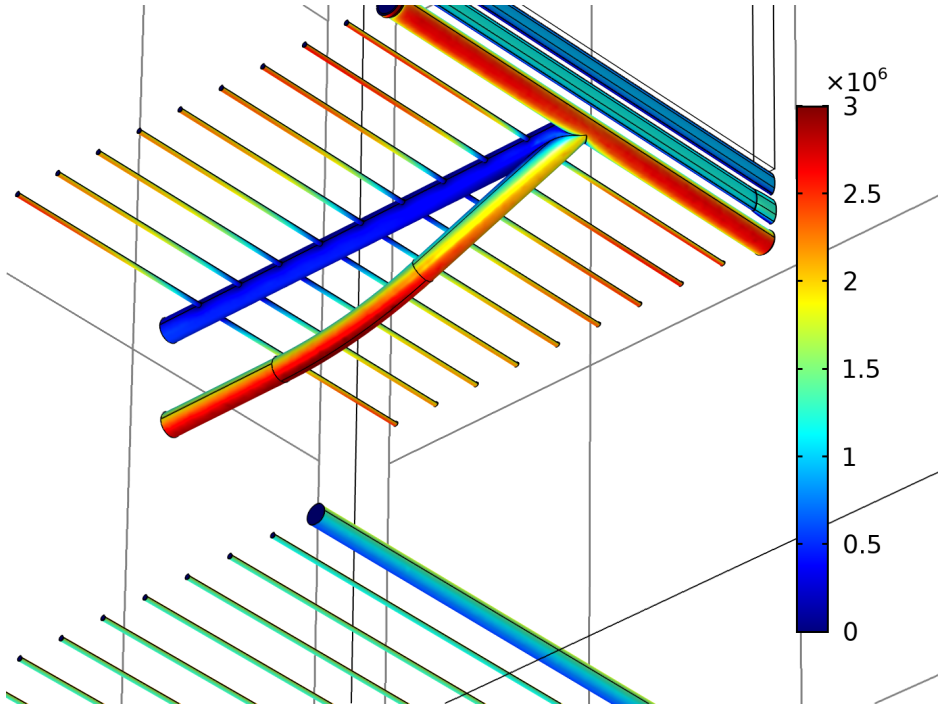

Figure 1.10: Electrostatic calculation of the surface E field on a section of the cathode (upper) and ground grid (lower) structures. The outer tube and the bottom tube of the cathode structure have high surface E field. The maximum E field is approximately 30 kV/cm at the curved section of the bottom tube (Credit: BNL).

1.4.4 Ground Grid

An array of ground grid modules is installed above the PMTs and below the cathode plane to provide a low E field environment for the PMTs and shield them from a potential HV discharge from the cathode plane.

A ground grid module, shown in Figure 1.12, is made from stainless steel (AISI Type 304) tubes and sits above a 3 × 3 array of PMTs at 1.02 m pitch. The ground grid modules are placed on the cryostat floor at a pitch of 3.06 m. The 4 legs for each ground grid module are 2.72 m apart, taking into account the 0.34 m pitch of the membrane corrugation so that the feet are always on the flat part of the membrane. To avoid damage to the membrane floor, the feet will be covered with a Teflon sheet, which will electrically isolate them from the membrane cryostat. The modules are not physically in contact with each other, and can be individually read out to monitor HV stability if needed. Otherwise, electrical contact to the membrane (detector ground) will be through the legs, via springs that penetrate the Teflon sheets or grounding wires to the edges of the cryostat. To cover the entire area of the cathode, a total of 80 ground grid modules are arranged in a 4 × 20 array. Preliminary analysis on the ground grid structure indicates approximately 1 cm of sag in the center of a unit grid. Detailed studies of the grid geometry are ongoing to ensure that the requirement for the maximum local field is satisfied. Figure 1.10 shows the surface E field on the cathode and ground grid near the cathode edge. The maximum E field is under the curved section of the lower truss member at the 30 kV/cm limit.

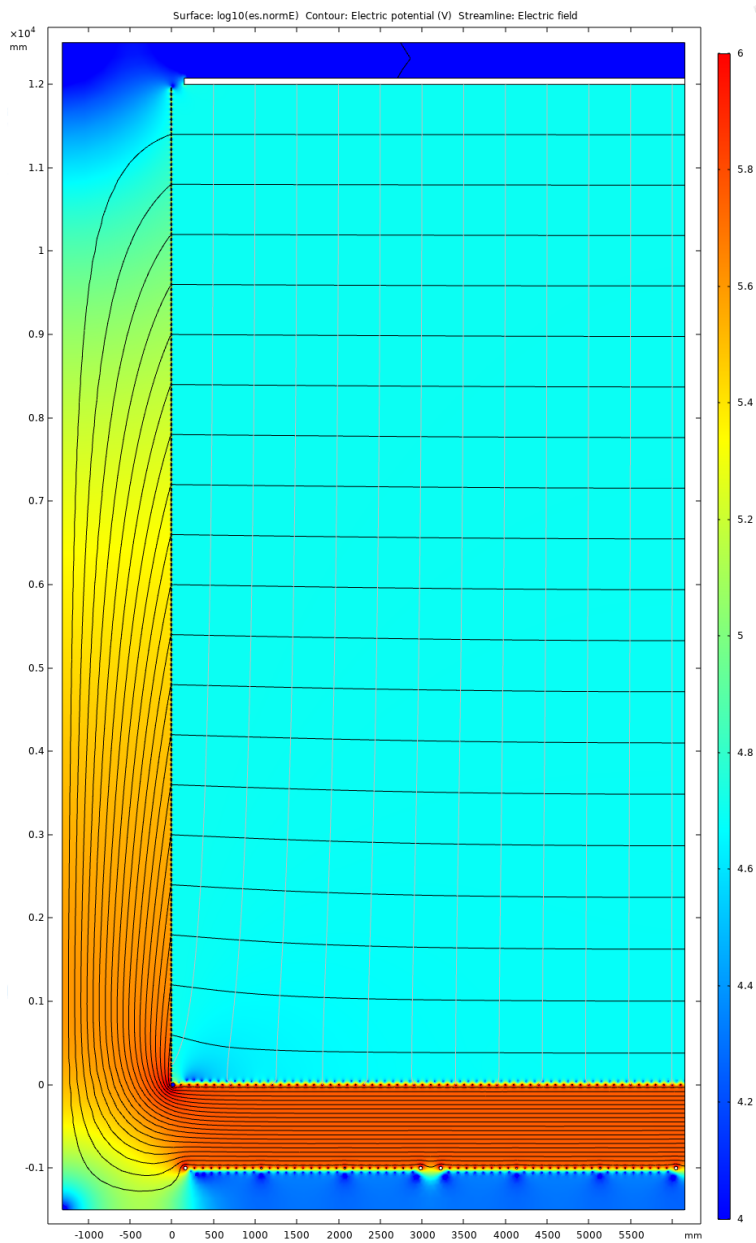

Figure 1.11: 2D plot of the E field (color gradient), equipotential contours (black), and electric field lines (gray) in one half of TPC, looking along the beam direction. The right vertical edge is a symmetry plane. The E field unit is in Log_{10}(V/m). (Credit: BNL).

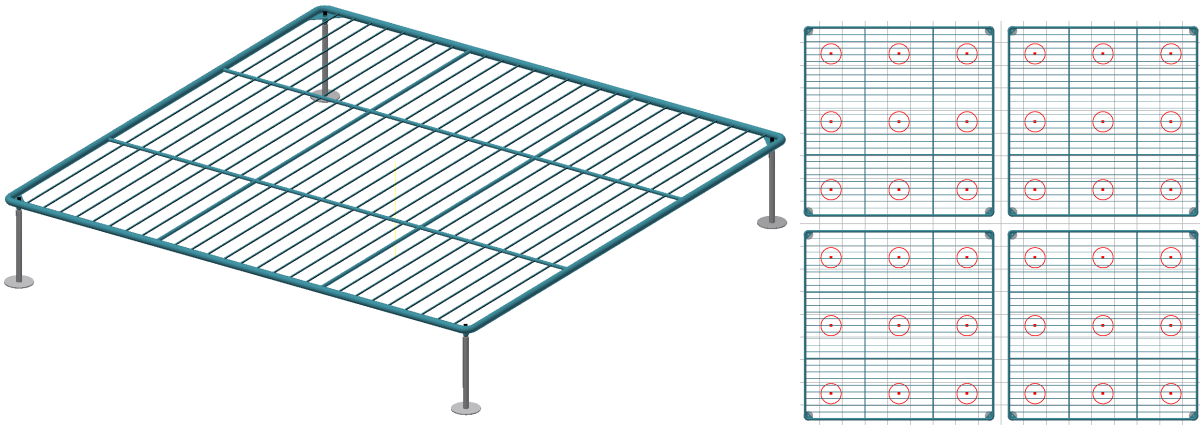

Figure 1.12: Left: A view of a ground grid module; Right: ground grid position relative to the membrane corrugation and PMT locations (Credit BNL).

1.4.5 Field Cage

Similar to the DUNE SP FC, the DUNE DP FC is modular; it is broken down into super-modules, modules and submodules, as listed in Table 1.2. Since the E field must be vertical, the FC's equipotenial conductors, the field-shaping rings, run horizontally around the perimeter of the active volume. The conductors are extruded aluminum open profiles.

Profile sections are arranged into FC submodules. An FC submodule is 2 m high and 4 m wide. Six submodules stack vertically to make a full 12 m high module. Three adjacent modules form a super-module. One row of HVDBs mounts to each end of the middle module's profiles. On each side of the middle module, a 1 GΩ resistive sheath connects each profile with its same-height counterpart in the side module. Surge suppressing varistors are connected in parallel to protect the resistors. Similar resistive interconnects are made between pairs of profiles of adjacent super-modules to provide additional redundancy in the FC electrical connection, leveraging the row of HVDBs in the neighboring super-modules. The connected profiles reach the same bias voltage since no current flows along the ring that they form.

The profiles at the same height in adjacent modules are interconnected horizontally through resistive sheaths. All the same-height profiles form a closed, electrically continuous rectangular ring. The four walls surrounding the TPC's active volume are formed using 199 of these rings stacked vertically in 6 cm pitch. The aluminum profiles are attached to I-beams made of pultruded FRP.

FRP is non-conductive and strong enough to withstand the FC loads. This material meets the Class A International Building Code classification for flame spread and smoke development, as characterized by ASTM E84[6].

The entire FC is constructed from 12 super-modules with nominal dimensions of 12 m width and 12 m height. There are five super-modules along each long side wall, and one each along the short end walls. The cryostat inner length dimension is 62 m. To gain a safe clearance from the cryostat

[6] https://www.astm.org/DATABASE.CART/HISTORICAL/E84-07.htm

wall at the bottom of the TPC where the cathode is at −600 kV, the end wall FC super-modules are designed to be installed 0.5 m from the edge of the active volume. At the top, the inner surfaces of the FC profiles are positioned 15 cm away from the CRPs' active area to allow the FC support structure to pass through and to provide a uniform drift field. For the tilted end wall super-modules, this 15 cm offset applies only to their top edges due to the 2.4 degree tilt. Each super-module, including its top stainless steel beam, weighs about 1200 kg. Figure 1.13 shows a side view of one end of the HV system components depicting the 2.4 degree tilt.

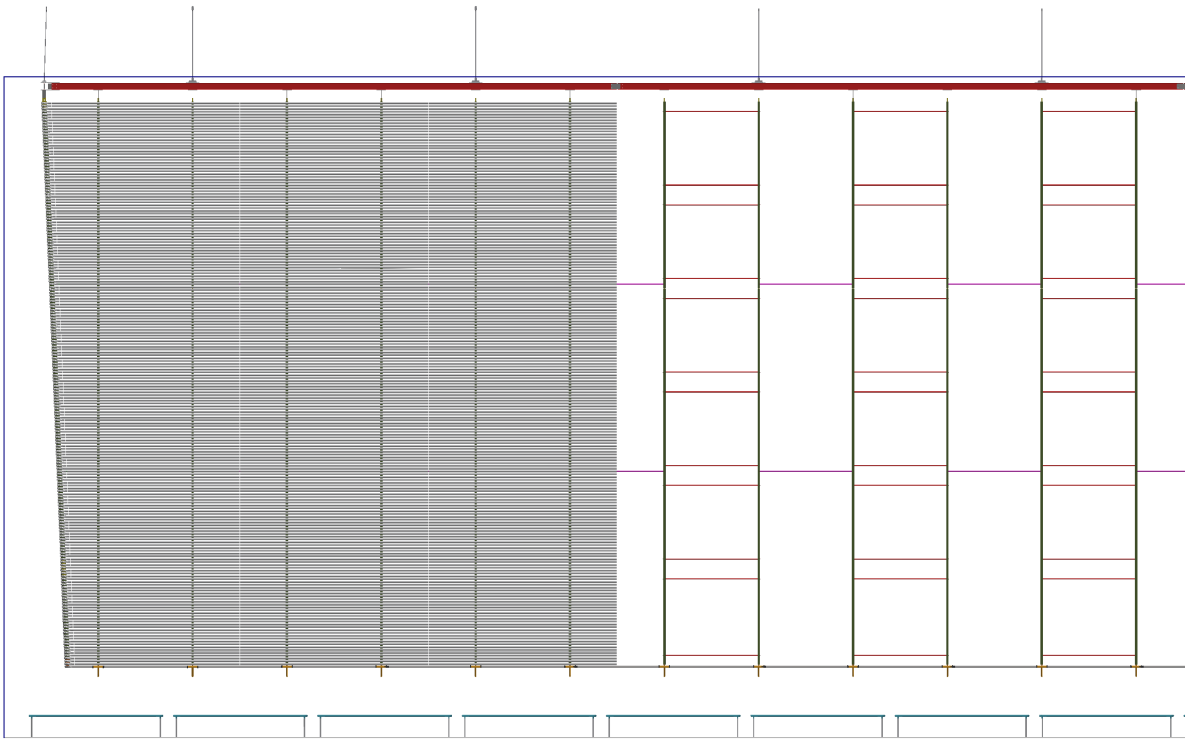

Figure 1.13: A side view of one end of the HV system components in the TPC showing the top frame, left-most super-module with profiles, and the ground grid array on the bottom. The end wall super-module on the left is pushed away from the cryostat wall by 0.5 m on the bottom to gain additional HV clearance (Credit: BNL).

Each super-module is built from three 4 m (W) × 12 m (H) modules, each of which is made of six 4 m (W) × ∼2 m (H) submodules. All submodules share the same basic construction: two 10 cm (H) × 5 cm (W) FRP I-beams with two stainless steel cross bars that form a rigid frame structure, as shown in Figure 1.14. Extruded aluminum profiles of 4 m length are mounted at a 6 cm pitch on one side of the FRP I-beams using screws and slip nuts inside the profiles, as can be seen in the photo in Figure 1.14, top-right inset. Most of the submodules are 4 m (W) × 1.98 m (H). Figure 1.14 shows the design of a non-corner FC submodule.

The DP photon detection system (PDS) has designed tetra-phenyl butadiene (TPB) coated reflector/wavelength shifting (WLS) panels to be installed on the top half of the FC inner surfaces in order to enhance the light collection and to improve the PD response uniformity throughout the entire active volume, as described in Section 3.3.3. The dimension of a reflector/WLS unit panel assembly to be mounted on the FRP I-beams of the FC submodules is 199 cm (W) × 186 cm (H). The reflector/WLS panel assembly at the inter-super-module areas will have special extended

assemblies to accommodate the 2.4 degree tilt of the end walls: 260 cm (W) × 186 cm (H) for the corner side wall FC submodules and 290 cm (W) × 186 cm (H) for all other FC submodules at the intersection of two FC super-modules. The reflector/WLS unit module will be mounted on the FRP I-beams of the FC submodules with six screws. The details of the reflector/WLS panel assembly design can be found in Sections 3.3.3 and 3.4.

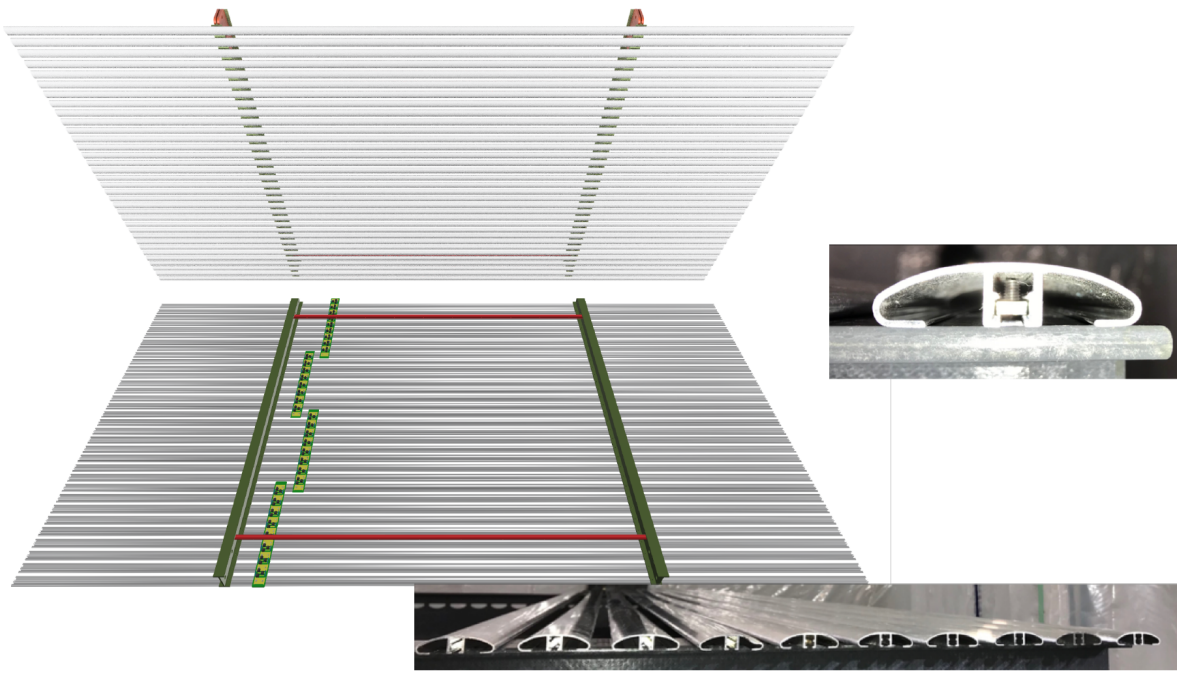

Figure 1.14: Sketches of an FC submodule viewed from inside (bottom) and outside the the FC (top), along with a photo of a partly completed submodule (bottom-right inset) and a close up photo of the cross section of a profile attached to the FRP using a slipnut (top right inset). The inside view shows the two vertical FRP I-beams (green) and two horizontal metal cross bars (red) forming the structural frame work on which 33 aluminum profiles of length 4 m are attached. The outside view shows that outer surface of the FC module is insulator-free to avoid HV instabilities due to surface charging (Credit: BNL).

The extruded aluminum profiles are mounted on the cryostat-wall-side surface of the flange of the 10.2 cm (4 in) FRP I-beam via two stainless steel screws and aluminum slip nuts in the center enforcement rail of the profile, as can be seen in Figure 1.14, bottom-right inset. Each profile is secured fully on one of the 10.2 cm I-beam flanges and more loosely on the other, but sufficient to hold the profile in place. This prevents stress and distortion resulting from the small CTE mismatch between the aluminum profiles and the stainless steel frame structure.

The top submodule has an extended 10.2 cm FRP beam with holes to connect it to the stainless steel I-beam hanging from the ceiling. Each of the FRP I-beams of the bottom submodule has a cutout to hold the cathode plane onto it. The four middle submodules are symmetric along the height and identical, and thus interchangeable.

The corner submodules have similar construction, but with features specific to their locations. On an end wall super-module, the corner modules have 90 °-bent profiles on one side. Along the walls running the length of the cryostat, the modules near the end walls have profiles cut at different

lengths to accommodate the 2.4 degree incline of the end wall super-modules. Figure 1.15 shows a view of the bottom corner of the FC showing the 90°-bent FC profiles on the end wall module and the cathode structure near the end wall.

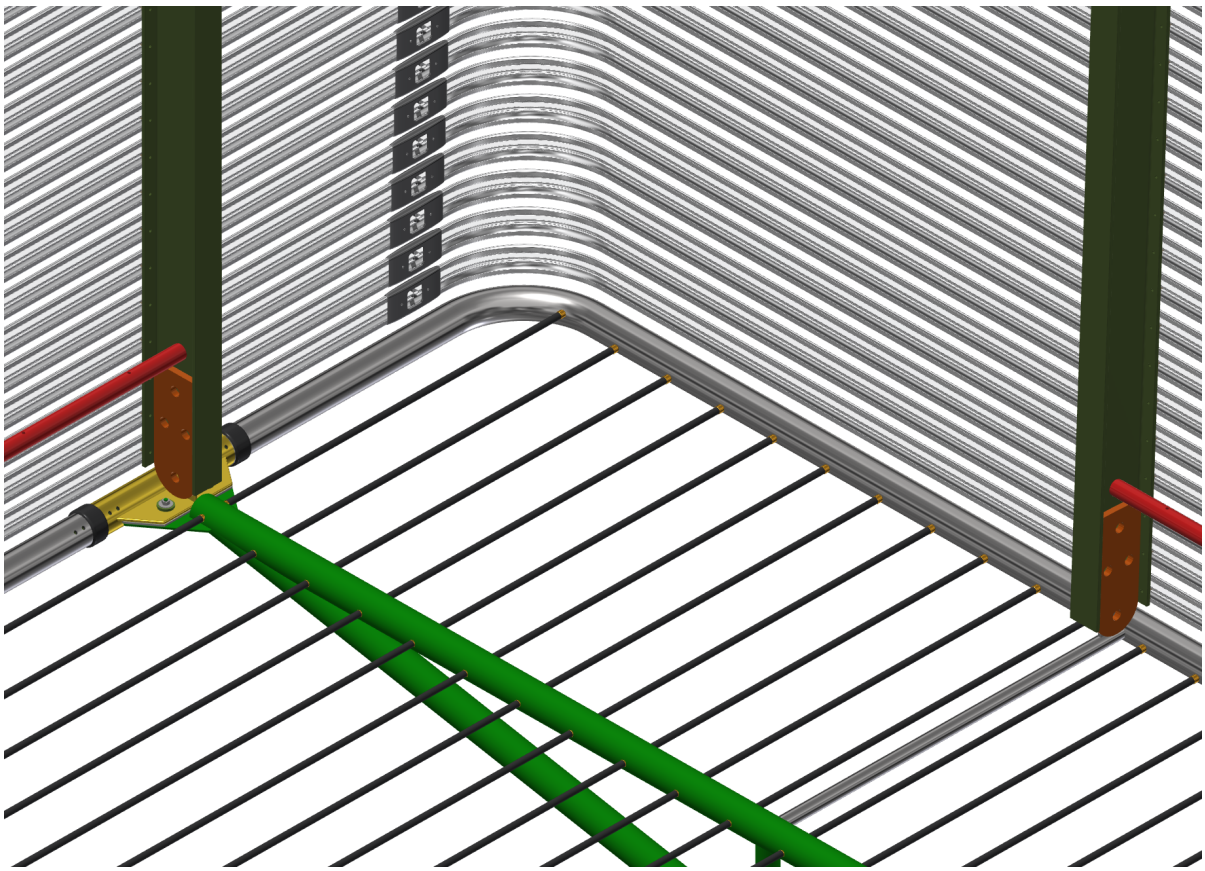

Figure 1.15: A view of a bottom corner of the FC showing the 90°-bent FC profiles on the end wall module and the cathode structure near the end wall (Credit BNL).

The end wall FC modules have a slightly larger pitch between the FC profiles to ensure proper alignment when tilted at the designed angle, and are therefore mounted with a slight angle against the FRP I-beams by means of tapered spacers.

Approximately 500 N of force is needed to keep the end wall FC super-modules inclined. This force is transferred through the interconnected cathode outer tubes to keep the two end walls symmetrical. There will be a few centimeters of sag in the middle of the end walls that will not affect the TPC operation.

Each 12 m module has one top submodule with 33 profiles, four middle submodules with 33 profiles each, and one bottom submodule with 34 profiles, for a total of 199 profiles per module. The nominal voltage of the top-most field-shaping ring is −9 kV. The top submodule makes the mechanical connection to the ceiling of the cryostat from which the entire FC hangs, as shown in Figure 1.5, left. The bottom modules make both mechanical and electrical connections to the cathode. Figure 1.16 shows the interconnection details between the FC submodules (left) and between the bottom FC submodule and the cathode structure (right).

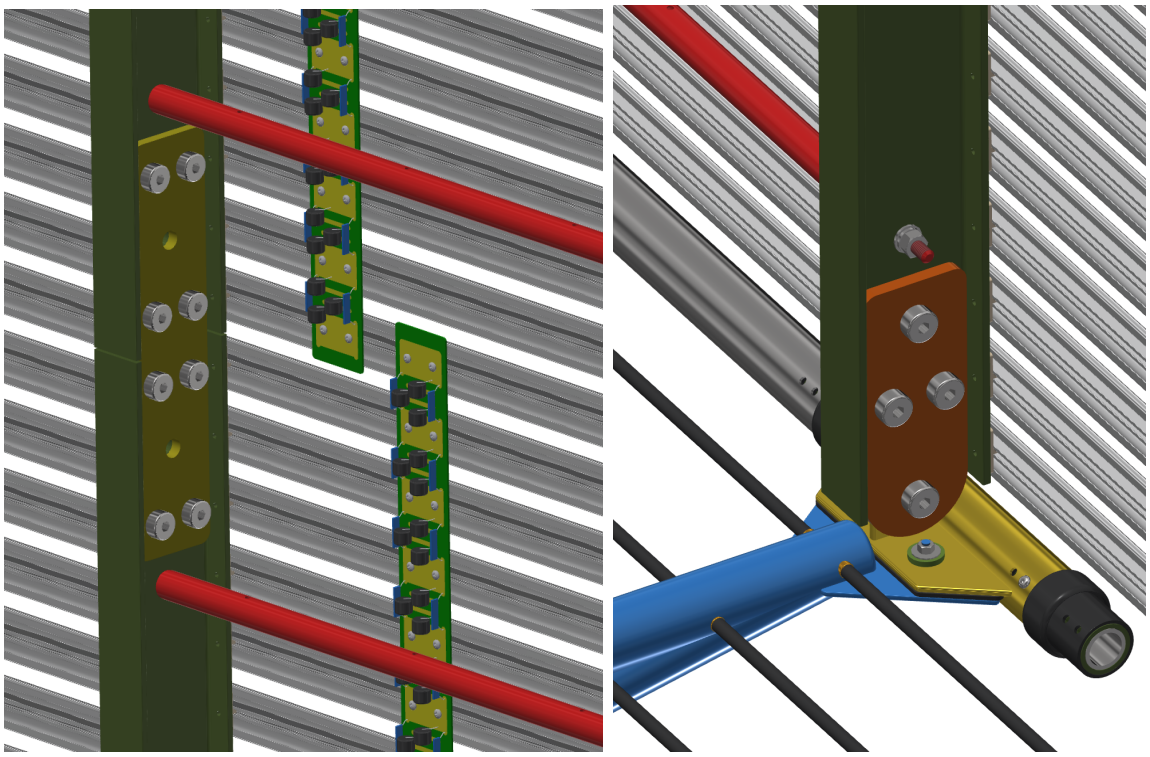

Figure 1.16: Left: Interconnect details between FC submodules; Right: Interconnect details between the bottom FC submodule and the cathode structure. All metal fasteners used here are aligned with the centers of nearby FC profiles and connected electrically to the FC profiles at the same height (Credit: BNL).

1.4.6 Electrical Interconnections

A rib runs down the center of each aluminum profile to provide mechanical strength and act as a rail for the slip nuts that hold the profile onto the supporting FRP frame. The rib also serves as a rail for the square nuts that hold the HV divider boards for both mechanical and electrical connections, and the nuts for securing the resistive sheath (see Figure 1.17 a). The set of all profiles at a given height are electrically connected together, end to end. Each neighboring pair is connected via a resistive sheath screwed onto the nuts in the center ribs across the two profiles, as shown in Figure 1.17 b and c. These images show a 3D-printed mock up plastic sheath with a profile inserted and connected to it using metal screws to allow electrical conduction.

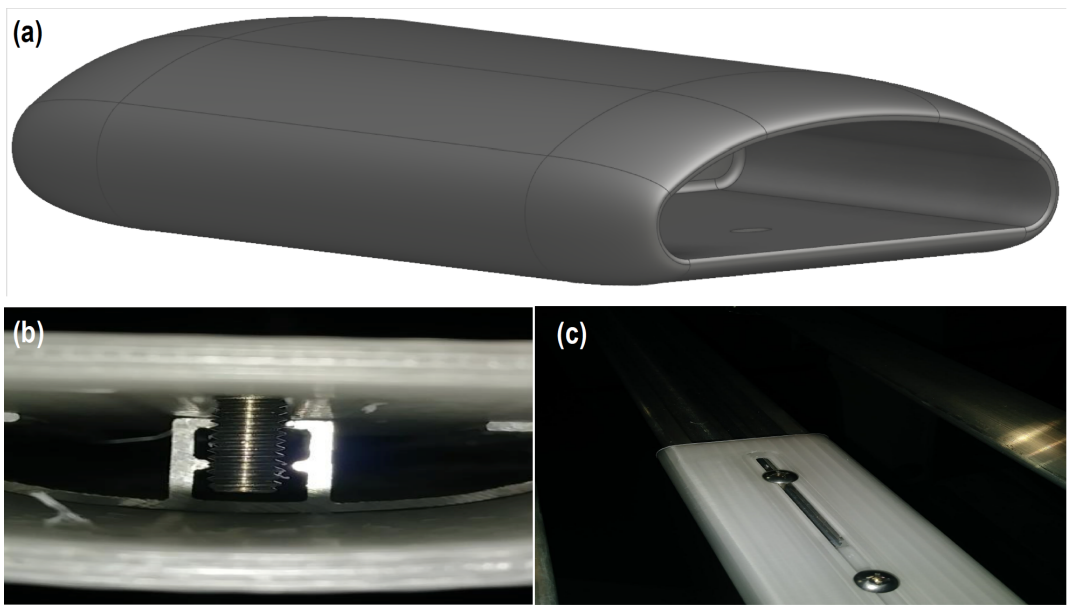

Figure 1.17: a: A CAD drawing for the resistive sheath with a smoothed edge b: A cross-sectional photograph of the mock up plastic sheath screwed onto the profile center rib; c: The bottom view, active volume side, of a sheath connecting two neighboring profiles.

The resistive chain for voltage division between the profiles provides a linear voltage gradient between the cathode and the top-most field-shaping ring. This chain is critical because it determines the strength of the E field between one profile and its neighbors as well as between the profile and other surrounding parts like the grounded stainless steel cryostat membrane. The E field must be kept well below $30\,\mathrm{kV\,cm^{-1}}$ at all points in the LAr bath to keep TPC operation safe, as listed in Table **??**.

Each stage of the HVDB consists of two $5\,\mathrm{G\Omega}$ resistors in parallel for inter-board redundancy and two variable resistors of threshold voltage $2\,\mathrm{kV}$ to protect the resistors in case of a sudden discharge. With 199 stages under $600\,\mathrm{kV}$ potential, the total expected current at $600\,\mathrm{kV}$ is therefore $1.2\,\mu\mathrm{A}$ per row of HVDB. A total of 12 rows, one per super-module, connected in parallel, will be employed for ample redundancy in the DUNE DP module, yielding an expected overall current in the FC system of $14.3\,\mu\mathrm{A}$. For optimization, one HVDB will connect 11 stages. Thus eighteen 11-stage HVDBs are required for one 12.01 m tall module and one 1-stage HVDB is required at the bottom to make the final connection between the bottom-most field-shaping ring and the cathode.

Figure 1.3 shows one ProtoDUNE-DP HVDB board and Figure 1.4(d) shows the connection of one row of HVDBs strung vertically along the entire height of the FC as installed in ProtoDUNE-DP. The cathode plane is mounted to the bottom of the FC, together forming one contiguous unit of field-providing structure. The bottom-most HVDB makes the connection between the cathode and the bottom-most field-shaping ring.

1.4.7 HV Return and Monitoring Devices

To maintain the potential difference between the top-most field-shaping ring and the extraction grid of the CRP, either a dedicated HV supply or an adjustable resistor chain will be used in the HV return outside the cryostat. This requires an independent 10 kV feedthrough similar to those developed for the extraction grid.

Several devices will monitor the HV:

- The Heinzinger units have typical sensitivities down to tens of nanoamperes with current readback capability. The units can sample the current and voltage every few 100 ms.

- Inside the cryostat, so-called pick-off points near the anode will monitor the current through the HVDB resistor chain. Additional pick-off points could be implemented on the ground grid below the cathode to monitor possible stray currents.

1.5 Quality Assurance and Quality Control

1.5.1 Field Cage

Upon receipt, FRP I-beams and other parts undergo a visual inspection for defects, in particular those affecting structural integrity, such as cracks, air bubble holes, depressions, and variations from flatness. The parts are sorted into three preliminary categories: category 0 (pass), category 1 (problematic but repairable), and category 2 (severe and unusable).

The visual inspection is followed by critical dimension measurements to verify individual submodule assembly and module interconnection integrity. These measurements focus on cross sectional dimensions for rods, plates, and bars, as well as length, straightness, flatness, and camber of the beams and flanges. All measurements must satisfy the mechanical tolerances provided by the design drawings and the standard industry quality criteria.

The FRP I-beams and parts in category 1 undergo a repair process during the preparation stage. Another set of measurements is performed after the repair to redetermine the part's category.

Those in category 2 are returned to the vendor for replacement.

All FRP parts that pass inspection are prepared for use, which involves QC at each step. Each part is first defibered, deburred, sanded to smooth the edges, then varnished to suppress any remaining fibers. Once the part is prepared, it is stored in a humidity- and temperature-controlled drying area for 24 to 48 hours to fully cure the varnish. After full curing, each module is laser-engraved with a unique part number and recorded in a QC database.

At this point, the submodule is pre-assembled on a table before packaging to ensure all parts fit, including inserts, screws, and slip nuts. When fitness is verified, the submodule is disassembled, and all components are packed along with 10 to 20% spare hardware to ensure that each package is self-sufficient for final assembly. It is shrink-wrapped into a compact package of dimensions 10 cm × 10 cm × 2 m and the edges are wrapped with thick plastic sheets to protect the parts from potential mechanical damage. Each package is given a submodule number for further tracking. This submodule number stays with it throughout assembly at Sanford Underground Research Facility (SURF) and final installation, so that the submodule can be assigned to a specific module, and checked and recorded once it is installed in the module.

1.5.2 Electrical Interconnections and HV Divider

Resistors, Varistors and HVDBs: All resistors used for HVDB production are numbered and undergo a three-stage QC test for final selection. Resistance is measured at voltages up to 4 kV in 500 V steps for each stage. The first stage of testing is done at room temperature, the second in LN_2, and the third again at room temperature after warming up. The measured values are histogrammed for final selection to look for groupings of resistance values. It is more important that the resistance values be close to each other than that they be at any particular value (unless they are too far from the design values). The resistors for which the resistance values are within 1% of each other are selected.

All varistors for board production are also numbered for QA purposes and undergo a three-stage QA testing program for the final selection. Each test stage is a clamping voltage measurement, first at room temperature, then at LN_2 temperature, and again after warming back up to room temperature. The measured values are histogrammed for final selection; those with clamping voltages closest to the design values are selected to ensure proper protection.

Once the parts are selected, they are sent over to the vendor for mounting. When the completed HVDBs are delivered, they undergo a three-stage QA testing program. Each stage involves a resistance measurement of the whole board and each stage of the board, first at room temperature, then in LN2, and again after warming back up to room temperature. The measured resistance values are histogrammed for the final board selection. The boards can fall into one of three categories: category 0 (pass), category 1 (problematic but repairable), and category 2 (severe and unusable). If at any testing stage the resistance is more than 0.5 % away from the mean, the part does not fall into category 0. Boards in category 1 are sent back to the vendor with the selected resistors, so that the parts that failed one stage or another can be replaced with resistors selected during the QA.

Aluminum Profiles and Resistive Sheath: The QA testing of the aluminum profiles and the re-

sistive sheath is done on prototype production samples before full production begins. The samples are visually inspected for shape and adherence to the design drawing and for surface smoothness, surface-coating quality, and smoothness of the bend (for profiles with the 90° bend).

The resistive sheath samples are visually inspected for shape and adherence to the drawing, for edge smoothness, resistance and mechanical fitness, as well as for how tightly they fit to the profiles while still allowing easy coupling to the neighboring profile and good electrical contact. Each sheath is numbered and undergoes a three-stage QA test for final selection, similar to the resistors. Resistance is measured at voltages up to 4 kV in 500 V steps for each stage: at room, LN_2, and again room temperature. The measured values are histogrammed for final selection to look for groupings of resistance values.

Power Supply and Feedthrough: The power supply is tested extensively along with the controls and monitoring software. Capabilities to test include

- ramping and changing the set voltage, including ramp-rate change and pause capabilities and settings;
- Acceptance of a user-defined current limit: this parameter sets the maximum value of current; at this point the supply must reduce the voltage output;
- acceptance of a setting for the trip-threshold current: at this point the supply must reduce the voltage output (In previous experiments, the trip function in software would set the output to 0 kV.); and
- recording the current and voltage readback values with a user-defined frequency and recording of any irregular current or voltage events.

1.5.3 Quality Control During Assembly and Installation

Assembly, testing, transportation, and installation procedures must ensure adequate QC of all HV system components. The entire assembly and installation of the HV system will be performed at SURF.

The FC submodules are assembled inside the cryostat on an assembly table with a precision alignment bar. Each submodule package is visually inspected for external damage and is opened carefully to avoid damage to the FRP parts. Bags of hardware are removed and set aside. The two 10.2 cm (4 in) FRP I-beams, two stainless steel cross bar tubes with diameters of 2.5 cm (1 in), and connecting brackets are visually inspected for any damage incurred during transport. Once these parts pass inspection, they are assembled into the frame on the assembly table. The aluminum profiles are visually inspected and felt by hand for severe scratches and sharp points. The profiles that pass are placed onto a flange of the FRP I-beams, with a slip nut inserted into the rail on the profile reinforcement rib on either end. Assembly and alignment follow the process described in Section 1.7.2. The alignment of the profiles is checked using a straight-edge along one end of the profiles. The submodules that pass are put on the wheel base and stored until they can be

installed.

The HV divider boards are visually inspected for any damage during the transport and the resistance of each stage is tested on-site at room temperature to ensure the integrity of the board and the electrical connections of the resistors before installing the boards onto the submodule. Cathode and ground grid modules are checked for the required planarity and mechanical integrity. In addition, during the installation phase, the electrical continuity between the modules is checked.

The feedthrough and the HV extender are tested simultaneously at the European Organization for Nuclear Research (CERN), preferably with the power supply to be used in the detector. To pass, the feedthrough must hold the target voltage ($-600\,\mathrm{kV}$) in ultra-pure LAr (TPC-quality purity corresponding to a free electron lifetime, $\tau \geq 7\,\mathrm{ms}$) for at least 24 hours. The ground tube submersion and E field environment of the test set up must be comparable to the real FC set up or a more challenging environment. Additionally, the feedthrough must be UHV-grade leak tight.

Upon arrival at SURF, the power supply used in the DUNE DP module HV system is tested before installation, with output voltages and currents checked on a known load.

1.6 Safety

In all phases of HV system deployment of the DUNE DP detector module, including fabrication, installation, and operations, safety is the highest priority. As was done for ProtoDUNE-DP, all assembly, testing, transport, and installation procedures will be documented. Explicit attention is paid to how well ProtoDUNE-DP procedures transfer to the DP detector module. The most critical of these are noted in the preliminary HV risk assessment (see Section 1.10.3).

1.6.1 Production Safety

Personnel participating in the production process will undergo thorough training on the hazards present in the process. Pallet jacks, dollies, and hoists will be used for lifting to avoid any injuries from moving heavy equipment. Personnel will be trained according to the site's back injury prevention procedures to use these and to avoid overextending as they lift and move parts and equipment I-beam and the stainless steel tube manipulation will require extreme care to avoid injury and damage to any parts or equipment. Personnel will take care to avoid spilling liquid (ethanol, Simple Green™ cleaner, varnish, or de-ionized water) on the floor to prevent slips and falls, and will mop up any spilled liquid immediately. All personnel will use gloves, protective glasses, and mask while working with ethanol, epoxy, varnish and cleaner. They will use the appropriate respiratory protections following the production site's respirator program rules and receive respirator training as required.

1.6.2 Handling Safety

The structural and electrical designs for the DUNE DP HV system are based on designs that have been vetted and validated in ProtoDUNE-DP construction, which as of April 2019 is in its final phase of deployment at CERN. In parallel with the ProtoDUNE-DP construction and operation, HV tests at CERN were performed using full-voltage and a full-scale HV feedthrough, power supply, and monitoring system in dedicated HV test facilities. This has also provided an opportunity to complete full safety reviews. Operating the FC at its full voltage produces a substantial amount of stored energy. The modular design of the cathode specifically addresses this safety concern: in the event of a power supply trip or other failure that unexpectedly drops the HV, the segmented cathode structure prohibits the stored charge from crossing to neighboring cathode modules, thus limiting the power dissipated.

Integral to the DP FC design, both in ProtoDUNE-DP and the DUNE DP module, are the pre-assembled modular panels (called FC submodules) of field-shaping profiles with individual HVDBs. The structural design and installation procedures used in ProtoDUNE-DP were developed as prototypes for use at the far detector (FD) site and were vetted by project engineers, engineering design review teams, and CERN's safety engineers. Some revisions to these designs are expected based on lessons learned in ProtoDUNE-DP installation and operations. These revisions will be reviewed both within the DUNE project and by Fermilab ES&H personnel. The attention paid up-front to potential hazards, personnel preparation, and use of equipment puts the overall DUNE DP module HV design on solid footing in terms of safety.

Assembly of the FC submodules and HVDBs involves labor from the collaboration members, technical staff, and students, and does not present unusual industrial hazards. The HV consortium will work closely with each production site to ensure that procedures meet both Fermilab's and institutional requirements for safe procedures, personal protective equipment, environmental protection, materials handling, and training. Most part fabrication will be done commercially and shipping will be contracted through approved commercial shipping companies. Before a site is approved as a production venue, an external safety panel will visit the site for review to ensure best practices are in place and followed.

1.7 Transport, Assembly, and Installation and Integration

1.7.1 Transport and Handling

The FC FRP I-beams, the stainless steel cross bar tubes, and other parts are shipped in standard wooden crates. Parts for each submodule are packed into one compact flat pack of 0.1 m × 0.1 m × 2 m sealed in multiple layers of shrink wrap and a thick, soft cushion of plastic layers for edge protection. Since each submodule package is so compact, each wooden crate 1.5 m (H) × 1.3 m (W) × 2.5 m (D) can transport 110 submodule flat packs stacked in 10 (W) × 11 (H) formation. The total number of submodule flat packs needed for the entire FC is 216, excluding spares, thus all FC frame parts can be transported in two crates. Each of these fully loaded crates will weigh

less than 2500 kg. Since the cage for underground transport at SURF is 3.6 m (H) × 1.38 m (W) × 3.7 m (D) with a load capacity of 13,000 lbs, or approximately 6000 kg, in principle, all FC frame parts can be transported underground in one cage trip.

The extruded aluminum profiles for FC are shipped separately in standard wooden crates. In all, 199 profiles of ∼4 m length are needed for each 12.01 m FC module, for a total of 7164 to transport underground, excluding spares. The same number of resistive sheaths are shipped separately in standard wooden crates.

The (12 m (L) × 30 cm (H) × 2.5 cm (W)) trusses for the cathode modules are welded off-site and shipped to SURF in transport containers. The (12 m (L) × 2.5 cm (D)) resistive rods are also constructed off-site and shipped in standard wooden boxes. The installation procedure takes into account the lack of storage space at the 4850L and cathode modules are transported underground in an assigned order, corresponding to their installation sequence starting from the end of the cryostat opposite the TCO, as are the FC super-modules.

The power supply, feedthroughs, and HV extender are sent to SURF in standard shipping crates. Unwrapping requires clean areas and careful handling. Surfaces can be cleaned with alcohol and allowed to dry.

1.7.2 Assembly

FC submodules are assembled inside the DUNE DP module cryostat. An assembly table with a precision alignment bar for rapid profile alignment is used for this task. The submodule package is opened on the table and the mechanical frame is assembled from two 10.2 cm (4 in) FRP I-beams and two 2.5 cm (1 in) diameter stainless steel tubes.

Once the frame is assembled, the aluminum profiles are mounted on the flange of the FRP I-beams and secured using two slip nuts inserted on either end and two button-head, hex-drive metal screws with one side secured tightly and the other loosely, but solidly secured to allow motion from thermal contraction. The submodules designated for the middle of a super-module must have a square nut inserted between the two slip nuts for HVDB mounting. Care must be taken to avoid scratching the profiles during the mounting process.

When all screws are hand-tightened as much as possible, the final torque is applied using a power screwdriver with a preset torque. The final alignment of the profiles is then made by hand, tightening only one or two screws on the tightly secured side as needed. A wheel base made of unistrut bars is then mounted to the bottom of the submodule, and the entire unit is placed in a designated area to await installation. Each submodule is clearly labeled with its number for tracking purposes.

Cathode modules will be installed along with their neighboring FC super-modules as described in Section 1.7.3.

1.7.3 Installation and Integration

All FC submodules are assembled inside the cryostat on an assembly table as described in Section 1.7.2. Resistive sheaths for submodule interconnections and the square nuts to hold HVDB are pre-inserted to each profile at this stage. Once a submodule is fully assembled, a transport wheel base is mounted on it for easy relocation. When three top submodules, three bottom submodules, and 12 middle modules are assembled, installation into a super-module will be performed starting at the far end of the cryostat.

The installation sequence for a super-module is described below and depicted in Figure 1.19:

1. Hang a 12 m stainless steel I-beam from two stainless steel cables through the feedthroughs and raise it to approximately 2.5 m above the temporary floor.

2. Place three top submodules under the stainless steel I-beam, and connect each to the I-beam using two sets of stainless steel L-brackets, stainless steel inserts, stainless steel screws, stainless steel lock washers, and stainless steel nuts.

3. Slide the two resistive sheaths (that are pre-inserted to the middle submodule) over and tighten them onto the two neighboring profiles to make the resistive connections between profiles in the row.

4. Mount HVDBs to the center submodule in the row, using aluminum button-head screws and a square nut pre-inserted in the profile reinforcement rail. This process completes one row of the submodules for a super-module, as depicted in Figure 1.19(a).

5. Mount the PDS reflector/WLS panel assemblies on the FRP I-beams of the FC, starting from one end of the row and progressing towards the other, covering the entire surface, as depicted in Figure 1.19(a'). The extended PDS reflector/WLS panel assemblies at the end wall corner FC submodules will have dimensions 290 cm (W) $\times$ 186 cm (H) whereas the assemblies at the side wall corner FC submodules will have dimensions 260 cm (W) $\times$ 186 cm (H).

   The extension of the assemblies to be mounted at corner ends of the side wall FC modules is much shorter than the other extended modules to safely accommodate the 2.4 degree tilt of the end walls. The panel assemblies and the installation procedures are described in Sections 3.4 and 3.12.3 respectively.

6. Raise the completed top row by approximately 2.5 m, place three middle submodules under the top row, and connect each to its corresponding top submodule above using 1 cm thick G-10 connection plates and stainless steel screws and nuts, as depicted in Figure 1.19(b).

7. Slide the two resistive sheaths in the center submodule over and tighten them onto the profiles to make the electrical connections between the submodules.

8. Mount HVDBs to the middle module using aluminum button-head screws and a square nut.

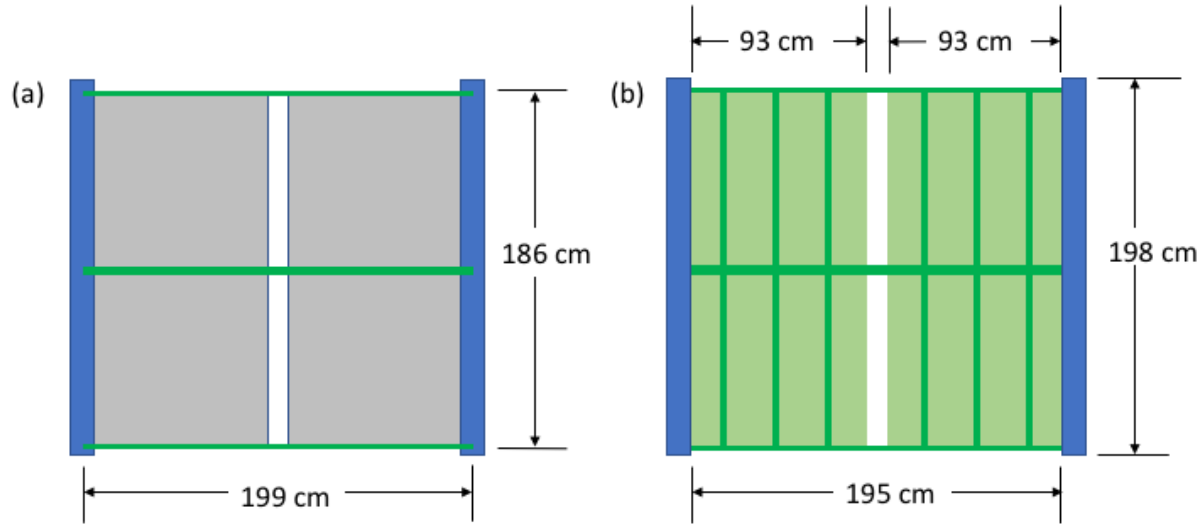

Figure 1.18: The PDS reflector/WLS panel assembly mounted on the FC FRP I-beams. (a) The coated surface of the panel assembly, which faces the active volume. The blue bars represent the I-beams onto which the panel assembly mounts. (b) The uncoated reverse G-10 surface of the panel assembly. The six vertical (darker green) bars provide mechanical support to the panel assembly.

9. Mount the PDS reflector/WLS panel assemblies onto the FRP I-beams of the FC starting from one end of the row and progressing towards the other, covering the entire surface, as depicted in Figure 1.19(b').

10. Repeat steps 6 through 9 once to complete the assembly of the top half of the super-module and PDS reflector/WLS panel assemblies, as depicted in Figure 1.19(c) and (c').

11. Repeat steps 6 through 8 three more times to complete the assembly of the bottom half of the super-module, as depicted in Figure 1.19(d).

The entire HVS, including FC, cathode, ground grid, and the PDS reflector/WLS panels are installed in the following sequence.

1. Construct the end wall super-module (with 90 degree bent corner profiles) at the end of the cryostat opposite the TCO.

2. Mount a U-shaped stainless steel cathode end wall perimeter tube (∼50 mm diameter) to the bottom of the end wall super-module.

3. Install the two super-modules along the side wall immediately next to the end wall module.

4. Make the electrical connections to the end wall super-module.

5. Pull in the bottom of the end wall super-module (with the cathode perimeter tube) 50 cm from its free hanging position, align it to the side wall super-modules on each side wall, and anchor it to the temporary floor.

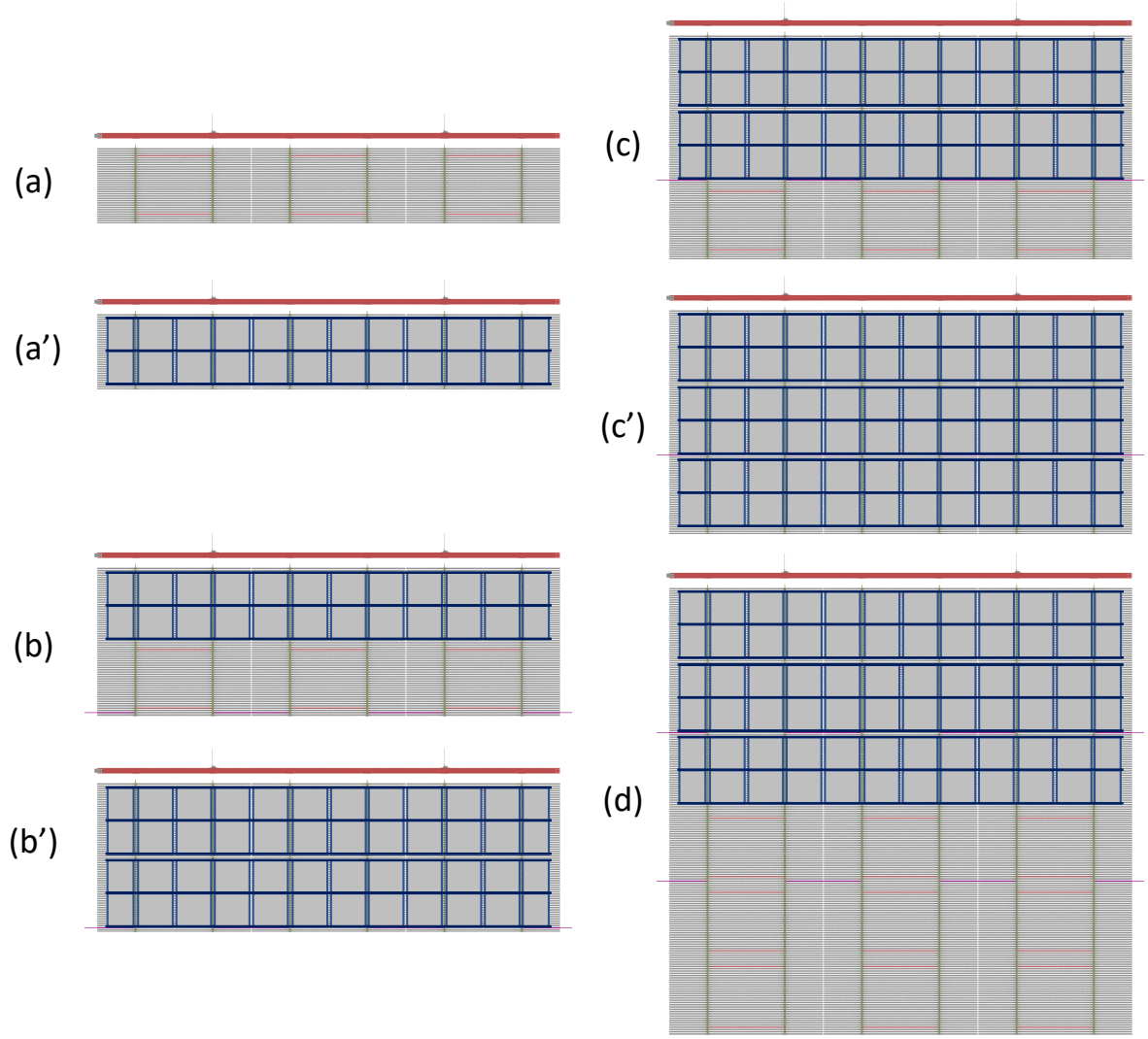

Figure 1.19: FC super-module installation sequence. The red bar at the top of each diagram is the stainless steel I-beam. The white vertical bars separate the three sets of vertical modules and the green vertical bars are the FRP I-beams. (a) The three top submodules are mounted to the 12 m I-beam. (a') One row of PDS reflector/WLS assembly panels is installed on the inner surface of the FC FRP I-beams. (b) The three middle submodules are mounted to their corresponding top submodules. (b') The second row of PDS reflector/WLS assembly panels is installed. (c) The next set of three middle submodules are mounted below the previous set. (c') The third and the last row of PDS reflector/WLS assembly panels is installed. (d) A completed super-module, its top half covered with PDS assembly panels.

6. Electrically connect the end wall super-module and side wall super-modules using the pre-inserted resistive sheath.

7. Assemble a cathode module in place at the bottom of the two side FC modules immediately next to the end wall super-module.

8. Connect the stainless steel perimeter cathode tube already mounted on the end wall super-module to the corresponding cathode tubes on the side wall super-modules, and anchor it to the false floor to ensure the mechanical stability of the end wall super-module until the entire FC is constructed.

9. Once the FC and cathode are completely installed, remove the temporary floor under the cathode, and clean the membrane floor.

10. Place ground grids under the cathode plane with their legs extended.

11. Install the PDs under these ground grids.

12. Remove the leg extensions of the ground grids and lower them to their nominal height.

13. Repeat steps 7 through 12 to install the cathode, ground grid, and the PDs for the installed FC modules.

14. Install the remaining side wall super-modules.

15. Repeat steps 7 through 12 except for the last 4 m wide module of the side wall super-modules that connect to the end wall super-module on the TCO end of the cryostat.

16. Repeat steps 7 through 12 one last time.

17. Remove the floor anchors for the two end wall super-modules.

1.8 Design Validation and Verification Plan

Section 1.3 describes the changes to the design relative to ProtoDUNE-DP. These changes on the cathode design are made to address the sudden release of the energy stored between the cathode plane and the ground grid. The change mainly consists of replacing the continuous metallic structure employed in ProtoDUNE-DP with a segmented and resistive one.

On the FC side, the main changes are the removal of all insulating materials facing the cryostat wall, and the assembly and installation procedure which will be based on 12 m× 12 m super-modules. It is planned to test this procedure with mock-up modules in Ash River, which can be carried out independently with the planned electrical performance testing in ProtoDUNE-2. The electrical behavior of the cathode and FC structure will be studied in a simulation to confirm the

design intention and identify weaknesses.

Tests of the 600 kV HVPS and cryogenic feedthrough are at the moment planned to be performed in a dedicated cryostat (as for the 300 kV one at CERN) whenever the joint R&D with Heinzinger can make them available.

1.9 Interfaces

The interface documents related to DP HVS are given in Table 1.3. Some of the basic interfaces are summarized below.

Table 1.3: DP HVS interface documents.

Interfacing System	Description	Linked Reference
PDS	FC, cathode, ground grid and PDS PMT and reflector/WLS panel assemblies installation sequence, possibility of individual ground grids on the PMT support structures	DocDB 6799 [3]
CRP	HVFT penetration through CRP; installation sequence	DocDB 6754 [4]
Facility	cryogenic pipes locations; FC suspension and HV feedthroughs ports	DocDB 6985 [5]
cryogenic instrumentation and slow controls (CISC)	HVPS control, monitoring, and interlock system; cameras	DocDB 6787 [6]
Calibration	calibration laser placement and FC openings	DocDB 14005 [7]

1.9.1 Internal Cryogenics System

The interface with the cryogenics system involves coordinating the placement of the cryogenic pipes. The locations of the ground grid feet and the PMTs must clear the cryogenic pipes and the membrane corrugations on the floor. As of this writing, the nominal position of the vertical gas purging pipe is uncomfortably close to the FC wall.

1.9.2 Cryostat

The cathode and FC are suspended under the cryostat roof through special feedthroughs. The HV feedthrough requires a port on the cryostat at a specific location. The locations, size, height, and load-bearing capability of these roof penetrations are being coordinated to allow detailed design of the HVS.

1.9.3 Charge Readout Plane

The HV and CRP systems are independently suspended and do not physically touch each other. The relative vertical position between the top FC profiles and the CRP affects the drift field uniformity near the CRP. The CRP dynamically follows the liquid surface whereas the height of the HVS is fixed, so the maximum excursion of the CRP-liquid level must be controlled to avoid excess drift and extraction field distortion.

The HV feedthrough and extender structure goes through a corner of the CRP. A special CRP module must be constructed to allow the HV feedthrough to be installed.

1.9.4 Photon Detection System

The cryostat penetrations and feedthroughs for these two systems are completely independent, as are their control electronics. The interfaces envisaged are effectively at the level of design requirements and installation coordination, and include

- maintaining a safe minimum distance between the PDs and the −600 kV cathode;
- defining a mutually agreed upon optical transparency of the cathode + ground grid combination. In general, a more open cathode and ground grid will have a higher E field on the cathode/ground grid surfaces;
- defining the PD power dissipation limit (production of bubbles would compromise HV stability);
- agreement on the design of the reflector/WLS panel assemblies to be mounted on the inner walls of the FC;
- understanding of the impact to the FC structure (weight, force from liquid flow);
- developing an efficient installation plan; and
- installing individual ground grids on the PMT supports (under discussion with the PDS consortium).

1.9.5 Cryogenics Instrumentation and Slow Control

The HVS relies on CISC to control the HVPS and monitor the supply and return currents from the FC power return circuits. An interlock of the HV power supply with the liquid level should be implemented to prevent HV discharge in gaseous argon. A controlled shutdown of the HVPS with the opening of the cryostat pressure relief valve must also be implemented. A few strategically

placed cryogenic cameras near key HVS components would be very helpful.

1.9.6 Calibration

Due to the strong likelihood of non-negligible space charge distortion from positive ions in the DP module, calibration lasers are essential to provide accurate mapping of the drift field inside the TPC. The calibration laser beams must pass through the TPC's FC. Locations of the laser heads and their openings on the FC must be coordinated.

1.9.7 Technical Coordination

The shipping, storage, underground transportation, assembly, and installation of all HVS components are coordinated with technical coordination (TCN) and the Joint Project Office (JPO) (see Volume 5, Technical Coordination).

1.10 Organization and Management

1.10.1 HV Consortium Organization

The HVS consortium includes all the institutions participating in the design, construction, and assembly of the HV systems for both ProtoDUNE-SP and ProtoDUNE-DP. It currently comprises several USA institutions and CERN, the only non-USA participant. As it has been for ProtoDUNE, CERN is strongly committed to taking on a significant role in terms of funding, personnel, and providing infrastructure for R&D and detector optimization. Moreover, CERN will be responsible for a significant fraction of subsystem deliverables; as such, CERN is actively in search of additional European institutions to join the consortium. Table 1.4 shows the list of institutions participating in the HVS consortium.

In the current HV consortium organization, each institution naturally assumes the same responsibilities that it assumed for ProtoDUNE-SP and ProtoDUNE-DP.

The consortium organizational structure includes a scientific lead from CERN, a technical lead from BNL and a TDR editor from the University of Texas at Arlington. HVS design and integration is presently led by CERN. The consortium is organized into working groups addressing the design and R&D issues, as well as producing and installing the hardware.

- WG1. Design optimization for the SP and DP detector modules; assembly, system integration, detector simulation, and physics requirements for monitoring and calibrations.

- WG2. R&D activities and facilities.
- WG3. SP-CPA: Procuring resistive panels, frame strips, and electrical connections of planes; assembly, QC at all stages, and shipping of these parts.
- WG4. DP cathode and ground grid: procuring material; construction, assembly, shipping to South Dakota, QA, and QC.
- WG5. SP top field cage (top FC), bottom field cage (bottom FC), and endwall field cage (endwall FC) modules.
- WG6. HV supply and filtering, HV power supply and cable procurement, R&D tests, filtering and receptacle design and tests.

Taking advantage of identified synergies, some activities of the SP and DP working groups are merged: HV feedthroughs, voltage dividers, aluminum profiles, FRP I-beams, and assembly infrastructure.

Table 1.4: Institutes participating in the HVS consortium

Institution	Country
CERN	Switzerland
Argonne National Lab	USA
Brookhaven National Lab	USA
University of California Berkley / LBNL	USA
University of California Davis	USA
Fermilab	USA
University of Houston	USA
Kansas State University	USA
Louisiana State University	USA
SUNY Stony Brook	USA
University of Texas Arlington	USA
Virginia Tech	USA
College of William and Mary	USA

At present, the HV consortium is gathering institutions to participate in the design, construction, and assembly of the HV systems for both SP modules and DP modules. The consortium is likely to expand in the near future. Discussions are underway with institutions, in particular from the EU, to balance USA participation with additional international partners.

1.10.2 Planning Assumptions

The present baseline design for all elements of the HV system for the DUNE DP module follows the experience with ProtoDUNE-DP as well as the ProtoDUNE-SP designs, including production

and assembly.

It is assumed that no major issues in the HV system operation of ProtoDUNE-DP will be encountered, and that the basic HV system concepts are sound.

However some design modifications and optimizations have been implemented to take into account the doubled drift distance, requiring an increase in HV delivered to the cathode from −300 kV to −600 kV and the much higher energy stored in the cryostat as a result, and the increased detector volume compared to ProtoDUNE-DP.

Therefore the DUNE DP HV system distribution and the related cathode structure still require intense R&D, given the unprecedented value of the required HV (−600 kV) and the surface area covered by the cathode plane compared to ProtoDUNE-DP. The related results could lead to revising design details such as the shape of the cathode elements and of the ground grid structures, the distance from the cryostat walls, the distance between the cathode and the ground grid protecting the PDs, and resistive connections of the cathode modules. We must ensure that the E field strength in the LAr remain below the critical value of about 30 kV/cm everywhere and that the energy stored in the FC is not released catastrophically to the cryostat membrane.

ProtoDUNE-DP will be the testing ground where we come to understand and optimize detector element assembly, installation sequence, and integration, as well as requirements in human resources, space, tooling, and schedule.

1.10.3 Risks

The risk items presented in Table 1.5 for the DUNE DP module are derived from those that will be addressed in ProtoDUNE-DP. Some of these are common to ProtoDUNE-DP and the DP module. Other items (from 11 to 14), involving long term stability and funding, are instead specific to the FD DP modules construction and installation.

Items common to ProtoDUNE-SP have not caused significant problems during commissioning and early operation of ProtoDUNE-SP, with the partial exception of item 3. For this specific issue, the operation of ProtoDUNE-DP is essential because the HVS layout is different, and the absolute voltage on the cathode is much higher. Item 4 will require an accurate analysis of collected muon data to disentangle space charge effects. These risks still persist for the detector modules, given the much larger detector scale and the more complex underground installation environment.

Table 1.5: Risks for DP-FD-HV

ID	Risk	Mitigation	P	C	S
RT-DP-HV-01	Broken resistors or varistors on voltage divider boards	Redundancy of resistors, varistors, and HVDBs.	L	L	L

RT-DP-HV-02	E field uniformity is not adequate for muon momentum reconstruction	Regularly map out field using a laser calibration sysem.	L	L	L
RT-DP-HV-03	E field is below specification during stable operations	Improve purity by more aggressive filtering.	M	M	L
RT-DP-HV-04	Space charge from positive ions distorting the E field beyond expectation	Minimize insulators facing cryostat wall ground.	M	M	L
RT-DP-HV-05	Damage to cold electronics (CE) in event of discharge	Minimize the energy released in a short time using highly resistive connections.	L	L	L
RT-DP-HV-06	Energy stored in FC (in DP) is suddenly discharged	Delay energy discharge by connecting neighboring Al profiles with resistive sheaths.	L	L	L
RT-DP-HV-07	Detector components are damaged during shipment to the far site	Make sufficient spares and increase the number of shipping boxes.	L	L	L
RT-DP-HV-08	Damages (scratches, bending) to aluminum profiles of Field Cage modules	Make sufficient spares and increase the number of shipping boxes.	L	L	L
RT-DP-HV-09	Bubbles from heat in PMTs or resistors cause HV discharge	A large area of cathode consists of high resistance rods, delaying the energy release.	L	L	L
RT-DP-HV-10	Free hanging frames can swing in the fluid flow		L	L	L
RT-DP-HV-11	FRP/ Polyethene/ laminated Kapton component lifetime is less than expected		L	L	L
RT-DP-HV-12	Lack of collaboration effort on this HV system	Continue recruiting collaborators.	L	L	L
RT-DP-HV-13	International funding level for DP HVC too low	Employ cost saving measures and recruit collaborators.	L	L	L

RT-DP-HV-14	Underground installation is more labor intensive or slower than expected	Increase labor contingency and refine labor cost estimates. Further improve installation procedure.	L	L	L

1.10.4 High-level Cost and Schedule

A first high-level summary of the cost estimate for the HV system of one DUNE DP module was obtained by extrapolating from the as-realized ProtoDUNE-DP costs and effort, except for the cathode, which was introduced as a new concept and whose estimation is more uncertain. Moreover, these estimates do not include any projected cost savings that would be realized by producing many units at each production site. However, substantial savings from higher-volume production is still possible. For ProtoDUNE-DP, the assembly sites produced only small numbers of each unit, and thus remained on the learning curve. Table 1.6 shows the DP HVS cost summary.

Table 1.6: DP High Voltage System Cost Summary (TO BE COMPLETED)

Cost Item	M&S (k$ US)	Labor Hours
Project Management		
Physics and Simulations		
Design, Engineering and R&D		
Production Setup		
Cathode and ground grid		
FC submodule		
HV feedthrough cold test		
Production		
Cathode		
Ground grid		
FC components		
HVDB		
FC submodules		
HV components		
DUNE FD Integration & Installation		

Table 1.7 shows the tentative DP HVS schedule assuming that the DP module technology is selected for the second DUNE far detector module.

Table 1.7: HVS Consortium Schedule (DP)

Milestone	Date (Month YYYY)
Technology Decision Dates	March 2020
Final Design Review Dates	Sept. 2020
Start of module 0 component production for ProtoDUNE-II	March 2021
Start of ProtoDUNE-SP-II installation	March 2021
End of module 0 component production for ProtoDUNE-II	September 2021
Start of ProtoDUNE-DP-II installation	March 2022
South Dakota Logistics Warehouse available	April 2022
production readiness review (PRR) dates	September 2022
Start of FC production	September 2022
Start of HVDB production	September 2022
Beneficial occupancy of cavern 1 and central utility cavern (CUC)	October 2022
Start of cathode production	January 2023
Start of HVPS, feedthrough & HV extender production	March 2023
CUC counting room accessible	April 2023
Start of ground grid production	May 2023
Top of detector module #1 cryostat accessible	January 2024
Start of detector module #1 TPC installation	August 2024
End of HVPS, feedthrough & HV extender production	January 2025
Top of detector module #2 accessible	January 2025
End of FC production	March 2025
End of HVDB production	March 2025
End of cathode production	May 2025
End of ground grid production	May 2025
End of detector module #1 TPC installation	May 2025
Start of detector module #2 TPC installation	August 2025
End of detector module #2 TPC installation	May 2026

1.11 Appendix - Alternatives

1.11.1 Calibration Laser Penetrations

Despite its underground environment, the DUNE DP module is likely to have non-neglegible space charge distortion due to the ion feedback from the multiplication of ^{39}Ar ionizations through the LEMs. The LAr convective flow will make the space charge density distribution difficult to model accurately. Therefore, using UV laser beams is highly desirable to calibrate the charge signal based on the measured field distortions throughout the TPC volume.

We have designed a 15 cm offset between the FC and the edges of the CRP, so it may be possible to place laser heads through this gap to scan the TPC active volume. Obviously, the stainless steel FC support I-beam is in the way, but it should be fairly straightforward to make openings through the I-beam to allow a $\sim$10 cm outer diameter (OD) object through. This feature will be designed and developed if the calibration consortium decides to implement a laser system. Naturally, the cryostat design would need to incorporate the penetrations for the lasers.

1.11.2 Individual Ground Grids on PDS PMTs

Installing an individual ground grid for each PMT, in place of the ground grid table structure, is under consideration in collaboration with the PD consortium. Since the individual ground grid cages would potentially have thinner wires and be closer to the PMT windows, thus generating smaller shadows, they are expected to increase the light transparency to the PMTs.

The HV consortium will study the operational feasibility of the design under DUNE DP module conditions. Engineering teams from both consortia will jointly develop the design of the individual grids, the HV consortium would produce them, and the PD consortium would install them with their individual grid cages.

Chapter 2

TPC Electronics

2.1 System Overview

The function of the dual-phase (DP) time projection chamber (TPC) electronics system is to collect and digitize the signals from the charge-readout planes (CRPs) (see chapter **??**) and photon detection systems (PDSs) (see chapter 3). The first task is accomplished by the charge readout (CRO) and the second by the light readout (LRO) subsystems.

The design of the electronics system for the DUNE DP module is the outcome of an R&D program that began in 2006 and completed in 2016. This effort was initially targeted towards readout of very large liquid argon detectors and since 2011 it was focused on electronics optimization for DP detector technology. The charge readout in a DP TPC offers some key advantages in comparison to that of a single-phase (SP) detector. Most notably, while the DP front-end electronics possesses the same low noise properties of the liquid argon-immersed cold electronics of SP (110 K vs 87 K operation), the sub-system and all other electronics components for DP remain fully accessible for service, repair, replacement, or upgrade at any time during detector operations. This accessibility is achieved by integrating the analog front-end cards in dedicated feedthroughs (signal feedthrough chimney (SFT chimney)). This organization has also an impact on grouping of channels and their matching to the digitization electronics. The latter is decoupled from the analog stage and located on the roof of the cryostat at room temperature, which permits the use of low-cost high-speed networking technologies commonly employed in telecommunication industries (e.g., Micro Telecommunications Computing Architecture (μTCA) standard). In addition, for the same detector mass the number of CRO channels is naturally smaller than for an SP equivalent module (153,600 channels for DP module with $\sim$3 mm readout pitch to be compared 384,000 channels for SP module with $\sim$5 mm readout pitch) as a consequence of a longer geometry of the drift volume.

The design, finalized for DUNE in 2016, went through several prototyping phases. The optimization aspects included matching the dynamics of the cryogenic charge amplifiers to the DP readout structure and wide signal dynamic range as well as tailoring the digital front-end system accordingly. The S/N provided by DP readout offers the possibility of performing efficient lossless

compression at digitization stage without pedestal suppression (zero-suppression) while ensuring continuous acquisition and data transmission to data acquisition (DAQ) backend. A key criterion of the R&D was to develop and build custom analog and digital electronics circuits, which are both cost-effective and easily scalable to meet the needs of a large-scale neutrino liquid argon (LAr) detector. In 2016 we launched full-scale production of all of the components necessary for the charge readout of ProtoDUNE-DP. In the same year a subset of the produced electronics was also deployed in the WA105 DP demonstrator at CERN, a preliminary DP LArTPC with an active volume of $3 \times 1 \times 1\,\mathrm{m}^3$ (CRP area of $3 \times 1\,\mathrm{m}^2$), that took data in the summer and fall of 2017. The operation of the WA105 DP demonstrator [8] gave early validation of the electronics design choices and provided checks on various performance markers, such as noise. As an example, Figure 2.1 shows a distribution of charge measured from reconstructed cosmic muon tracks for each of its collection views. After taking into account recombination, the average minimum ionizing particle (MIP) charge loss expected in LAr is approximately 10 fC/cm. The effective gain of the CRP in the WA105 DP demonstrator was between 3 to 4, which is lower than the target gain of 20 for DP module operation. Despite these lower-than-expected signals, the electronics system for CRO allowed us to perform measurements.

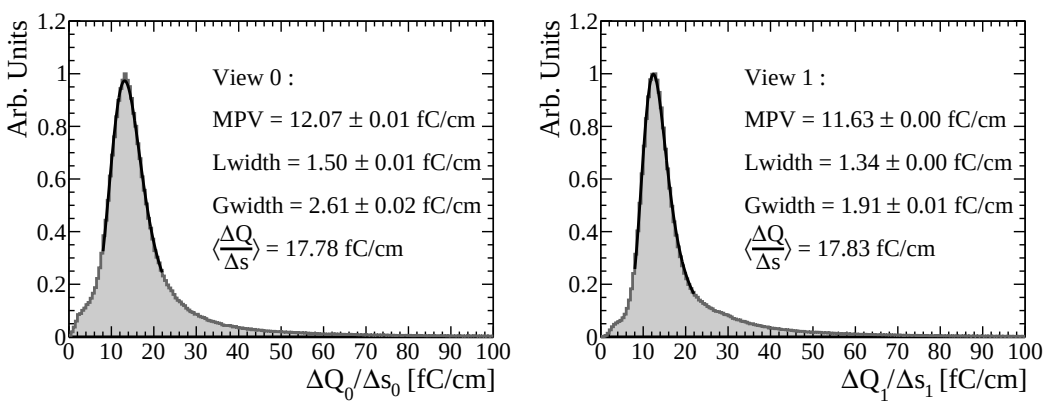

Figure 2.1: Charge distributions from cosmic ray tracks for each collection view measured in WA105 DP demonstrator from [8]. View 0 (1) corresponds to 3 m (1 m) long anode strips. In addition to the mean value of the distribution, each panel also shows the results—Most Probable Value (MPV) and widths of the Landau (Lwidth) and Gaussian (Gwidth)—obtained from a fit of the Landau function convoluted with a Gaussian distribution.

Measurements from WA105 DP demonstrator have assured us of the soundness of the existing design and all necessary elements of the CRO electronics system have been produced and tested for ProtoDUNE-DP. Technical issues with CRPs have delayed the completion of ProtoDUNE-DP preventing in turn the operation of the electronics. These issues have been largely resolved and cosmic ray data should be available by summer 2019. However, given past experience from WA105 DP demonstrator and tests already performed on the production for ProtoDUNE-DP we do not require particular additional inputs from ProtoDUNE-DP operation for the design of the electronics system for DP module presented here. We additionally note that the DUNE Executive Board has yet to formally ratify the set of specifications and requirements for DP module. This action should be taken in spring 2019; in the meantime this chapter has been developed using provisional specifications outlined in Section 2.1.2.

2.1.1 Introduction

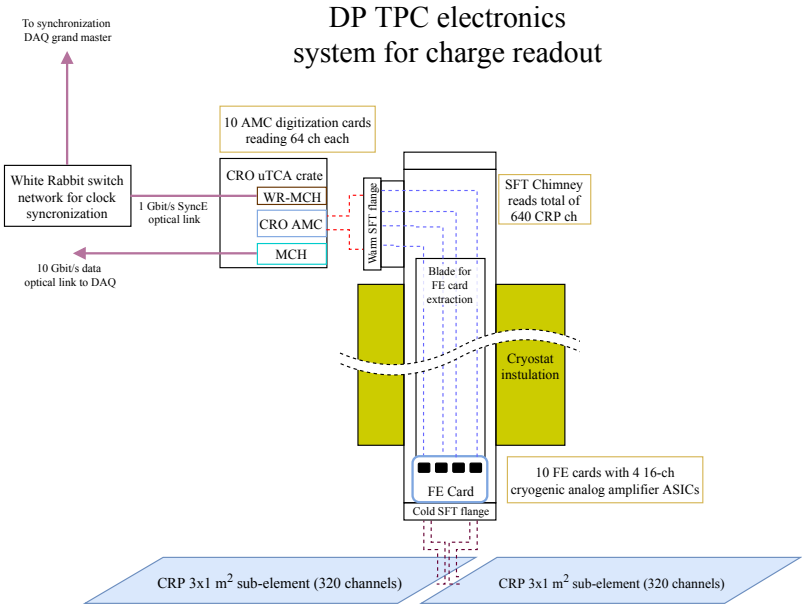

Figure 2.2: Schematic layout of the DP CRO subsystem.

The CRO electronics system, schematically illustrated in the Figure 2.2, is designed to read the charge collected on the 3 m long CRP strips arranged in two collection views (all with a pitch of 3.125 mm) and provide continuous, non-zero-suppressed, and losslessly compressed digital signals. The system consists of (1) the front-end (FE) analog electronics operating at cryogenic temperatures that amplifies and shapes the signals from CRP strips, and (2) the (warm) digital electronics external to the cryostat that digitizes the analog signals, compresses the resulting digitized data, and transmits them to the DAQ system. The cryogenic FE analog electronics uses an application-specific integrated circuit (ASIC) chip with a dynamic range up to 1200 fC to handle the charge amplification in the CRPs. The analog FE cards are housed in dedicated SFT chimneys accessible from the outside at all times, thus removing any significant risks associated with their long-term survivability. The SFT chimneys are approximately 2.3 m long stainless steel pipes that traverse the entire insulation layer of the cryostat, allowing placement of the FE electronics close to the CRPs to minimize cable capacitance (noise). In addition, their metallic structure shields the FE cards from any interference from the warm digital electronics and ambient environment. The analog signals are digitized by advanced mezzanine cards (AMCs), which are housed in the commercial μTCA crates on top of the cryostat near the SFT chimneys.

The CRO data are sampled at the rate of 2.5 MHz with 12 bit resolution. This frequency, commonly used in LArTPC experiments, is well matched to the 1 µs pulse-shaping time of the FE electronics and the detector response times determined by the electron drift velocity in the LAr. The corresponding sampling resolution along the drift coordinate is better than 1 mm.

The LRO electronics system, illustrated in the Figure 2.3, collects and digitizes signals from the PDS, which consists of tetra-phenyl butadiene (TPB)-coated 8 in photomultiplier tubes (PMTs) (Hamamatsu[1] R5912-02-mod) placed beneath the TPC cathode. The PDS detects the primary

[1] Hamamatsu™R5912-02-mod, `http://www.hamamatsu.com/`.

scintillation signals, which provide the absolute time reference for interaction events. The same electronics also enables recording light signals generated by photons from what is called the proportional scintillation component, i.e., the light created by the electrons extracted and amplified in the gaseous phase. A fraction of this light can reach the PMTs after traversing the entire detector volume. The LRO electronics, consisting of analog and digital stages, is housed in the μTCA crates on top of the cryostat structure (as are the CRO electronics). The LRO AMC card design shares a similar architecture with the AMCs for the charge readout. Apart from a dedicated front-end stage, the LRO AMC inherits completely the well-tested circuitry and firmware of the CRO AMC and common operation environment. The LRO μTCA crates are connected to specific LRO signal feedthrough flanges on top of the cryostat (see chapter **??**).

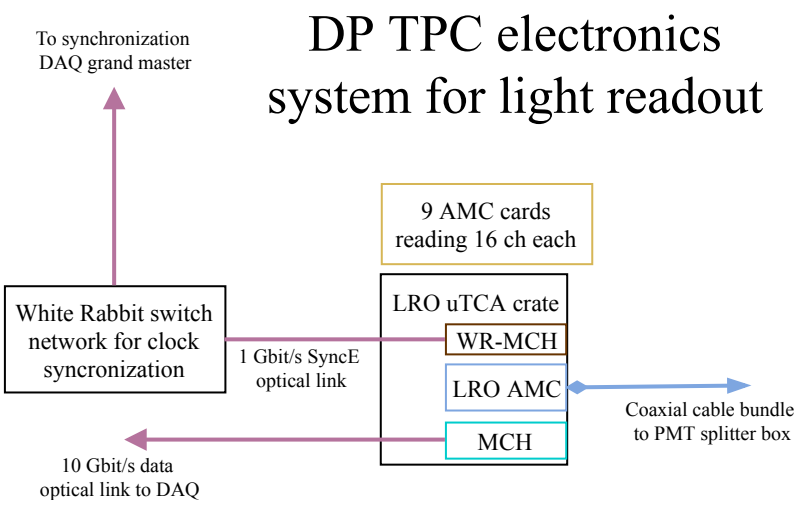

Figure 2.3: Schematic layout of the DP LRO subsystem.

Each μTCA crate for either charge or light readout is connected to the DAQ system via an optical fiber link that supports at least 10 Gbit/s. Each crate also contains a White Rabbit μTCA Carrier Hub (WR-MCH) for time synchronization of the digital electronics. This timing slave unit is connected via 1 Gbit/s optical fiber to a master node that serves as a synchronization reference for all connected slave nodes on the network. This system for time synchronization is built around the commercially available components from the White Rabbit (WR) project[2] with *ad hoc* hardware and firmware development. The system performs automatic and continuous self-calibrations to account for any propagation delays and can provide sub-ns accuracy for timing synchronization.

2.1.2 Design Considerations

The CRO electronics design includes the analog FE cards (containing pre-amplifier ASICs operating at cryogenic temperatures) and digitization cards with their synchronization system installed outside of the cryostat. All these original components have been expressly developed and designed for DP module. The system reads and digitizes signals from 153,600 channels (the total number of CRO channels per one DP module) and can continuously stream the losslessly compressed data to the DAQ with no zero suppression.

[2] `https://www.ohwr.org/projects/white-rabbit`.

The design of the electronics systems was developed to meet the specifications summarized in Table 2.1.

Table 2.1: Specifications for DP-ELEC

Label	Description	Specification (Goal)	Rationale	Validation
DP-FD-1	Minimum drift field	$> 250\,\mathrm{V/cm}$ ($> 500\,\mathrm{V/cm}$)	Lessens impacts of e^--Ar recombination, e^- lifetime, e^- diffusion and space charge.	ProtoDUNE
DP-FD-2	System noise	$< 2500\ e^-$ ($\sim 1000\ e^-$ (achieved in WA105))	Provides >5:1 S/N on induction planes for pattern recognition and two-track separation.	ProtoDUNE and simulation
DP-FD-3	Light yield	$> 1\,\mathrm{PE/MeV}$ (min), $> 3\,\mathrm{PE/MeV}$ (avg)	Corresponds to point where improvements in resolution with increasing light yield slow down significantly.	Simulated SN neutrinos in FD.
DP-FD-4	Time resolution	$< 1\,\mu\mathrm{s}$ ($< 100\,\mathrm{ns}$)	Enables 1 mm position resolution for 10 MeV SNB candidate events for instantaneous rate $< 1\,\mathrm{m^{-3}ms^{-1}}$.	
DP-FD-5	Liquid argon purity	$< 100\,\mathrm{ppt}$ ($< 30\,\mathrm{ppt}$)	Provides >5:1 S/N on induction planes for pattern recognition and two-track separation.	Purity monitors and cosmic ray tracks
DP-FD-13	Front-end peaking time	$1\,\mu\mathrm{s}$ (Adjustable so as to see saturation in less than 10 % of beam-produced events)	Vertex resolution	
DP-FD-14	Signal saturation level	7,500,000 e^-	Maintain calorimetric performance for multi-proton final state.	

DP-FD-19	ADC sampling frequency	$\sim$ 2.5 MHz	Match 1 µs shaping time.	Nyquist requirement
DP-FD-20	Number of ADC bits	12 bits	ADC noise contribution negligible (low end); match signal saturation specification (high end).	Engineering calculation and design choice
DP-FD-21	Cold electronics power consumption (for DP??)	< 50 mW/channel	No bubbles in LAr to reduce HV discharge risk.	Bench test

- The CRO electronics must measure signals up to 1200 fC without reaching saturation. The system has reached this following Monte Carlo (MC) studies on the maximal occupancy per channel in shower events [9]. For a nominal CRP gain of 20, a MIP signal from a particle traveling horizontally with an azimuthal angle of 0° (the lowest limit) should be approximately 30 fC. This gives a maximal operational range of 40 MIPs.

- The electronic noise in the CRO analog electronics must be <2500 e^-. This condition can be derived from the requirement on the minimal S/N, which should be more than 5:1 once the charge attenuation is taken into account. Given the maximum drift distance of 12 m, the largest attenuation factor due to electro-negative impurities, assuming the 3 ms (minimally required) electron lifetime and the drift field of 0.5 kV/cm, is 0.08. The smallest MIP signal with the CRP effective gain of 20 is, therefore, 2.5 fC (15,600 e^-).

- To achieve optimal vertex resolution, the peaking time of the FE analog amplifiers must be 1 µs. The optimal resolution is determined by the single track resolution and the separability of two or more tracks close to one another.

- The sampling frequency must be 2.5 MHz to match the peaking time of the FE electronics.

- The power dissipated by the FE analog electronics must be below 50 mW/channel to minimize heat input to the cryostat volume.

- The FE analog electronics must be replaceable without contaminating the main LAr volume to guarantee the long-term reliability of the system.

- The analog-to-digital converter (ADC) resolution must be such that the noise is at the level of an ADC count, given a dynamic range wide enough to match the response of the FE amplifier. This can be achieved with a 12 bit ADC.

- The warm digital electronics must accommodate standard industrial components and solutions to keep costs low and to benefit from technological evolution, e.g., higher network

speeds.

As described in subsequent sections, the system exhibits significantly better performance than set forth in the requirements.

The (lossless) data compression efficiency is dependent on the noise level. A compression factor of four is obtained with noise at approximately 1.5 ADC counts, and a compression factor of approximately 10 with an RMS noise level less than 1 ADC.

The LRO system must detect signals from a minimum of one photoelectron on one PMT, giving a precise timestamp that can be used in conjunction with the charge signals to determine the absolute event time (t_0). Precise measurements of LRO signal charge at a single photoelectron level allow continual monitoring of the PMT gain, as well as determination of the number of photons in each scintillation event. The continuous ADC streaming of data, downsampled to 400 ns as for the CRO signals, allows measurement of the scintillation time profile. The LRO system also reads 20 channels from reference silicon photomultiplier (SiPM) sensors from the photon detector (PD) calibration system.

The cryogenic analog electronics for the CRO is housed in the dedicated SFT chimneys. Its design enables access to the FE card so that it can be replaced without contaminating the pure LAr in the main cryostat volume. The chimneys have a cooling system that can control the temperature around the FE cards to roughly 110 K to reach their optimal noise level; this compensates for the heat input from the chimneys into the cryostat volume.

The digital electronics for both charge and light readout is in the warm environment on the top of the cryostat support structure. This removes any constraints associated with accessibility and operation in cryogenic environments, allowing use of standard components and industrial solutions in the design. Digital electronics must be continuously and automatically synchronized to more than 400 ns to ensure the correct temporal alignment of the ADC samples from all of the readout channels. This is a minimal requirement dictated by a sampling rate of 2.5 MHz.

Key parameters for the electronics system design are summarized in Table 2.2.

2.1.3 Scope

The scope of the TPC electronics system covers procurement, production, testing, validation, installation, and commissioning of all components necessary to ensure the complete readout of the charge and light signals from a given DP module. This includes

- Cryogenic analog FE cards for charge readout;
- AMC cards for charge and light readout;
- The WR-MCH cards for AMC clock synchronization;

Table 2.2: Key parameters for the TPC electronics system design for one DP module.

Parameter	Value
CRO channels	153,600
CRO continuous sampling rate	2.5 MHz
CRO ADC resolution	12 bit
CRO data compression factor	10
CRO data flow	430 Gibit/s
LRO channels	720
LRO continuous sampling rate	2.5 MHz
LRO ADC resolution	14 bit
LRO data compression factor	1
LRO data flow	24 Gibit/s

- μTCA crates;
- Switches for the WR network;
- SFT chimneys;
- LV power supplies, distribution, and filtering system for the FE cards;
- Flat cables connecting the FE cards to the warm flange interface of the SFT chimneys;
- VHDCI cables connecting the warm flange interface of the SFT chimneys to AMCs.

The total number of components to be procured to instrument one DP module are given in Table 2.3.

Table 2.3: Numbers for DP electronics components to procure for one DP module.

Name	Number
CRO cryogenic ASICs (16 ch)	9600
CRO cryogenic analog FE cards (64 ch)	2400
CRO AMCs	2400
SFT chimneys	240
Flat cables for SFT chimney (68 ch)	2400
Flat cables for SFT chimney (80 ch)	2400
VHDCI cables (32 ch)	4800
LRO AMCs with analog FE	45
μTCA crates	245
WR-MCH units	245
WR switches (18 ports)	16

2.2 System Design

The CRO FE analog electronics uses a cryogenic ASIC chip with a large dynamic range (up to 1200 fC) to accommodate the charge amplification in the CRP. The FE cards read 64 CRP channels each. They are mounted in dedicated SFT chimneys <1 m from each CRP to minimize noise caused by long cables (large cable capacitance). The cards remain accessible throughout the DP module operation. Each SFT chimney accommodates 10 FE analog cards, which corresponds to the readout of 640 CRP channels per chimney. Therefore, 240 SFT chimneys must be installed for the charge readout in a given DP module.

The differential analog signals from the analog FE cards, carried by the twisted-pair ribbon cables and routed through an interface flange of the SFT chimneys, are digitized by the AMC cards located outside the cryostat. These cards are installed in μTCA crates placed near the SFT chimneys (one crate per chimney). In the current design, each AMC digitizes 64 channels, corresponding to one FE analog card. Each μTCA thus contains 10 AMCs reading a total of 640 channels. However, using AMCs that support a higher channel density is under investigation to reduce costs.

The LRO FE analog and digital electronics are based on a custom-built AMC. The card contains a CATIROC ASIC [10], which is used to determine the precise charge and start times of signals from the individual PMTs. In addition, a 14 bit 65 MHz ADC digitizes data for continuous streaming of PMT signals. Each card reads up to 16 channels. A potential upgrade under consideration would increase the channel density per card to 32 channels. The LRO cards are housed in five dedicated μTCA crates close to the PMT instrumentation feedthroughs.

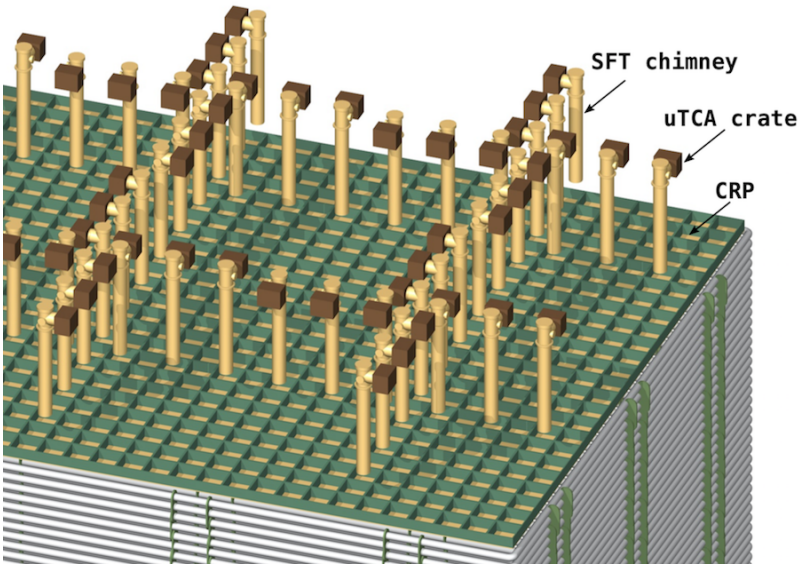

Figure 2.4: Corner view of DP module showing the pattern of the SFT chimneys and μTCA crates for charge readout above CRPs.

Every μTCA crate contains a network switch, MicroTCA Carrier Hub (MCH), through which data are sent to the DAQ and to a (WR-MCH) for time synchronization to trigger timestamp distribution to the AMCs. The MCH and WR-MCH require one optical fiber link each.

The MCH switch streams the data from AMCs using a dedicated optical link. ProtoDUNE-DP uses a MCH operating at 10 Gbit/s, however, we are considering a move to 40 Gbit/s links for the DP module implementation because of new technology with associated cost reductions and a possible increase in the channel density of each AMC.

The WR-MCH time synchronization unit is based on the WR system, which provides hardware and protocols for the network-based sub-ns synchronization between a master and different slave nodes. The connection of the WR-MCH to the WR network is done via 1 Gbit/s synchronous Ethernet optical link. WR-MCH distributes the timing information for synchronizing the AMCs via the μTCA backplane. In addition, this unit can transmit triggers to the digitization units within the crate by sending dedicated data packets containing trigger timestamp information.

Figure 2.4 shows a corner view of the DP module illustrating the pattern of the SFT chimneys and the attached μTCA crates above the CRPs. Each crate/SFT chimney collects signals from 3 m long strips of two $1 \times 3\,\mathrm{m}^2$ CRP segments. Each chimney completely penetrates the cryostat insulation layers (not shown in the figure).

Table 2.4 provides a summary of some of the principal components and channel granularity in the DP electronics design.

Table 2.4: Principal components and channel granularity of the DP module electronics system for charge and light readout.

Name	Number
CRO SFT chimneys/μTCA crates	240
CRO channels per SFT chimney/μTCA crate	640
CRO cryogenic analog FE cards per SFT chimney	10
CRO AMCs per μTCA crate	10
LRO FE cards per μTCA crate	9
LRO channels per μTCA crate	144
LRO μTCA crate	5
WR-MCH per μTCA crate	1

2.2.1 Cryogenic Analog Front-end Electronics

The cryogenic amplifier ASIC is the principal component of the FE analog cards. Its design is based on CMOS 0.35 µm technology and is a result of R&D begun in 2006, which created several versions of the cryogenic amplifier for both SP and DP liquid argon time-projection chamber (LArTPC) detectors. Two principal versions of ASIC chips have been produced for DP LArTPC operation. In the first version, the amplifiers have a constant gain in signal inputs of 0 to 1200 fC (0 to 40 MIP). In the second, the amplifiers have a higher linear gain for signals up to 400 fC (roughly 10 MIP signals) and a logarithmic response in the 400 to 1200 fC range. This double-slope behavior is obtained by using a MOSCAP capacitor in the feedback loop of the amplifier that changes its capacitance above a certain signal threshold. The goal of this solution is to optimize the resolution

for few-MIP charge depositions while preserving the overall large dynamic range of the amplifier.

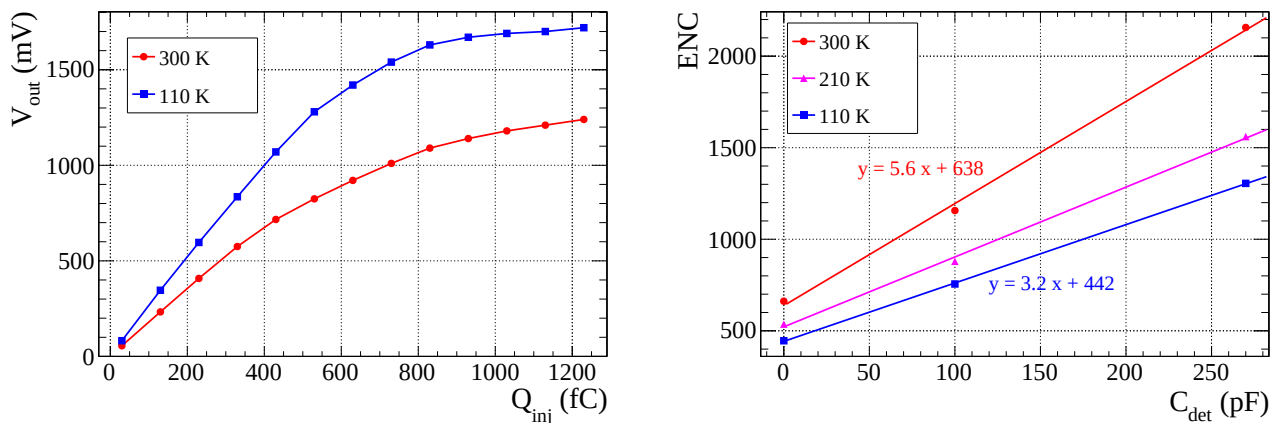

Figure 2.5: Cryogenic FE ASIC properties: amplifier response (left) and noise (right) at different temperatures measured at the output of differential buffer.

We selected the ASIC version with the double-slope gain for ProtoDUNE-DP and are adopting it for the DP TPC electronics design. The left plot in Figure 2.5 illustrates the response of this amplifier to different values of the injected charge, and the right plot shows the measured noise in units of ENC as a function of the detector capacitance at different temperatures. For the CRP anode (detector) capacitance of 480 pF per 3 m strip, the expected noise is approximately 2000 e^- at 110 K. Each ASIC contains 16 amplifier channels with differential line buffers and has a power consumption of 11 mW/channel, surpassing the <50 mW/channel requirement.

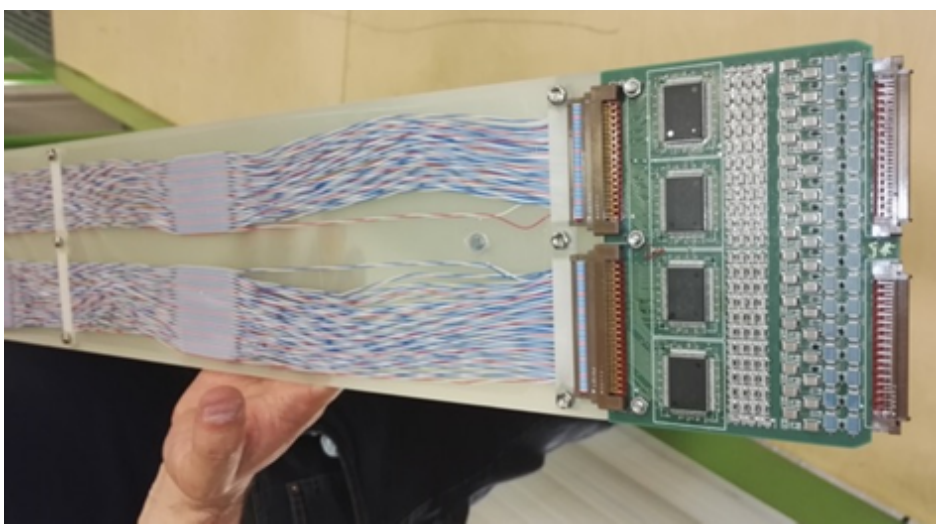

Figure 2.6: Photo of an analog cryogenic FE card mounted on the extraction blade, which is a part of the SFT chimney subsystem.

Each cryogenic FE card, shown in Figure 2.6, holds four ASIC amplifier chips (black rectangular elements in the picture) and a few passive discrete components. The input stage of each amplifier channel has a 1 GΩ resistor to ground followed by a 2.2 nF decoupling capacitor; both are rated for high voltage (HV) operation. The resistor grounds the CRP anode strips.

A TVS diode[3] protects each input stage against discharges coming from the DP module. This component was selected after studying how well different devices protected against electrostatic discharges of a few kV and an energy similar to that of the large electron multipliers (LEMs) in the CRP. This assumes the worst possible scenario where the spark propagates directly to the input of the pre-amplifier. The electrostatic discharge protection components were systematically subjected to about 1000 discharges using an automated system built with fast HV-rated reed relays that controlled charging and discharging cycles of an HV capacitor emulating the energy of a spark from a LEM. No degradation in performance was observed in the selected TVS diodes after this stress test: sparks were still quenched the profile of the time response was unchanged.

The FE cards also house the blocking capacitors for further filtering of LV power lines. These are first filtered at the power supply and transported via shielded cables.

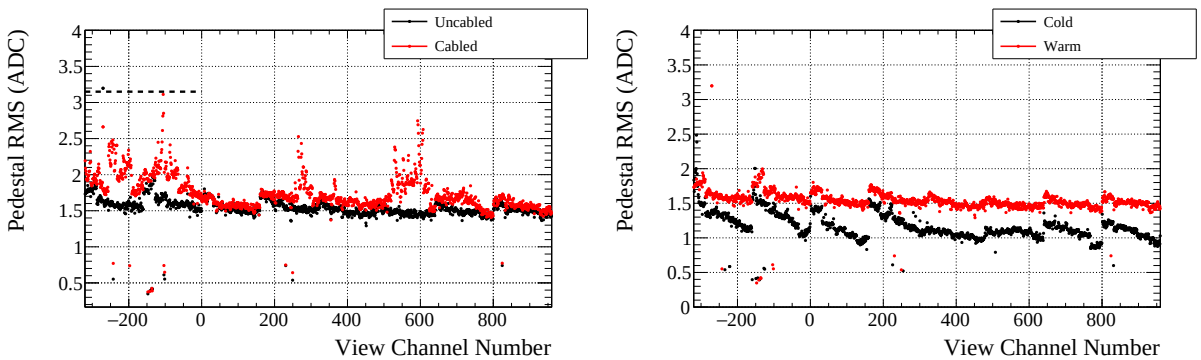

Figure 2.7: Noise of measurements in the WA105 DP demonstrator under different conditions. Left: warm only, with the slow control cables connected to the cryostat flanges (red points) and disconnected (black points). The horizontal dashed line in this plot indicates the noise level expected for 3 m strips. Right: warm (red points) and cold (black points) with the slow control cables disconnected. The channels with negative (positive) channel number correspond to the strips of 3 m (1 m).

Although the FE amplifier ASICs are in a shielded environment in the chimneys, which act as Faraday cages, interference from other equipment (via a noisy ground or ground loops) could significantly degrade the noise performance from the design target. Figure 2.7 shows results of noise measurements performed under different conditions in the WA105 DP demonstrator. The channels reading 3 m (1 m) long strips correspond to negative (positive) channel numbering in the plots, and the 1 ADC count is equivalent to about 900 electrons. The left plot in Figure 2.7 shows the noise measurements at warm temperatures with and without slow control cables (CRP HV, CRP motors, level meters, temperature probes, etc.) connected. The noise is clearly affected by the grounding of the slow controls: the average value of the noise RMS is approximately 1.7 ADC with slow control cables connected and decreases to approximately 1.5 ADC counts when they are removed. The grounding scheme of the WA105 DP demonstrator is not the one planned for the DP module, where all electrical equipment is referred uniquely to the cryostat ground and is completely insulated from the external environment.

One interesting feature, particularly visible with the cables disconnected, is the similarity of the noise measured for the channels connected to the 1 m and 3 m long strips in the WA105 DP demonstrator. Given that the longer strips have three times the input capacitance of the shorter

[3] Bourns™ CDSOD323-T08LC TVS diode.

ones, the expected noise (see Figure 2.5) for these should twice as large as indicated by the dashed line in the plot. In addition, the noise on the short strips is lower than expected (1.5 ADC) for the 160 pF/m strip input capacitance (1.7 ADC). The reason for this behavior in the WA105 DP demonstrator is still under investigation. Measurements have already shown that the capacitance of the CRP anode strips is not purely to ground, but rather driven by the inter-strip couplings, which creates a more complicated electrical network.

Figure 2.7 (right) also compares the noise measurements in the WA105 DP demonstrator taken with the FE electronics at warm (red points) and cold (black points) at around 150 K. The slow control cables were disconnected in both cases. However, the cold measurements were performed with the recirculation pump active and the cathode HV connected. The RMS noise averaged over all channels decreases by about 25%, from roughly 1.5 ADC to 1.1 ADC, when the FE analog cards are cold. For comparison, the expected signal for an MIP with a CRP gain of 20 should be around 200 ADC counts.

The overall grounding principle of the WA105 DP demonstrator used the cryostat as the ground reference. The LV power supplies for the FE analog electronics and the μTCA crates were powered using insulating transformers to ensure that no other ground could interfere. In contrast, the design of the slow control system did not include any insulation transformers. This equipment was grounded to the building electrical network, thereby interfering with the ground of the cryostat. Stricter treatment of the ground connections, as implemented for ProtoDUNE-DP and planned for the DP module, and a lower SFT chimney operating temperature of approximately 110 K (from 150 K) should help further reduce noise from the levels observed in the WA105 DP demonstrator.

2.2.2 Signal Feedthrough Chimneys

The SFT chimneys are designed to enable access to the FE analog electronics for repair or exchange while the DP module is filled and in operation. In addition, their metallic structure acts as a Faraday cage isolating the FE ASICs from environmental interference. Each SFT chimney hosts 10 analog cryogenic FE cards (reading 640 channels in total). Figure 2.8 shows details of the design.

The chimneys are closed at the bottom and top with vacuum-tight feedthrough flanges that dispatch the signal and slow control lines to/from FE electronics located inside. The feedthrough at the bottom, the cold (signal) feedthrough, isolates (ultra-high vacuum tightness standard) the inner volume of the DP module from the chimney volume and interconnects the signals from the CRP to the analog FE cards. The feedthrough at the top, the warm (signal) feedthrough, seals the chimney from the outside environment. It also passes the LV and control lines to the FE electronics inside and brings out the differential analog signal lines from the FE amplifiers.

The SFT chimney volume is filled with nitrogen gas at near-atmospheric pressure. The temperature inside the chimney can be adjusted using a heat exchanger copper coil cooled with LAr, which is located at the bottom close to the cold feedthrough around the FE cards. This cooling system mitigates the heat input to the main DP module volume and provides an optimal (lowest noise) operating temperature for the FE electronics of approximately 110 K. A pressure release valve,

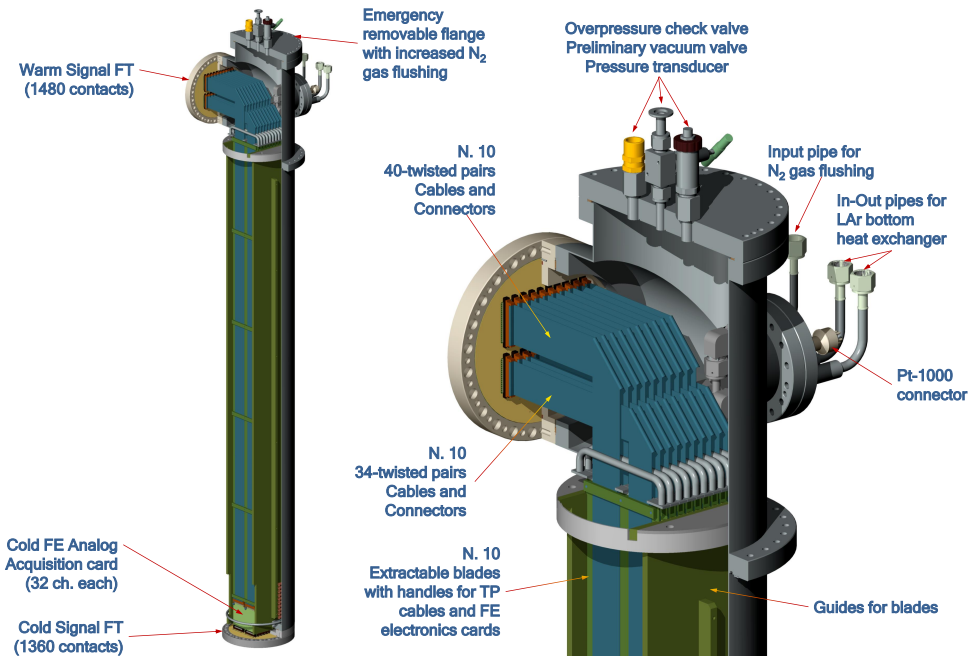

Figure 2.8: Details of the signal feedthrough (SFT) chimney design.

indicated in Figure 2.8, protects the structure from an accidental overpressure in the inner volume.

The expected heat input from a given SFT chimney is about 20 W. This number includes the heat through the twisted-pair cables connected to the warm feedthrough, the heat in the SFT outer metallic tube, as well as the heat dissipation by the FE cards. A total heat input from all 240 SFT chimneys is at the level of 5 kW.

The analog FE cards are inserted directly onto the PCB of the cold feedthrough of SFT chimney (see Figure 2.9). The other side of the PCB (facing the inside of the cryostat) hosts the connectors for the flat cables coming from the CRP anodes. The FE cards are mounted on 2 m long blades made from FR4 that enable the insertion and extraction of the electronics and also support the flat cables carrying signals, low voltages, and slow control to and from the warm flange interface. The blades slide along the rails installed inside the chimney on opposite sides; these rails guide the FE cards to their respective connectors on the cold feedthrough.

Before commissioning a DP module, the chimneys are evacuated via a dedicated ISO standard KF16 port (see Figure 2.8) and then filled with nitrogen gas. This ensures removal of any moisture that would otherwise condense around the FE cards once the DP module is filled with the LAr and potentially damage the electronics. To access the FE cards once the DP module is cold, the stainless steel flange at the top of the SFT chimney (Figure 2.8) must be removed. This procedure requires continuous flushing of nitrogen gas at slight over-pressure (with respect to atmospheric pressure) to prevent humid air from entering. Once a chimney is opened, the blades can be extracted with the FE cards after unplugging the flat cables (two per card) connected to the inner side of the warm flange (Figure 2.8).

The procedure to access the FE cards under cold operation was successfully tested during the

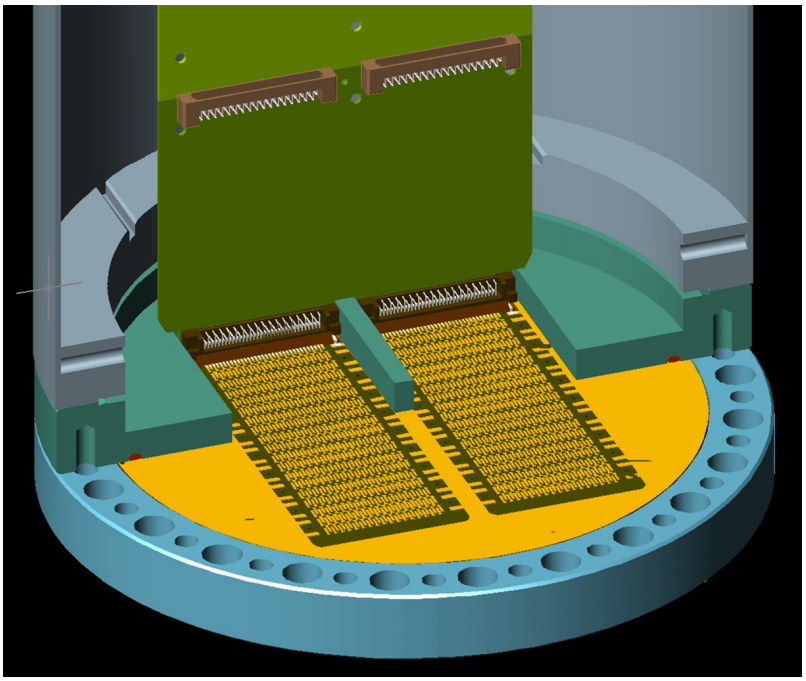

Figure 2.9: SFT chimney cold feedthrough flange with one of the FE cards mounted.

WA105 DP demonstrator run. The top of the chimney was very close to room temperature, allowing the cable connections to be manipulated on the warm feedthrough flange without cryogenic gloves. The movement of the blades on the rails and the FE card extraction and insertion showed no mechanical problems due to the shrinking of various elements at lower temperatures. The signals from the FE cards that underwent this process were also checked, and all channels functioned properly.

2.2.3 Digital Advanced Mezzanine Card Electronics for Charge Readout

The CRO AMC cards read and digitize the data from the FE amplifiers and transmit them to the DAQ system. They also include a last stage of analog shaping before ADC input. The development of these cards went through two intermediate prototyping stages before defining the architecture of the final version for DUNE in 2016. The analog FEs produce differential unipolar signals defined with respect to a baseline offset. Before digitization, this offset is removed, and the signals are subtracted in the analog input stage of the digital electronics. Each card has eight ADC chips (Analog Devices, AD9257[4], Table 2.5), two dual-port memories (Integrated Device Technology IDT70T3339[5]), and a field programmable gate array (FPGA) (Alterra[6] Cyclone V) on board. The FPGA provides a virtual processor (NIOS) that handles the readout and the data transmission. The choices for all of the components are optimized to meet design requirements and technical criteria such as costs, chip footprint (small enough to fit on the AMC), power consumption, and

[4]Analog Devices™, `http://www.analog.com/media/en/technical-documentation/data-sheets/AD9257.pdf`.

[5]Integrated Device Technology™ (IDT), `https://www.idt.com/document/dst/70t33391999-data-sheet`.

[6]Alterra™, `https://www.altera.com/products/fpga/cyclone-series/cyclone-v/overview.html`.

ease of use (available functionality).

Table 2.5: Main characteristics of ADC AD9257.

Item	Characteristics
Channels	8
Sampling	up to 40 MSPS
Resolution	0.122 mV
Dynamic range	14 bit/ 2.0 V
Differential non-linearity	typical ±0.6 Least Significant Bit (LSB) with min. −1.0 and max. 1.7 LSB
Integral non-linearity	typical ±1.1 LSB with min. −3.1 and max. 3.1 LSB

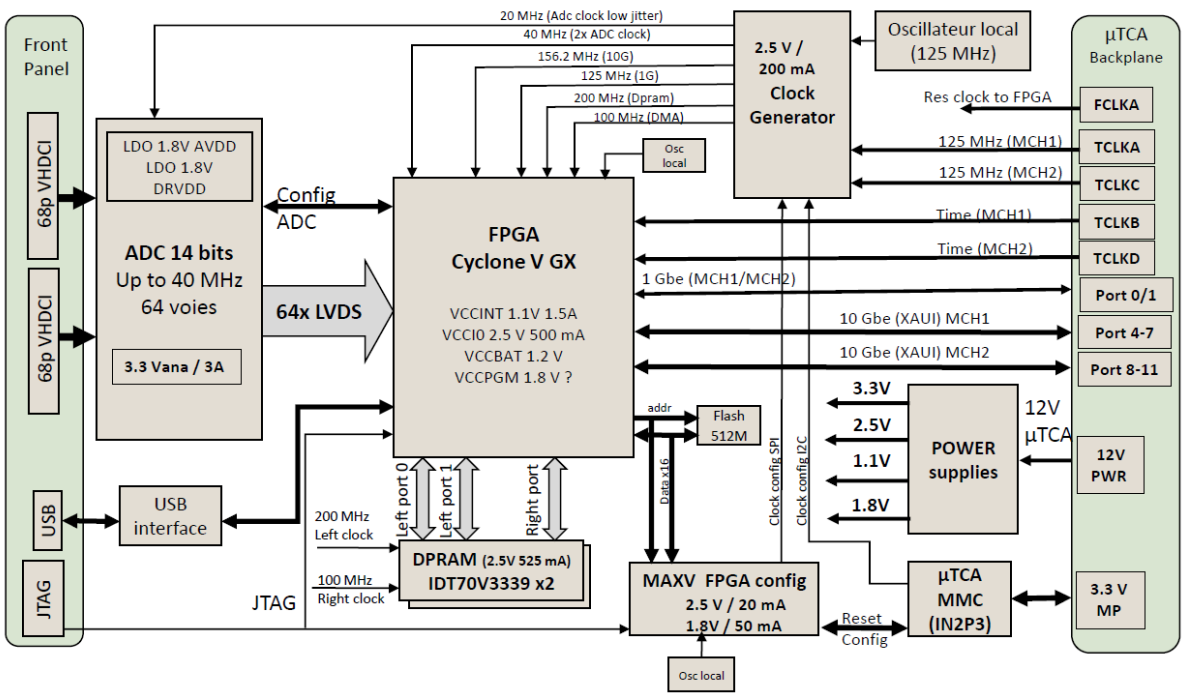

Figure 2.10: Block diagram of CRO AMC.

Figure 2.10 illustrates the AMC functionality. Each AMC generates a continuous compressed stream of 2.5 MSPS 12 bit data per readout channel. The on-board ADCs operate at a rate of 25 MHz per channel. The data are down-sampled in the FPGA to 2.5 MHz by performing ten-sample averaging, which leads to further digital filtering of the noise. The data, consisting of only the 12 most significant bits from each digitized 14 bit sample, are then compressed using an optimized version of the Huffman algorithm [11] and organized into frames for transmission. The frames contain the absolute timing information of the first data sample for reliability. In the current design, each AMC has 64 channels and reads one analog FE card.

The AMCs are housed in μTCA crates and send their data via the MCH switch. The timing synchronization of AMCs is achieved via a WR-MCH module (also housed in the crate) that is

connected to the WR network. In addition, a WR-MCH could also be used for triggered AMCs readout if it were sent dedicated packets containing trigger timestamp information over the WR network.

In ProtoDUNE-DP, AMCs are operated in the triggered mode, reading a 4 ms drift time window at a trigger rate of 100 Hz, which is not far from continuous readout mode. The analog data are continuously digitized and buffered. It is possible to acquire a sub-sample of these data by providing the AMC with a timestamp generated by an external trigger. The timestamp defines the start time for the data sequence to be read, while the length of the sequence is determined by the size of the drift window. In ProtoDUNE-DP, this length corresponds to 10,000 400 ns samples per full drift window (4 ms). Triggers (beam counters, cosmic-ray counters, PMTs detecting the UV light, and starts of beam spills) are timestamped in a dedicated WR slave node (White Rabbit TimeStamping Node (WR-TSN)), an FMC-DIO mezzanine[7] mounted on a WR SPEC[8] carrier card. WR-TSN, hosted in a computer, runs a custom firmware developed for ProtoDUNE-DP. The WR-TSN is connected to the WR grandmaster for synchronization and transmission of trigger information. The timestamp data produced by the WR-TSN are sent over the WR network as Ethernet packets with a customized protocol.

2.2.4 Electronics for Light Readout

The LRO card is a 16 channel AMC containing one 16 channel 14 bit 65 MHz ADC (AD9249) and one CATIROC ASIC. Figure 2.11 illustrates the prototype board used for ProtoDUNE-DP, and Figure 2.12 is a photograph. In this prototype, a mezzanine board containing the ASIC and ADC sits on a commercial mother board (Bittware S4 AMC[9]) with a high specification FPGA (Alterra[10] Stratix IV). In the final implementation for the DP module, the mezzanine is integrated with the layout of the AMC board developed for the charge readout. A proposed upgrade, a 32 channel card, would reduce the required number of cards and increase the channel density to 352 channels per μTCA crate.

The analog signals from each PMT channel are split equally into two separate branches, waveform and CATIROC (see Figure 2.11). The waveform branch goes through an anti-aliasing low-pass filter after which the 14 bit 65 MHz ADC (AD9249) produces continuous digitization of the PMT waveform data, which are then down-sampled to 2.5 MHz before transmission to DAQ. The CATIROC branch is routed directly to the CATIROC ASIC for precise measurements of pulse charge and timing. Both paths produce data continuously and independently.

[7] Seven Solutions™, `https://sevensols.com/index.php/fmc-dio/`
[8] Seven Solutions™, `https://sevensols.com/index.php/products/spec/`
[9] Bittware™, Inc., `https://www.bittware.com/fpga/intel/boards/s4am/`.
[10] Alterra™, `https://www.altera.com/products/fpga/stratix-series/stratix-iv/overview.html`.

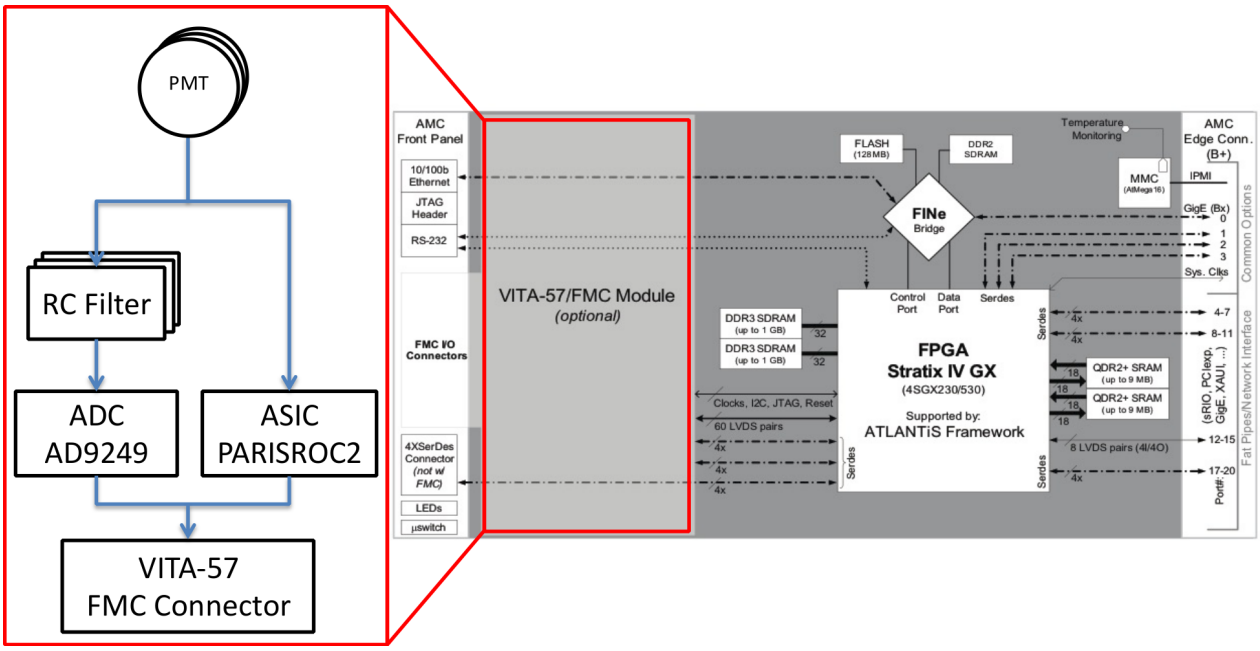

Figure 2.11: Block diagram of LRO prototype.

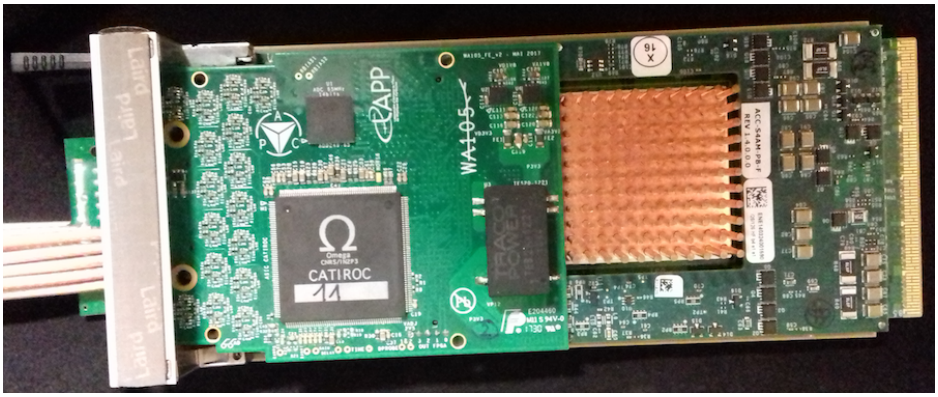

Figure 2.12: A photo of the LRO prototype.

2.2.4.1 Waveform branch

Table 2.6 shows the main characteristics of the ADC used for continuous digitization of the PMT signals in the waveform branch.

Table 2.6: Main characteristics of ADC AD9249.

Item	Characteristics
Channels	16
Sampling	65 MSPS
Resolution	0.122 mV
Dynamic range	14 bit/ 2 V
Differential non-linearity	typical ±0.6 LSB with min. −0.9 and max. 1.6 LSB
Integral non-linearity	typical ±0.9 LSB with min. −3 and max. 3 LSB

For normal operation in continuous mode, the FPGA down-samples the digitized signals to a coarse 400 ns sampling to match the CRO and limit the quantity of data streamed. Use of a higher-specification ADC, with time sampling of 15.4 ns, allows more flexibility. For particular calibration runs, waveforms with finer time sampling could be read out, allowing studies of, e.g., the LAr scintillation time profiles. During normal operation, moreover, online pulse processing is possible within the FPGA using finer time-sampled waveforms (before the down sampling); this enables continuous measurements of quantities like the rise and fall times of the pulses. Even at the coarse sampling rate of 400 ns, studies of the LAr scintillation time profile are possible (given the long fall-time constant of ∼1500 ns), as is matching of the electroluminescence signal (also known as proportional scintillation light) to the charge signal. Low light-level signals, from single or a few photoelectrons, will show no time structure but will consist of one sample several LSB above the baseline.

2.2.4.2 CATIROC branch

The CATIROC is a 16 channel ASIC dedicated to charge measurement and precision timing of negative-polarity PMT signals [10]. It auto-triggers on single photoelectrons and can sustain a high dark rate up to 20 kHz/channel. Charge measurements are possible over a range of 160 fC to 70 pC (corresponding approximately to a range of 1 to 400 photoelectrons with a PMT gain of 1×10^6). Timing measurements per channel can reflect an accuracy of 200 ps.

Figure 2.13 shows the schematic of the CATIROC ASIC. Its main properties are summarized in Table 2.7. The slow channel, from which precision charge and timing measurements are made, is formed by two variable-gain (8 bit) amplifiers followed by two variable slow shapers (one high gain for small signals and one low gain for larger signals) and two track-and-hold stages. The slow shaper has a tunable shaping time (up to 100 ns) and a variable gain. If the high gain is saturated, corresponding to passing a predetermined threshold common to all 16 channels, the

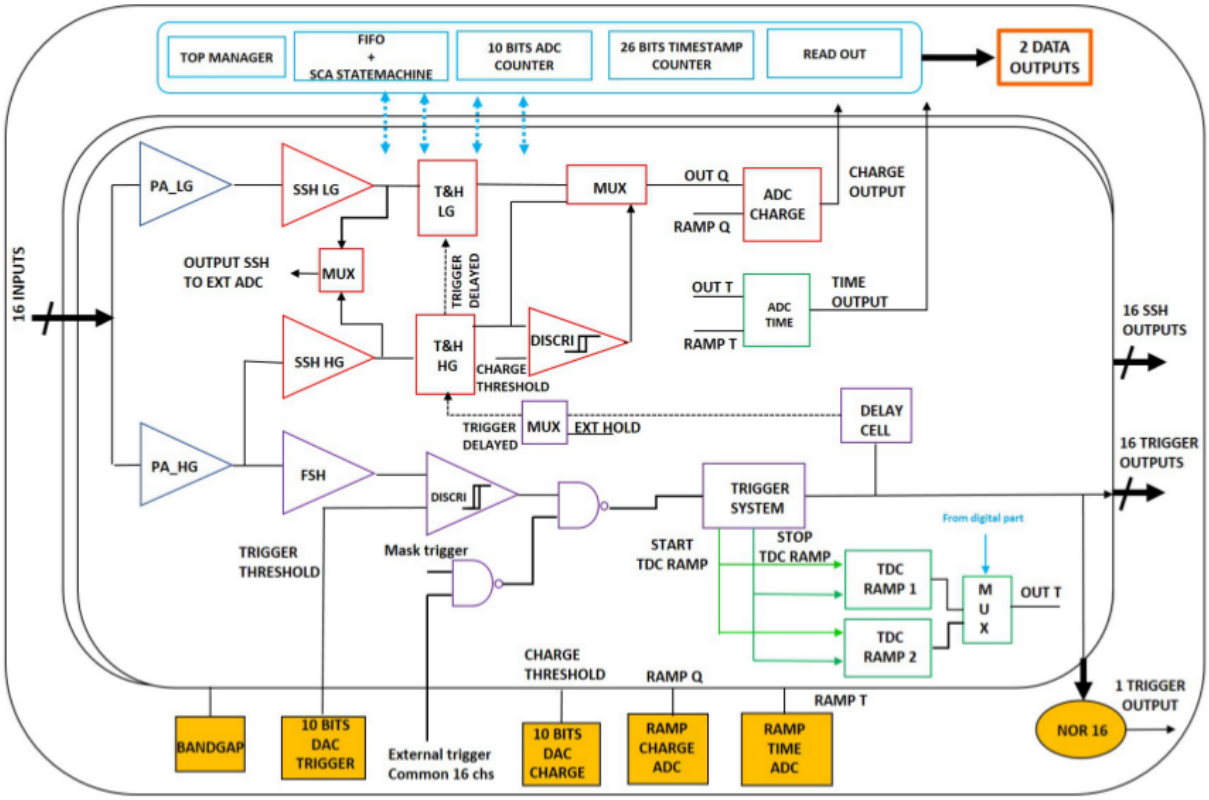

Figure 2.13: Functional diagram of CATIROC ASIC.

lower gain value is chosen. The chosen charge value is converted by an internal 10-bit Wilkinson ADC operating at 160 MHz. This slow channel operates in a ping-pong mode, with two capacitors to store the slow shaper signals, giving an effective buffer of two events. If both capacitors are full, a deadtime of 5 µs arises.

The fast channel is used to auto-trigger the ASIC and make fine timing measurements. It comprises a high-gain preamplifier, fast shaper (shaping time 5 ns), and discriminator with a 10 bit programmable threshold common to all 16 channels. The output of the discriminator is used for the two time-to-digital convertors to get the fine timing. A coarse timestamp could also be obtained from a 26 bit counter running at 40 MHz. Only data from triggered channels are digitized; their information is transferred to the internal memory, which the external FPGA reads.

2.2.5 Network-based μTCA Architecture

The digital electronics use the μTCA standard, which offers an industrial solution in a very compact and easily scalable architecture to handle a large number of channels at low cost. The standard (and related standards such as Advanced Telecommunications Computing Architecture (ATCA) and AMC) is widely used in the telecommunication industry and is being adopted by the HEP community. The backplane of the μTCA crates host high-speed serial links that support a variety of transmission protocols (e.g., Ethernet, PCI Express, SRIO). In addition, dedicated lanes are

Table 2.7: Main characteristics of CATIROC.

Item	Characteristics
Number of channels	16
Signal polarity	negative
Timing	Timestamp: 26 bit counter at 40 MHz Fine time: resolution <200 ps
Charge Dynamic Range	160 fC to 100 pC
Trigger	auto-trigger Noise = 5 fC Minimum threshold = 25 fC (5σ)
Digital	10 bit Wilkinson ADC at 160 MHz Read-out frame of 50 bits
Outputs	16 trigger outputs NOR16 16 slow shaper outputs Charge measurement over 10 bits Time measurements over 10 bits
Main Internal Programmable Features	Variable preamplifier gain Variable shaping and gain Common trigger threshold Common gain threshold

available to distribute clock signals to all boards hosted in the crate. The Ethernet-based solution has been adopted for both the data and clock distribution in this design of the DP electronics system for both charge and light readout.

Each AMC, either for charge or light readout, is plugged into the μTCA and connected to the crate MCH board through the backplane serial links. The MCH provides switch functionality that enables AMCs to communicate with one other or with external systems through the MCH uplink interface. In the DP electronics system design, MCH also manages the WR clock distribution.

Table 2.8: Bandwidth requirements per μTCA crate for continuous data streaming. A compression factor of 10 for the charger readout data is assumed.

Parameter	Value
CRO data rate	1.8 Gibit/s
LRO data rate	4.7 Gibit/s
Current MCH bandwidth	10 Gibit/s
Upgradable MCH bandwidth	40 Gibit/s

In the current DP module design, as for ProtoDUNE-DP, the MCH operates with a 10 Gbit/s uplink. Given that a μTCA crate hosts 10 AMCs for charge readout, the required bandwidth to stream data to the DAQ is about 1.8 Gbit/s. This assumes that data exiting the AMCs are losslessly compressed with the compression factor 10. The bandwidth required per crate link for streaming the LRO data is 4.7 Gbit/s. The 10 Gbit/s MCH is therefore sufficient to support these

data rates. However, the technology is moving toward supporting 40 Gbit/s rates. In addition, channel density per AMC could also be increased to optimize costs. For these reasons, an upgrade to a 40 Gbit/s MCH is possible in the future. This also indicates that the optical links connecting the DAQ system to μTCA MCH should operate at 40 Gbit/s. Table 2.8 provides a summary of the required and supported bandwidths per μTCA crate for continuous data streaming.

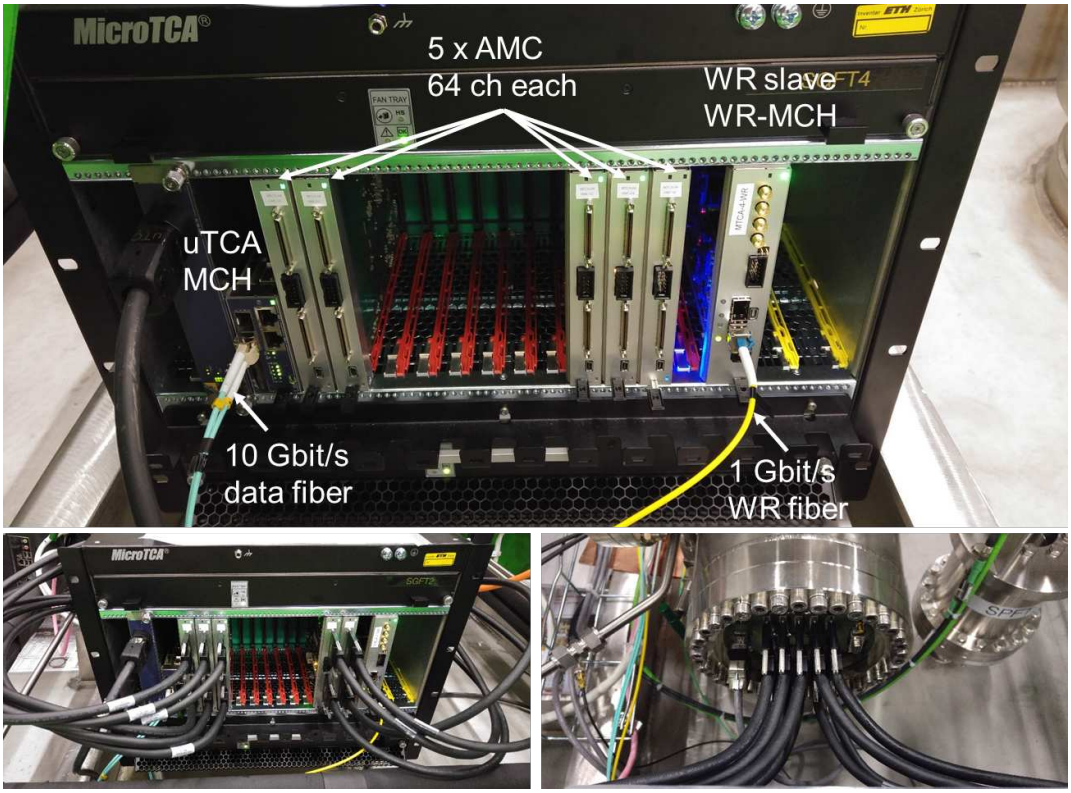

Figure 2.14: Pictures of an instrumented μTCA crate from the WA105 DP demonstrator. The crate contains five AMC cards, corresponding to the number of readout channels per SFT chimney. The lower images show the crate after the cables are connected to the warm flange of the SFT chimney.

Figure 2.14 shows photographs of one instrumented μTCA crate used for the charge readout of the WA105 DP demonstrator at CERN. In this detector, each SFT chimney reads 320 channels, thus requiring only five AMCs per the μTCA crate. The two optical fiber links, one (10 Gbit/s) for data and the other (1 Gbit/s) for clock and trigger timing distribution, are labeled in the top image.

2.2.6 Timing Distribution

The time synchronization system selected for the DP module uses a WR network that combines the synchronous 1 Gbit/s Ethernet (SyncE) technology with the exchange of PTPV2 packets to synchronize clocks of distant nodes to a common time. A high-stability GPS disciplined oscillator (GPSDO) with accuracy similar to an atomic clock provides a clock reference signal to be distributed over the physical layer interface of the WR Ethernet network. The network topology uses specially designed switches that have standard IEEE802.1x Ethernet bridge functionality with

additional WR-specific extensions to preserve clock accuracy. Time and frequency information are distributed to the nodes on the WR network via optical fibers. The WR protocol automatically performs dynamic self-calibrations to account for any propagation delays and keeps all connected nodes continuously synchronized to sub-ns precision.

The sub-ns precision on the clock synchronization is not strictly needed for aligning samples in the different AMC digitization units because the timing granularity on the data is 400 ns. However, the WR timing system offers the advantage of having readily available industrial components and the necessary protocols for their synchronization with automatic calibration of delay propagations. R&D on this timing distribution solution started in 2006; the final design for integrating this system, in the WA105 DP demonstrator, ProtoDUNE-DP, and the DP module readout, was completed in 2016.

In the implementation specific to ProtoDUNE-DP, a GPS-disciplined clock unit (Meinberg LANTIME M600[11]) feeds 10 MHz and 1 PPS reference signals to a commercial WR switch (Seven Solutions WRS v3.4[12]). The switch acts as grandmaster of the WR network. It is connected via 1 Gbit/s optical links to both the dedicated WR timestamping node (WR-TSN) and the WR end-node slave cards present within each μTCA crate (WR-MCH), keeping these synchronized to its reference time. The WR grandmaster also communicates through a standard Ethernet port with the LANTIME unit for its date and time synchronization via Network Time Protocol (NTP). The WR-TSN module receives analog TTL-level trigger signals, generates their timestamps, and transmits them over the WR network to the connected WR-MCH units. This timestamp information is then used by AMCs to find the data frame corresponding to the trigger.

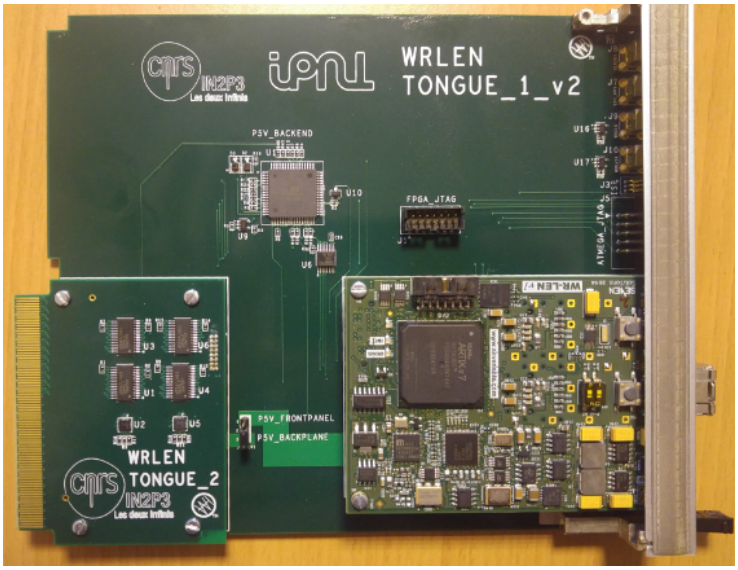

Figure 2.15: Picture of the WR slave node card (WR-MCH) present in each μTCA crate for time synchronization. The WR-LEN mezzanine card is visible in the bottom right corner.

The WR-MCH card (Figure 2.15) enables clock/timing/trigger distribution to AMCs. It communicates with them via dedicated lines in the backplane of the μTCA crate using a customized

[11] Meinberg™, `https://www.meinbergglobal.com/english/products/advanced-1u-ntp-server.htm`.
[12] Seven Solutions™, `http://sevensols.com/index.php/products/white-rabbit-switch/`.

data-frame protocol. The module contains a commercial WR slave node card, the WR Lite Embedded Node (Seven Solutions OEM WR-LEN[13]), as mezzanine card. WR-LEN runs on customized firmware that also enables it to decode the trigger timestamp data packet received over the WR network.

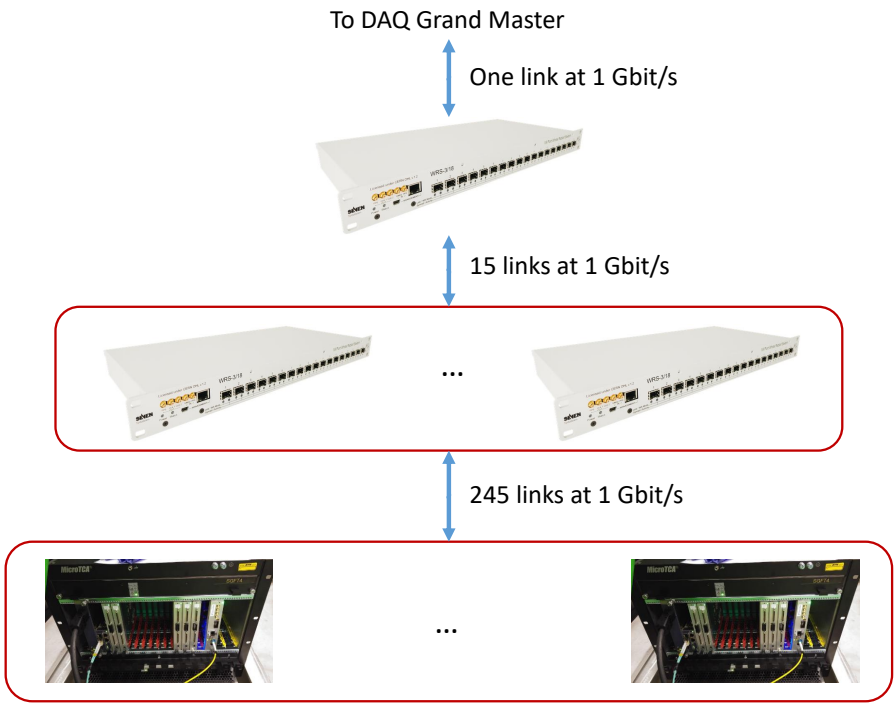

Figure 2.16: Architecture of WR network for time synchronization of digital readout electronics.

Figure 2.16 illustrates the architecture of the WR network layout for one DP module. It is built in a hierarchical structure from 16 WR switches with 18 ports each, chained with 1 Gbit/s optical fibers. The switch at the top of the hierarchy interconnects the synchronization WR grandmaster from the DAQ system with the 15 switches in the middle layer. These are, in turn, connected to the WR-MCH slave nodes in each μTCA crate (245 in total for charge and light readout).

2.3 Production and Quality Assurance

The DP TPC electronics system relies on commercially available products as well as custom made electronics elements. The quality control (QC) of the former will be done by the manufacturer, while production and any necessary QC of the latter will be ensured by the consortium institutions.

[13] Seven Solutions™, `http://sevensols.com/index.php/products/oem-wr-len/`.

2.3.1 Charge Readout Electronics

We envision splitting production of the front-end analog and digital electronics among several sites in France and Japan. The delivered cards will be divided between institutions in France, Japan, and the USA, where they will be tested and calibrated. Each card test site will be equipped to do QC and quality assurance (QA) checks as well as perform calibration of analog and digital cards. A common database will be developed and populated with test results.

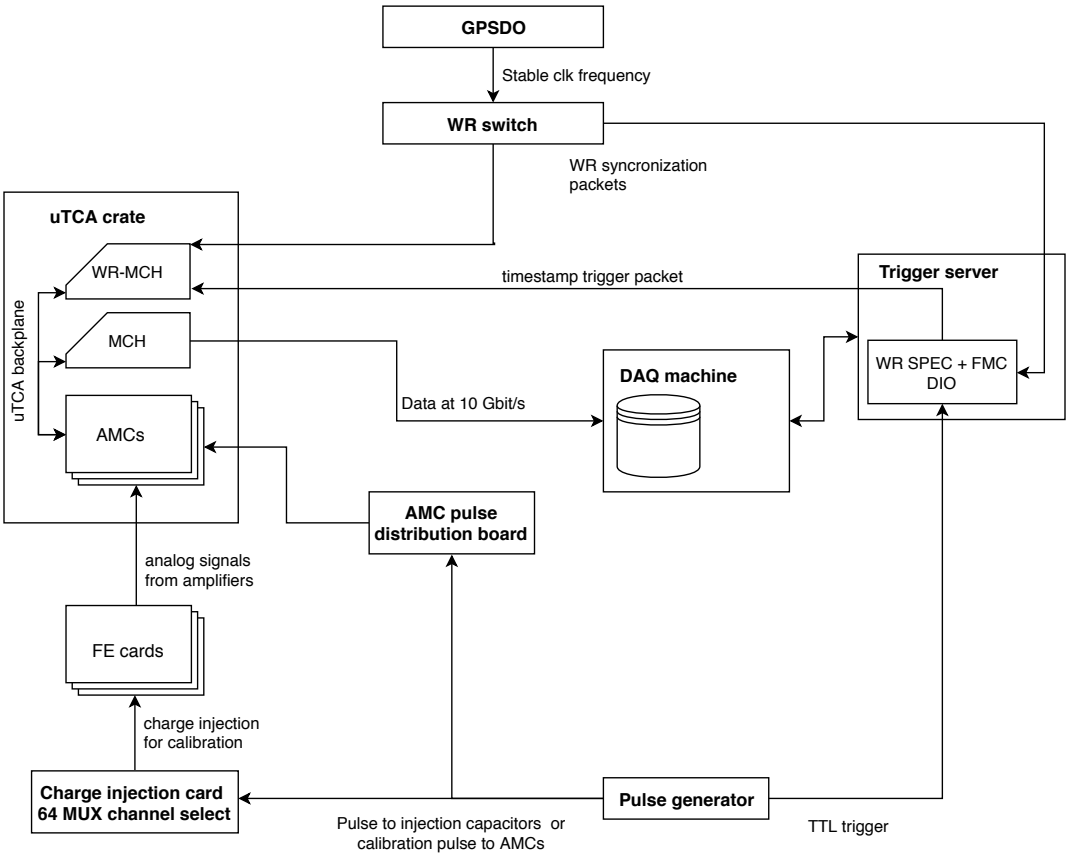

Figure 2.17: Overview of the configuration for quality control and calibration of CRO electronics system.

Based on the experience with the production of CRO readout electronics for ProtoDUNE-DP, Figure 2.17 schematically illustrates the necessary equipment and set-up for the QC of the production and calibration tasks. A μTCA crate equipped with MCH and WR-MCH will host AMCs to be tested and calibrated. Triggering follows the same scheme as in ProtoDUNE-DP relying on the distribution of timestamped trigger packets over the WR network to AMCs. The triggers are generated by a high precision pulse generator synchronously with the calibration pulse signals sent to the analog or digital electronics.

Five institutions (IPNL in France; KEK, NITKC, and IU in Japan, and SMU in the USA) share testing responsibilities for the cryogenic FE analog cards. The cards will be shipped to each testing site where collaborators will check performance parameters such as noise levels, dead channels, hot channels, and gain and its uniformity across channels, at both room and operating cold temperature. A dedicated calibration card has been developed, which injects via a precision capacitor a known amount of charge into individual ASIC channels to verify their functionality and calibrate

the gain of the amplifiers. The channels selection is automatically performed via a multiplexer.

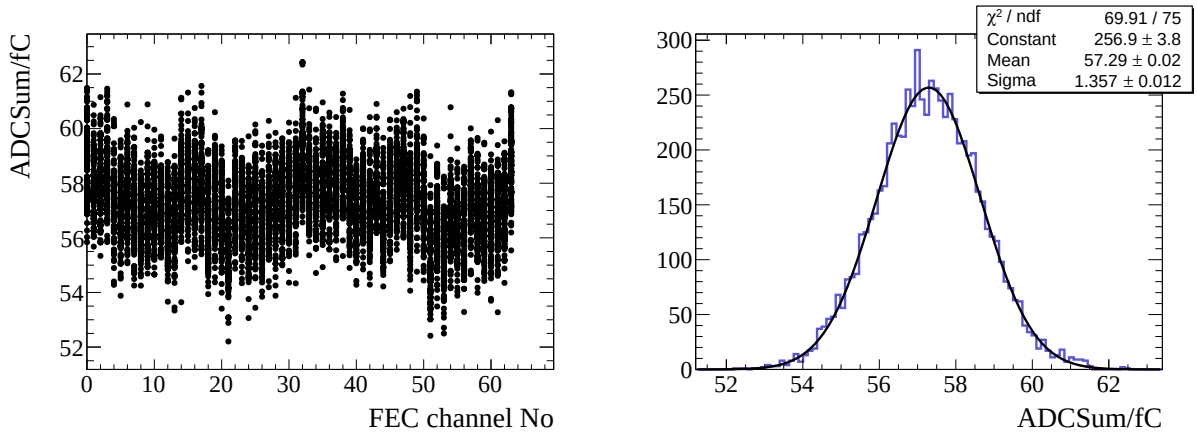

Figure 2.18: Channel-to-channel gain uniformity measured on FE cards produced for ProtoDUNE-DP. The plot on the left illustrates the gain (in units of pulse integral per unit of injected charge) as a function channel number for all the tested cards, while that on the right shows the overall distribution of the gain values fitted to the Gaussian function.

As an example, Figure 2.18 illustrates the channel-to-channel gain uniformity from the measurements performed with the FE cards produced for ProtoDUNE-DP. The figure on the left shows the gain (in units of pulse integral per unit of injected charge) as a function of channel number for all the cards tested, while that on the right shows the resultant distribution. The small systematic variations in the gain visible in the left-hand plot arise from channel-to-channel variations in the injection card used for calibration of the FE amplifiers. Overall the gain uniformity for all the channels is at the level of 2 %.

Production of the AMC cards for the charge readout is currently shared among four institutions (IPNL, KEK, NITKC, and IU). The cards ordered and delivered to each of these four institution are subjected to QC tests agreed upon by all participants. The functionality of AMCs could be verified by performing acquisition of the pedestal data. In the case of ProtoDUNE-DP production, this test allowed us to identify all the problems in the cards, almost all of which were a result of defective soldering that was not spotted by the automated QC procedure of the manufacturer. To calibrate the ADC buffer of the CRO AMCs, we inject a known pulse (Figure 2.17) into the input stage and measure the resulting pulse height after the digitization.

2.3.2 Light Readout Electronics

The number of LRO AMC cards required is small enough for production to follow in the same manner as for the production for ProtoDUNE-DP. The electronic components of the cards, which meet the required specifications, are purchased commercially. This part of the project will be managed by a qualified engineer working with a specialist in QA.

The cards are delivered to designated consortium institutions. Upon delivery, teams conduct basic quality tests, including visual inspection and electrical testing, to ensure conformity of production.

Another series of tests will ensure the cards' correct functionality and will also evaluate their performance. Measurements include linearity measurements of each ADC channel and linearity of the response of the ASIC. The level of cross-talk on the ASIC is also quantified.

A dedicated single-channel set up, with a PMT (Hamamatsu R5912-02-mod), and with the identical cabling and splitter as in the DP module, can be used to characterize the expected noise level of each channel and the response to single photoelectrons, up to saturation.

After shipment to Sanford Underground Research Facility (SURF) and on-site installation, a series of tests will be performed with a pulse generator to verify that the cards are in good working condition. Noise-level measurements are also included during integration.

2.3.3 Timing System and μTCA

Production of the cards and procurement of necessary WR components for WR-MCH units will be performed by four consortium institutions (IPNL, KEK, NITKC, and IU). The QC procedure for WR-MCH cards consists of

- checking the alignment of one-pulse-per-second signal (1PPS signal) signals between the WR switch acting as the network grand master (Figure 2.17) and each WR-MCH slave node, and
- performing data acquisition with functioning AMCs and verifying the quality of collected data.

The 16 WR switches and the 245 μTCA crates containing the power modules, carrier hubs (MCH), and fan units, are commercial products. The manufacturer is responsible for the necessary QA and QC of these components, requiring no further testing on the part of the DP electronics consortium. Once the components are delivered to the designated institutions, they can be sent to SURF for installation.

2.3.4 Signal Feedthrough Chimneys

The production of SFT chimneys and QC will be carried out by the LAL laboratory. Large engineering efforts (led by R. Marie, LAL) have been invested in the past six months to optimize technical aspects of the design with the aim of minimizing costs and simplifying the production process.

A number of items must be manufactured to produce the SFT chimneys. These include

- the PCB flanges for the warm and cold feedthrough flange interfaces,
- the stainless steel pipe structure,

- the flanges containing the interfaces to the gas and liquid lines and slow control,
- the blades and railing, and
- the heat exchanger system.

The flat cables that connect the FE cards to the warm flange are commercially available products and part of the SFT chimney procurement process.

The manufactured components are delivered to designated institutions participating in the DP electronics consortium where teams verify signal continuity for both cold and warm flanges, then assemble the components into SFT chimneys and test for leaks. They also check blade insertion, and test flat cables. After verification, they pack the assembled SFT chimneys and ship them to SURF.

The commercial VHDCI signal cables (connecting the AMCs to the SFT chimneys) are procured and tested with the SFT chimney warm flanges.

2.4 Transport and Handling

The SFT chimneys are 2350 mm long and weigh 180 kg. The cold and warm flanges are mounted at the assembly site, and the chimneys undergo leak-testing before they are shipped in wooden crates (approximate dimensions $2.5 \times 0.5 \times 0.5\,\mathrm{m}^3$) to SURF. Once at SURF, the crates are moved underground and placed on the roof of the cryostat by the underground installation team (UIT). The DP electronics consortium is then responsible for unpacking the crates and installing the SFT chimneys.

The boxes containing the electronic cards and μTCA crates are also handled by DP electronics consortium personnel. These should be lightweight and easy to carry. A box containing 100 AMC cards has a maximum dimension of 60 cm and weighs less than 10 kg.

2.5 Interfaces

The DP electronics system interfaces to several other systems, starting with the CRP and the PD systems. The digitized data must, in turn, flow to the DAQ via the optical links in each μTCA crate. The SFT chimneys integrate into the cryostat structure and connect to the cryogenics and gas systems. The slow-control system takes on management of the low-voltage power supplies for the FE analog electronics and μTCA crates and monitors various sensors in the SFT chimneys. Table 2.9 provides references to the associated interface documents for each interface.

Table 2.9: TPC Electronics System Interface Links.

Interfacing System	Description	Linked Reference
CRP	signals from charge collection strips	DocDB 6751 [12]
PD	signals from light detection sensors	DocDB 6772 [13]
DAQ	transmission of digitized CRO and LRO data	DocDB 6778 [14]
cryogenic instrumentation and slow controls (CISC)	SFT chimney sensors, control of low-voltage power supplies for FE cards, monitoring of μTCA crates	DocDB 6784 [15]
Underground installation	transport of material and underground installation procedure	DocDB 7009 [16]
Integration facility	logistics and use of integration facility	DocDB 7036 [17]
Calibration	calibration database format	DocDB 7063 [18]
DUNE physics	simulation of the electronics system	DocDB 7090 [19]
Software and computing	reconstruction and analysis tools for charge and light signals	DocDB 7117 [20]

2.5.1 Electronics System to CRP and Photon Detection Systems

The cold feedthrough flange of the SFT chimneys forms the interface between the CRP and the CRO electronics system. On the side facing the cryostat, the flange PCB has 20 68 pin connectors (KEL 8930E-068-178MS-F[14]) for plugging in the flat cables from the CRP. These flat cables are 68 channel twisted-pair cables, each carrying signals from 32 anode strips and within the scope of the CRP system. Each analog FE card reads 64 anode strips, i.e., signals from two KEL connectors. The order in which the cables are connected to the cold flange determines the mapping of the electronic channels to the physical location of the strips on the CRP and is coordinated carefully with the CRP consortium. Figure 2.19 shows two images of the cold feedthrough from the WA105 DP demonstrator.

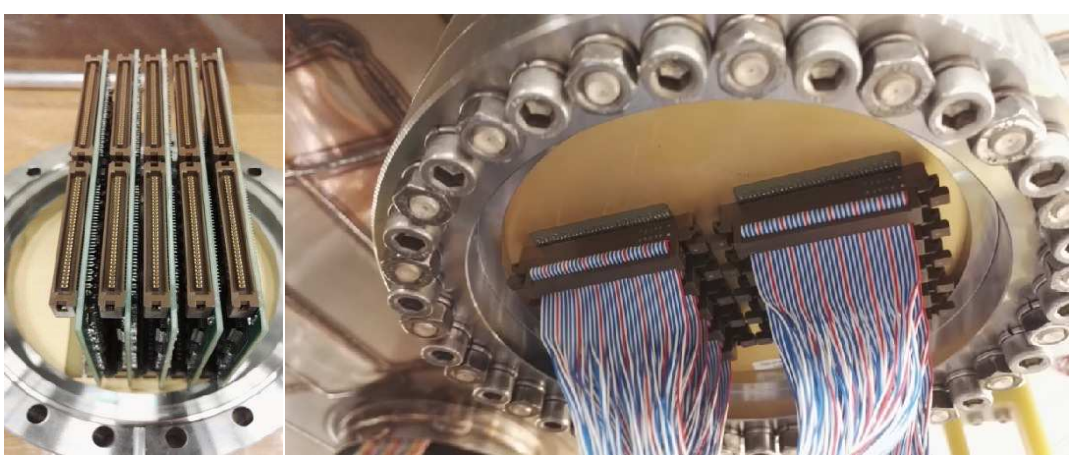

Figure 2.19: Images of the WA105 DP demonstrator SFT cold feedthrough with the FE cards inserted (right) and signal cables from CRP connected (left). The WA105 DP demonstrator SFT chimneys read only 320 channels thus requiring 5 FE cards.

[14] KEL Corporation™, `https://www.kel.jp/english/product/product_detail/?id=490&pageID=3%20`.

The LRO electronics system is connected to dedicated LRO signal feedthrough flanges on top of the cryostat via coaxial cables provided by PDS consortium. The LRO electronics is designed for negative polarity PMT signals, with the amplitude of single photoelectrons on the input of the card between 1 and 10 mV. Assuming a typical PMT gain of 1×10^6 (not accounting for attenuation of the signals), the CATIROC ASIC can measure a range of 1 to 400 photoelectrons (160 fC to 70 pC). The ADC samples from 1 mV to 1 V corresponding to 1 to 1000 photoelectrons; including the time response of the scintillator, the range can increase to approximately 6000. Increasing the gain of the PMT to 1×10^7, reduces the upper values by a factor of 10. The internal noise level of the CATIROC is below 0.1 mV. The objective for the noise level of the ADC is for each channel to have an RMS noise level of more than 0.5 LSB, aiming for 1 LSB 0.1 mV.

2.5.2 Electronics System to DAQ System

The DP module DAQ is identical to that of the SP module. Although the architecture of the detector readout electronics is different for each technology, the output format of the generated data is common and both are synchronized to the same global clock signals. The readout data are continuously streamed via 10 Gbit/s optical links by each detector module FE electronics system to the DAQ. There they are aggregated and trigger primitives are constructed based on a common set of algorithms. A final trigger decision is then taken and, depending on the outcome, relevant data time slices are moved to a persistent storage. Figure 2.20 provides a schematic illustration of these concepts.

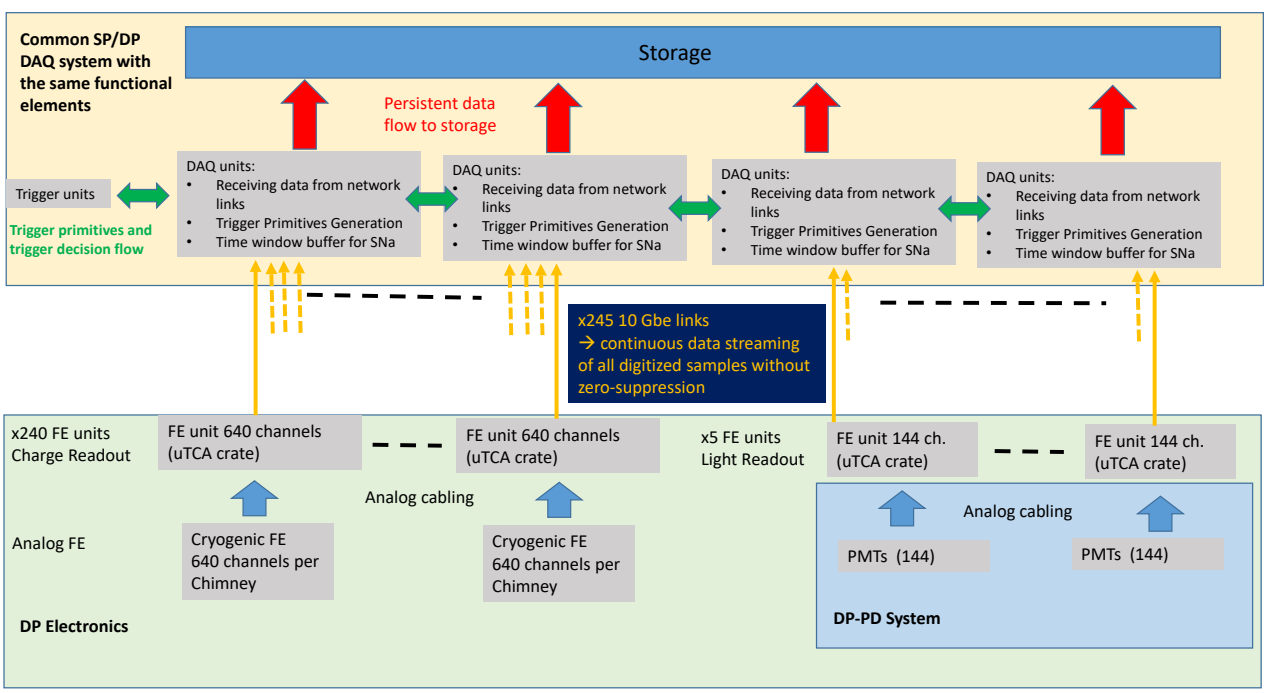

Figure 2.20: Schematic illustration of the interface of DP TPC electronics to DAQ.

The hardware interface between the DP CRO and LRO electronics subsystems and DAQ has two components. The first is the 10 Gbit/s optical fibers for data transfer between the μTCA crates

and the network interface of the DAQ system. The second is a 1 Gbit/s optical fiber that connects the DAQ WR grandmaster switch to the DP electronics timing system.

The 245 10 Gbit/s optical links stream the digitized data to the DAQ from the CRO (240 links) and LRO (5 links) electronics housed in the μTCA crates on top of the cryostat. The fibers, provided by the DAQ consortium, are specified as multimode OM3 fibers [21] with LC-LC connectors suitable for transmitting data over distances up to 300 m. On the side of the μTCA crate, the fibers connect to an optical transceiver in the MCH (two SFP+XAUI links) [22]. On the DAQ, they connect to the level-1 machines of the trigger farm or to switches, depending on the network topology adopted in the DAQ system design.

The 1 Gbit/s link going from the WR grandmaster to the DP electronics time distribution network provides synchronization to the reference clock common to the entire far detector (FD) and derived from a GPSDO clock unit installed on the surface. The clock information is distributed to the WR-MCH slave module in each μTCA crate via a set of WR switches. These switches and the interconnecting 1 Gbit/s fibers form the timing subsystem of the DP electronics system. The WR synchronization protocol includes the automatic and continuous calibration of the propagation delays between the master and the connected slaves. This allows maintenance of the overall synchronization between different nodes at the sub-ns level. The WR grandmaster will be located in one of two places:

- On the surface near the GPSDO. In this case, the system automatically accounts for the incurred latency due to the extensive length of a fiber that brings timing information underground.

- Underground in the central utility cavern (CUC). In this case, propagation delays between GPSDO and the WR grandmaster are calibrated manually, and a timing correction is applied to the data afterward.

The software interface between the DAQ and the electronics system includes tools for handling data transmission and buffering, i.e., data formatting in user datagram protocol (UDP) packets, compression and decompression, and exchange of the control packets.

2.5.3 Electronics System to Cryostat and Cryogenics

The interface points between the cryostat and the DP electronics system are the cryostat penetrations, each of which accommodates a SFT chimneys of external diameter 254 mm. Each chimney has a CF-273 flange welded to its outer structure (see Figure 2.21). After the chimney is inserted, this flange is in contact with the corresponding flange on the crossing (or penetration) pipe embedded in the cryostat structure to which it is eventually fastened. A CF-273 copper gasket is used to ensure vacuum tightness at this interface.

Each chimney contains a heat exchanger copper coil cooled with LAr. Two stainless steel pipe connections (inlet and outlet) with 10 mm (12 mm) inner (outer) diameter must be branched: the inlet to the system for the LAr delivery and the outlet to recirculation. In addition, a connection

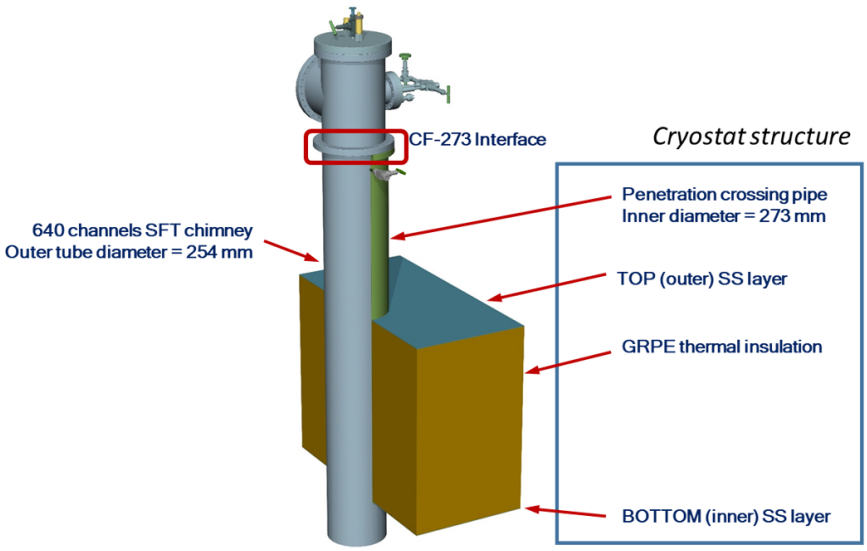

Figure 2.21: Details of SFT chimney interface to the cryostat structure.

for a nitrogen gas line with the same pipe dimensions as those for LAr cooling is used for filling the chimney after it is closed following the installation of the FE electronics. The nitrogen line is also required for flushing the chimney in case access is needed to the FE cards after the DP module is cooled.

The μTCA crates for charge readout are installed within <0.5 m of the SFT chimneys on the cryostat roof. The five μTCA crates for light readout are also placed on the roof at locations optimized with respect to the PMT signal cable routing. The volume required to accommodate the crates is roughly $60 \times 50 \times 40\,\mathrm{cm}^3$.

2.5.4 Electronics System to Slow Control System

Integration with the slow control of the LV power supply system for the FE cards and μTCA crates must enable remote management and monitoring. In addition, the SFT chimneys contain several sensors that require monitoring, e.g., a pressure transducer that measures the pressure inside the chimney and at least two temperature probes (PT1000) that monitor the gas temperature inside the chimney, one near the cold flange at the bottom and one close to the warm flange at the top. The CISC consortium is responsible for the readout of the μTCA crate information and the sensors in the SFT chimneys.

2.6 Installation, Integration, and Commissioning

Installing the TPC electronics systems requires several stages. The chimneys are installed before starting the CRP installation inside the cryostat. Once the CRPs are installed, the chimneys are cabled to them. Next the FE cards are mounted on the blades and inserted. The installation of the digital electronics and μTCA crates is postponed until all the heavy work is done on top of the cryostat. This prevents damage to fragile components (like the optical fibers) due to movement of material and traffic. Once the μTCA crates are installed and all the digital cards are inserted, the AMCs are cabled to the warm flanges of the SFTs for the charge readout, then connected to the PMT signal cables for the light readout. Finally, the 10 Gbit/s and 1 Gbit/s optical links to the DAQ and WR timing network are connected. At this point the full system is ready for commissioning.

2.6.1 SFT Chimneys

Installing the SFT chimneys requires a compact gantry crane with movable supports along the length of the cryostat. Enough overhead room to accommodate a chimney's 2.4 m length is required to allow the crane to freely move the chimney along the transverse direction. The crates containing the SFT chimneys are placed along the edges of the cryostat roof. An unpacked chimney is hoisted and transported to the appropriate penetration crossing pipe for installation. Once in place, the chimney is fastened to the flange on the crossing pipe.

In parallel with the SFT chimney installation, the FE cards are unpacked on top of the cryostat, mounted on the blades, then once the SFT chimneys are secured in the cryostat structure, the instrumented blades are inserted before sealing the chimney. The LAr and gas nitrogen delivery pipes will already be installed, making it possible to connect to the pipes. The pressure probes and temperature sensors are also connected to the slow control system, at this stage.

2.6.2 Digital μTCA Crates

Installation of the μTCA crates with the digital electronics occurs in the final stage of the DP module installation to avoid damaging the fragile equipment. The crates are placed in their designated positions on the cryostat and connected to the power distribution network. The AMC cards and WR-MCH modules are inserted into their slots. The VHDCI cables are then attached, connecting the CRO AMCs to the warm flange interface of the SFT chimneys. The fibers from the timing system are connected to the WR-MCH.

2.6.3 Integration within the DAQ

Integrating the DP TPC electronics with the DAQ system requires connecting the 10 Gbit/s fiber links to each of the 245 μTCA crates. Connecting the timing system to the synchronization WR grandmaster is done via a single 1 Gbit/s fiber link.

The necessary software for the DAQ to read and decode the data packets sent by each μTCA crate is provided by the electronics consortium.

2.6.4 Integration with the Photon Detection System

The cables carrying the PMT signals from the splitter boxes are connected to the LRO analog electronics in each μTCA crate. The positioning of the crates is optimized with respect to the layout of PMT cables. In addition, the PDS calibration system is connected to specified inputs on the cards.

2.6.5 Commissioning

The SFT chimneys are commissioned first. This consists of evacuating their inner volume then filling it with nitrogen gas at slight overpressure. The leak rate must be checked when the chimney is under vacuum, and the nitrogen pressure must be monitored once the chimney is filled to verify that no damage occurs to the flange interfaces during installation.

The electronics system is commissioned after completing the installation of the μTCA crates with the AMCs and cabling the WR network for the timing synchronization. Functionality of the full DAQ system is not strictly required at this stage. The data from each crate is read with a portable computer connected to the crate using either the MCH 10 Gbit/s or 1 Gbit/s interface. Non-functioning channels are identified by pulsing the CRP strips, and the data quality is examined to ensure the correct functioning of the digital electronics and the temporal alignment of the data segments.

2.7 Risks

Table 2.10: Risks for DP-FD-TPC

ID	Risk	Mitigation	P	C	S
RT-DP-TPC-01	Component obsolescence over the experiment lifetime	Monitor component stocks and procure an adequate number of spares at the time of production	L	M	L

RT-DP-TPC-02	Modification to the LRO FE electronics due to evolution in design of PD design	A strict and timely following of the evolution of DP PDS	L	L	M
RT-DP-TPC-03	Damage to electronics due to HV discharges or other causes	FE analog electronics is protected with TVS diodes. Electronics can be easily replaced.	L	L	L
RT-DP-TPC-04	Problems with FE card extraction due to insufficient overhead clearance	Addressed by imposing a clearance requirement on Long-Baseline Neutrino Facility (LBNF)	L	L	L
RT-DP-TPC-05	Overpressure in the SFT chimneys	The SFT chimneys are equipped with overpressure release valves	L	L	L
RT-DP-TPC-06	Leak of nitrogen inside the DP module via cold flange	Monitor chimney pressure for leaks and switch to argon cooling in case of a leak	L	L	L
RT-DP-TPC-07	Data flow increase due to inefficient compression caused by higher noise	Have a sufficiently large (a factor of 5) margin in the available bandwidth	L	L	L
RT-DP-TPC-08	Damage to μTCA crates due to presence of water on the roof of the cryostat	LBNF requirement that the cryostat top remains dry	L	L	L
RT-DP-TPC-09	Clogging ventilation system of μTCA crates due to bad air quality	LBNF requirement that the air quality is comparable to a standard industrial environment	L	L	L

The design of the DP electronics system takes into account several risks, summarized in Table 2.10. While the actual design was completed in 2016, the production for the DP module is expected to start as early as 2022. In the interim, the DP TPC electronics consortium team that performed the original R&D for the electronics design will continuously monitor the market to ensure that all single component parts needed to assemble the electronics cards remain in stock on the timescale required for production of the cards for DUNE. Any elements identified as at risk will be replaced in the executive design with functionally equivalent parts. While this may necessitate some minor design adaptations (e.g., modifying the PCB layout to accommodate a different component footprint), the overall functionality of the system will remain unchanged. An industry survey will also be undertaken for the FE ASIC manufacturing process, such that, if a real risk is identified, the ASIC production can be re-qualified for a different production process. The long-term component obsolescence (RT-DP-TPC-01) over the lifetime of the experiment ($>$ 20 years) will be mitigated by procuring an adequate number of spares at the time of production.

A strict and timely reassessment of the FE requirements necessitated by an evolution of the DP PDS should allow us to modify the LRO FE electronics design accordingly (RT-DP-TPC-02).

We believe that the FE cards have suitable protection to prevent damage caused by CRP discharges (RT-DP-TPC-03) since the TVS diodes have provided sufficient protection in WA105 DP demonstrator. By design, the FE cards remain accessible and could be replaced. However, the SFT chimneys require sufficient overhead clearance (RT-DP-TPC-04) to extract and re-insert the blades holding the FE cards. This is addressed by imposing a clearance requirement on LBNF.

The SFT chimneys are equipped with safety valves that vent excess gas if pressure suddenly rises (RT-DP-TPC-05). The over-pressure threshold must be set low enough that the flanges suffer no significant damage. The pressure of the nitrogen inside the SFT chimneys must be monitored to detect potential leaks. In the event of a leak via the cold flange (RT-DP-TPC-06), the chimney volume will be filled with argon gas to mitigate the risk of nitrogen contamination quenching the scintillation light.

To ensure the continuous flow of digitized data to the DAQ (RT-DP-TPC-07), the data rate must stay below the MCH bandwidth. In the event data compression becomes less efficient because of higher noise, this bandwidth could be exceeded. To mitigate this risk, we currently have a factor of 5 margin in the available bandwidth: 10 Gbit/s MCH compared to the expected rate of 1.8 Gbit/s (Table 2.8).

LBNF requirements that the top of the cryostat remain dry and the air quality remain comparable to a standard industrial environment (e.g., at European Organization for Nuclear Research (CERN) or Fermilab) mitigate the risk of potential damage to the μTCA crates from water condensation (RT-DP-TPC-08) or poor air quality (RT-DP-TPC-09). It is essential to avoid large quantities of dust in the detector caverns at SURF after the μTCA crates are deployed.

2.8 Safety

The installation and operation of the electronics system does not pose any particular or abnormal safety risks. Equipment handling during installation underground must follow the safety protocols established by the UIT.

During operation, the LV power supplies for the FE cards and μTCA crates are powered from the standard mains system. They do not require any additional protection beyond that provided by the power distribution system underground.

The SFT chimneys are cooled with LAr. In the event of leaks, the cooling circuit of each SFT chimney is protected by the over-pressure release valve that will vent excess gas from the inner volume.

2.9 Organization and Management

This section discusses the organization of the DP TPC electronics consortium responsible for delivering the CRO and LRO electronics for DP module. We present the planning assumptions, and give the schedule for production, integration, and installation of the system components. In addition, we provide a detailed breakdown of the core costs for principal components.

2.9.1 Consortium Organization

The DP TPC electronics consortium currently includes eight participating institutions (Table 2.11): APC, IPNL, LAL and LAPP laboratories from France, Iwate University, KEK, and NITKC from Japan, and Southern Methodist University from the USA. Following the structure established within DUNE, the consortium management team consists of a leader (France) and a technical lead (Japan).

Table 2.11: Institutions participating in the TPC electronics consortium

Institution	Country
APC	France
IPNL	France
LAL	France
LAPP	France
Iwate University	Japan
KEK	Japan
NITKC	Japan
Southern Methodist University	USA

2.9.2 Planning Assumptions

The design of the DP TPC electronics system relies on elements already developed for ProtoDUNE-DP and tested in the WA105 DP demonstrator. Commissioning of ProtoDUNE-DP in summer 2019 should provide some additional information but is not expected to alter the design of principal components. Potential improvements related to the increase in channel density supported by the AMCs is possible to further reduce costs.

2.9.3 Institutional Responsibilities

The description of the work breakdown structure (WBS), including the assignments of the responsible institutions is documented in DocDB 5594 [23].

2.9.4 High-level Cost and Schedule

Table 2.12: Milestones of the TPC electronics consortium.

Milestone	Date (Month YYYY)
Costing model for technical design report finalized	March 2019
Start of ProtoDUNE-SP-II installation	March 2021
Start of ProtoDUNE-DP-II installation	March 2022
South Dakota Logistics Warehouse available	April 2022
Beneficial occupancy of cavern 1 and CUC	October 2022
CUC counting room accessible	April 2023
Top of detector module #1 cryostat accessible	January 2024
Start of component production and procurement	January 2024
Completion of production of μTCA infrastructure components	July 2024
Completion of production and validation of WR system components	July 2024
Start of detector module #1 TPC installation	August 2024
End of detector module #1 TPC installation	May 2025
Top of detector module #2 accessible	January 2025
Completion of production and tests of SFT chimneys	January 2025
Completion of production and tests of cryogenic FE analog electronics	January 2025
Completion of production and tests of AMCs for CRO and LRO	January 2025
Start of detector module #2 TPC installation	August 2025
SFT chimneys installed	November 2025
Cryogenic FE electronics installed	December 2025
μTCA crates and WR network installed	December 2025
Installation of AMCs completed	January 2026
Commissioning of the DP TPC electronics system	January 2026
End of detector module #2 TPC installation	May 2026

The key schedule milestones are listed in Table 2.12. The given dates assume the DP TPC will be the second FD detector module to be installed.

The detailed cost model for the DP TPC electronics system has been developed based on scaling the costs for the ProtoDUNE-DP electronics system. The core costs for producing the electronics system to instrument a single DP module are summarized Table 2.13.

Table 2.13: DP TPC electronics system cost summary.

Item	Core Cost (k$ US)
CRO cryogenic analog FE cards	
SFT chimneys	
VHDCI cables	
μTCA crates	
WR-MCH units	
CRO AMCs	
LRO AMCs with analog FE	
WR switches and optical transceivers	
Low voltage power supplies	

Chapter 3

Photon Detection System

The photon detection system (PDS) of the DUNE DP module uses large-area cryogenic photomultiplier tubes (PMTs) coated with tetra-phenyl butadiene (TPB) to detect the 127 nm light produced by argon scintillation. The PMTs are installed on the cryostat floor, underneath the TPC transparent cathode. The PMTs view the entire, homogeneous, liquid argon (LAr) volume of one far detector (FD) module. The design described in this chapter builds on experience from several LArTPC optical readouts, and particularly from the WA105 DP demonstrator and from the ProtoDUNE-DP detectors at CERN.

The chapter is organised as follows. Sec. 3.1 introduces the physics requirements to be met by the PDS and additional opportunities offered by the system. Sec. 3.2 gives gives an overview of the PDS baseline design, together with the detector specifications to be satisfied. Secs. 3.3–3.6 describe in detail the PDS baseline design, namely the PDS photosensor system (Sec. 3.3), the mechanical aspects (Sec. 3.4), the readout electronics (Sec. 3.5) and the calibration system (Sec. 3.6). Secs. 3.7–3.9 demonstrate how the PDS baseline design has been validated using detailed simulations (Sec. 3.7 and 3.9) and experience from prototypes (Sec. 3.8). Secs. 3.10–3.15 cover PDS project aspects, namely: quality control (Sec. 3.10), interfaces (Sec. 3.11), installation (Sec. 3.12), risks (Sec. 3.13), safety (Sec. 3.14), and high-level schedule and cost (Sec. 3.15). Finally, Sec. 3.16 discusses a limited number of alternatives to this baseline design.

3.1 Physics Requirements and Goals

The PDS of the DUNE FD provides information on three key detection aspects of the experiment:

1. Event (and sub-event) time reconstruction;
2. Event triggering;
3. Event energy reconstruction.

As discussed below, these detection aspects enabled by the PDS affect the entire primary physics program of DUNE: long-baseline neutrino oscillations, nucleon decay, and supernova neutrino burst (SNB). In the following, we list the scientific requirements the PDS will meet (Sec. 3.1.1), as well as additional scientific opportunities PDS offers (Sec. 3.1.2). Among requirements, we only list how PDS primarily affects the DUNE primary physics program, namely:

1. A capability or measurement uniquely provided by the PDS;

2. A capability or measurement redundant with time projection chamber (TPC) information, but where redundancy is considered essential;

3. A capability or measurement competitive with TPC information.

3.1.1 Scientific Requirements

3.1.1.1 Event fiducialization for non-beam events

The accelerator complex for beam events provides absolute event time in the DUNE TPC, but the PDS must provide absolute event time for non-beam events. Event time reconstruction is necessary to determine the drift distance within the TPC. This is essential for a number of reasons, particularly for defining a fiducial volume along the TPC drift direction, which is the vertical one for dual-phase (DP). The cosmic ray activity in one FD module is of order 0.05 Hz, or about 1×10^8 /(Mt · year). Although smaller, the atmospheric neutrino event rate in one FD module is also significant, of order 1×10^5 /(Mt · year). These rates can be compared with the background levels target for nucleon decay (NDK) searches at DUNE. For the NDK channels where DUNE can provide the best sensitivities, the goal is to operate in nearly background-free conditions even after an exposure of several years, that is, with background levels of order 10 /(Mt · year) or less. Hence, the cosmic ray activity must be suppressed by at least seven orders of magnitude to enable optimal NDK searches. PDS information is essential to reach the required levels of suppression of cosmic ray-induced (and atmospheric neutrino-induced) backgrounds. Because most cosmic ray activity will enter from the top of the detector, a NDK candidate must be fully contained within the detector. For the most relevant direction, namely the vertical one, the fiducial requirement can only be imposed if PDS information is available. Because this capability is uniquely provided by the PDS and because it critically affects the NDK program, **we consider event fiducialization of NDK candidates to be the most important requirement of the PDS**. High signal efficiency is critical in rare event searches like NDK, so **we require a $> 90\%$ efficient event time determination via the PDS throughout the TPC active volume for NDK signal events**. NDK event fiducialization may be prevented not only if NDK-induced LAr scintillation flashes are undetected, but also if the PDS detects spurious LAr scintillation flashes within the same event window, uncorrelated with the NDK activity. Additional flashes are produced, typically, by radiologically-induced detector activity. In this case, an ambiguity in the drift time determination of the NDK may arise, and the correct (NDK-induced) flash must be associated to the event. Hence, **we also require a $> 90\%$ NDK flash purity among all reconstructed NDK-like flashes within the same NDK event readout window**. Similarly, the PDS is also needed to determine the full containment of

atmospheric neutrino interactions in DUNE.

3.1.1.2 Supernova burst triggering

A burst of several hundred neutrino interactions per DUNE FD module is expected over a timescale of about 10 s from a core-collapse supernova at a 10 kpc distance from the Earth, near the center of our galaxy. As the SNB interaction rate scales as $1/r^2$, where r is the supernova distance from us, SNB detection at DUNE is in principle possible up to distances of order 50 kpc. This would be the case for an SNB occurring in the Large Magellanic Cloud, for example. The dominant neutrino interaction channel in DUNE is the charged current (CC) electron neutrino interaction on an argon nucleus, with typical deposited energies from electrons and nuclear de-excitation gammas of order 20 MeV, producing short tracks throughout the TPC active volume.

In DUNE, one can in principle trigger on SNBs using either TPC or PDS information. In both cases, the trigger scheme exploits the time coincidence of multiple signals (TPC stubs or PDS optical clusters[1]) over a timescale matching the SN luminosity time evolution. In the case of an SNB trigger being generated, the data acquisition system would write to disk the full (non-zero-suppressed) detector information for a time range spanning several tens of seconds surrounding the trigger timestamp. Considering the rarity of SNBs in our galactic neighbourhood, and given the importance of SNB detection, we consider it essential to develop both a redundant and a highly efficient SNB triggering scheme in DUNE. Concerning redundancy, **we require that the DUNE FD may trigger on an SNB independently using TPC or PDS information**, hence minimizing SNB inefficiencies stemming from downtime or malfunctioning of the TPC, the PDS, or their associated trigger schemes. As for trigger efficiency, **we require the PDS alone to be able to trigger with $> 90\%$ efficiency on an SNB at a 20 kpc distance from Earth**, hence up to distances covering the entire Milky Way. Considering the very large amount of detector information being generated by an SNB trigger, we also require that the SNB trigger efficiency be reached for a **fake trigger rate not exceeding 1 /month**.

3.1.1.3 Scintillation-based calorimetry

The most important physics goal of the DUNE FD is to carry out a comprehensive program of neutrino oscillation measurements using ν_μ and $\bar{\nu}_\mu$ beams from Fermilab. Because of this, the DUNE FD performance in terms of neutrino energy reconstruction and neutrino flavour classification is of paramount importance. As detailed in this volume, the TPC should provide a 10–15% neutrino energy resolution for ν_e CC interactions in the few-GeV energy range, using charge information alone. At these energies, however, the PDS will also detect thousands of PEs. Thus, a competitive calorimetric measurement of the event energy can also, in principle, be obtained using the light intensity detected by the PDS, if spatial non-uniformities in PDS response can largely be corrected

[1] Throughout this chapter, we use the term "optical flash" for the process of scintillation light production in LAr. We use "optical hit" to identify a reconstructed optical signal in a single photo-detector channel. We use the term "optical cluster" to name the reconstructed object given by a collection of optical hits seen by separate photo-detectors and that are correlated in time/space.

for. **We require the PDS alone to be able to reconstruct the neutrino energy of a few-GeV electron neutrino CC interaction with 20% root mean square (RMS) resolution or better**, thus providing a measurement competitive to the TPC-based one. Such an independent and competitive energy measurement would also be useful as a risk mitigation measure for degraded TPC performance. The TPC- and PDS-based energy measurements may be combined, possibly providing better energy resolution than TPC alone. We give two arguments supporting this possibility. On one hand, the charge and light signals may be combined to reduce electron-ion recombination fluctuations, ensuring a more compensating LAr calorimeter response. On the other hand, charge and light readout planes are located at opposite detector ends in the DP design, providing maximal complementarity between the two sub-systems. Neutrino interactions occurring near the light readout at the bottom of the cryostat will be maximally affected by electron attachment of the charge signal, while they will have the highest light detection probabilities possible. The situation is reversed for neutrino interactions near the charge readout plane. The PDS may provide a competitive energy measurement not only for beam neutrinos, but also at lower energies, particularly for SNB neutrinos. For a discussion of why an accurate energy measurement is beneficial also for SNB events, see Sec. 3.1.2.1.

3.1.2 Additional Scientific Opportunities

3.1.2.1 Electron attachment correction for the charge-based energy measurement in non-beam events

Given the maximum drift distance of 12 m in the DP TPC and assuming a (minimally-required) 3 ms electron lifetime, the charge could be attenuated by more the one order of magnitude along drift due to electron attachment on electro-negative impurities. If left uncorrected, electron attachment would therefore cause great deterioration in the charge-based energy measurement in such relatively short electron lifetimes. Because of the longer drift distance, this effect is much more dramatic in the DP than the single-phase (SP). For non-beam events, the only possible way of correcting for the electron attachment is through PDS-based event timing[2]. This will be exploited in DUNE to better discern, for example, the spectral features in the energy spectrum of the SNB flux. An improved charge-based energy measurement would improve both the determination of the pinched-thermal spectral parameters of the progenitor, and the detection of the sharp, time-dependent spectral features from collective neutrino oscillations. A similar argument applies to the charge-based energy measurement in the study of atmospheric neutrino oscillations, where good neutrino energy reconstruction is also very important.

3.1.2.2 Event timing in high multiplicity supernova burst events

The early time distribution carries important information for core-collapse stellar models, which has not been observed thus far. The first neutrino release after core bounce is the ν_e-rich neutron-

[2]This is true for a single physics event (e.g., a neutrino interaction) per TPC event. Other than background flashes, the association between TPC tracks and PDS flashes has no ambiguities.

ization burst, lasting about 10 ms. For a supernova at 10 kpc distance, several tens of interactions induced by the neutronization flux should be detected in one FD module. In other words, the mean interval between successive neutrino interactions should be less than 1 ms in this case. For closer supernovae, information at even earlier (pre-bounce) times may be studied during the core infall phase. A 1 ms wide notch in the luminosity curve may be visible, corresponding to neutrino trapping in the ultra-dense matter. Such timescales can be compared with the typical time resolutions obtained with TPC and PDS information. For DP TPC and for a 1.6 mm/µs electron drift velocity, the drift time can be as large as 7.5 ms, with foreseen readout windows of 16.5 ms. Considering the uniform spatial distribution of neutrino interactions in the TPC, the intrinsic absolute time resolution expected in this case is of order $16.5\,\mathrm{ms}/\sqrt{12} \simeq 5\,\mathrm{ms}$. The TPC-based time resolution is therefore not sufficient to resolve these early time features, even in the case of sufficient neutrino statistics. On the other hand, the PDS may reconstruct one flash per SNB neutrino interaction at 1 µs-scale time resolution or more. Hence, PDS-based timing is definitely an added value for a nearby supernova.

3.1.2.3 Improved event identification via scintillation-based Michel electron tagging

There is another physics case where the PDS may detect more than one physics-induced flash per TPC event[3]. This can happen in the presence of particle decays in the final state of an event of interest, such as a neutrino interaction or a nucleon decay. In this case, multiple, correlated sub-events may be separated in time. Michel electron tagging from muon decay at rest is the most obvious opportunity for sub-event identification using PDS timing. Approximately one million scintillation photons are produced in the liquid argon per Michel electron. In addition, the timescale of muon decay is long, comparable to the timescale of the slow component of argon scintillation light. Although Michel electrons can also be identified through TPC track imaging, in some event topologies, PDS may outperform the TPC, for example where the muon and electron tracks are nearly parallel. In summary, the PDS may better identify the event final state than TPC-only information. Considering the large fraction of μ^- capture on argon (about 75%), Michel electron tagging also provides valuable μ^-/μ^+ separation. The latter can, in turn, provide separation between muon neutrinos and antineutrinos.

3.2 Design Overview

The DP PDS is optimized for the physics program of the full-size DUNE DP detector. Phenomena leading to interactions in the DUNE detectors and to be studied span several orders of magnitude of energy scale, from a few MeV to several GeV, with commensurate range in light yield. In particular, low-energy signals like SNB neutrinos and proton decay, impose more stringent requirements on PDS performance than the primarily higher energy, beam-synchronous, neutrino oscillations physics.

[3]We use the qualifier 'physics-induced' to distinguish those light flashes from the ones induced by radiological or cosmogenic activity in the detector or by electronics noise.

3.2.1 Scintillation Light Production in the DP Detector Module

DP PDS detects light produced from two sources: the scintillation process originated by ionizing particles propagating in the liquid argon (usually referred to as the S1 signal) and by the electroluminescence process due to drift electrons extracted from the liquid phase and accelerated in the argon vapor at the top of the cryostat (usually referred to as the S2 signal). Charge readout anode planes instrument the top while photodetectors are at the bottom of the cryostat. The interplay between the charge and light from an event enables pattern recognition and measuring the energy of interactions.

Ionizing radiation in liquid noble gases leads to the formation of excimers in either singlet or triplet states, which decay radiatively to the dissociative ground state with characteristic S1 fast and slow lifetimes (fast is approximately 6 ns and slow approximately 1.3 μs in LAr with the so-called second continuum emission spectrum peaked at the wavelength of approximately 127 nm, 126.8 nm with a full width at half maximum of 7.8 nm [24]). This prompt and relatively high-yield (about 40,000 photons per MeV at zero E field) of 127 nm scintillation light is exploited in an LArTPC (both DP and SP) to provide the absolute time (t_0) of the ionization signal collected at the anode, thereby providing the absolute value of the drift coordinate of fully contained events and a prompt signal used for triggering. Figure 3.1 shows the light production mechanism in LAr.

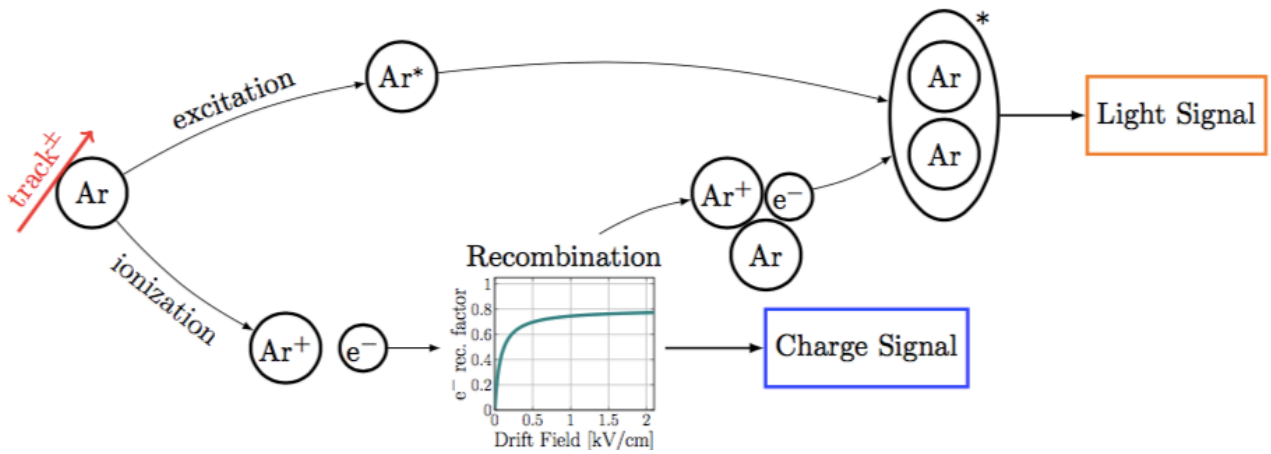

Figure 3.1: A sketch depicting the mechanism of light production in argon.

The secondary scintillation in the argon gas (i.e., the vapor phase) is unique to the DP detector module technology. It is the luminescence in gas caused by accelerated electrons in the E field and in the large electron multiplier (LEM) anode through Townsend amplification. The S2 signal provides information on the drift time and amount of ionization charge, thus supplementing information from the charge readout on the anode plane. For a given argon gas density, the number of S2 photons is proportional to the number of electrons, the E field, and the length of the drift path in gas covered by the electrons. In an extraction field of 3.0 kV/cm in gas, one electron generates about 100 downward-moving photons that cross the liquid argon surface [25]. The time scale of S2 reflects the extraction time of original ionization from the liquid phase into the gas phase. Therefore, for about 0.5 kV/cm drift E field, this time scale is of the order of hundreds of microseconds. The time between the occurrence of the primary scintillation light and the secondary scintillation light is equivalent to the drift time of the electrons from the ionization coordinate to the LAr surface. This

provides an accurate determination of the drift time in the active volume and, hence, a correction tool for the electron attachment (and the associated energy measurement).

3.2.2 Detector Sub-systems and Layout

The baseline design of the light collection system calls for 20.3 cm (8 in) diameter cryogenic PMTs from Hamamatsu Photonics[4] (model R5912-MOD20) distributed uniformly on the floor (bottom) of the cryostat and electrically shielded from the bottom cathode plane. Other PMT manufacturers being considered include Electron Tubes Limited [5] and HZC [6]. According to the baseline design, 720 PMTs, approximately 1 per m^2, will be installed. The outline of the DP module is shown in Figure 3.2.

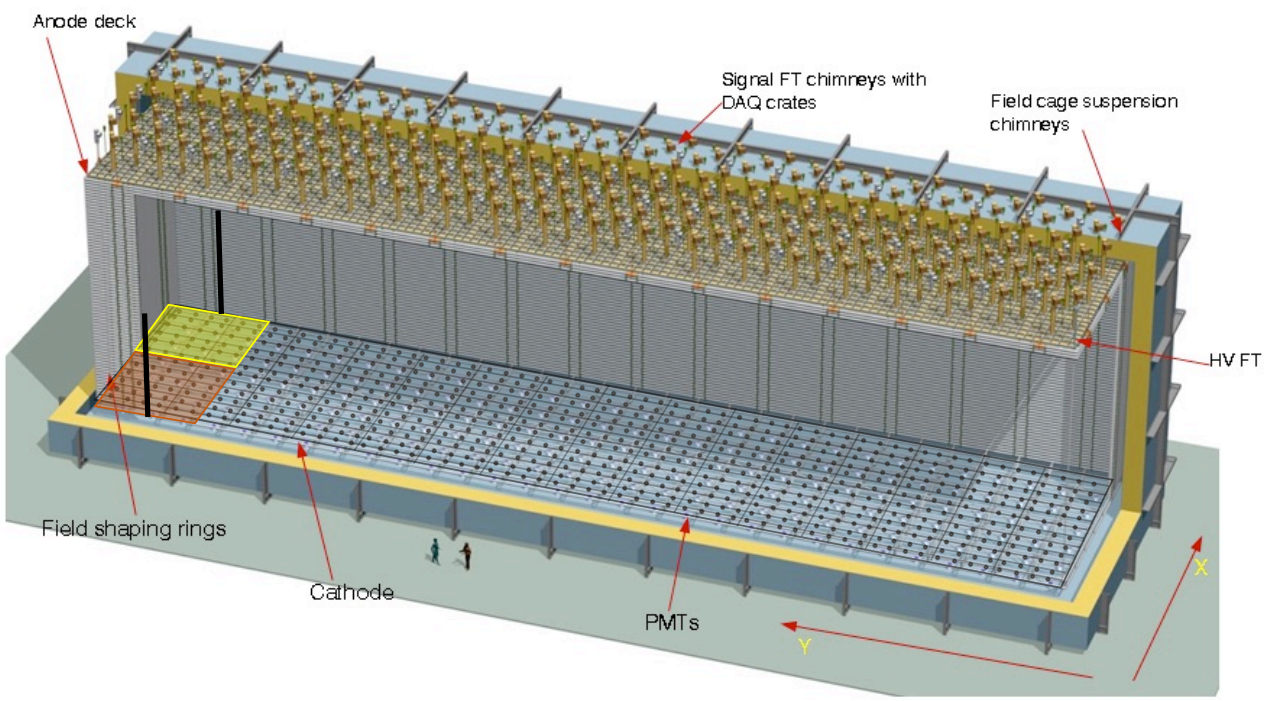

Figure 3.2: The DP module (partly open) with cathode, PMTs, field cage (FC), and anode plane with chimneys.

The PMTs are individually powered to values between 1.5 to 2.0 kV to separately adjust the PMT gains. The Hamamatsu R5912 PMTs are not sensitive to the 127 nm scintillation light, so a wavelength shifter is required. A thin layer of TPB [26] coating is applied directly on the PMT window by evaporation. Section 3.3 describes the photosensor system.

The 720 PMTs are individually attached to the cryostat floor 1.02 m apart in both directions, via a PMT support structure that counteracts the PMT buoyancy. In order to enhance the light collection and to improve the photon detector response uniformity throughout the entire TPC

[4] Hamamatsu Photonics™, `http://www.hamamatsu.com/resources/pdf/etd/LARGE_AREA_PMT_TPMH1286E.pdf`
[5] Electron Tubes Ltd™, `http://www.electron-tubes.co.uk//`
[6] HZC Photonics™, `http://hzcphotonics.com/en_index.html`.

active volume, TPB coated reflector/wavelength shifting (WLS) panels will be installed on the top half of the FC inner surfaces. Considering the linear relationship between the number of PMTs and the detected light yield, and the mild dependence of the PDS physics performance on light yield and channel granularity, the optimization process that resulted in this baseline design can be considered very robust. The mechanical aspects of the PMT support structures and the reflector/WLS assemblies are described in Section 3.4.

The front-end PMT base circuit for reading the photo-electron signals relies on a positive high voltage (HV) supplied to the PMT anode and on a grounded photo-cathode. A single cable for each PMT carries both power and signal. HV and signal splitters located outside the cryostat separate the fast PMT response signal from the positive HV with capacitive decoupling. The PDS readout electronics is described in Section 3.5.

A photon calibration system is required to determine the PMT gain and to monitor the stability of the PMT response. The LED-driven fiber calibration system of the PDS is described in Section 3.6.

The basic unit of installation/operation is called a sector. The sectors are indicated as transparent red and yellow panels in Figure 3.2. One DP PDS sector is 6 m × 6 m and houses 36 PMTs. A total of 20 sectors will be installed in the detector. A single HV cable per PMT will be installed in the cryostat. The cable trays for the two sectors in Figure 3.2 are indicated as black vertical lines.

The high voltage cables will penetrate a feedthrough flange and end with SHV connectors, with the calibration fibers also penetrating a feedthrough flange and end with SMA connectors. One DN250 flange is used per sector of DP PDS. One flange will house 36 SHV and 6 SMA connections. The DP PDS design will have 20 penetrations on the cryostat roof, one per sector.

The high voltage and signal crates will be at a density of one per sector for a total of 20 HV/signal racks on the cryostat roof. Figure 3.3 illustrates the layout of the feedthroughs and the HV/signal/calibration racks for four sectors. The racks will contain the HV crates, HV/signal splitters, the Micro Telecommunications Computing Architecture (μTCA) crates for the front-end electronics, and the calibration LED driver and the associated electronics for 36 PMTs.

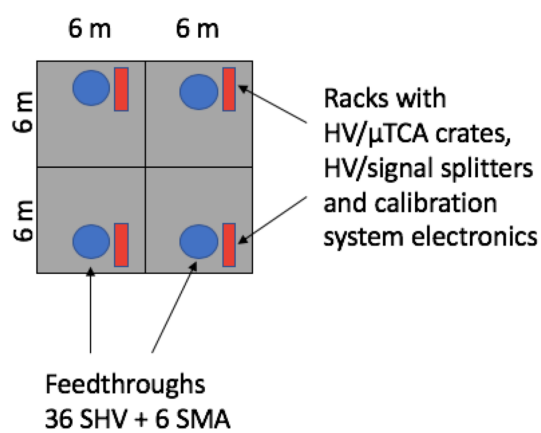

Figure 3.3: The sketch of the cryostat roof layout for DP PDS penetrations.

The cathode plane, described in Chapter 1, is placed approximately 2 m above the bottom of the

cryostat. Given the high dielectric constant of the LAr phase, the PMT plane is a safe distance from the cathode plane. To protect the PMTs, the ground grid is installed and placed at an identical potential as the PMT photocathode (0 V).

3.2.3 Operational Modes

The physics program defines the operational modes of the DP PDS. Measuring the neutrino oscillation parameters requires recording events upon receiving an external trigger from the beam, while non-beam physics such as SNBs, proton decay, or other rare events require special trigger conditions that include the PDS. Another operation mode is the PMT calibration run, which is initiated by the light calibration system with its dedicated hardware trigger. Thus, the operation modes are

- External trigger: A typical case is when the beam generates a hardware trigger (a beam gate); it also includes software-generated triggers for test data.
- Non-beam physics trigger: The electronics based on the PDS signals provides the trigger for, among other events, SNB and proton decay events;
- Calibration trigger: The trigger is provided by the light calibration system during PDS calibrations.

The external and non-beam physics triggers run in parallel to ensure that rare events like SNBs are recorded efficiently.

3.2.4 Detector Design Specifications

The DP PDS detector specifications are given in Table 3.1. The physics-driven rationale for each detector specification, and the means to validate them, are also summarized in the table. Validation of the detector specifications uses data from PDS prototypes (Section 3.8) and from a full simulation/reconstruction of signal and background optical flashes in the DP detector module (Section 3.9).

Table 3.1: Specifications for DP-PDS

Label	Description	Specification (Goal)	Rationale	Validation
DP-PDS-1	Light yield	> 1 PE/MeV at anode, > 5 PE/MeV avg over active vol	Enable drift position determination of NDK candidates. Enable PDS-based triggering on galactic SNBs.	Full sim/reco of NDK, SNB ν and radiological events.

DP-PDS-2	Time resolution	$< 1\,\mu s$ ($< 100\,ns$)	Enables 1 mm pos resolution for 10 MeV SNBs candidate events for instantaneous rate $< 1\,m^{-3}ms^{-1}$.	
DP-PDS-3	LAr nitrogen contamination	$< 3\,ppm$	Higher contaminations signifcantly affect the no. of photons that reach the PMT.	
DP-PDS-4	Relative timing accuracy among hits	$< 100\,ns$RMS	Enable effective clustering of PMT signals based on relative hit timing information.	Full sim/reco of NDK, SNB ν and radiological events.
DP-PDS-5	Hit signal-to-noise ratio	> 5	Efficiently reconstruct single-photoelectron hits while rate of electronics noise hits remains manageable.	Single-photoelectron and baseline noise RMS measurements in $3 \times 1 \times 1$ prototype.
DP-PDS-6	PMT dark count rate	$< 100\,kHz$	Avoid effects on clustering algorithm and PDS-based calorimetry.	Characterization of PMTs at cryo temps prior to installation.
DP-PDS-7	Analog range per channel	$> 100\,PE/(channel \times 6\,ns)$	Minimize hit saturation for scintillation-based calorimetry over 6 ns prompt light period, esp. for beam events.	Full sim/reco of beam ν interactions.

3.3 Photosensor System

The baseline photodetector for the light readout is the Hamamatsu R5912-MOD20 PMT. This is the same model used in ProtoDUNE-DP. The Hamamatsu R5912-MOD20, depicted in Figure 3.4, is an 8-inch diameter, 14-stage, high gain PMT (nominal gain of 10^9). The maximum quantum efficiency of the R5912-MOD20 PMT is approximately 20 % at 400 nm. In addition, this PMT was designed to work at cryogenic temperatures by adding a thin platinum layer between the photocathode and the borosilicate glass envelope to preserve the conductance of the photocathode at low temperatures. This particular PMT has proved reliable in other cryogenic detectors. The same or similar PMTs have successfully operated in other LAr experiments like MicroBooNE [27],

MiniCLEAN [28], ArDM, ICARUS T600 [2], and ProtoDUNE-DP [29]. Discussions with other manufacturers like Electron Tubes Limited (UK) [30] and HZC (China) [31] are on-going to include them in the program.

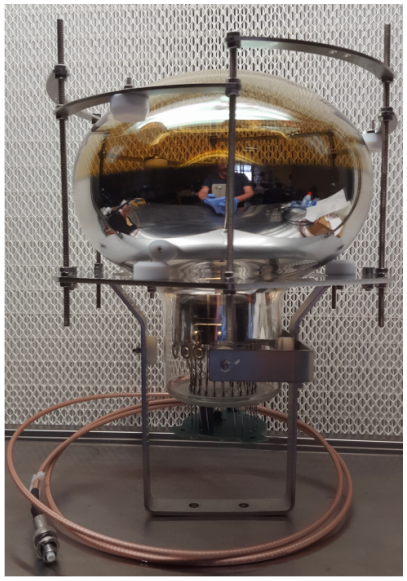

Figure 3.4: Picture of the Hamamatsu R5912-MOD20 PMT [32].

The baseline number of PMTs is 720 with 80 spares. Several operations and tests must be performed with the PMTs before they are installed. The PMTs must be ordered with sufficient lead time to complete the following planned operations: assembling the voltage divider circuit, mounting on the support structure, testing at room and cryogenic temperatures, packing and shipping to the Coating, Testing and Storage Facility (CTSF). The TPB coating of the PMT windows will be done at the CTSF. The PMTs will be re-tested for validation of basic functionality at the CTSF and at SURF before installation (see Section 3.12). Considering the large number of PMTs required by DP PDS, the purchase order must be completed at least two years before installation. A staged or staggered order with a steady supply of PMTs would be most convenient and will be negotiated with the manufacturer.

3.3.1 Photodetector Characterization

Before installation, the most important characteristics of the PMT response must be determined with two goals: to possibly reject under-performing PMTs and to store the characterization information in a database for later use during the DP module commissioning and operation.

The basic and most important parameters to characterize are the dark count rate versus high voltage and the gain versus high voltage. Both parameters must be measured at room and cryogenic temperatures. As with the baseline PMT model, the rates of pre-pulsing and after-pulsing should be negligible, but they will be measured as part of testing.

From the mechanical point of view, the test set up requires a light-tight dark vessel filled with cryogenic liquid (argon or nitrogen) and an infrastructure for filling and operating the vessel with

temperature and liquid-level controls. For ProtoDUNE-DP, 10 PMTs were tested at a time over a week because cryogenic tests of PMTs require several days for PMT thermalization [33]. Figure 3.5 shows the ProtoDUNE-DP PMTs being installed in the testing vessel. Increasing the capacity of the vessel, and thus the number of PMTs that can be tested simultaneously, could reduce the duration of the characterization test per PMT.

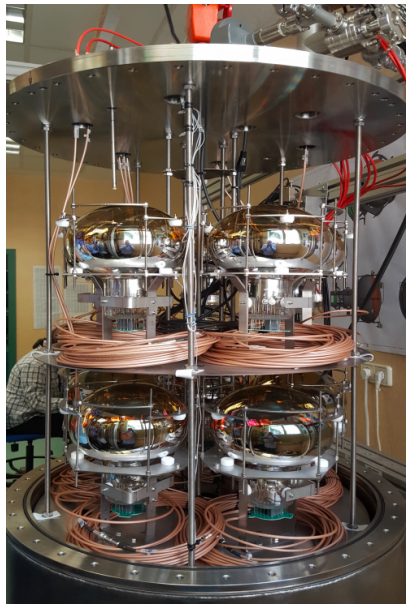

Figure 3.5: Picture of the PMTs being installed in the testing vessel used for the ProtoDUNE-DP PMTs.

Figure 3.6 shows a sketch of the proposed set up for PMT characterization tests. For the electronics, the test set up requires an HV power supply, a discriminator, a counter for the dark rate measurements, a pulsed light source, and a charge-to-digital or analog-to-digital converter for the PMT gain versus voltage measurements. All instruments must allow computer control to automate data acquisition.

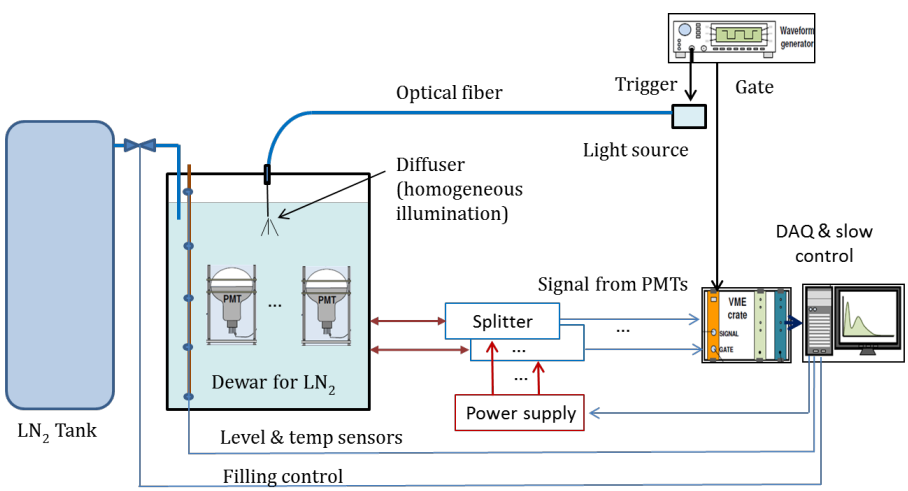

Figure 3.6: Sketch of the set up for PMT characterization tests.

3.3.2 High Voltage System

Based on the experience with the WA105 DP demonstrator prototype, the A7030 power supply modules from CAEN [7] are selected as the baseline power supply of the PMT HV system. These modules provide up to 3 kV with a maximal output current of 1 mA and a common floating ground to minimize noise. Module versions with 12, 24, 36, or 48 HV channels are available. The HV polarity can be chosen for each module. Using the baseline PMT powering scheme, modules with positive HV polarity will be acquired for the experiment. Modules with 36 HV channels and Radiall 52[8] connectors are under consideration. The corresponding HV cable connects the modules with the HV splitters, described in Section 3.5.2. For 720 PMTs, 20 A7030 modules (+ 2 spares) are needed. These 20 HV modules will be installed in mainframes from CAEN.

Each PMT is powered individually. This allows the gain of all PMTs to be set individually by adjusting their operating high voltage. This will be controlled by software. The software will interface to the PMT calibration system and its database to extract the gain curves needed to set and/or equalize gains.

3.3.3 Wavelength Shifting

The DP PDS requires wavelength-shifting of the 127 nm scintillation photons toward visible wavelengths that can overlap with the photocathode luminous sensitivity. Coating the PMT glass bulbs over the photocathode area with a thin film of TPB has already been validated [26] and is adopted as the baseline plan.

TPB is a wavelength shifter that has high efficiency for converting LAr scintillation VUV light toward the light for which the PMT photocathode is more sensitive.

A thin layer of TPB is deposited on the PMT glass by means of a thermal evaporator that consists of a vacuum chamber with two copper crucibles (Knudsen cells) placed at the bottom of the chamber, see Figure 3.38 in Section 3.12. A PMT is mounted on a rotating support that ensures a uniform coating layer and placed at the top of the evaporator with the PMT window pointing downward. The crucibles, filled with the TPB, are heated to 220 °C. At this temperature, the TPB evaporates through a split in the crucible lid into the vacuum chamber, eventually reaching the PMT window.

Several tests were performed to tune the evaporator's parameters, e.g., the coating thickness (TPB surface density) and the deposition rate. A PMT mock up covered with mylar foils was used for these tests. A TPB surface density of 0.2 mg/cm^2, the value for which the PMT efficiency is stable as a function of the surface density, was chosen for ProtoDUNE-DP. Efficiency measurements were performed by using a VUV monochromator and by comparing the cathode current of a coated PMT with the current value of a calibrated photodiode. From these efficiency tests, we concluded that approximately 0.8 g of TPB must be placed in the crucible for each evaporation to achieve

[7] CAEN™, `http://www.caen.it/csite/CaenFlyer.jsp?parent=222`
[8] Radiall™, `https://www.radiall.com/`.

the desired PMT coating surface density. This value optimizes the quantity of TPB used per evaporation while keeping the coating surface density fluctuations below 5%. Two to four PMTs with these specifications can be coated per day at a single coating station. Several coating stations will be required to keep the installation and testing schedule (see Section 3.12 for details). An average quantum efficiency of 12 % at 127 nm has been measured for TPB-coated PMTs [34].

In order to enhance the light collection and to improve the photon detector response uniformity throughout the entire TPC active volume, TPB coated reflector/WLS panels will be installed on the FC inner surfaces. The impact on the light yield and physics measurements was evaluated for two particular cases: The full coverage of the FC inner walls with the panels and the coverage of only the upper half of the FC. The conclusion from the simulation studies is that half coverage is sufficiently performant as shown in Fig. 3.17. In order to reduce the cost still keeping the PDS response uniformity, the baseline design is to equip only the top half of the FC walls.

The reflector/WLS panel will be constructed with 1 mm thick 93 cm × 93 cm G10/FR4 plates. The central 91 cm (H) × 93 cm (W) area only on one side of the panel will be laminated with a reflective foil, which will then be evaporated with TPB. The top and bottom 1 cm portion of the panel without coated foils will be sandwiched between horizontal support bars. Sketches of the panel are shown in Fig. 3.7. The support structure of the panels is described in Section 3.4.

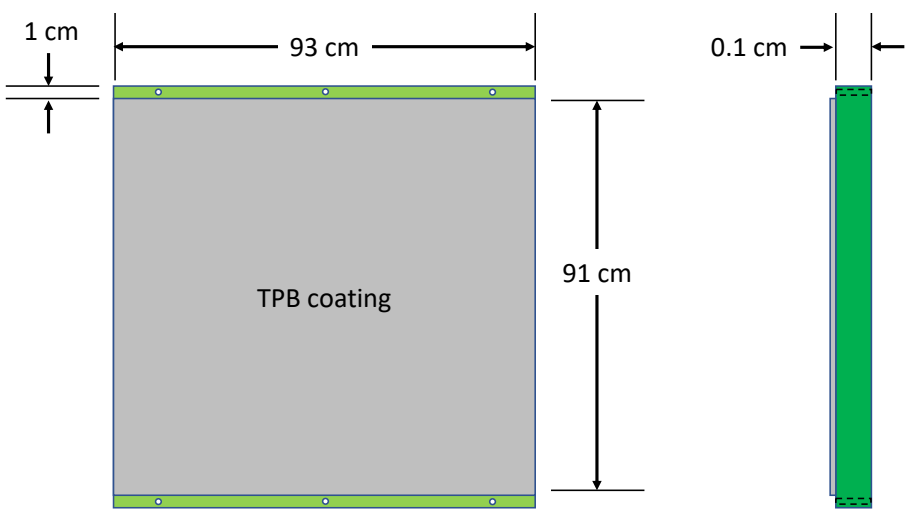

Figure 3.7: Sketches of the front (left) and side (right) views of the reflector/WLS panel (not to scale).

3.4 Mechanics

3.4.1 PMT Support Structure

A uniform array of 720 cryogenic Hamamatsu R5912-MOD20 PMTs, below the transparent cathode structure, will be fixed on the membrane floor in the areas between the membrane corrugations. The arrangement of the PMTs accommodates the cryogenic piping on the membrane floor, and other elements installed in this area.

The mechanics for the attachment of the PMTs were carefully studied. The PMT buoyancy must be counteracted while avoiding stress to the PMT glass due to differentials in the thermal contraction between the support and the PMT itself. The attachment is done via a stainless steel support base point-glued to the membrane via four adhesive injection holes. The weight of the support and PMT (approximately 7 kg) exceeds the buoyancy force of the system. Given the large standing surface of the stainless steel plate, these supports also ensure stability against possible lateral forces acting on the PMTs due to the liquid flow. Figure 3.8 shows the PMT with its support base attached to the bottom of the ProtoDUNE-DP cryostat.

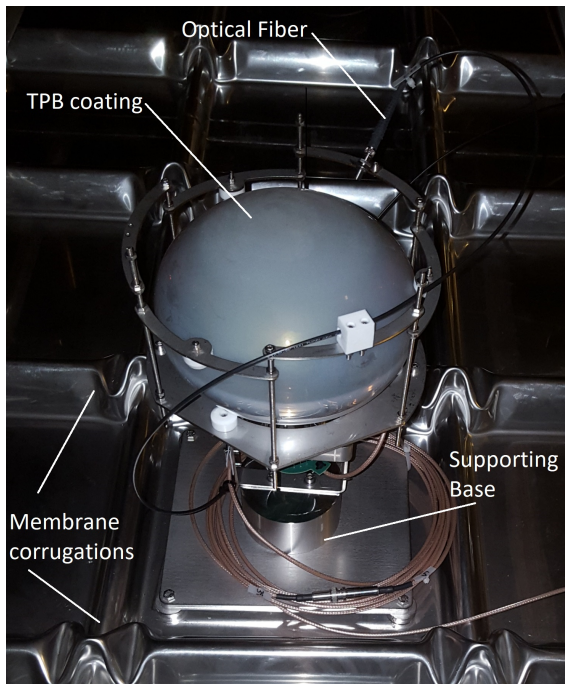

Figure 3.8: Picture of the cryogenic Hamamatsu R5912-MOD20 PMT fixed on the membrane floor of ProtoDUNE-DP. The optical fiber of the calibration system is also visible.

The support frame structure mainly comprises 304L stainless steel with some small Teflon (PTFE) pieces assembled by A4 stainless steel screws that minimize the mass while securing the PMT support to the cryostat membrane. The design takes into account the shrinking of the different materials during the cooling process to avoid breaking the PMT glass. Over-pressure tests were carried out for ProtoDUNE-DP, and further tests ensure correct performance under pressure. An individual PMT mount has been designed and tested in the WA105 DP demonstrator prototype [35], and the same design is used for ProtoDUNE-DP.

Installation of an individual ground grids mechanically attached to the PMT support structures is also under consideration by the HV and DP PDS consortia (See Appendix 3.16.1).

3.4.2 Reflector/WLS Panel Assemblies

The reflector/WLS panels that will be mounted on the inner surface of the FC will be 1 mm thick 93 cm × 93 cm G10/FR4 plates, with the central 91 cm (H) × 93 cm (W) area laminated with

reflective foil, which is coated with TPB (see Fig. 3.7). The panels will be supported by G10/FR4 support bars. Six horizontal bars of 199 cm (three at the front and three at the back), six vertical bars of 186 cm (all at the back) and four reflector/WLS panels will form a unit reflector/WLS panel assembly to be mounted on the FC. The panels will be sandwiched between the horizontal support bars along the non-laminated edges. Six vertical bars will be placed on the side of the panels without the reflective coating, aligning the holes. The structure will then be assembled by placing 24 screws.

The horizontal support bars will be attached to the FRP I-beams of the FC, which are spaced 2 m apart, by stainless steel screws. One end of the bar will be tightly screwed, while the other loosely to allow motion due to differential thermal contractions. Figure 3.9 shows sketches of the horizontal support bars with one of the two screw holes elongated to allow the support bar movement on the mounting screw.

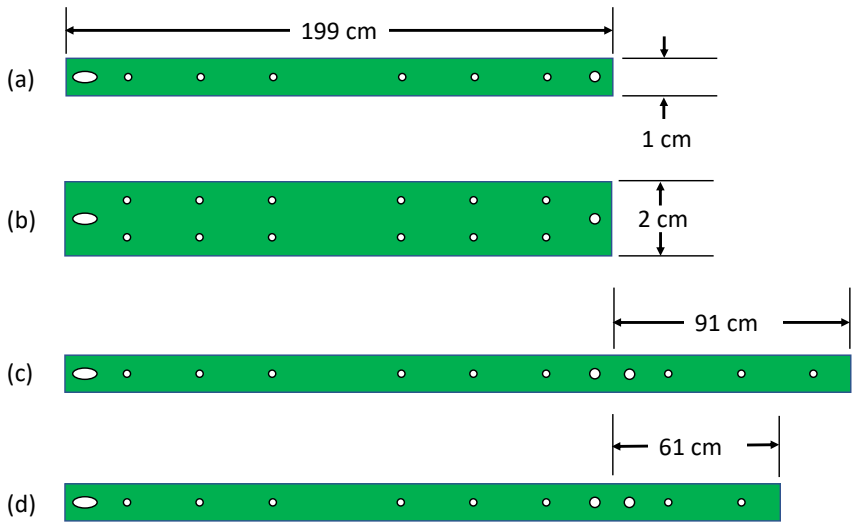

Figure 3.9: Sketches of the reflector/WLS panel assembly horizontal support bars (not to scale). (a) The top and bottom bars, (b) the middle bar, (c) the extended top and bottom bars to be mounted on the end submodules of the FC super-modules, and (d) the special extended top and bottom bars to be mounted on the end submodules of the corner FC side wall super-modules.

The reflector/WLS panel assemblies at the inter-super-module areas will have extended structures: 260 cm (W) × 186 cm (H) for the corner side wall FC sub-modules to accommodate the 2.4 degree tilt of the end walls, and 290 cm (W) × 186 cm (H) for all other FC sub-modules at the intersection of two FC super-modules. The extended assemblies will house 6 reflector/WLS panels, two of them in an extended part which is not supported at the end. Figure 3.9 (c) shows the sketch of the support bar to be installed at the end submodules of the FC super-modules except the end submodules of the corner FC side wall super-modules of which the corresponding horizontal support bar is shown in Fig. 3.9 (d). The special extended assemblies to be installed at the end submodules of the corner side wall super-modules will be 30 cm shorter than the regular extended assemblies to accommodate the approximately 25 cm approach of the end walls at middle drift distance (6 m).

Figure 3.10 shows inside (left) and outside (right) sketches of a unit reflector/WLS assembly. The blue bars are the I-beams of the FC, the dark green bars are the horizontal and vertical support

bars of the reflector/WLS panel assembly. The grey surfaces are the TPB coatings on the panels. The vertical and horizontal gaps between the reflector/WLS panels allow liquid flow.

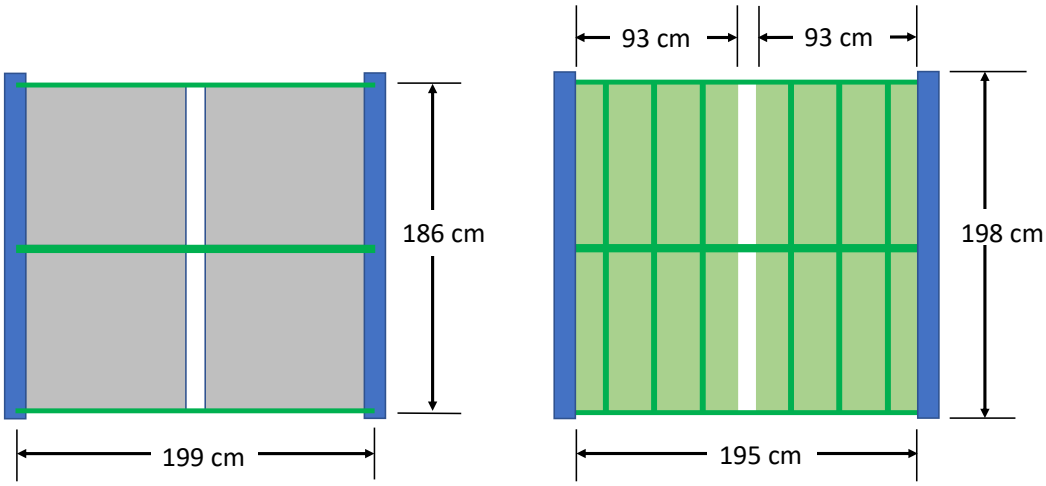

Figure 3.10: Sketches of the inside with the reflective/WLS coating (left) and outside without the reflective/WLS coating (right) views of a partial FC submodule with a reflector/WLS panel assembly. The blue bars are the FRP I-beams of the FC. The dark green bars are the horizontal and vertical support bars. The grey surfaces are the TPB coatings on the panels.

3.5 Readout Electronics

3.5.1 Photomultiplier High Voltage Dividers

The PMT has a grounded cathode and a positive HV applied to the anode. A single cable for each PMT carries both power and signal. This configuration, which requires half as many cables and feedthroughs on the detector than the negative voltage configuration, offers a clear advantage given the large number of PMTs in the detector. In addition, the cathode grounding shows fewer dark counts than the anode grounding scheme. Although a coupling capacitor must be used to separate the HV from the PMT signal, this signal and power splitting can be done externally, mitigating this drawback. Figure 3.11 shows the positive power supply and cathode grounding scheme.

The PMT base circuit uses only resistors and capacitors. The components are carefully selected and tested to minimize variations in their characteristics with temperature. The polarization current of the voltage divider (total circuit resistance) is chosen to fit the PMT light linearity range (up to 100 PEs per 6 ns, see Tab. 3.1) and maximum power requirements (<0.2 W/PMT). The dynodes' voltage ratio will follow manufacturer recommendations for increasing linearity range on the space-charge effect area (tapered divider). In addition, capacitors are added to the last stages to increase the PMT linearity in pulsed mode.

The PMT base connects to the feedthrough with the RG-303/U cable, selected for its low atten-

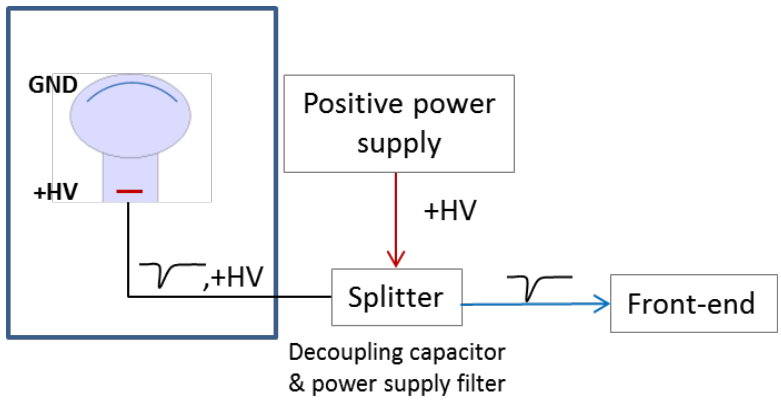

Figure 3.11: Positive power supply and cathode grounding scheme.

uation and its proven reliability in cryogenic environments. The short cable is directly soldered to the PMT base on one end and, on the other end, attaches to the long HV cable with an SHV connector. The long cable connects to the feedthrough flange.

3.5.2 High Voltage and Signal Splitters

HV and signal splitters separate the fast PMT response signal from the positive HV with capacitive decoupling. A low-pass filter between the HV supply and the PMT reduces the noise.

It is possible for radiated electromagnetic interference (EMI) picked up by the cables, and for conducted noise from the HV power supply, to be synchronous across many PMT channels (i.e., coherent noise). This noise could add up to produce false detector triggers. Because the PMT signal can be as low as a few mV, control of the EMI over the circuit is very important. The splitter HV input filter should reduce the EMI induced and conducted by the power supply cables. Enclosing each splitter channel in its own metallic grounded box reduces the EMI directly received in the splitter circuit and the cross-talk between different splitter channels.

Figure 3.12 shows a generic splitter circuit where R1 and C1 form the HV input low-pass filter (with a cut-off frequency below 60 Hz). The resistor R7 and the LED are for safety only, warning when HV is applied to the splitter. The C4 capacitor splits the signal coming from the PMT from the HV, and R2 prevents the PMT signal from going to ground through the C1 capacitor. R4 and R5 are $0\,\Omega$ optional resistors that allow some flexibility in the grounding configuration. Finally, R3 ensures the discharging of C4 if the splitter is not connected to the $50\,\Omega$ input at the data acquisition (DAQ) system. The RC time constant of the capacitor C4 and the load ($50\,\Omega$) must be as large as possible to minimize baseline oscillations due to the charge-discharge of the capacitor. Values of C4 between 150 nF and 300 nF have already been tested. Figure 3.13 shows the HV/signal splitter box of ProtoDUNE-DP.

For the connections between the HV power supply and the splitters and between the splitters and the cryostat feedthroughs, HTC 50-3-2 cables have been chosen as baseline. The HTC 50-3-2 has a similar attenuation as the RG-303/U (used inside the cryostat), but costs 8 to 10 times less.

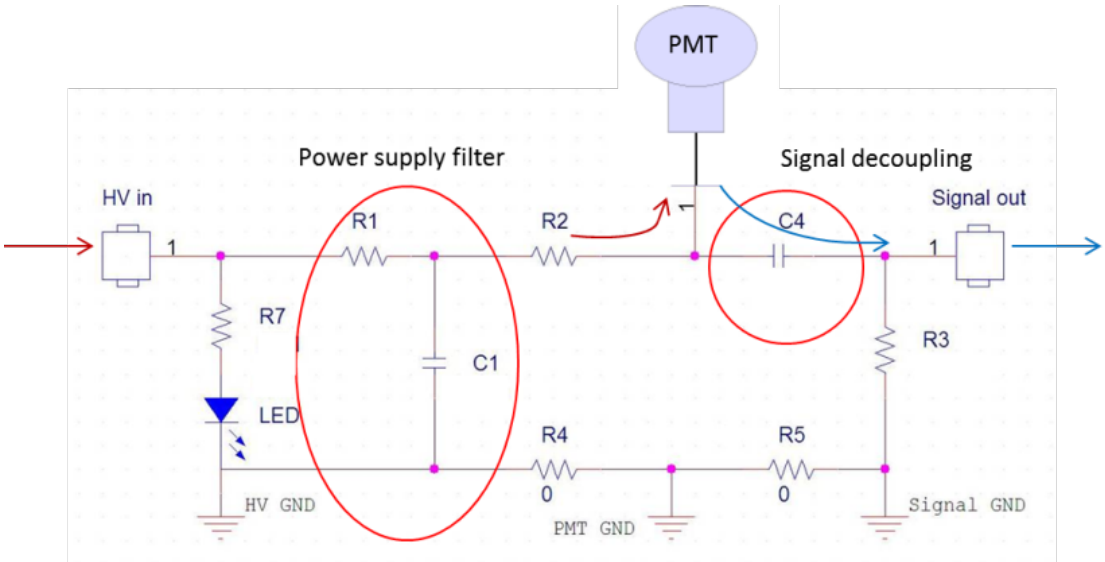

Figure 3.12: Generic splitter circuit diagram.

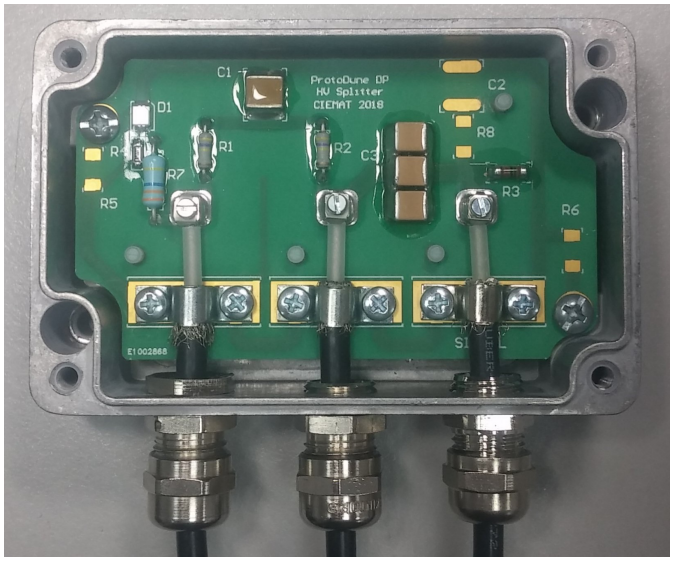

Figure 3.13: Picture of the splitter box for ProtoDUNE-DP.

Both cables are attached on one end directly to the HV splitter and have an SHV connector on the other end. An RG-58 cable terminated on the connector required by the light readout card provides the connection between the splitter and the card. The PMT readout card is described in Chapter 2.

3.5.3 Signal Readout

To meet the physics requirements, the following is the information that must be extracted from the PMT signals:

- S1 fast component shape, charge, and timing;
- S1 slow component shape and charge;
- S2 shape, charge, and timing (distance from S1 and duration);
- single photoelectron (SPE) charge spectrum for gain calculation during PMT calibration;
- trigger signal generation by the coincidence of several PMT signals.

In general, the PMT signal dynamic range goes from the mV level to several volts (over 50 Ω load). The lower limit of the PMT dynamic range is given by the lowest level of the SPE signal that meets the signal to noise ratio specification. Thus, the PMT gain should be set at the value that makes the SPE level meet this condition. The upper limit of the dynamic range is given by the PMT signal amplitude for the maximum number of photoelectrons (PEs) expected per sampling time unit. This amplitude can be calculated approximately as number of PEs × SPE amplitude (at the gain required to meet the S/N ratio at SPE level). Figure 3.14 shows the SPE waveforms (left) and amplitudes from the WA105 at different voltages (right).

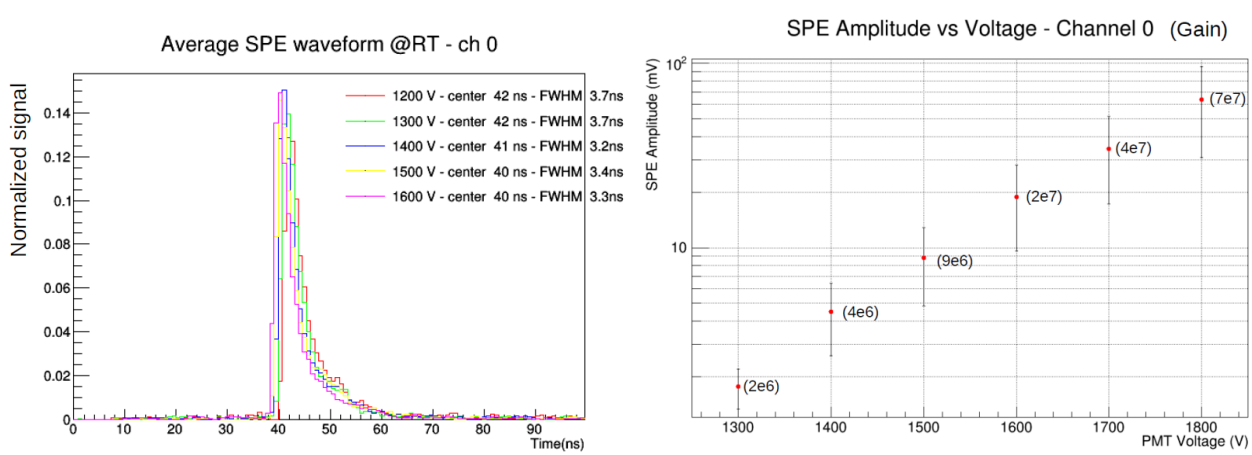

Figure 3.14: SPE waveforms (left) and amplitudes from the WA105 at different voltages (right).

Because the long cables from the PMTs to the front-end (FE) electronics are very long, the cable noise could be high. If a noise level around 1 mV is considered, the PMT gain must be set around

10^7 to have the required S/N ratio of 5. The average SPE pulse width is approximately 3.5 ns full width at half maximum (FWHM). If an accurate signal reconstruction is required, the sampling period should be of the level of the ns. If only charge information is relevant, the sampling period can be higher, but the signal must be low-pass filtered before sampling. This filtering affects the signal level making the discrimination of signal from noise more difficult and requiring an increase of the PMT gain to meet the S/N specification.

The sampling frequency also affects the time tagging precision. The time uncertainty due to the PMT alone is approximately 3 ns (transit time spread). Other factors, like Rayleigh scattering, increase this uncertainty, as does the sampling period. Therefore, the higher the sampling frequency, the better for detector performance but at the cost of increased data rate and storage requirements.

The light signal must be synchronized with the DAQ. All DAQ electronics use the White Rabbit (WR) protocol for synchronization. A dedicated WR μTCA [36] slave node is on the light readout FE electronics as sync receiver, distributing clocks to different FE cards.

Several PDS specifications affect the signal readout design, such as the required relative timing accuracy among hits, hit signal-to-noise ratio, and analog range per channel. The PDS specifications are listed in Table 3.1.

3.6 Calibration System

A photon calibration system is required in the DP module to calibrate the PMTs installed in the LAr volume. The goal is to determine the PMT gain and monitor the stability of the PMT response. One of the main goals of the PDS is to provide a trigger for non-beam physics. The trigger is based on the amplitude of PMT signals. The amplitudes of the PMT signals are summed for groups of certain PMTs and/or for all PMTs and then, these input signals are discriminated according to the trigger logic. An equalized PMT response allows using the same threshold definition for all PMT groups, simplifying the determination of trigger efficiency. In addition to measuring the PMT gain, the calibration system is also designed to monitor the stability of the PMT response. In addition to the necessary PMT characterization at cryogenic temperature before installation [33], and based on past experience with WA105 DP demonstrator detector operations [8], we conclude that a light calibration system is needed during experiment data taking.

3.6.1 Calibration System Design

An LED-driven fiber calibration system [37, 38, 39, 40, 41] is designed so a configurable amount of light reaches each PMT. The calibration light is provided by a blue LED of 465 nm using a Kapustinsky [42] circuit as LED driver and transmitted by a fiber system ending with an optical fiber installed at each PMT (see Figure 3.15). Twenty groups of six LEDs placed in a hexagonal geometry and a reference sensor check the performance of the LED in the center of each group.

The direct light goes to the fiber, and the stray light to the silicon photomultiplier (SiPM) used as reference sensor. Each LED is connected to an external fiber going to one feedthrough. Then, fibers are connected inside the cryostat, and each fiber is attached to a 1-to-7 fiber bundle, so that one fiber is finally installed pointing at each PMT. The PMTs are oriented with the first dynode perpendicular to the Earth magnetic field and the fiber parallel to the first dynode to have a similar gain to the one obtained with diffuse light. The components placed outside the cryostat at room temperature form the *external system*, and the ones installed inside it at cryogenic temperature form the *inner system*.

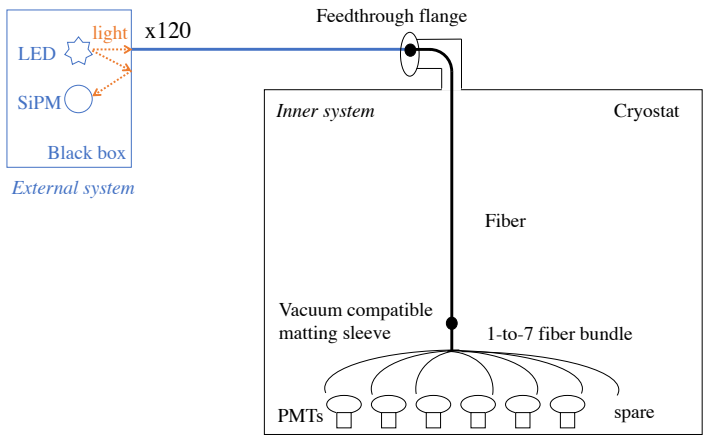

Figure 3.15: Sketch of the DUNE FD PDS light calibration system. The external system at room temperature is shown in blue and the inner system at cryogenic temperature in black.

The design of the external components is driven by the need for a cost-effective system. An additional requirement is that a reference light sensor monitors the amount of the injected light. The light is injected in form of several ns long pulses provided by a Kapustinsky circuit. The set up consists of a commercial black box in which a light guide structure is mounted. There are 20 structures, and each has six arms and a central part, as shown in Figure 3.16. On each of the six arms, an electronics board containing a Kapustinsky circuit is mounted. The LED, NSPB300B from Nichia Corp.[9], with a peak wavelength of 465 nm is placed on the PCB in front of an optical SMA to SMA feedthrough. On the other side of each feedthrough, an optical fiber, FG105LCA-CUSTOM-MUC from Thorlabs[10], is connected. The fiber transports the light to one of the 120 feedthroughs in the instrumentation flange on top of the cryostat. While a large fraction of the LED light is emitted forward, a small fraction, the stray light, is emitted under a large angle and reaches by reflection to the central region of the light guide structure where it is detected by a SiPM, MicroFJ-30035-TSV-TA from SensL[11].

The inner system is designed to minimize light losses at cryogenic temperatures. The external fibers are connected to 120 female optical feedthroughs from Allectra[12] installed at 20 flanges. Inside the cryostat, a single long fiber, FT800UMT from Thorlabs, goes down from each optical

[9] www.nichia.com
[10] www.thorlabs.com
[11] www.sensl.com
[12] www.allectra.com

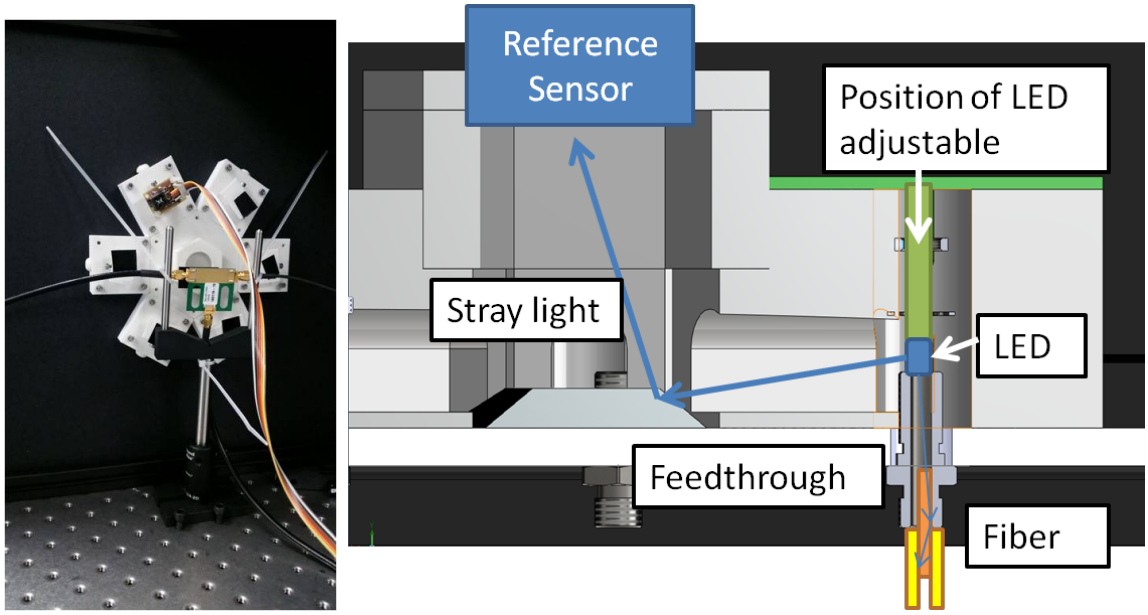

Figure 3.16: (Left) Picture of the light guide structure during the development phase. The six arms are visible, and on one of them a prototype LED driver is mounted. (Right) Schematics of the light way from the LED to the reference sensor.

feedthrough routed along the walls of the cryostat to the bottom of the cryostat where a 1-to-7 fiber bundle, comprising FT200UMT fibers from Thorlabs, is connected to each long fiber. A total of 720 of these fibers are guided to the PMTs at the bottom of the detector. The end of the fiber is fixed at the PMT support structure pointing the photocathode. The fibers and bundles are 0.39 NA TECS^{TM} hard-clad, multimode, step-index fibers with high OH (hydroxyl) content to increase the light transmission at low wavelengths. To optimize the light transmission of the fiber-bundle connection, the inner fibers have a diameter of 800 µm, big enough to distribute uniformly the light at the bundle entrance, total diameter 700 µm. From the mechanical point of view, the described approach of bundles attached to fibers is safer than connecting the bundles directly to the feedthroughs. To have good homogeneity of the light at the fiber-bundle connections, SMA connectors are chosen. Vacuum compatible SMA to SMA mating sleeves are required to avoid LAr freezing inside the connector, which would reduce light transmission.

Alternatives to the calibration system baseline design described here are also being considered. See Appendix 3.16.2.

3.7 Photon Detector Simulation

A detailed simulation of the PDS response is essential both to compare with data from PDS prototypes (see Section 3.8) and to validate the FD baseline design for its projected performance (see Section 3.9).

3.7.1 Simulation Framework And Assumptions

The simulation of the PDS response is integrated in LArSoft, the liquid argon software toolkit used by the DUNE Collaboration for simulation and reconstruction. The simulation is divided in three steps: light generation, light propagation, and light detection.

For a minimum ionizing particle (MIP), an energy of about 2 MeV/cm is deposited in LAr. Through decays of excited argon states and ion recombination, about 40,000 scintillation photons are emitted per MeV deposited at null drift field. At the nominal drift field of 500 V/cm, this amount reduces down to about 24,000 photons per MeV as the recombination process weakens. This signal, known as S1 (see Section 3.2), is common to the single and dual phase technologies.

In the gas layer of the dual phase design, the electrons are amplified through Townsend avalanche in the LEM holes and lead to an electroluminescence signal called S2 (see Section 3.2). The electroluminescence gain, G_{EL}, i.e., the number of photons produced per electron crossing the liquid-gas interface, depends on the voltages applied to the LEM. In our simulations, we typically assume a gain of 300 photons per extracted electron. The S1 and S2 signals have similar characteristics for wavelength and time constants.

Because of different mechanisms during photon propagation (Rayleigh scattering, absorption by impurities in the LAr or by elements constituting the detector), only 1×10^{-3} fraction of the photons produced in the LAr active volume reaches the PMT photo-cathodes. The direct simulation of the large number of photons generated for each track crossing the active volume would require a considerable amount of CPU power and time. Profiting from the fact that the photon emission is isotropic and the detector is uniform and symmetric, it was decided to generate the photon propagation in the detector in a dedicated Geant4 simulation only once and then to store the results in a photon library.

The active volume is divided into voxels, and a large number of photons are isotropically and uniformly generated in every voxel. The number of photons collected by each PMT and the propagation time are stored and later parametrized. For long voxel-PMT distances (typically larger than 1 m), a landau function is well suited to reproduce the time distribution. The detection probability, called visibility, the landau parameters (most probable value, σ) and the minimal time needed by the photon to reach the PMT are stored in a photon library for all voxel-PMT combinations. When a track is generated in the standard DP LArSoft simulation toolkit, for each step of the track, the light map is looked up to assign the number of photons to be collected at each PMT and the arrival time distribution due to the propagation.

To generate photon libraries, a comprehensive modelling of the geometry for the WA105 DP demonstrator, ProtoDUNE-DP, and DP FD detectors are implemented in geometry description markup language (GDML) files. The GDML files include the main elements relevant for light propagation, such as the cathode, the FC, the LEMs, and the ground grid. Most detector elements are assumed to be fully absorptive. Thus, when photons reach any of these surfaces, they are removed from the simulation. One exception is WLS reflector foil surfaces, which are assumed to have 100 % WLS efficiency for 127 nm LAr light and 93% reflectivity for 430 nm light re-emitted by the wavelength shifter material. To quantify the effect of the WLS reflector foils for the DP

FD module, three geometries have been tested: no foils, foils entirely covering all four FC vertical walls (full foils, in the following), and foils covering only the upper half of the FC (half foils, in the following). For the PDS prototypes, no foil geometries have been simulated.

As far as LAr optical properties are concerned, the simulations assume a 61 cm Rayleigh scattering length for 127 nm light, no Rayleigh scattering for visible light, and a 20 m absorption length for all wavelengths. The response of the PMT is simulated assuming an effective quantum efficiency of 0.12 for 127 nm light. This value includes the TPB response of the coated photo-cathode [34]. For visible light emitted by WLS foils, the PMT quantum efficiency is taken to be 0.20. A dark count rate of 1.7 kHz at cryogenic temperature is assumed, as obtained during ProtoDUNE-DP PMT calibration [33]. A linear response of the PMT is assumed, multiplying the number of photons reaching the photo-cathode with the single photo-electron response measured in the laboratory for a gain of 1×10^7. In this case, the single-PE response has a time width of 6 ns, and an amplitude of 15 mV. The digitization of the waveform is simulated considering a sampling rate of 250 MHz[13], a resolution of 0.5 mV/ADC, and an electronics noise of 0.8 ADC counts RMS as measured in WA105 DP demonstrator, see Section 3.8. Therefore, based on WA105 DP demonstrator measurements, the SPE to baseline noise RMS ratio assumed in the simulations exceeds 30.

3.7.2 Expected Light Yields

Table 3.2 gives the detected light yields expected in the DUNE FD geometry, for the three different WLS reflector foil geometries mentioned above. The yield is computed by averaging over all LAr voxels contained in the TPC active volume. A voxel size of 1 m^3 is considered in DP FD simulations. The average yield is 5.4, 8.0 and 12.2 PEs/MeV for the no foils, half foils and full foils geometries, respectively. The higher yield for the foil geometries is partly due to the higher number of photons reaching the PMT photo-cathodes, and partly due to the higher PMT quantum efficiency for visible light. As shown in Table 3.2, a 11.3% (33.8%) fraction of photons reaching the PMTs is WLS visible light, in the half foils (full foils) geometry.

Table 3.2: Average light yields in the DUNE FD geometry for different WLS reflector foil configurations. The total incident light yields and the fractions of incident WLS light at the PMT photo-cathodes, as well as the total detected light yields, are given.

Configuration	Incident light yield (photons/MeV)	Fraction of incident WLS light (%)	Detected light yield (PEs/MeV)
No Foils	45	0.0	5.4
Half Foils	62	11.3	8.0
Full Foils	83	33.8	12.2

We can also see the effect of the WLS reflector foils on the expected light yields in Fig. 3.17, where the yields are shown as a function of the drift coordinate (left panel) and transverse coordinate (right panel), and averaging over the two other spatial coordinates. The drift coordinate is the vertical one, while the transverse coordinate is the horizontal direction perpendicular to the

[13] This is the sampling frequency used in the WA105 DP demonstrator readout, but slower frequencies of 65 MHz or 2.5 MHz are being considered for the DP PDS.

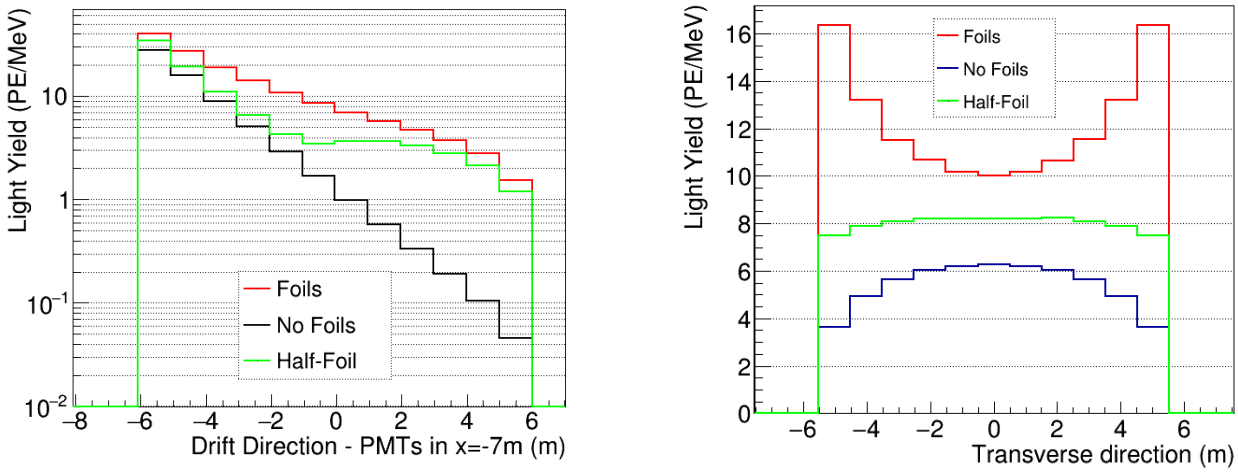

Figure 3.17: Expected light yield in the full DP FD cryostat. The yield units are number of photoelectrons per MeV of deposited energy. The 1D yields are shown as a function of the drift (transverse) direction in the left (right) panel, averaging over the other two spatial coordinates (not shown). The three histograms correspond to three different geometries: no WLS reflector foils, foils fully covering FC, foils covering upper FC half.

neutrino beam direction. The left panel provides better appreciation of the main trend in the spatial response, namely the light yield reduction with increasing distance from the cathode. The WLS reflector foils are particularly useful in improving the yields at small drift distances, where the yields are lower. The foils reduce the very large non-uniformity in spatial response between cathode and anode by more than one order of magnitude. The full foils geometry provides better yields than half foils in the lower half of the detector. The difference between the two geometries is less significant at small drift distances. Being the most inefficient region of the PDS, the latter is the most important one to optimize through foils. In addition, the right panel shows that the half foils geometry is the one providing the best uniformity along the transverse direction. These plots justify why the half WLS foils geometry has been selected for the PDS baseline design.

Figure 3.18 shows the detected light yield, for the half foils baseline geometry, as a function of drift and transverse directions simultaneously, and averaging over the beam direction. Near the cathode plane ($Y = -6\,\mathrm{m}$ in this figure) the highest light yield is expected near the center of the active volume ($X = 0$). The opposite is true near the anode plane ($Y = 6\,\mathrm{m}$).

3.8 Validation with Data from Photon Detector System Prototypes

The LAr TPC DP proposed technology is the result of years of R&D. From small-scale chambers to the DUNE module, many prototypes have been constructed, each with some design modifications and optimizations. Relevant to the PDS itself, the WA105 DP demonstrator, operated at CERN in 2017, the ProtoDUNE-DP, to be commissioned in 2019 and the DUNE far detector module

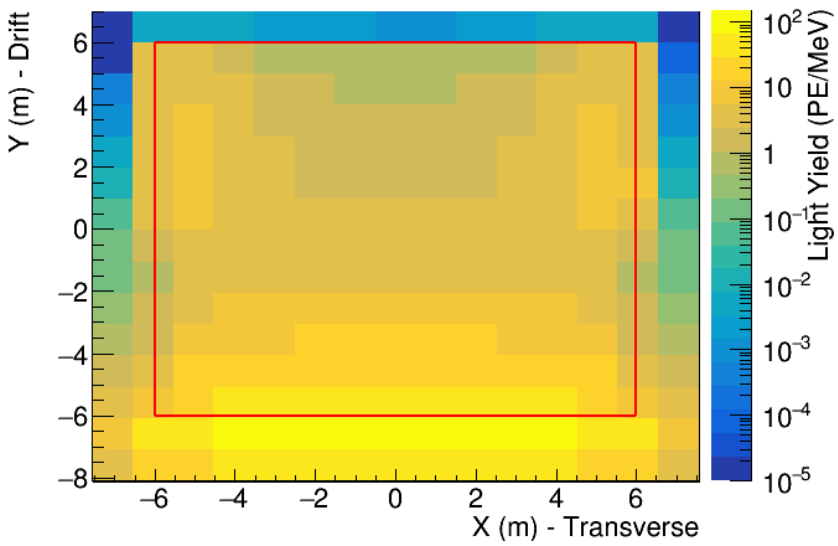

Figure 3.18: Expected light yield in the full DP FD cryostat, for the half WLS reflector foils geometry. The yield units are number of photo-electrons per MeV of deposited energy. The 2D yield is shown as a function of the drift (vertical axis) and transverse (horizontal axis) directions, averaging over the third spatial coordinate (not shown). The red contours indicate the TPC active volume. The PMTs are located at a drift coordinate of −7 m.

similarities and differences will be described here.

3.8.1 Design Similarities and Differences Between Prototypes and Far Detector System

The first tonne scale dual phase LAr TPC demonstrator took cosmic data between June and November 2017 at CERN. Located 1 m below the charge collection plane, underneath the cathode and the ground grid, the photon detection system consisted of five PMTs (Hamamatsu R5912-MOD20, described in more detail in Section 3.3) evenly distributed along the 3×1 m^2 area (one PMT every 50 cm). The demonstrator was an opportunity to test different PDS designs, particularly the TPB coating and PMT bases. Three PMTs had the TPB coating applied directly onto their windows using evaporation, but for the other two, the TPB was deposited on a 4 mm thick transparent Plexiglass plate mounted on top of the PMTs. While the latter solution has the advantage of being simpler and less risky to manipulate, it reduces acceptance and possibly efficiency because of the internal reflections between the TPB and the Plexiglass surfaces. Pictures of the WA105 DP demonstrator PDS are shown in Figure 3.19.

Two power supply polarities were used. Three PMTs were equipped with a negative HV base, i.e. a negative bias voltage was applied to the photocathode, and the anode was grounded. This system requires two cables: one for the HV system and one for the signal. A positive base served the other two PMTs: a single cable positively biased the anode and carried the signal, and the cathode was grounded. The HV and the signal were then externally decoupled using a splitter,

Figure 3.19: The WA105 DP demonstrator PDS. Top left: PMT with the TPB deposited on the plexiglass plate; top right: PMT with the TPB coated onto the photocathode; bottom: The five PMTs installed in the WA105 DP demonstrator underneath the ground grid.

see Section 3.5.2. The latter design has the advantage of reducing the number of feedthroughs and cables while also reducing the noise. Overall, four configurations were tested (see Table 3.3). During the $3\times1\times1$ m^3 operation, the PMTs operated at a rather uniform gain of around 10^6 with a readout sampling of 250 MHz.

Table 3.3: Configuration of the five PMTs installed in the WA105 DP demonstrator.

PMT	Base	Coating	Voltage (kV)	Gain (10^6)	Noise (ADC)
1	Negative	Coating	−1.2	0.92±0.13	0.7
2	Negative	Plate	−1.2	1.01±0.12	0.7
3	Positive	Coating	1.1	0.95±0.11	0.4
4	Positive	Plate	1.1	1.26±0.15	0.4
5	Negative	Coating	−1.2	1.33±0.15	0.8

In ProtoDUNE-DP, 36 PMTs are installed 6 m below the collection plane, again underneath the cathode and the ground grid. The PMT density is lower than the demonstrator. Their positioning over the 36 m^2 area was optimized with simulations. The number of PMTs is higher around the center of the active volume and lower near the FC borders. This positioning maximizes the amount of light collected from cosmic rays.

After evaluating the demonstrator configurations, the TPB was directly evaporated onto the PMT windows, and the PMT base was chosen to have positive polarity. This configuration maximizes

collection efficiency and reduces both the number of cables and the electronic noise.

For DUNE FD PDS, TPB will be directly applied to the PMT windows, and the positive biasing scheme will be implemented. The aspect ratio between cathode size and drift distance is larger than in ProtoDUNE-DP, so the amount of light loss by absorption on the FC should be smaller. Therefore, the DUNE FD PDS layout should be uniform with PMTs on a regular lattice with 1.02 m spacing. On the other hand, light attenuation due to absorption in the LAr itself will be larger in the DUNE DP detector module.

3.8.2 WA105 DP demonstrator Light Data Results and Simulation Validation

Analysis of data taken during the WA105 DP demonstrator operation provides the first validation of and improvements in the light simulation developed so far. The demonstrator ($3 \times 1 \times 1$ m^3 active volume) has linear dimensions comparable with the Rayleigh scattering length, which is approximately 60 cm. As a consequence, the light absorbed by elements of the detector (such as the FC, LEM, or cathode) may become a problem. Hence, light maps were created with particular care for precision in reproducing the demonstrator's geometry.

Two triggering schemes were used during the WA105 DP demonstrator operation. The first was provided by an external muon tagger, the cosmic ray tagger (CRT), to record horizontal muons. The CRT was made of plastic scintillator planes on each side of the detector. The second was provided by the PMTs themselves, requiring that the five sensors record sufficient light in coincidence. In this configuration, more vertical muons and showers were recorded.

Using the CRT trigger condition, a rough track reconstruction is possible because the CRT provides coordinate information with 11 cm^2 resolution. Hence, even without charge information, as for data taken at null field, it is possible to select muon-like tracks and retrieve the shortest distance between the track and each PMT. A schematic drawing of the WA105 DP demonstrator detector is presented in Figure 3.20 with the relevant track parameters.

From the PDS point of view, the WA105 DP demonstrator operation lasted several months because light was collected during cool down, filling, and commissioning stages of the demonstrator. The PDS performed with high stability during this entire period. In Figure 3.21, the pedestal mean and RMS are shown for one positive and one negative base PMT as a function of time for 5 months of operation.

Figure 3.22 shows the average waveforms for PMT 5 in gas and liquid argon with no drift field. These waveforms are fitted with a gaussian to describe the response function convoluted with a sum of three exponentials to describe the fast, slow, and intermediate components. The extracted values agree with the literature, although the lifetime of the fast component has been fixed at 6 ns in the fitting procedure.

Many studies show that τ_{slow}, the slow component (Section 3.2.1) is very sensitive to the amount of impurities in the liquid. To monitor the purity of the liquid argon as a function of time, the

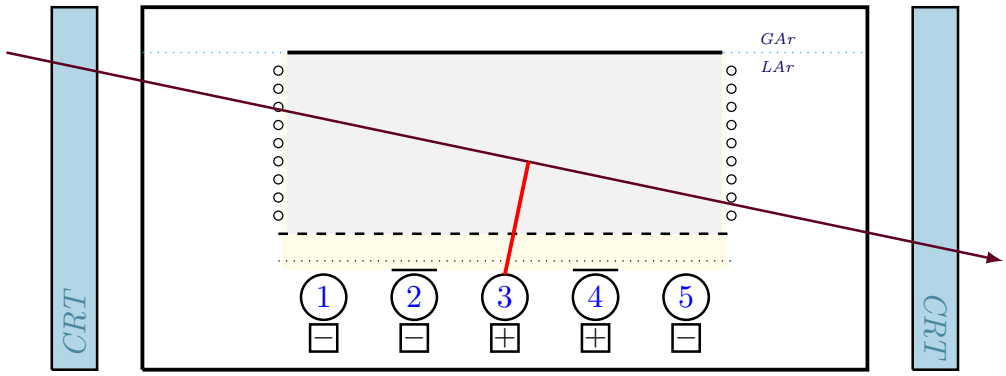

Figure 3.20: Schematic view of the WA105 DP demonstrator. The fiducial volume is in gray and limited from the collection plane area to the cathode. The active volume is in yellow. Its volume is defined by the collection plane: the FC to the top of the PMTs. A track that would be detected by the CRT is shown with its minimum distance to PMT 3 in red.

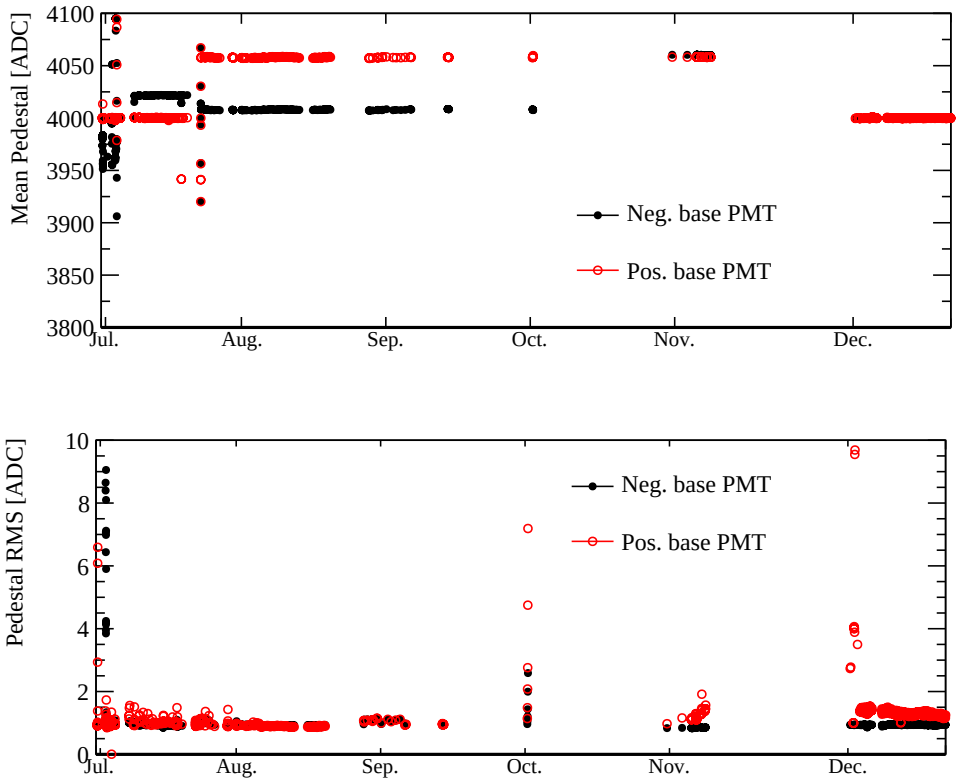

Figure 3.21: Pedestal mean (top) and RMS (bottom) for one negative base PMT (black) and one positive base PMT (red) between July and December 2017 during the operation of the WA105 DP demonstrator.

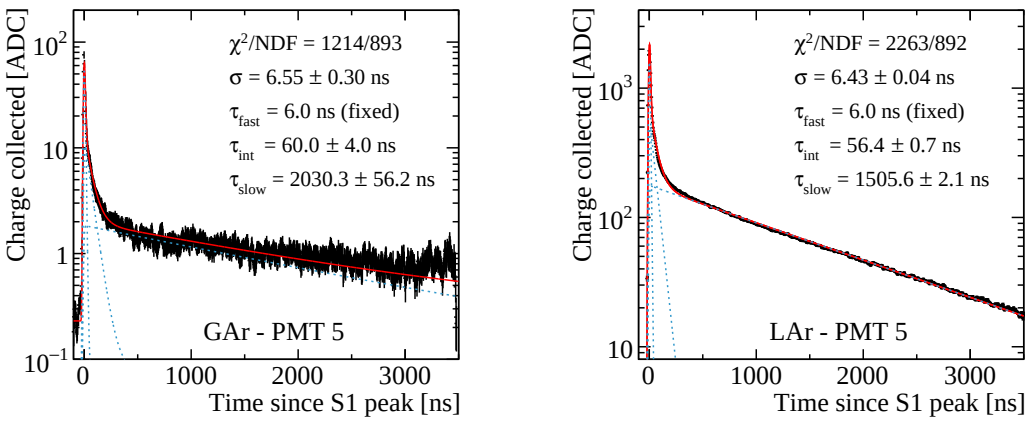

Figure 3.22: Scintillation time profile in the absence of drift field recorded in GAr (left) and LAr (right) in black. In red, the fit performed with a sum of 3 exponentials (describing the fast, intermediate, and slow components, all shown as dotted blue lines) convoluted with a gaussian to take into account the response function of the PMT. The extracted lifetimes are shown in the figure.

same fit has been performed on several runs under similar conditions. Figure 3.23 presents the evolution of τ_{slow} for 15 days of operation. The results exhibit a very stable amount of impurities, which agrees with the stability of the electron lifetime measured using the charge collection.

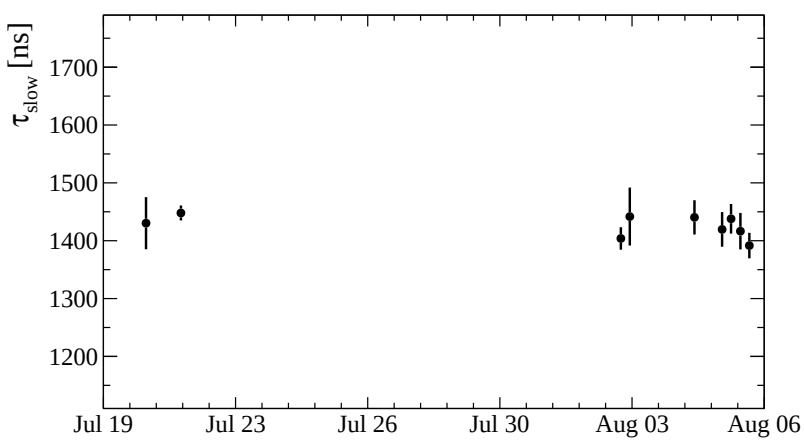

Figure 3.23: Evolution of τ_{slow} over 15 days of operation of the WA105 DP demonstrator. The points are the averages over the values extracted from the fits to the waveforms of the 3 negative base PMTs for runs taken with no drift field. Preliminary results.

The S2 light has also been recorded in dedicated runs using a 1 ms recording time window. Figure 3.24 shows the average waveforms from runs with a drift field of 0.5 kV/cm and an extraction field of 2 kV/cm (3 kV/cm) in liquid (gas). In the figure, one run has no amplification field, the others have the LEMs polarized to provide an amplification field of 25.5 kV/cm. The effect of the LEMs on the amount of S2 light generated is clear. The S2 light extends for about 600 μs after emission of the prompt signal, agreeing with the electron drift time over 1 m in such drift field.

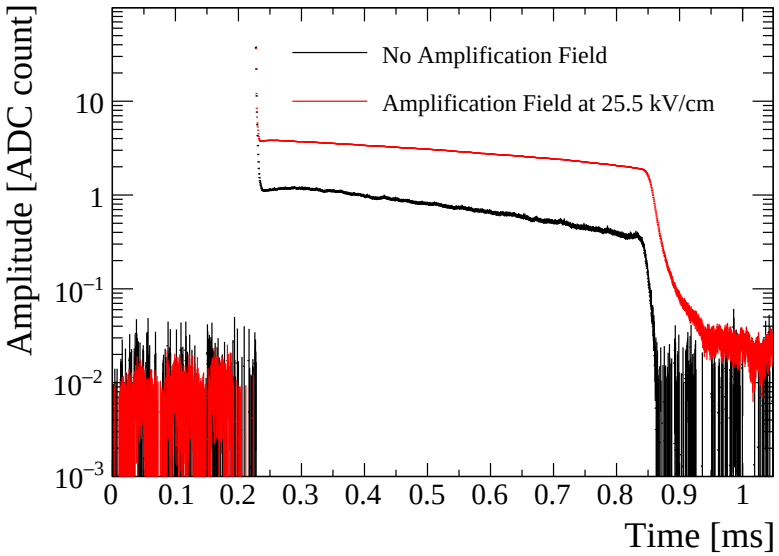

Figure 3.24: Average waveforms of negative based PMTs in a 1 ms window. Both runs were taken with a drift field of 0.5 kV/cm and an extraction field of 3 kV/cm in gas. The S2 light extends for about 600 μs, as expected.

Using data taken at null field in CRT triggering mode, muon-like tracks are selected. Further, the tracks must cross the active volume for distances longer than 3.1 m. The S1 charge collected by each PMT is calculated by integrating the analog-to-digital converter (ADC) values in a 1 µs window starting from the S1 peak; this charge value is then converted into the number of detected PEs using the calibrated PMT gains in Table 3.3.

In the simulation, 4 GeV muons are generated from one CRT panel to the other with data-driven kinematics. The number of PEs collected by each PMT is generated according to the light maps. To suppress spurious triggers, data analysis uses a selection of the minimum amount of light recorded by all PMTs; this does not apply to Monte Carlo (MC). Moreover, the PMT signal must not saturate the readout only for data analysis, but not MC. Figure 3.25 compares the number of PEs collected in data analysis and in MC. The data and MC agree well with one another.

In the WA105 DP demonstrator, the PMT gain was adjusted so S1 and S2 light could be seen and thus increase the trigger rate while minimizing the PMT ADC saturation. In DUNE DP, the situation will be different as the volume is much larger and part of the triggering modes will be independent from the PMTs. Hence the PMT gain will be adjusted accordingly and the events saturating the ADC should not be as problematic as it could be in WA105 DP demonstrator.

The PEs collected per PMT depends strongly on the shortest track-PMT distance. Many factors can affect how much charge is collected, primarily, the scattering length, also known as the Rayleigh scattering length. This quantity is still subject to debate among the LAr community because its measurement is fairly complicated. Current estimates of the scattering length range from 20 cm to 1 m. In the WA105 DP demonstrator simulation, the scattering length was set to $L_{ray} = 55$ cm. Figure 3.26 shows the charge collected as a function of the shortest track-PMT distance in the

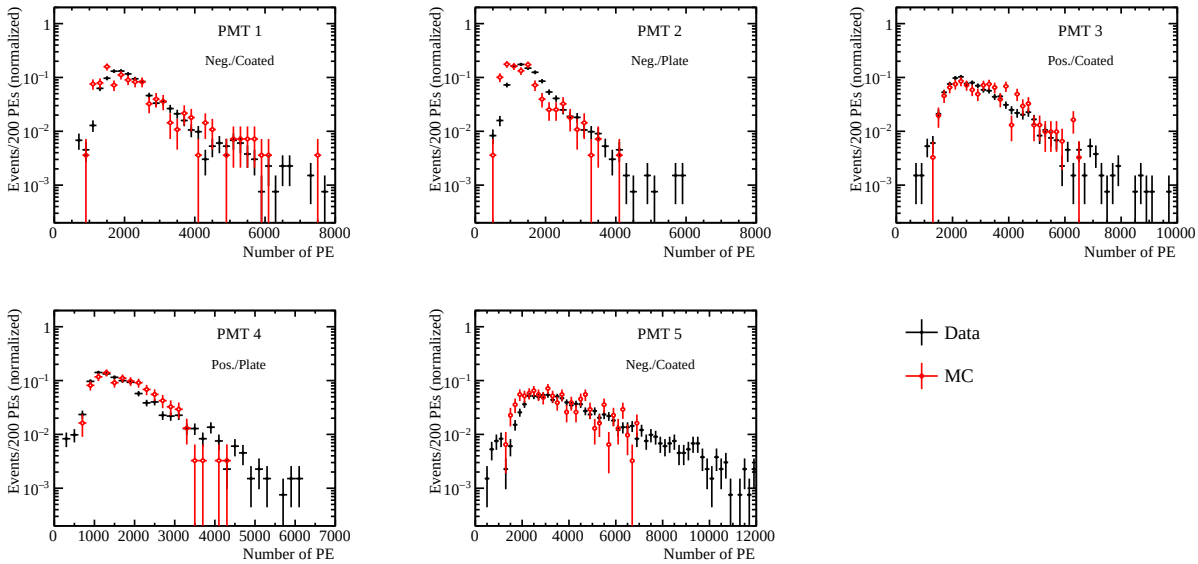

Figure 3.25: Charge collected by the PMTs in a 1 μs window containing the S1 peak for muon-like tracks triggered by the CRT panels. The data is shown in black and the simulation in red. The distributions are normalized to unity for clarity. Preliminary results.

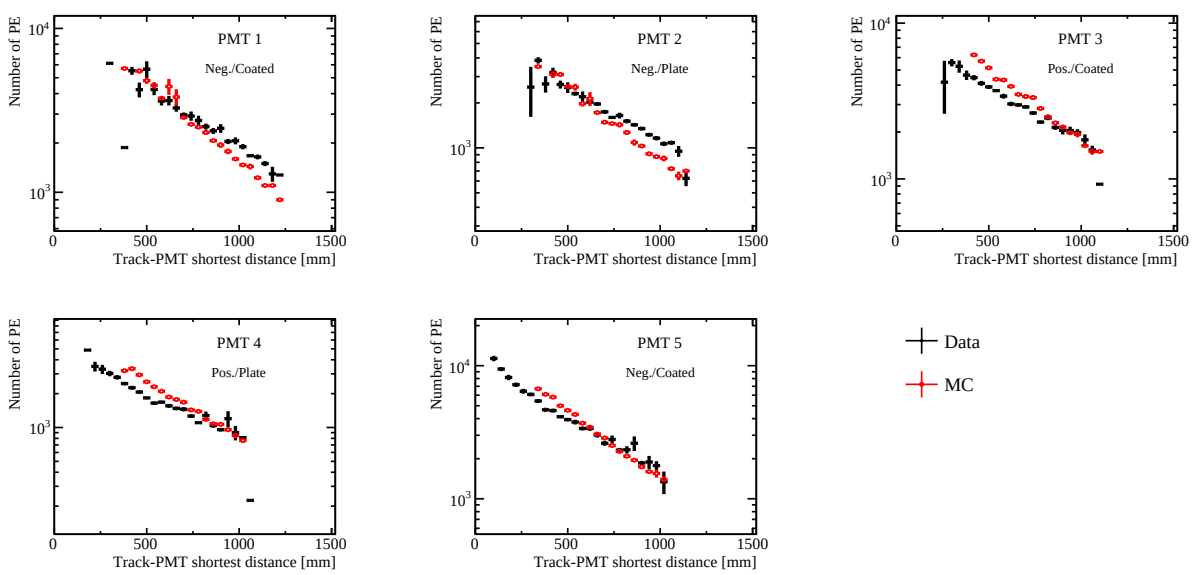

Figure 3.26: Profile histograms of charge collected as a function of the track-PMT shortest distance. The data is in black, the simulation in red. Preliminary results.

form of profile histograms. The overall trend is very similar for data and MC, also across all the PMTs. However, the profile histogram slopes indicate that the assumed scattering length in MC could be better tuned to reproduce the data, e.g., toward larger values of the Rayleigh scattering length.

3.8.3 Installation of the ProtoDUNE-DP Photon Detector System

At the time of writing, no scintillation light data from ProtoDUNE-DP are yet available. Nevertheless, important lessons from ProtoDUNE-DP have already been learned, thanks to the recent installation of its photon detector system. They are summarized below. Figure 3.27 shows the placement of the 36 PMTs in ProtoDUNE-DP on the cryostat floor, performed in February 2019.

Figure 3.27: Installation of the ProtoDUNE-DP photon detector system.

One of the most critical points of the installation is the order of the tasks. Since the installation activities lasted several days in the ProtoDUNE-DP case, and will last several months for an FD module, and given that other persons have to work near the PDS components, the risk of damage has to be considered. The fragility of the components determines the installation order. The PMT supporting bases and the signal-HV PMT cables must be be installed first, then the PMTs can be mounted on their holders and connected to the cables, and finally the calibration fiber system has to be installed. The need of protecting the components has to be evaluated if there are subsequent activities around them. For example, Fig. 3.27 shows how temporary protective plates were placed in front of the ProtoDUNE-DP PMT photo-cathodes, and the PMT units were enclosed in temporary plastic bags.

The conceptual division of the FD PDS into several sectors is crucial. In ProtoDUNE-DP, the 36 PMTs were divided into six groups of 6 PMTs each. This arrangement simplified the installation of the calibration fibers considering that each fiber bundle has 7 fibers, including one spare fiber per bundle.

Concerning organizational matters, ProtoDUNE-DP experience shows that several documents should be prepared prior to installation, including a detailed description of all the tasks to be performed, a time estimation for all of them, and a list of the necessary items. In addition, the required status of the detector before each installation stage should be indicated. This information must be as detailed as possible. The benefits of a detailed planning are:

- All the persons participating in the PDS installation know their roles.
- The required material is foreseen and available when needed.
- The interaction with other installation crews is planned.
- The expected time for the installation is known in advance and extra time for unexpected events can be added.
- It is possible to communicate beforehand all the requests to the coordinator of the installation.
- The overlapping of activities and the waiting times are minimized.

3.9 Baseline Design Validation and Projected Photon Detector Performance

After the initial simulation studies described in the IDR [43], we have progressed toward a more realistic understanding of the projected PDS performance using the LArSoft framework:

- Optical simulations are now performed in the DP FD module geometry. In the FD IDR, physics studies assumed the ProtoDUNE-DP geometry. Considering the lack of any optical segmentation in the DP design, light is simulated in the full 12.096 kt TPC active volume. Simulation assumptions for light generation and light transport are described in Section 3.7.1. For each of the 720 PMTs, simulations take into account how the photon detection probabilities and the photon propagation times vary throughout the TPC active volume.

- The electronics response and the reconstruction of optical hits and optical clusters has been simulated. Simulation assumptions for light detection by the PMTs are also described in Section 3.7.1. Optical hits are the reconstructed optical signals on single PMT waveforms and are characterized by a hit time, amplitude, and charge. Optical hits must have an amplitude of at least 10 ADC counts above baseline. Optical clusters refer to a collection of PMT hits correlated in time and space. They are typically induced by the same underlying flash of scintillation light in LAr. The parameters of the clustering algorithm are discussed later in this section.

- The physics studies now also include radiological backgrounds. Simulating radiological backgrounds is critical in realistically optimizing the optical reconstruction parameters. The ra-

diological model includes several radio-isotopes throughout the LAr volume, with 1.01 Bq/kg of ^{39}Ar providing the most activity. In addition, an impinging neutron flux of $10^{-5}\,\mathrm{cm}^{-2}\mathrm{s}^{-1}$ is accounted for.

Expected PDS light yields in the ProtoDUNE-DP and DP FD module geometries are discussed in Section 3.7.2

3.9.1 Event t_0 Reconstruction

As discussed in Section 3.1, event t_0 reconstruction for non-beam events via the PDS is particularly important to fiducialize nucleon decay candidates in DUNE. Proton decay signal events with a $p \to K^+\bar{\nu}$ final state have been simulated with GENIE [44] throughout the DP TPC active volume, and their optical clusters were reconstructed using the full simulation and reconstruction chain. NDK events should deposit approximately 400 MeV visible energy in the LAr. The same reconstruction algorithm has also been applied to the simulated radiological backgrounds. In a first cluster reconstruction step, three parameters are optimized to group optical hits into separate clusters:

Maximum cluster duration: maximum time difference among all PMT hits in the cluster.

Maximum hit time distance: maximum time difference between successive PMT hits in the cluster. By definition, this quantity is smaller than, or equal to, the maximum cluster duration.

Maximum hit distance: maximum spatial distance between neighbouring PMT hits in the cluster.

For each chosen set of parameters (maximum cluster duration, maximum hit time distance, maximum hit distance), a threshold for minimum cluster charge (in PEs) is defined, so a fixed, and tolerable, radiological background rate above threshold and per 8 ms maximum drift time is obtained. The chosen parameters are those that maximize the efficiency of detecting a NDK cluster higher than this minimum cluster charge. For the PDS baseline design with half foils, the optimal values for the maximum cluster duration, maximum hit time distance and maximum hit distance were found to be 100 ns, 100 ns and 5.5 m, respectively. In other words, optical hits belonging to the same cluster are required to be nearly coincident in time, but only loosely correlated in space. As expected, it was also found that this optimization process yields a different result for a no foil PDS configuration, where light is more concentrated in space.

After clustering optical hits as described above, and without applying any threshold on cluster charge, several optical clusters per event are reconstructed. At this stage, any deposit resulting in at least one optical hit is reconstructed by the PDS, giving negligible NDK optical cluster inefficiency but very high radiological background cluster multiplicity per event.

In a second optimization step, we define the t_0 candidate clusters in the event as the ones fulfilling one additional condition: **cluster spatial position**.

Albeit much less accurate than the TPC response, the PDS response also provides some spatial

information about the event in the plane perpendicular to the drift direction. The position of the t_0 candidate cluster in the plane perpendicular to the drift must be within 1.5 m of the simulated NDK decay vertex[14]. Because radiological clusters are randomly distributed with respect to the NDK vertex, this position matching provides a strong background cluster suppression of about two orders of magnitude.

We define the **NDK t_0 reconstruction efficiency** as the efficiency to reconstruct at least one t_0 candidate cluster associated to the NDK energy deposit. As shown below, the cluster spatial position requirement causes some inefficiency for events farther from the PDS because of poorly reconstructed cluster spatial position in the plane perpendicular to the drift.

In general, several t_0 candidate clusters will be reconstructed per event, induced by the NDK signal, by radiological activity, and by PMT dark counts. If more than one choice exists, event t_0 information is associated to the t_0 candidate cluster of highest charge. For events where at least one t_0 candidate cluster exists, we define the **NDK t_0 reconstruction purity** as the probability for the highest charge t_0 candidate cluster in the event to be associated with the NDK signal. A purity value < 1 can be obtained if the highest charge t_0 candidate cluster is due to radiological activity. The choice of the t_0 candidate cluster with the highest charge is made to maximize purity because radiological clusters have, on average, fewer reconstructed PEs per cluster. As discussed in Section 3.1, we require a high purity to minimize t_0 reconstruction ambiguities.

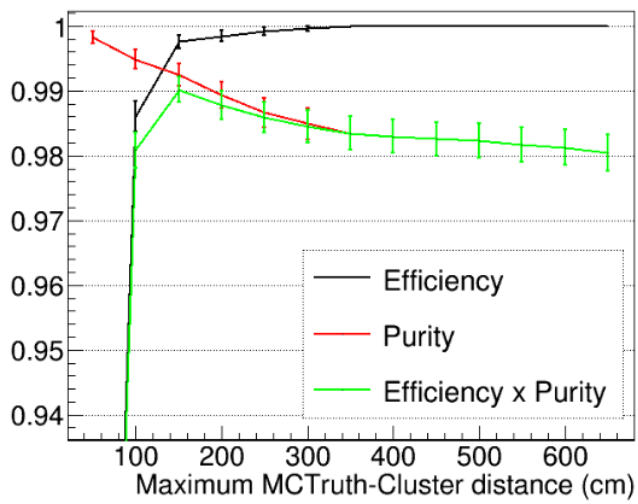

Figure 3.28: Efficiency, purity, and efficiency times purity for the t_0 candidate cluster to be correctly associated to the NDK energy deposit, as a function of the maximum 2D distance between the PDS-reconstructed position of the t_0 candidate cluster and the actual NDK vertex, in the plane perpendicular to drift. A maximum distance of 1.5 m optimizes the product of efficiency times purity.

Figure 3.28 illustrates how the NDK signal efficiency, purity, and efficiency×purity averaged over the entire TPC active volume vary as a function of the maximum 2D distance between the t_0 candidate cluster reconstructed position and the NDK vertex actual position in the plane perpen-

[14]The matching in position with the MC truth information is of course only possible in simulations. However, we expect the TPC imaging performance to be so superior to the PDS one that matching PDS position with MC truth position is essentially equivalent to matching PDS position with TPC reconstructed position.

dicular to drift. A maximum distance of 1.5 m optimizes the product of efficiency×purity. For this optimal distance, an average efficiency value of 99.8% and purity value of 99.2% are obtained.

Figure 3.29 shows how the NDK t_0 reconstruction efficiency and purity vary as a function of the nucleon decay vertex distance from the cathode plane for the optimal cluster reconstruction parameters described above. Two configurations are compared: the proposed baseline design with half foils, and a design with no foils along the FC. For the baseline design, both the efficiency and purity remain $> 90\%$ throughout the TPC active volume, satisfying the detector requirements laid out in Sec. 3.1.1. From Figure 3.17, a light yield of 1 PE/MeV is expected at the anode plane in the half foil simulation. Because of this, the PDS minimum light yield required at the anode position is also 1 PE/MeV (see Table 3.1).

On the other hand, for the no foil configuration, both efficiency and purity drop rapidly at large distances from the cathode. This is due to the marked reduction in the detected NDK light yield as the energy deposition occurs at increasingly larger distances from the cathode, see Figure 3.17. In this case, the efficiency (purity) remains $> 90\%$ only for distances up to 10 m (7 m) from the cathode. This large improvement in efficiently and accurately reconstructing event t_0 information for NDK events is the main, but not only, motivation to introduce reflector/WLS foils along the FC walls in the baseline design.

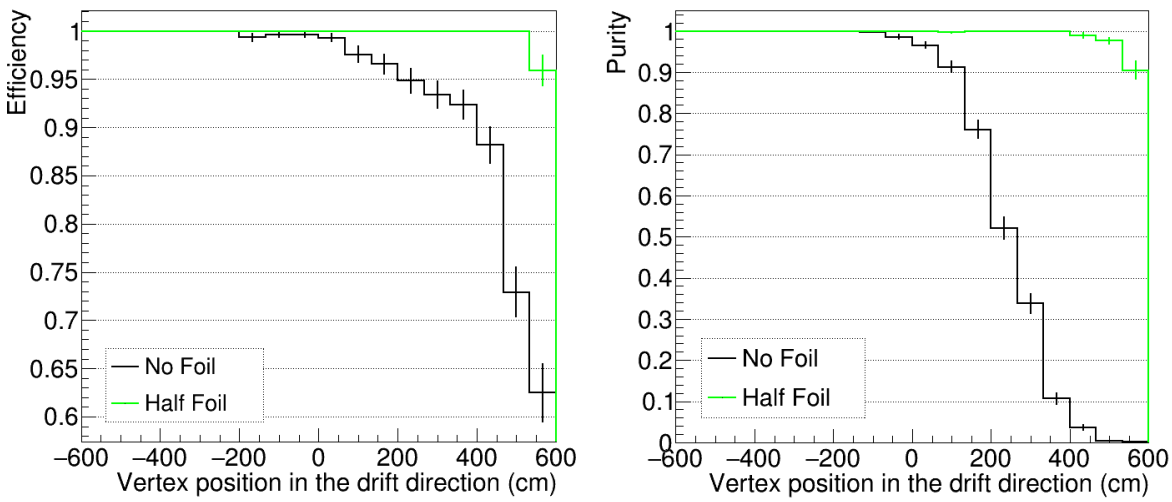

Figure 3.29: Nucleon decay t_0 reconstruction efficiency (left panel) and purity (right), defined in text, as a function of decay vertex distance from the cathode. Two PDS designs are compared: no foils and half foils (baseline). The anode plane is at a drift position of 600 cm, the cathode plane at a drift position of −600 cm, and PMT plane is at a drift position of −700 cm.

3.9.2 Supernova Burst Triggering

We have also studied how well the DP PDS triggers on an SNB occurring in our galactic neighbourhood. As described in Section 3.1, this is one of the primary goals of the PDS. To this end, SNB ν_e CC interactions have been generated with MARLEY [45] in our baseline PDS design with reflector/WLS panel assemblies installed in the top half of the FC. In DUNE, a real-time algorithm

should provide trigger primitives by searching for PMT hits and optical clusters, where the latter combine several hits together based on their time/spatial information. Compared to the NDK case, the reconstructed optical signals are much weaker because the typical deposited energies per SNB neutrino interaction are approximately 20 MeV. The online clustering process is similar to the offline cluster reconstruction discussed in Section 3.9.1, albeit with some differences related to the lack of trigger information and detailed event reconstruction at this stage:

- Real-time optical clusters must have a minimum hit multiplicity to suppress clusters induced by radiological activity or PMT dark counts. The higher the hit multiplicity, the lower the background cluster rate.

- PDS spatial information is only used to group hits into separate clusters, not to match PDS clusters with TPC tracks in the plane perpendicular to the drift as in Section 3.9.1.

- Real-time optical clusters must be continuously reconstructed, while in Section 3.9.1, only the 7.5 ms period preceding a charge-based trigger signal, corresponding to the maximum drift time, is considered.

In this case, the optimal real-time cluster reconstruction parameters, including a minimum hit multiplicity per cluster requirement, yield a 0.05 Hz radiological background cluster rate for an SNB ν_e CC signal cluster efficiency of 11.8 %. Once the optimal cluster parameters are found, the computation of the PDS-based SNB trigger efficiency as a function of SNB distance is performed as follows:

- First, the minimum number of reconstructed clusters required in a 2 s time window to issue a trigger is found[15]. The minimum cluster multiplicity is set by the requirement of one fake trigger per month at most (see Section 3.1) and by the radiological background cluster rate. The higher the background cluster rate, the higher the minimum cluster multiplicity must be to meet the <1/month fake trigger rate requirement. As mentioned above, the clustering optimization procedure yields a background cluster rate of 0.05 Hz or, on average, 0.1 clusters per 2 s window. For such a background rate level, a minimum cluster multiplicity of $\geq$3 per 2 s time window is required for a <1/month fake trigger rate.

- Second, and given the cluster parameters and minimum cluster multiplicity defined in the first step, the SNB triggering efficiency as a function of the number of SNB interactions is computed. For a 11.8 % average efficiency of reconstructing single SNB ν_e interactions with the PDS, and a minimum cluster multiplicity of 3 to issue a trigger, approximately $3/0.118 \simeq 25$ interactions must occur in the FD module and within 2 s to obtain a non-negligible trigger efficiency.

- Third, and finally, the SNB triggering efficiency as a function of SNB distance is obtained. We use the theoretical assumptions shown in Figure 3.30 to extract the number of SNB neutrino interactions in a 2 s time window and in one DP FD module as a function of SNB distance. The left panel of Figure 3.30 shows the time-integrated expected number of SNB neutrino interactions as a function of distance, while the right panel in Figure 3.30 shows

[15] A 2 s time window was found to be optimal and is assumed throughout this section.

the assumed time profile of the burst during the first 10 s. Several hundred SNB neutrino interactions are expected in one DP FD module for a 10 kpc distant SNB[16], and about half of them are expected within the first 2 s. Given our earlier estimate that about 25 interactions should be sufficient for a non-negligible trigger efficiency, clearly, the PDS should provide high SNB trigger efficiency for an SNB at a 10 kpc distance.

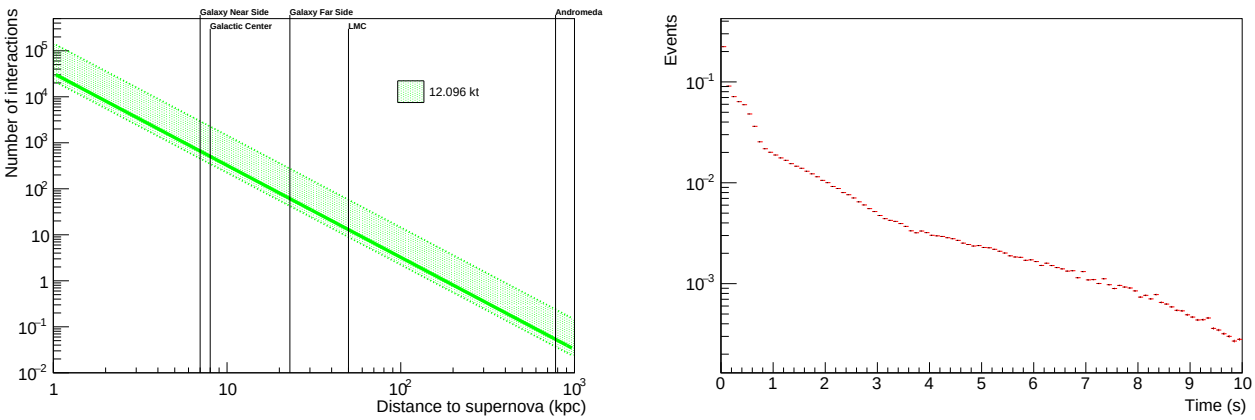

Figure 3.30: Left panel: expected number of SNB ν_e CC interactions in one 12.096 kt active mass DP module as a function of SNB distance. The different green lines indicate different SNB models. Right panel: expected time profile of the SNB.

The SNB triggering efficiency, computed following the procedure described above and as a function of SNB distance, is shown in Figure 3.31. The figure shows how the SNB triggering efficiency is affected by different choices in cluster reconstruction parameters. The best trigger efficiency found for the cluster parameters, yielding the lowest background cluster rate, is 0.05 Hz. In this case, a trigger efficiency in excess of 90% is obtained up to SNB distances of approximately 25 kpc. Therefore, the PDS should yield a highly efficient trigger for SNB occurring anywhere in the Milky Way.

Figure 3.32 shows how the SNB trigger efficiency of the baseline configuration with WLS reflector foils along the upper FC half compares with alternative choices, namely no foils and full foils. Our minimum SNB trigger efficiency requirement of 90% at 20 kpc (see Sec. 3.1.1) should be (barely) reachable even for the no foil configuration. In this case, the average light yield is expected to be about 5 PEs/MeV, see Table 3.2. For this reason, Table 3.1 quotes >5 PEs/MeV as the average light yield requirement. On the other hand, the results improve noticeably with increased foil coverage, as >90% trigger efficiency extends to approximately 25 and 36 kpc for the half foil and full foil configurations, respectively.

3.9.3 Event Energy Reconstruction

In addition to timing and triggering information, the PDS can also provide event energy information via the intensity of the reconstructed optical flashes. We focus in this section on beam

[16] It is customary to evaluate the performance of SNB detectors for a SNB distance of 10 kpc, as this is approximately the distance to the Galactic Center.

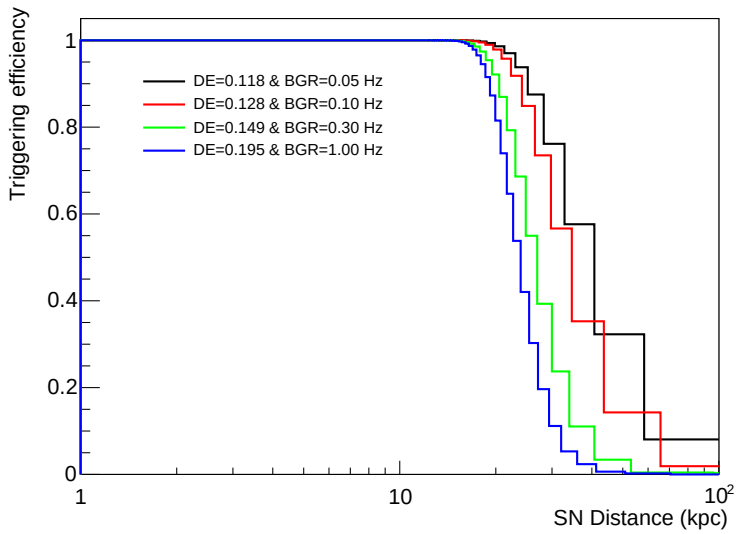

Figure 3.31: SNB triggering efficiency using DP PDS information as a function of SNB distance. Different curves indicate different choices of the optical cluster reconstruction parameters, resulting in different SNB ν_e signal detection efficiencies (DE) and radiological background rates (BGR).

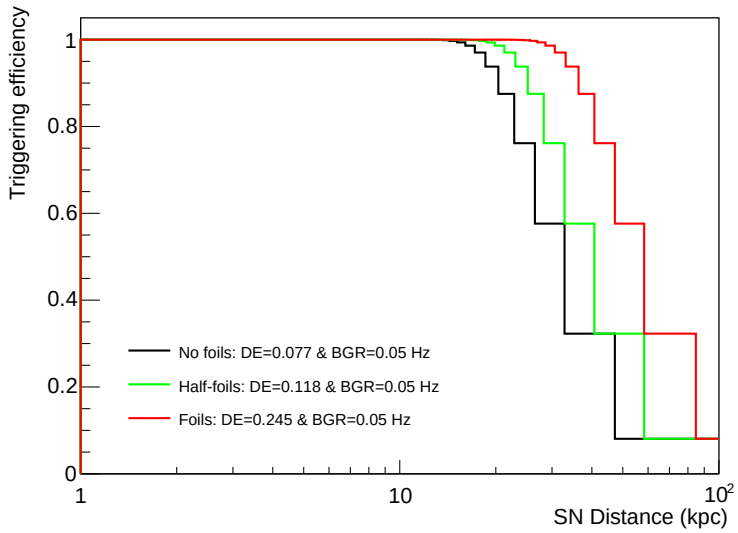

Figure 3.32: SNB triggering efficiency as a function of SNB distance for three different WLS foil configurations.

neutrino interactions generated via the GENIE event generator [44], as described in Section 3.1.1.

A first requirement for a competitive energy reconstruction performance with the PDS is that optical hit saturation effects are kept to a manageable level by the PDS and associated readout electronics. Figure 3.33 shows the expected average hit charge and average hit amplitude as a function of drift position of the neutrino interaction vertex for 3 GeV beam ν_e CC interactions. For each event, the average is computed by considering hit PDS channels only, that is, PMTs detecting a charge of at least 1 PE. The average hit charge per event is approximately 50 to 300 for 3 GeV beam ν_e CC interactions throughout the TPC active volume. The average charge is expressed in PEs, with the average amplitude in PEs per 4 ns time bin. This time bin width is comparable with the 6 ns timescale characteristic of the prompt scintillation light in LAr. For events near the cathode plane, about 300 PEs per hit channel are detected, corresponding to a maximum amplitude over 4 ns of about 50 PEs. The factor of 6 difference between average charge and average amplitude is because only 23 % of the scintillation light is prompt and (to a smaller extent) because of additional time smearing introduced by light propagation to the same PMT from different LAr voxels containing energy deposits. From these plots, we conclude that the PDS signal readout should withstand signal amplitudes of at least 100 PEs over 6 ns to mitigate saturation effects (see Table 3.1).

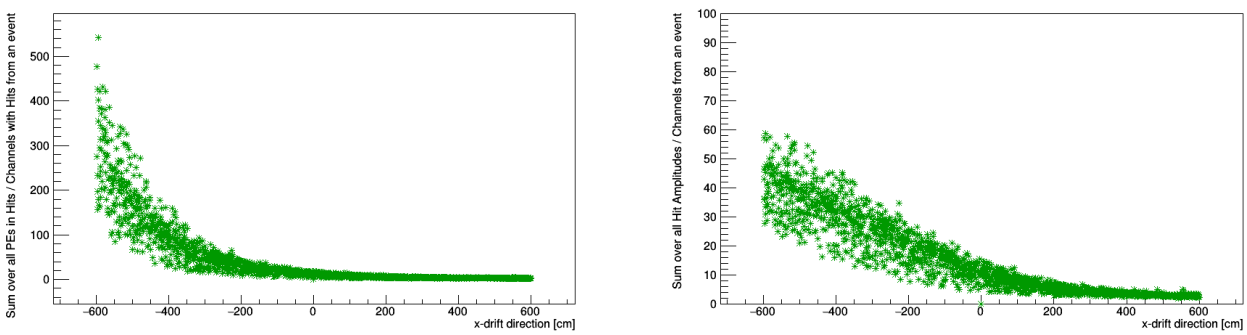

Figure 3.33: Expected average hit charge (left panel, in PEs) and average hit amplitude (right panel, in PEs per 4 ns time bin) as a function of event drift position for 3 GeV beam ν_e CC interactions. The scatter plots contain one entry per event, and the average is for hit PDS channels only.

The neutrino energy for the same 3 GeV beam ν_e CC interactions has been reconstructed using PDS information as follows:

$$E_{\text{reco}} = \frac{Q}{\varepsilon_{\text{PMT}} \cdot V_{PDS}(\vec{x}_{\text{int}}) \cdot Y} \tag{3.1}$$

where Q is the total charge (in PEs) of all PMT hits reconstructed in the event, ε_{PMT} is the PMT quantum efficiency, $V_{PDS}(\vec{x}_{\text{int}})$ is the PDS visibility at the neutrino interaction vertex $\vec{x}_{\text{int}}$, defined as the fraction of LAr scintillation photons that reach one of the PMT photo-cathode surfaces, $Y = 2.4 \times 10^4$ photons/MeV is the scintillation light yield, and E_{reco} is the resulting reconstructed energy. In Eq. 3.1, we include PMT dark counts in time coincidence with the beam, and we assume that TPC information will provide the neutrino interaction vertex information that is needed for the visibility estimate. The event energy reconstructed in this way is shown in the right panel of Fig. 3.34, for a sample of neutrino interactions occurring in the LAr fiducial volume. The distribution peaks at about 2.2 GeV, somewhat lower than the generated neutrino energy of 3 GeV. A gaussian fit to this distribution yields about a 20% resolution. This value meets the requirement described in Sec. 3.1.1, and confirms that the PDS should be able to provide energy

information that is competitive with the DUNE TPC. Figure 3.1.1 also shows, in the left panel, the true deposited energy E_{depo} in the LAr active volume for the same simulated events. This distribution shows how an ideal detector could reconstruct event energy, for beam neutrino events. From the comparison of E_{depo} and E_{reco}, we conclude that a significant portion of the bias and smearing seen in E_{reco} is already present at the E_{depo} level, and hence cannot be corrected for in a model-independent way. Figure 3.35 shows that E_{reco} and E_{depo} are highly correlated, as expected.

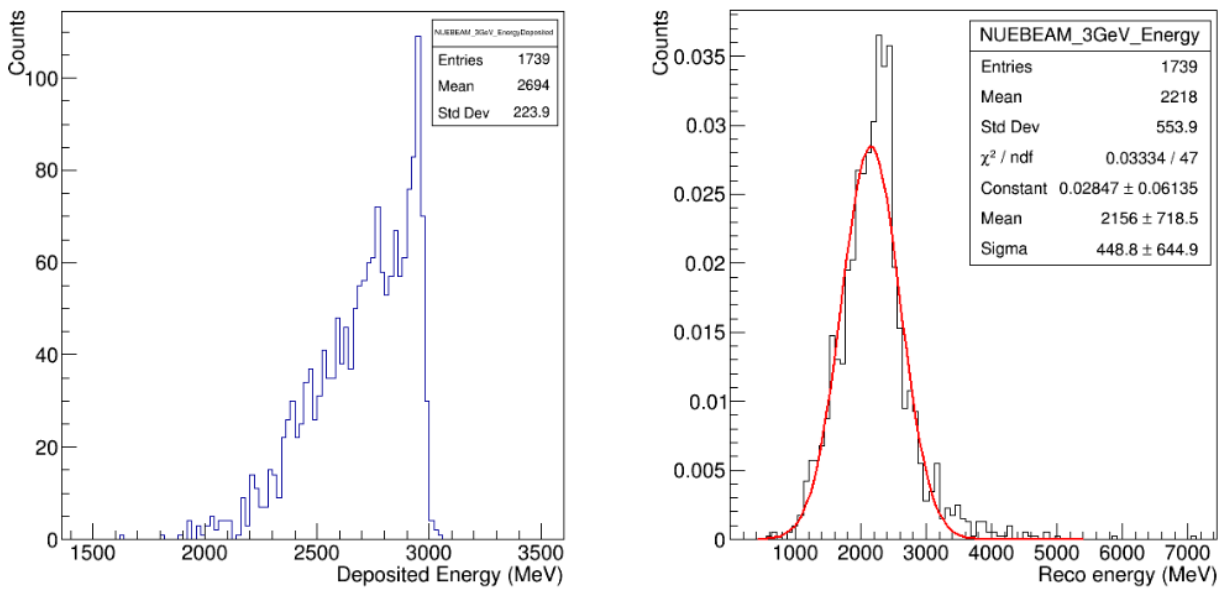

Figure 3.34: Expected deposited energy in LAr (left panel) and PDS-reconstructed energy (right panel) for 3 GeV beam ν_e CC interactions in the LAr fiducial volume. A gaussian fit is superimposed to the reconstructed energy distribution.

We expect to improve the energy resolution performance shown above in two ways:

Improved PDS design: the results shown above were obtained for the no WLS foil detector configuration. Studies for the baseline half foil configuration are ongoing. Because of the more uniform response of the baseline design, we expect that the energy resolution will improve.

Improved energy reconstruction algorithm: Eq. 3.1 assumes that all the energy is deposited at the neutrino vertex. In practice, events have a certain spatial extent and energy deposition pattern, which the TPC can accurately measure. A reconstruction algorithm that accounts for the event extent is expected to perform better, and is under development.

3.10 Quality Control and Quality Assurance

The quality assurance (QA) and quality control (QC) procedures for the DP PDS are based on our experience with the ProtoDUNE-DP. The PMTs of the DP PDS will go through a series of performance and functionality tests at various locations until commissioning. The mechanical

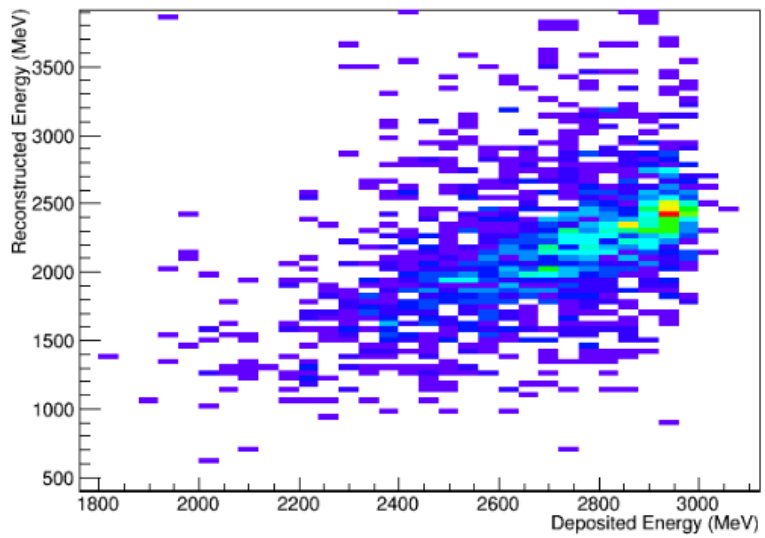

Figure 3.35: Correlation between PDS-reconstructed energy (vertical axis) and true deposited energy in LAr (horizontal axis) for 3 GeV beam ν_e CC interactions in the LAr fiducial volume.

assembly of the PMTs will go through mechanical tests, the high voltage cables will be tested for continuity and resistance, the high voltage/signal splitters will be tested for electronics integrity, and the calibration fibers will be tested for high quality transmission. Below are the details of the quality assurance and control procedures.

3.10.1 Quality Control During Production and Assembly

The QC performed at the different institutions, after receiving the PMTs from the manufacturer, include QC testing before accepting or returning the PMTs using established acceptance and rejection criteria. QC also includes checking the construction of the base boards, support structures, cables, HV/signal splitters, and light calibration units. QC also includes mechanical tests of the assembly and performance tests of the PMTs and electronics, both at room temperature and when necessary, at cryogenic temperatures. The institutes that perform these tests are referred to as production and assembly sites.

- The PMTs will be visually inspected as they are received from the manufacturer.

- The PMT support structure design is already validated by immersing its mounted PMT in cryogenic temperatures and at an over-pressure equivalent to a depth of 12 m in LAr. Design validation tests are carried out to confirm that the PMT base design fulfills the specifications at room and cryogenic temperatures. A cable with a safe high voltage (SHV) connector is soldered to each PMT base to facilitate the different base and PMT tests and the final PMT connection during the installation. The PMT bases are labeled (on the cable) to track them. After production of the PMT base boards, each is individually tested before connecting to the PMTs to verify that components are correctly mounted. Later they are cleaned and tested at maximum voltage in an argon gas environment to confirm that no sparks occur.

After mounting the bases on the PMTs, they are tested again at maximum voltage to confirm that no sparks occur due to poor soldering.

- All the light readout units (PMT + base + support) will be tested and characterized in liquid nitrogen to check performance at cryogenic temperature and to obtain a database with the most important parameters for each PMT (for example, gain versus voltage, dark counts). The PMT base number attached to each PMT will also be included in the database.

- The wrapping materials and techniques are studied with one fully assembled light readout unit. The handling, transportation, and installation scenarios are carefully studied, and the transportation box design is validated. The transport box and PMT wrapping must ensure complete darkness.

- The light output of the LEDs and fiber light transmission from the light calibration system will be measured with a power meter.

- The high voltage cables will be tested for continuity and for resistance.

- The high voltage/signal splitters will be tested for electronics integrity followed by performance tests with a reference PMT.

3.10.2 Quality Control at the Coating, Testing and Storage Facility

The PMTs will be transported to the CTSF, envisaged to be established near the experiment site. As the PMT boxes are received, they will be visually inspected to verify they were safely transported. The TPB coating of the PMT windows will be performed at the CTSF. The PMT windows will be cleaned before the coating is applied. The QC of the cleaning will be qualitative based on experience. The PMTs will then be placed in the evaporator, and the coating will be applied. The first few samples will undergo microscopic examination and surface uniformity tests, and the coating procedure will be validated. Subsequent production PMTs will be randomly sampled for basic coating QA.

Once the coating is finished, the PMTs will be packed in special underground transport assembly and placed inside the original transportation boxes. The PMTs, however, will not be placed in the cartons. They will have protective covers over the windows. Before being placed in the transportation assembly, the PMTs will undergo functionality tests individually. Once all the PMTs in a box are validated, the box will be closed and transported to the underground hall.

The CTSF is also the primary reception point for the other DP PDS equipment, including cables, fibers, light calibration systems, and HV/signal splitters. These boxes will be inspected for verify they were safely transported. Unless signs of damage to the transportation boxes are obvious, no QC inspection will be performed on the individual items. If damage is identified, the boxes will be opened and visual/functional QC tests will be performed. If damaged items can be repaired, that will be done at the CTSF. If the damage is not repairable, the items will be returned to the manufacturer or the production/assembly sites.

3.10.3 Quality Control at the Underground Areas

After transportation from the CTSF to SURF, the PMTs will be tested for proper functionality in a dedicated light-tight box in the clean room. During installation, the PMT database will be updated with the position of each PMT (identified by its serial number and base number) in the detector module. After installation, the full connection from the FE to the PMTs will be checked. The FE channel and splitter number connected to each PMT will be included in the PMT database.

The HV/signal cables and the calibration fibers will be transported to the cryostat roof long before the PMTs themselves. As they arrive, they will be checked for potential damage during transportation. These tests will include continuity tests for the HV/signal cables and qualitative transmission tests for the calibration fibers.

The last step of QC will be to test the entire system using the full readout chain (Section 3.12.4).

3.11 Interfaces

The PDS has several interfaces with other subsystems and the global DUNE systems. The interface documents related to DP PDS are given in Table 3.4. Only some of the basic interfaces are summarized below.

Table 3.4: DP PDS interface documents.

Interfacing System	Description	Linked Reference
DP electronics	Electronics racks, connectors	DocDB 6772 [13]
HV	FC, cathode, ground grid and PDS PMT and reflector/WLS panel assemblies installation sequence, possibility of individual ground grids on the PMT support structures	DocDB 6799 [3]
DAQ	Data format, trigger distribution	DocDB 6802 [46]
CISC	Layout of cryogenic instrumentation, slow control of the PDS power supplies and calibration system	DocDB 6781 [47]
DUNE Physics	Physics requirements	DocDB 7087 [48]
Software and Computing	Development of simulation, reconstruction, and analysis tools	DocDB 7114 [49]
Calibration	Global monitoring of PDS PMTs	DocDB 7060 [50]
Detector and Facilities Infrastructure	PMT supporting bases, cable trays, feedthrough flanges, access to conventional facilities, participation in the DUNE detector safety system (DDSS)	DocDB 6979 [51]
UIT	Transportation of the PDS components to and between underground areas, clean room activities, storage, and installation	DocDB 7006 [52]

- DP Electronics: The PDS shares the same FE electronics standard as the charge readout, which is μTCA-based [36]. The DP electronics will provide data in continuous streaming of all PDS channels over the 10 Gbit/s links. The number of photomultipliers to be read out is 720, to be distributed among 60 AMC cards (20 μTCA crates for the 20 PDS sectors, 36 readout channels in 3 AMC cards/crate). Readout racks for the sectors will be 6 m apart along the 60 m side and on both sides. Deeper understanding of PMT characteristic (e.g., saturation, recovery time, ringing, pre- and after-pulsing) will be provided by DP PDS. The type of connectors used at the FE input panel will be determined by the DP Electronics Consortium and will be implemented by DP PDS.

- HV: This interface includes the consideration of the distance between the cathode/ground grid and the PMT planes, the installation of the reflector/WLS panel assemblies on the inner surface of the FC and the possible implementation of the ground grid at the individual PMT level. The HV consortium and PDS consortium will be communicating to harmonize the underground installation.

- DAQ: The hardware interface uses mainly optical fibers. DP PDS provides trigger and data in continuous streaming; the interface also includes the DAQ software.

- CISC: The main interface points with the cryogenic instrumentation and slow controls (CISC) are the layout of the cryogenic instrumentation (e.g. purity monitors, temperature sensors and light emitting system for the cameras) and the PMT support structures and cabling, as well as the slow control of the PDS power supplies and calibration system. The PDS PMTs are part of 20 sectors with 36 PMTs each and will be controlled with 20 HV crates.

- DUNE Physics: DP PDS has interfaces with the overall physics requirements on energy and time as well as classification of events, decay modes, and neutrino flavors.

- Software and Computing: This interface involves developing the simulation, reconstruction, and analysis tools.

- Calibration: The PDS participates in the DUNE global calibration task force and will provide handles to allow global monitoring of PMT performance.

- Detector and Facilities (Long-Baseline Neutrino Facility (LBNF)) Infrastructure: The PDS PMT supporting base on the cryostat floor; cold cables and cable trays; and the feedthroughs are the major interfaces with the facility. The cable trays from the ceiling feedthrough flanges to the bottom of the cryostat in which the cables and calibration fibers are routed fall under the responsibility of the facility. Installing the PMTs and connecting the fibers and HV/signal cables to the PMTs fall under the responsibility of PDS. Other interfaces with the facility include access to conventional facilities and participation in the DDSS.

- UIT: This interface with the underground installation team (UIT) includes the transportation of PDS components to and between underground areas, clean room activities, storage, and coordination of the installation with the other teams. The details are described in Section 3.12.3.

3.12 Installation, Integration, and Commissioning

3.12.1 Transport and Handling

PMTs will be transported on a standard EUR pallet that is 1.2 m × 1 m. Figure 3.36 shows the largest capacity commercially available box. The box can hold 36 PMTs in three levels of 4 × 3 arrays. Individual PMTs will be placed in cartons with their bases, support structures, and short HV cables soldered to the bases at the production/assembly sites. For shipping to CTSF, 36 PMTs will then be placed in the transport boxes.

XL plastic palletbox - 1200 x 1000 mm - 3 runners - height variable

Double plastic palletbox with three runners lengthwise, height variable from 870 to 1340 mm.

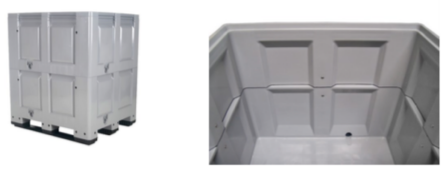

Capacity	1250 l
Weight	75 kg
Version	Double plastic palletbox with three runners lengthwise, height variable from 870 to 1340 mm.
Static stacked loading	Max. 3000 kg (5 on 1)
Colour	Grey (554), blue (623), red (215), green (447), orange (311), yellow (355)
Material	HDPE, foodstuffs-compatible
Base	Closed, reinforced
Side walls	Closed

Figure 3.36: An example transportation box to be used to transport items from remote sites to the CTSF and from CTSF to SURF.

Following the CTSF operations, the PMTs will be placed in a custom structure in 4 × 3 arrays. The structure will be assembled with metal and plastic parts so the entire structure, together with the PMTs, can be moved into the clean room underground. Three of these structures will be placed on top of each other inside the boxes with the crane. The individual cartons that held the PMTs will be recycled at the CTSF. The local movement of the transportation boxes in the CTSF can be done with compact warehouse forklifts. The CTSF will also be used as the storage area for the large PMT transportation boxes before they are sent to SURF. The boxes will be stored in single-shelf racks to the right and left of the entrance to the work area (Fig. 3.37). The first set of boxes will be placed on the floor and the second set will be on a shelf that is 1.5 m off the ground. This area can store the entire DP PDS PMT inventory of 720 PMTs in 20 boxes. The 80 spare PMTs can be placed in three boxes, which can be stored on the floor in the available space in the work area as the DP PDS CTSF operations are finished.

The large PDS boxes will be wrapped with plastic foil at the CTSF that will be opened in SASs

underground. After removing the plastic wrapping, the transport boxes, with their entire contents, will be moved into the cleanroom. The PDS boxes can be moved around the underground areas with a pallet jack. Each 4 × 3 structure will be removed from the transportation box and moved inside the cleanroom by the crane. The structure will go in the dark box for functionality tests of the 12 PMTs. The transportation boxes will be used for storage before installation. Empty boxes will be returned to CTSF. At most, three PDS boxes will be in the cleanroom at a time.

The 4 × 3 structure will be moved by crane into the cryostat and placed on the cryostat floor at a location convenient to the active installation area. The PMTs will then be installed one by one.

3.12.2 Coating, Testing and Storage Facility Operations

The CTSF will be 10 m × 8 m with a (12 ft) ceiling equipped with a gantry crane. The facility will be used to apply the TPB coating on the PMT windows, for QC of the PMTs, and for storage and preparation for transport to SURF. If the option of installing individual ground grids on the PMT support structures, which is under consideration by the DP PDS and HV consortia, is realized, this operation will also be performed at the CTSF. The layout of the CTSF is shown in Figure 3.37.

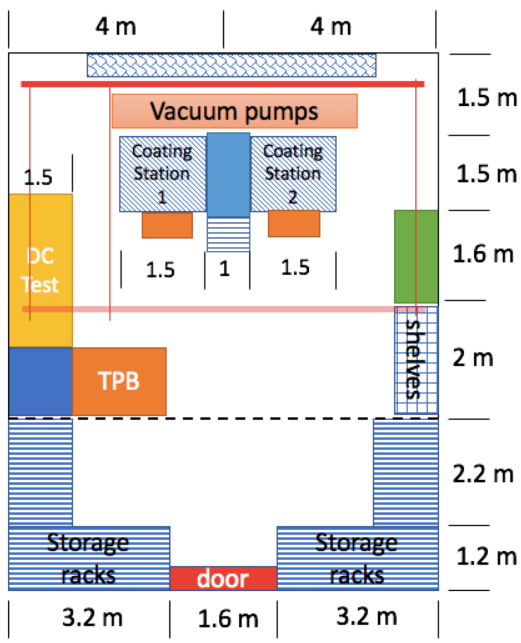

Figure 3.37: The layout of the CTSF.

Two coating stations will be 1.5 m × 1.5 m. Figure 3.38 shows pictures of a TPB coating station at the European Organization for Nuclear Research (CERN) thin film facility. Between the two coating stations, an elevated platform, accessible by stairs, will be placed. This platform will be used to reach the top of the evaporator (approximately 1.5 m high from the ground level) and inside the vessel. Cooling water, nitrogen, and electricity will be provided from the outlets placed along the 8 m wall (indicated with wavy lines in Figure 3.37). Vacuum pumps will be placed in the immediate vicinity of the evaporators. Control electronics will also be placed next to the evaporator chambers.

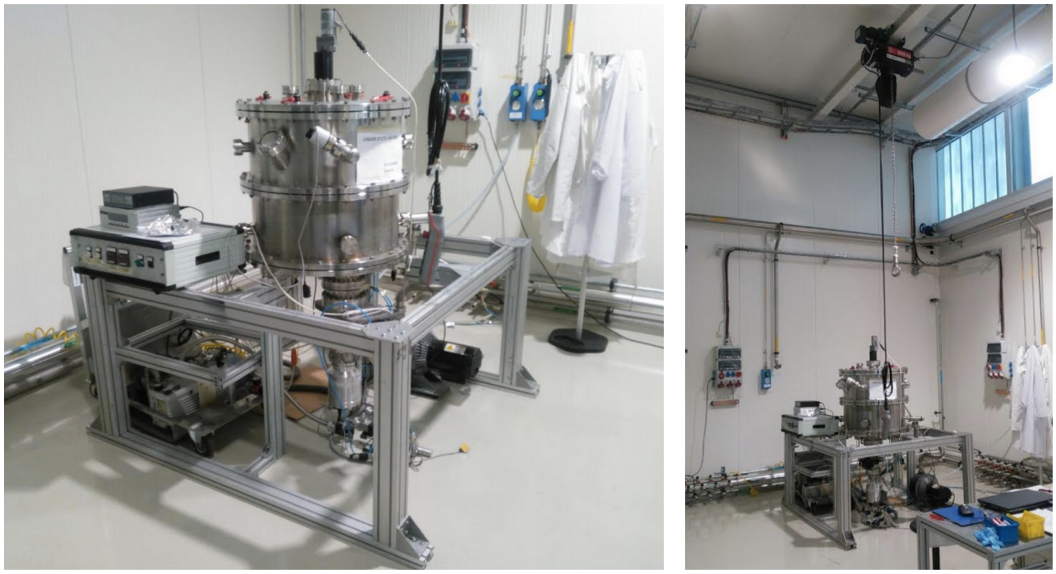

Figure 3.38: Pictures of a single TPB coating station (courtesy of Wil Vollenberg, CERN-TE Department).

The PMTs will be taken out of their individual cartons when they arrive at the CTSF. The PMTs will first be tested for basic functionality in their cartons to verify that they have been safely transported from the remote sites and will be kept in these boxes until the windows are coated. The PMT windows will be cleaned with acetone and isopropanol before the evaporation. This will be done in the flow device/fume hood shown as a green box along the 10 m wall in Fig. 3.37. The gantry crane (indicated with red bars in Fig. 3.37) can move parts between the coating stations and the work desks. It will be used to remove the vessel lid and support it while the PMT is installed for coating.

Following the evaporation procedure, an acrylic protective plates will be installed to cover the coated PMT windows. The PMTs will be tested again for basic functionality. They will then be attached to the 4×3 structure for transportation to SURF.

At the CTSF, the PMT windows will be coated at a rate of 4 PMTs/day or 20 PMTs/week and 80 PMTs/month. Given the installation rate of 120 PMTs/month, the CTSF operations should start before installation begins. CTSF has sufficient storage capacity for the entire PMT inventory of the PDS.

3.12.3 Underground Installation and Integration

The cryostat cable/fiber installation will precede the installation of the FC. The cables/fibers will be routed from the flanges to the bottom of the cryostat. The total cable/fiber mass (length) is approximately 50 kg (25 m) per sector with an average mass/length of 2 kg/m, where one sector comprises 36 PMTs (see Section 3.2.2). The free ends of the cables/fibers will be temporarily attached to the cryostat floor so they can be easily accessed during installation. The cable/fiber and tray installation will be done on both sides of the cryostat. At this stage, the HV cables

will be transported in a single box from the CTSF to SURF. At the same time, a separate box containing 120 calibration fiber + fiber bundle assemblies will be transported from the CTSF to SURF. The boxes will be transported to the cryostat roof so the cables/fibers can be hung through the feedthroughs for installation in the cable trays.

Once the plastic wrap is removed, the PDS PMT box and its entire contents can be moved to the clean room. The PMTs will undergo functionality tests inside the custom design dark box, which can cover the entire structure of 4×3 PMTs. The dark box will have a high voltage patch panel and allow consecutive tests of all 12 PMTs in one testing session without intervention. The test will be a simple check for healthy PMT operations. Once the operation of the PMTs is verified, the structure can be moved into the cryostat.

Inside the cryostat, the PMTs will be removed from the structure. The PMTs will be mounted on the membrane floor in the areas between the membrane corrugations using their support structures. The attachment is done using a stainless steel support base that can be point-glued to the membrane. The weight of the support and the PMT exceeds the buoyancy force of the system. Furthermore, these supports also ensure stability against possible lateral forces acting on the PMTs due to the liquid flow. Once the attachment is complete, the short HV cables will be connected to the cold HV cables with SHV barrel connectors. The calibration fibers will be routed and connected to the support structure. Once all the PMTs of a given PDS sector are installed, the cables and fibers will be fixed in their final positions.

The installation will be done at a rate of 30 PMTs/week. After installation, the empty PMT boxes and the transport structures will be taken back to CTSF.

Table 3.5 summarizes the quantities related to the DP PDS installation.

Table 3.5: Quantities related to the DP PDS installation.

Parameter	Value
Number of DP PDS sectors	20
Number of PMTs per sector	36
Number of calibration fibers per sector	6
Number of feedthrough flanges per sector	1
Total number of feedthrough flanges	20
Number of HV racks per sector	1
Frequency of transportations to SURF from CTSF	4 PDS boxes per month
Rate of installation	30 PMTs/week

The reflector/WLS panels will be assembled into a unit panel assembly on a dedicated table underground immediately prior to the installation following the procedure described in Section 3.4. They will be placed in a storage structure that can hold three regular and two extended reflector/WLS panel assemblies to be installed in one row of an FC super-module. The installation of the panel assemblies will be synchronized with the installation of the FC modules, which is described in Section 1.7.3 and depicted in Fig. 1.19. Once a row of the FC super-module is installed, the five reflector/WLS panel assemblies will be mounted on the FRP I-beams of the FC submodules, starting from one end of the row and progressing towards the other. Figure 3.39

depicts the installation sequence of a unit reflector/WLS panel. The sequence can be described as below:

1. Put the top two screws accessing the back side through the top liquid flow opening (Fig. 3.39 left).

2. Place two nuts in the closed holes of the long holding bar. Slide the long bar behind the panel to the level of the middle bar by holding it through the central liquid flow opening. Put the two middle bar screws and remove the long bar through the bottom liquid flow opening after sliding it all the way down (Fig. 3.39 center).

3. Put the bottom two screws accessing the back side through the bottom liquid flow opening (Fig. 3.39 right).

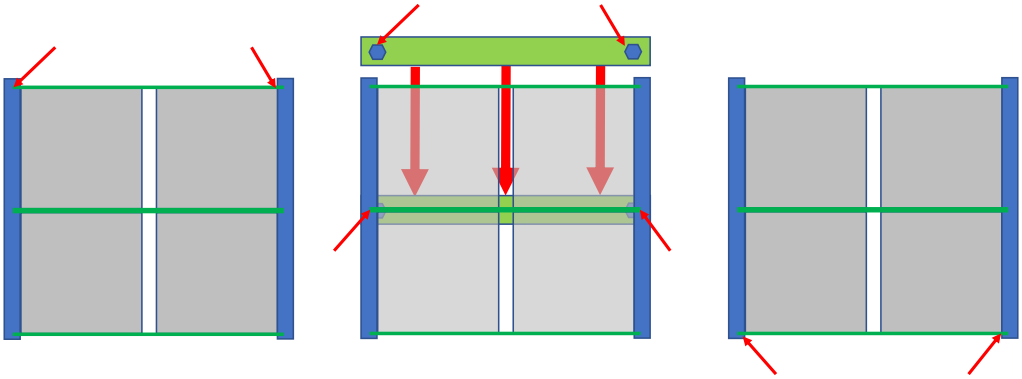

Figure 3.39: The schematic view of the installation sequence of a unit reflector/WLS panel assembly on the FC I-beams.

3.12.4 Commissioning

The commissioning of the PDS is performed in partitions. The size of a single partition will be mainly determined by the DAQ and the HV systems. The DAQ and HV partitions are commissioned, including the relevant control systems, before the PMTs are connected to these systems.

The exact availability of the cryostat as a sufficiently dark environment depends on the overall installation schedule. Once it is possible, the PMTs are powered up, and basic functionality and performance checks are carried out. These include pedestal data taking, i.e., recording event data with external periodic triggering, and tests with the calibration system where the data taking is triggered in synchronization with a light source, as described in Section 3.6.

Basic performance characteristics of the PMTs, e.g., the dark count rate and gain, will be validated with the commissioning tests. Issues related to installation can then be identified and eliminated. A commissioned sector becomes a part of the overall detector and can join the global calibration data taking and commissioning.

3.13 Risks

Table3.6 summarizes the risks associated with the DP PDS. Severity level assigned for each risk is indicated as L (low), M (medium), and H (high). Severity levels are split into three columns: probability for a risk to occur (P), and impact in terms of cost (C) and schedule (S) that the materialization of a risk would have. Below, we discuss these risks and mitigation plans for each risk item.

Table 3.6: Risks for DP-FD-PDS

ID	Risk	Mitigation	P	C	S
RT-DP-PDS-01	Insufficient light yield due to inefficient PDS design	Increase PMT photo-cathode coverage and/or WLS reflector foils coverage.	L	M	L
RT-DP-PDS-02	Poor coating quality for TPB coated surfaces and LAr contamination by TPB	Test quality and ageing properties of TPB coating techniques. Elaborate improved techniques if needed.	L	L	L
RT-DP-PDS-03	PMT channel loss due to faulty PMT base design	Optimize clustering algorithms. Improve PMT base design from analysis of possible failure modes in ProtoDUNE-DP.	L	L	L
RT-DP-PDS-04	Bad PMT channel due to faulty connection between HV/signal cable and PMT base	Optimize clustering algorithms. Connectivity tests in LN_2 prior to installation.	L	L	L
RT-DP-PDS-05	PMT signal saturation	Tuning of PMT gain. In worst case, redesign front-end to adjust to analog input range of ADC.	M	L	L
RT-DP-PDS-06	Excessive electronics noise to distinguish LAr scintillation light	Measurement of noise levels during commissioning prior to LAr filling. Modifications to grounding, shielding, or power distribution schemes.	M	L	L
RT-DP-PDS-07	Availability of resources for work at the installation/integration site less than planned	Move people temporarily from institutions involved in the PDS consortium to the integration/installation site.	L	L	L

RT-DP-PDS-08	Damage of PMTs during shipment to the experiment site	Special packaging to avoid possible PMT damage during shipment. Contingency of 10% spare PMTs.	L	L	L
RT-DP-PDS-09	Damage of optical fibers during installation	Fibers will be last DP-PDS item to be installed. Detailed documentation for all DP-PDS installation tasks.	L	L	L
RT-DP-PDS-10	Excessive exposure to ambient light of TPB coated surfaces, resulting in degraded performance	TPB coated surfaces temporarily covered until cryostat closing. Detailed installation procedure to minimize exposure to ambient light.	L	L	L
RT-DP-PDS-11	PMT implosion during LAr filling	No mitigation necessary, considering 7 bar pressure rating of PMTs and experience with same/similar PMTs in other large liquid detectors.	L	L	L
RT-DP-PDS-12	Insufficient light yield due to poor LAr purity	Procurement of LAr from the manufacturer will require less than 3 ppM in nitrogen.	M	L	L
RT-DP-PDS-13	PMT channel or PDS sector loss due to failures in HV/signal rack	Ease of maintenance outside cryostat and availability of spares for all components of at least one HV/signal rack.	L	L	L
RT-DP-PDS-14	Unstable response of the photon detection system over the lifetime of the experiment	Channel-level instabilities corrected via light calibration system. Detector-level instabilities corrected via cosmic-ray muon calibration data.	L	L	L
RT-DP-PDS-15	Bubbles from heat in PMTs or resistors cause HV discharge of the cathode	Verify the power density of the PMT bases are within specifications. Monitor and interlock PMT power supply currents.	L	L	L
RT-DP-PDS-16	Reflector/WLS panel assemblies together with the FC walls can swing in the fluid flow	Allow appropriate open areas within/between reflector/WLS panel assemblies to minimize drag.	L	L	L

3.13.1 Design and Construction Risks

- Because of the long drift distance and the position of the cathode and ground grid on top of the PMTs, the number of photons detected by the PMTs might not be sufficient at some geometrical acceptances (RT-DP-PDS-01). This is estimated as low-probability risk, given that the current PDS design has been optimized based on detailed simulations. The PDS baseline design includes WLS reflector foils precisely to address the risk of insufficient light levels, see Sec. 3.7. The detailed understanding of the light levels observed in the WA105 DP demonstrator and particularly in ProtoDUNE-DP will further mitigate this risk. The DUNE FD PDS design is essentially a large-scale replica of the recently installed ProtoDUNE-DP PDS. The most notable exception is the WLS reflector foils, that is considered to be tested in a ProtoDUNE-DP PDS upgrade. The largest variation in light yield occurs along the drift direction, where the extrapolation from ProtoDUNE-DP size to the DUNE FD module size is only a factor of two. If higher PDS detection efficiency turns out to be necessary, the number of PMTs may be increased and/or the surface area of WLS reflector foils may be increased.

- Past experience shows that the TPB coating might not be sufficiently stable (RT-DP-PDS-02). TPB emanation from coated surfaces (PMT photo-cathodes and WLS reflector foils) into the bulk LAr may cause WLS behaviour of the contaminated LAr bulk, or create a loss in optical performance of the coatings over time. This is estimated as low-probability risk. Certain coating techniques have shown to emanate TPB up to tens of parts per billion into argon by mass [53], although such impurity levels are not expected to be problematic. In addition, other LAr experiments using TPB coatings, most notably DarkSide-50 [54] and DEAP-3600 [55], have already shown percent-level stability in PDS light yields over timescales of 1–2 years. Nevertheless, different coating techniques vary greatly in terms of coating quality and stability. As risk mitigation measure, we plan to test the quality and ageing properties of the exact coating procedure to be followed for the PMT photo-cathodes and WLS reflector foils in ProtoDUNE-DP and in dedicated R&D setups. We will elaborate improved coating techniques if needed.

- An inadequate PMT base design may result in dead PMT channels during the long lifetime of the experiment (RT-DP-PDS-03). Such channel losses could not be recovered. This risk is estimated as low-probability. On the one hand, the loss of single PMT channels is expected to have a minimal impact on detector performance. Current PMT clustering algorithms (see Sec. 3.9) already allow for non-responsive PMTs along one row or column within one optical cluster. On the other hand, the PMT base design is a mature and simple design already tested in the WA105 DP demonstrator and to be tested in ProtoDUNE-DP. ProtoDUNE-DP operations will provide additional risk mitigation. If ProtoDUNE-DP experience with PMT bases proves to be unsatisfactory, design modifications will be introduced and tested.

- PMT cables are soldered to the PMT base and tested before installation. If the soldering is poorly done, some channels could show a bad waveform or no signal at all (RT-DP-PDS-04). Such noisy or dead channels could not be repaired. This risk is estimated as low-probability. On the one hand, and as discussed above, the loss of single PMT channels is expected to have a minimal impact on detector performance. On the other hand, the PMT with final

base plus soldered cable will be tested in LN_2 during the PMT characterization tests, see Sec. 3.3.1. In addition, several tests will be done in the base before the PMTs are installed: impedance, HV tests in gas Ar to avoid sparks, and full test of the PMT to verify signals are correct.

- PMT signal saturation at the front-end input (RT-DP-PDS-05) may occur as a result of operation at a higher-than-anticipated PMT gain, for example to compensate for a poor signal-to-noise ratio. PMT signals may also saturate because of an incorrect signal amplitude estimate. This risk is estimated to be medium-probability, also considering the highly non-uniform PDS spatial response. PMT signal saturation would have minimal impact on PDS t_0 reconstruction and triggering capabilities. It would have more impact on PDS energy reconstruction capabilities, although some amount of saturation can be tolerated also in this case (see Sec. 3.9). To mitigate this risk, we will avoid operating the PMTs at very high voltages. A balance between gain and saturation will be chosen.

- Excessive noise on PMT waveforms could appear because of poor grounding design, insufficient cable shielding or noisy power distribution (RT-DP-PDS-06). The risk is estimated as medium-probability. This problem could be detected during PDS commissioning. Doing so prior to LAr filling is essential, in case necessary modifications to grounding, shielding, or power distribution schemes affect components inside the cryostat.

3.13.2 Risks During Installation

- Availability of resources for work at the installation/integration site may be less than planned (RT-DP-PDS-07). This risk is estimated to be low-probability. The FD construction cost estimate assumes that qualified local labor can be identified for certain activities. The cost will increase if external labor is required. Labor costs might need to increase to attract qualified candidates. Labor resources from laboratories may need to be housed and used. We will ensure that sufficient funding is available to move people temporarily from institutions involved in the PDS consortium to the integration/installation site.

- If PMTs are not packaged properly, they could be damaged during shipment (RT-DP-PDS-08). In this case, the PMT cannot be used in the detector. This risk is estimated to be low-probability. We will use special packaging to avoid possible damage to the PMTs during shipment. In any case, we will have a 10% contingency spare PMTs.

- Fibers are fragile and could be broken during installation because of the high number of fibers in the detector (RT-DP-PDS-09). This risk is estimated to be low-probability. Personnel in charge of assembling the different parts of the detector must take special care during fiber installation.

- TPB coated surfaces (PMT photo-cathodes and WLS reflector foils) are sensitive to ultra-violet light exposure, which may cause degraded optical performance (RT-DP-PDS-10), see for example [56]. This risk is estimated to be low-probability. TPB coated surfaces will be covered with plastic bags or filters to avoid photo-degradation until closing of the cryostat.

The installation procedure for PMTs and WLS reflector foils will be defined in great detail, to minimize exposure to ambient light.

3.13.3 Risks During Commissioning

- Filling the detector with LAr could become a critical issue in the occurrence of a PMT implosion (RT-DP-PDS-11). If this happens, a chain reaction may develop, as in the Super-Kamkionande detector accident of 2001, destroying several other PMTs. If a PMT implosion occurs, the detector must be emptied, and the PMTs would have to be reinforced or removed. This risk is estimated to be low-probability. The Hamamatsu R5912 PMTs are rated for 7 bar pressure and the hydrostatic pressure on the cryostat floor will be about 2 bar. Similar 8-inch tubes, with same pressure rating, have been successfully used in other large detectors, such as MiniBooNE, SNO, ICARUS T600 and DEAP-3600, and in similar pressure conditions. In addition, a computational model to calculate the shock wave pressure resulting from tube implosion was developed for the MiniBooNE experiment, based upon the stored energy in an evacuated tube at a given depth [57]. It should be noted that the energy stored in an 8 inch PMT is over an order of magnitude less than in a 20 inch Super-K PMT. That study indicated a large safety factor against a chain reaction of PMT implosions, and for the more densely packed MiniBooNE PMTs.

3.13.4 Risks During Operation

- A high level of LAr contamination may result in an unacceptably short absorption length for argon scintillation light, thus in an unacceptably low detected light yield despite a satisfactory PDS design (RT-DP-PDS-12). This risk is estimated as medium-probability. A particularly harmful contaminant, as far as light detection is concerned, is nitrogen. The simulation studies presented in this chapter assume an argon scintillation light absorption length of 20 m, corresponding to about 3 ppm of N_2 impurity concentration. Such argon purity specification has already been achieved in large liquid argon time-projection chamber (LArTPC) detectors.

- The HV/signal racks will contain the HV crates, HV/signal splitters, the μTCA crates for the front-end electronics, and the calibration LED driver and the associated electronics for 36 PMTs. Failure in some of these components may result in failure of a single PMT channel or of an entire sector of 36 PMTs (RT-DP-PDS-13). This risk is estimated as low-probability. The loss of an entire PMT sector would have a major impact on detector performance. However, all of these components are located outside the cryostat and are easily replaceable. Spares will be available for all components of at least one HV/signal rack.

- The PDS response may vary over time (RT-DP-PDS-14) as a result of a variety of causes, such as time variations in the LAr purity, in the quality of TPB coatings, or in the PMT gains. This risk is estimated as low-probability. The quantum efficiency of the TPB-coated PMTs and their gain will be continuously monitored using the light calibration system (see Sec. 3.6). Once such channel-level time variations are corrected for, possible global changes

in LAr purity or in WLS reflector foils optical response will be addressed using cosmic-ray muon calibration data.

- If the PMT bases have overheating areas, bubbles might form which may then cause HV discharge of the cathode (RT-DP-PDS-15). This risk is estimated as low-probability. The power density of the PMT bases will be validated to be within the specifications during the production stage. ProtoDUNE-DP operations will be monitored closely. A global interlock/alarm mechanism will exist to signal possible discharges. In addition, a large area of the cathode consists of high resistance rods, delaying the energy release.

- The reflector/WLS panels mounted on the inner side of the FC walls might block the LAr convective flow and cause movement of FC - reflector/WLS panel assemblies (RT-DP-PDS-16). This risk is estimated as low-probability. A design that allows appropriate open areas within/between reflector/WLS panel assemblies to minimize drag is developed. The design will be validated with computational fluid dynamics (CFD) simulations.

3.14 Safety

DP photon detector (PD) Consortium will observe and comply with the institutional and national safety regulations of all of its production/assembly sites. The relevant safety documents for these sites will be reviewed by the consortium, and the regulations will be implemented by those responsible for local operations.

The production/assembly site is where high voltage cables, high voltage splitter boxes, calibration fibers, and the PMT mechanics will be prepared for final installation or assembly. The PMTs will be received, and the bases and mounting structures will be connected to the PMTs. The output of the production/assembly procedure will be the PMTs in their final mechanical and electronic structure. The assembly procedure requires several steps followed by specific quality control tests. The main safety risks during production are excessive heat from electrical/mechanical processing, chemicals for cleaning components, electrocution, and to some extent, heavy lifting and tripping hazards. Dedicated handling, cleaning, and equipment procedures will be developed by the production site host institution. The main safety risks during assembly are mechanical hazards such as sharp edges, heavy tools, and small parts. Procedures for using safety equipment like safety goggles, gloves, and safety shoes will be developed by representatives of the production/assembly site institution. Delicate material handling and transportation instructions will also be developed by the institution. These instructions will be incorporated into the assembled structure for any downstream operation site.

The testing locations at the CTSF and underground cleanroom will be responsible for the QC of the assembled PMT structure. These stations will also be responsible for testing the HV cables, HV splitters, and the calibration fibers. The previously developed handling instructions will be respected during the testing procedures. Possible safety concerns are electrocution and heavy lifting. The functional tests of the PMTs will involve powering up the PMTs for a predefined period. The testing procedures and the relevant safety regulations will be developed for and

incorporated into all the future PMT tests.

The production/assembly sites and the CTSF will also serve as transportation sites. The PMTs will be packed for transportation to the CTSF and SURF. The contents of the transportation boxes will be individual cartons for the PMTs with their bases, mounting assemblies, and short cables, placed into larger plastic pallet boxes in $4 \times 3 \times 3$ arrays for transportation from the production/assembly sites to the CTSF. Three stacked custom design structures that can hold an array of 4×3 PMTs will serve to transport PMTs from the CTSF to SURF. At this stage, the main safety concern is heavy lifting while at the same time obeying the delicate detector handling procedures. Personnel to move the 36-PMT plastic pallet boxes both indoors and outside for truck loading will have special training. The loading/unloading procedures for the PMT transportation boxes will be used at the production/assembly sites, CTSF, and the ground and underground stations of the experiment site. Similar procedures will be developed for transporting the HV cables and splitters and calibration fibers.

The TPB coating of the PMT windows will be done at the CTSF. The PMTs will be placed on shelves before they are removed from the transportation boxes, the windows will be cleaned, and TPB evaporation will be done before the PMTs are stored on shelves after the coating. The PMTs will then go through functional testing and placed in their transportation assembly to be taken to the underground hall. The main safety risks at the CTSF are electrocution, exposure to excessive heat and chemicals, and heavy lifting. Workplace safety regulations will be developed for the CTSF. This will include general electrical and mechanical safety rules. The gantry crane operator must have the necessary training. Transporting the PMT boxes in the CTSF must follow the general safety regulations.

The underground operation and installation safety rules will follow general facility rules. The common risks at the underground clean rooms, cryostat roof, and inside the cryostat are working in confined spaces and oxygen deficiency hazard. The DP PDS specific risks include electrocution for pre-installation testing, heavy lifting, and tripping.

Safety is the highest priority at all stages of DP PDS operations. The safety procedures are developed by the particular institutions involved in specific operations and are discussed and approved by the consortium. The guidelines and procedures for handling and transportation of the DP PDS materials will be made part of the CTSF and underground facility safety regulations.

3.15 Project Management

The DP PD consortium was formed in 2017; it comprises eleven institutions from France, Peru, Spain, UK, and USA. The charge of the DP PD consortium is to plan and execute the construction, installation, and commissioning of the DP PDS.

3.15.1 Consortium Organization

The current DP PD consortium leader is from CIEMAT (Spain) and the technical lead is from LAPP (France). They are members of the DUNE technical board and represent the consortium in the overall DUNE collaboration. The consortium leader is responsible for the subsystem deliverables and for effectively managing the consortium. The technical lead acts as the overall project manager and is the interface to the international project office; he is responsible for monitoring and reporting on progress on the agreed schedule and for interface documentation.

The institutions participating in the consortium are responsible for the design and/or construction of a particular subsystem. The national groups within the consortium plan to approach relevant funding agencies with a specific construction-phase proposal to obtain a likely funding line in 2019. The DP PD consortium is open to any new institution willing to join the current effort.

The current institutions participating in the DP PD consortium are listed in Table 3.7.

Table 3.7: Institutions participating in the DP PDS consortium.

Institution	Country
LAPP	France
PUCP	Peru
IFAE	Spain
CIEMAT	Spain
IFIC	Spain
UCL	United KIngdom
Argonne National Laboratory	USA
Duke University	USA
University of Iowa	USA
SDSMT	USA
University of Texas at Arlington	USA

The DP PD consortium is divided into four working groups: photosensors and electronics; calibration system; mechanics and integration; and simulation and physics. The corresponding current Working Group convener institutions are

- WG1: Photosensors and Electronics - CIEMAT,
- WG2: Calibration System - CIEMAT,
- WG3: Mechanics and Integration - University of Iowa
- WG4: Simulation and Physics - Duke University, IFIC, LAPP.

3.15.2 Planning Assumptions

The baseline design of the DP PDS is a complex optimization based on the results from and experience with the first tonne scale dual phase LAr TPC demonstrator (WA105 DP demonstrator), critical evaluation of the design and construction of WA105 DP demonstrator and ProtoDUNE-DP, physics objectives of the DUNE experiment, and the detailed simulation studies of DUNE DP as well as WA105 DP demonstrator and ProtoDUNE-DP.

The previous design and construction of the DP modules have enabled us to critically evaluate several scenarios and develop the DUNE PDS design optimized for maximum physics performance; simple construction, transportation, handling, and installation; and easy and robust operation.

Simulations are effectively used in designing and optimizing the DP PD system to meet the physics requirements:

- light collection efficiency,
- number of channels,
- photosensor requirements,
- dynamic range of readout electronics and timing resolution, and
- trigger strategy on non-beam events.

Although no major design modifications are foreseen, the ProtoDUNE-DP operations will be closely monitored to fine-tune the DUNE DP design.

3.15.3 Work Breakdown Structure and Institutional Responsibilities

The DP PD consortium has developed a detailed breakdown of deliverables and responsibilities DocDB 5606 [58] included in the overall DUNE collaboration work breakdown structure (WBS) DocDB 5594 [23] coordinated by the international project office. The main deliverables are divided into seven topics:

1. Management DP PDS (includes milestones and review dates),
2. Physics and simulations,
3. Design, engineering, R&D, and validation tests,
4. Production set up (includes tooling),
5. Production (includes component production, assembly, testing, and QC),

6. Integration (contributions to activities at global integration facility), and

7. Installation (contributions to activities at SURF).

3.15.4 High Level Schedule

The main high-level milestones of the DP PDS and the dates by which they will be accomplished are summarized in Table 3.8.

Table 3.8: DP PD Consortium Schedule

Milestone	Date (Month YYYY)
Start of ProtoDUNE-SP-II installation	March 2021
Start of ProtoDUNE-DP-II installation	March 2022
South Dakota Logistics Warehouse available	April 2022
Beneficial occupancy of cavern 1 and central utility cavern (CUC)	October 2022
CUC counting room accessible	April 2023
Top of detector module #1 cryostat accessible	January 2024
PMT procurement procedure and production	June 2024
PMT base design and manufacturing	June 2024
PMT support structure production and assembly	July 2024
Start of detector module #1 TPC installation	August 2024
End of detector module #1 TPC installation	May 2025
Top of detector module #2 accessible	January 2025
PMT characterization	April 2025
Fibers, light source tests and procurement	April 2025
Splitter production and tests	June 2025
TPB coating of the PMTs	July 2025
TPB coating of the reflector/WLS panels	July 2025
Start of detector module #2 TPC installation	August 2025
PMT cable and fiber routing in cryostat from flange to bottom	October 2025
PMT testing, installation in cryostat and cabling	April 2026
PMT support installation on the membrane	April 2026
Splitter installation	April 2026
Fiber calibration system installation	April 2026
End of detector module #2 TPC installation	May 2026

3.15.5 High Level Cost of Baseline Design

An initial cost estimate of the PDS for one 10 kt DUNE DP module was developed and presented in Table 3.9. This is based on ProtoDUNE-DP costs.

Table 3.9: DP PDS Cost Summary (TO BE COMPLETED)

Cost Item	M&S (k$ US)	Labor Hours
Project Management		
Physics and Simulations		
Design, Engineering and R&D		
Photosensors		
Mechanics		
Electronics, Cables and HV		
Calibration System		
Integration and Installation		
Production Setup		
Photosensors		
Mechanics		
Electronics, Cables and HV		
Calibration System		
Integration and Installation		
Production		
Photosensors		
Mechanics		
Electronics, Cables and HV		
Calibration System		
Integration and Installation		
DUNE FD Integration & Installation		

3.16 Appendix - Alternatives

3.16.1 Individual Ground Grids

In collaboration with the HV consortium, the installation of individual ground grids for each PMT in place of the ground grid table structure is under consideration. Since the individual ground grid cages will potentially have thinner wires and will be closer to the PMT windows, generating a smaller shadow, they should increase the acceptance of the PMTs.

The feasibility of the design in operation under DUNE DP conditions will be studied by the HV consortium. The design of the individual grids will be developed as a common effort of the two consortia engineering teams. The HV consortium will produce the grids. The grids will be installed at the CTSF by DP PD consortium. The PMTs will be installed with their individual grid cages by DP PD consortium.

3.16.2 Calibration System Alternatives

Alternatives to the baseline design of the calibration system described in Section 3.6 will be pursued with R&D measurements to make the system more effective, reduce the cost, and mitigate issues related to scaling to the DUNE DP size. These alternatives include reducing the number of fibers, studying other options for the reference sensor, and increasing the input light if necessary. To reduce the number of fibers, light diffusers can be used, so that one fiber can illuminate at least four PMTs. For instance, a diffuser could be placed at the ground grid, or in the case of individual ground grids, on the side walls. With the same aim of reducing the total number of fibers, an alternative calibration system with two fibers placed at the top of the field cage is being tested in ProtoDUNE-DP, so that one fiber can illuminate several PMTs. Other than the diffusers and fiber placement, considered alternatives are related to the external system and can be implemented with minimal interference with other subsystems.

Chapter 4

Cryogenics Instrumentation and Slow Control

4.1 Introduction

The cryogenic instrumentation and slow controls (CISC) consortium provides comprehensive monitoring for all detector components and for liquid and gaseous argon quality and behavior as well as a control system for many detector components. The dual-phase (DP) far detector (FD) uses the same control system as the SP module, as well as all SP cryogenic instrumentation. It also includes dedicated instrumentation for monitoring temperature and pressure in the gas phase. The gaseous argon instrumentation includes pressure meters and a vertical array of thermometers. A detailed description of instrumentation used in the SP module can be found in the corresponding chapter of Volume 3 of this technical design report (TDR).

The consortium responsibilities are split into two main branches: cryogenics instrumentation and slow controls (see Figure 4.1).

Each element of CISC contributes to the DUNE physics program primarily by maintaining high detector live time. As described in Volume 2 of this TDR, neutrino charge-parity symmetry violation (CPV) and resolution of the neutrino mass hierarchy over the full range of possible neutrino oscillation parameters will require at least a decade of running the FD. Similar requirements apply to searches for nucleon decay and supernova neutrino burst (SNB) events from within our galaxy. Throughout this long run time, the interior of any DUNE cryostat remains completely inaccessible. Repairs cannot be made to any damaged components within the TPC structure; hence, environmental conditions that present risks must be detected and reported quickly and reliably.

Detector damage risks peak during the initial fill of a module with LAr because temperature gradients take on their highest values during this phase. For example, thermal contractions outside of the range of design expectations could result in broken extraction grid wires or poor connections at the cathode high voltage (HV) feedthrough point that could lead to unstable E fields. Additional

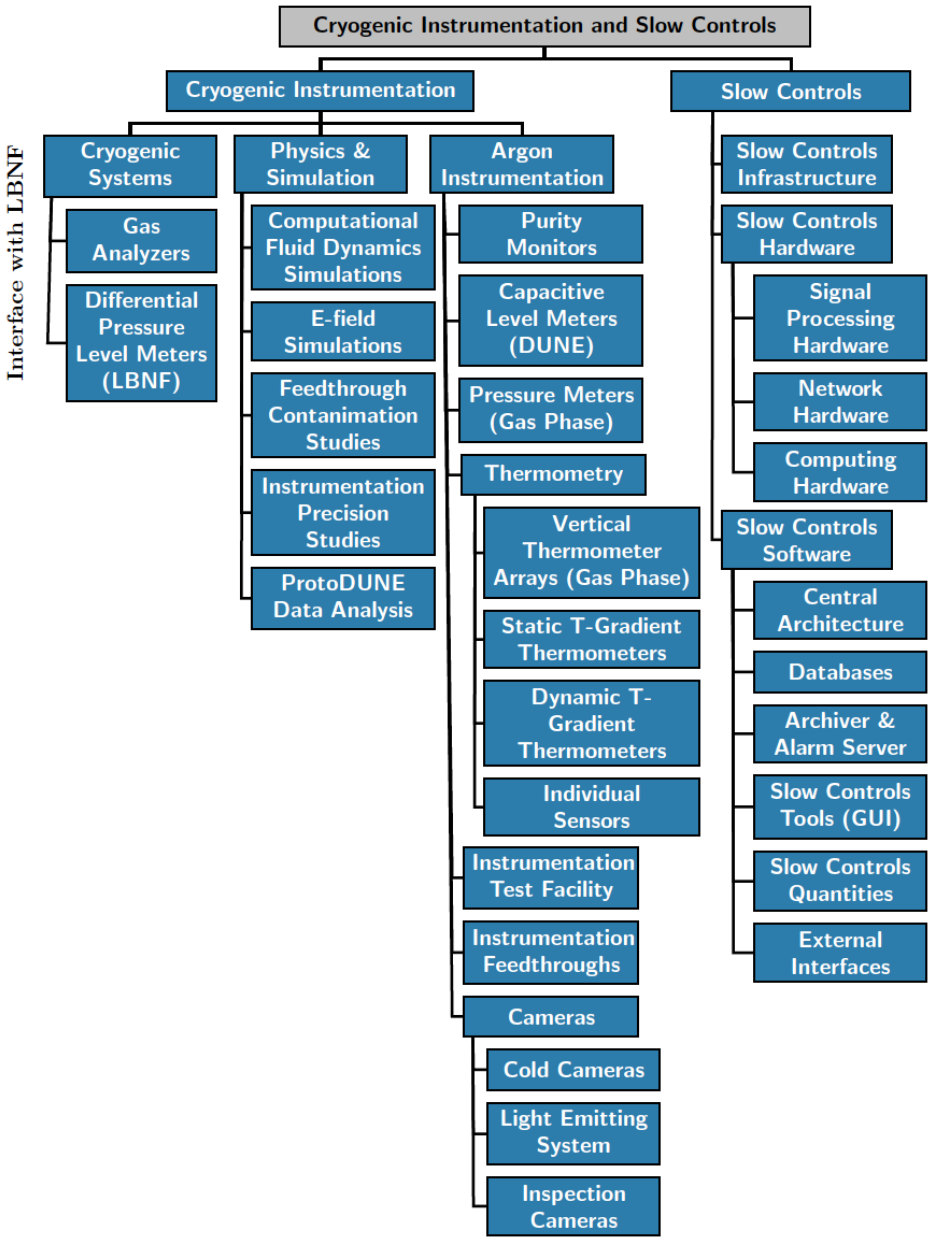

Figure 4.1: CISC subsystem chart.

care is needed to monitor the gas phase above the liquid level. The temperature and the pressure of the gas phase affect gas density, and consequently, the large electron multiplier (LEM) gain calibration. These considerations require a robust temperature monitoring system for the detector both in liquid and gas phase and a pressure monitoring system in the gas phase, supplemented with liquid level monitors and a high-performance camera system for visual inspection of the interior of the cryostat during the filling process. These systems are fully described in Section 4.2 of this chapter.

Argon purity must be established as early as possible in the filling process, a period during which gas analyzers are most useful, and must maintain an acceptable value, corresponding to a minimum electron drift lifetime of 3 ms throughout the data-taking period. Dedicated purity monitors (Section 4.2.1) provide precise lifetime measurements up to values of 10 ms (current capability based on ProtoDUNE-SP). Purity requirements are more stringent in a dual phase detector due to longer drift paths, so CISC plans to build longer purity monitors to increase this capability to approximately 20 ms for the DP FD. The purity monitors and gas analyzers remain important even after high lifetime has been achieved because periodic detector top-off fills occur; the new LAr must be very high quality to be introduced into the cryostat.

The CISC system must prevent fault conditions that could develop in the detector module over long periods of operation. A drop in liquid level could affect the behavior of the extraction grid, which lies 5 mm below the liquid surface; the liquid level monitors must head off this possibility. Very slow-developing outgassing phenomena could conceivably occur, with associated bubble generation creating another source of HV breakdown events. The cold camera system allows bubbling sites to be detected and identified, and mitigation strategies to be developed such as reducing HV operation for some time. A more subtle fault is the formation of quasi-stable eddies in argon fluid flow that could prevent positive argon ions from being cleared from time projection chamber (TPC) volume, resulting in space charge build up that would not otherwise be expected at the depth of the FD. The space charge could in turn cause distortions in the TPC drift field that degrade tracking and calorimetry performance. The high-performance thermometry of the DUNE CISC system creates input for well developed complex fluid flow models described in Section 4.1.3 that should enable detecting conditions associated with these eddies.

Finally, a high detector live-time fraction for operation over several years cannot be achieved without an extensive system for monitoring all aspects of detector performance, reporting this information intelligently to detector operators, and archiving the data for deeper offline studies. Section 4.1.1.2 details the DUNE slow controls system designed for this task.

Some of the baseline designs for the CISC systems (e.g., pressure meters in gas, capacitive level meters, slow controls system) have been used in ProtoDUNE-DP, and corresponding design parameters are extrapolated from these designs. For systems that are currently not deployed in ProtoDUNE-DP, the goal is deploy them in ProtoDUNE-DP-Run-II phase. The ProtoDUNE-DP data from Run-I and Run-II will be used to validate the instrumentation designs and to understand their performance. For some of the CISC systems (e.g., static and dynamic T-gradient thermometers, purity monitors), validation and performance in ProtoDUNE-SP will provide important inputs to DP FD. More details are provided in sections 4.1.3.1, 4.2.8, and 4.3.6.

4.1.1 Scope

4.1.1.1 Cryogenics Instrumentation

Cryogenics instrumentation includes purity monitors, various types of temperature monitors (gas and liquid phase), capacitive level meters, pressure meters (gas phase), and cameras with their associated light emitting systems. Also included are gas analyzers and differential pressure level monitors that are directly related to the external cryogenics system, which have substantial interfaces with the Long-Baseline Neutrino Facility (LBNF). LBNF provides the needed expertise for these systems and is responsible for the design, installation, and commissioning, while the CISC consortium provides the resources and supplements labor as needed.

A test facility for instrumentation devices is also necessary to cryogenics instrumentation. CISC is responsible for design through commissioning in the DP module of liquid and gaseous argon instrumentation devices (purity monitors, thermometers, capacitive level meters, pressure meters, cameras, and light-emitting system, and their associated feedthroughs) and the cryogenic instrumentation test facility (CITF).

Cryogenics instrumentation requires significant physics and simulation work, such as E field simulations and cryogenics modeling studies using computational fluid dynamics (CFD). E field simulations identify desirable locations for instrumentation devices in the cryostat, away from regions of high E field, so their presence does not induce large field distortions. CFD simulations help identify expected temperature, impurity, and velocity flow distributions and guide the placement and distribution of instrumentation devices inside the cryostat.

4.1.1.2 Slow Controls

The slow controls portion of CISC comprises three main components: hardware, infrastructure, and software. The slow controls hardware and infrastructure comprises networking hardware, signal processing hardware, computing hardware, and associated rack infrastructure. The slow controls software provides, for every slow control quantity, the central slow controls processing architecture, databases, alarms, archiving, and control room displays.

CISC provides software and infrastructure for controlling and monitoring all detector elements that provide data on the health of the detector module or conditions important to the experiment, as well as certain hardware. Slow controls includes the systems detailed below.

Slow controls base software and databases are the central tools needed to develop control and monitoring for various detector systems and interfaces. These include

- base input/output software;
- alarms, archiving, display panels, and similar operator interface tools; and

- slow controls system documentation and operations guidelines.

Slow controls for external systems collect data from systems external to the detector module and provide status monitoring to operators and for archiving. They collect data on beam status, cryogenics status, data acquisition (DAQ) status, facilities systems status, interlock status bit monitoring (but not the actual interlock mechanism), ground impedance monitoring, and possibly building and detector hall monitoring, as needed.

Slow controls for detector hardware systems covers software interfaces for detector hardware devices:

- monitoring and control of all power supplies,
- full rack monitoring (rack fans, thermometers and rack protection system),
- CISC instrumentation device monitoring (and control to the extent needed),
- calibration device monitoring (and control to the extent needed),
- charge-readout plane (CRP) instrumentation device monitoring (and control to the extent needed),
- power distribution unit and computer hardware monitoring,
- HV system monitoring through cold cameras, and
- inspection of detector components using warm cameras.

CISC will develop, install, and commission any hardware related to rack monitoring and control for the detector racks. Most power supplies may only require a cable from the device to an Ethernet switch, but some power supplies might require special cables (e.g., GPIB or RS232) for communication. The CISC consortium will provide these control cables.

CISC participates in additional activities outside the scope of the consortium that require coordination with other groups. This is discussed in Section 4.4.5.

4.1.2 Design Considerations

Important design considerations for instrumentation devices include stability, reliability, and longevity, so that devices can survive for at least 20 years. Such longevity is uncommon for any device, so the overall design allows replacing devices where possible. DUNE requires the E field on any instrumentation devices inside the cryostat to be less than 30 kV/cm to minimize the risk of dielectric breakdown in LAr.

An important consideration for event reconstruction is the maximum noise level, induced by in-

strumentation devices, that the readout electronics can tolerate. ProtoDUNE-DP is evaluating this. Table 4.1 shows the selected top-level specifications for CISC subsystems. Tables 4.2, 4.3, and 4.4 show the full set of specifications for the CISC subsystems.

Data from purity monitors and different types of thermometers will be used to validate the LAr fluid flow model. A number of requirements drive the design parameters for the precision and granularity of monitor distribution across the cryostat. For example, the electron lifetime measurement precision must be 1.4 % to keep the bias on the charge readout in the TPC below 0.5 % at 3 ms lifetime. For thermometers, the parameters are driven by ProtoDUNE-SP and ProtoDUNE-DP designs as well as the comparison of ProtoDUNE-SP data to CFD simulations. The temperature measurement resolution in liquid phase must be less than 2 mK, and the relative precision of those measurements must be less than 5 mK. The resolution is defined as the temperature root mean square (RMS) for individual measurements and is driven by the electronics. The relative precision also includes the effect of reproducibility for successive immersions in liquid argon (LAr). The relative precision is particularly important in characterizing gradients less than 20 mK. As described below, the laboratory calibration data and the recent analysis of thermometer instrumentation data from ProtoDUNE-SP shows that a 2.5 mK relative precision is achievable.

It is also important to monitor the temperature and pressure in the gas phase over the liquid phase because they affect the large electron multiplier (LEM) gain calibration. The gas pressure must be monitored to 1 mbar precision and accuracy. Near the surface of the liquid, the temperature gradient of the gas must be measured with an array of temperature probes with a vertical pitch that increases with height (from 1 to 5 cm). The LAr differential pressure level meters must be precise to 14 mm to measure accurately during filling. Moreover, multiple capacitive level meters with less than 5 mm precision will be needed to more precisely measure the LAr level and for LAr-level based interlocks for other systems (e.g., HV).

As shown in Table 4.3, several requirements drive the design of cold and warm cameras and the associated light emitting system. The components of the camera systems must not contaminate the LAr or produce bubbles to avoid increasing the risk of HV discharge. Both cold and warm cameras must provide coverage of at least 80 % of the TPC volume with a resolution of 1 cm for cold cameras and 2 mm for warm cameras on the TPC.

For the cryogenic test facility, a cryostat with a capacity of only 0.5 to approximately 3 m^3 will suffice and will keep turn around times and filling costs low. For gas analyzers, the operating range must allow us to establish useful electron lifetimes; details are in Table 4.2.

For slow controls, the system must be sufficiently robust to monitor a minimum of 150,000 variables and support a broad range of monitoring and archiving rates. The system must also interface with a large number of detector subsystems and establish two-way communication with them for control and monitoring.

Table 4.1: Specifications for DP-CISC

Label	Description	Specification (Goal)	Rationale	Validation

DP-FD-1	Minimum drift field	$> 250\,\mathrm{V/cm}$ ($> 500\,\mathrm{V/cm}$)	Lessens impacts of e^--Ar recombination, e^- lifetime, e^- diffusion and space charge.	ProtoDUNE
DP-FD-2	System noise	$< 2500\ e^-$ ($\sim 1000\ e^-$ (achieved in WA105))	Provides >5:1 S/N on induction planes for pattern recognition and two-track separation.	ProtoDUNE and simulation
DP-FD-3	Light yield	$> 1\,\mathrm{PE/MeV}$ (min), $> 3\,\mathrm{PE/MeV}$ (avg)	Corresponds to point where improvements in resolution with increasing light yield slow down significantly.	Simulated SN neutrinos in FD.
DP-FD-4	Time resolution	$< 1\,\mu\mathrm{s}$ ($< 100\,\mathrm{ns}$)	Enables 1 mm position resolution for 10 MeV SNB candidate events for instantaneous rate $< 1\,\mathrm{m^{-3}ms^{-1}}$.	
DP-FD-5	Liquid argon purity	$< 100\,\mathrm{ppt}$ ($< 30\,\mathrm{ppt}$)	Provides >5:1 S/N on induction planes for pattern recognition and two-track separation.	Purity monitors and cosmic ray tracks
DP-FD-15	LAr nitrogen contamination	$< 25\,\mathrm{ppm}$	Maintain 0.5 PE/MeV PDS sensitivity required for triggering proton decay near cathode.	
DP-FD-18	Cryogenic monitoring devices		Constrain uncertainties on detection efficiency, fiducial volume.	ProtoDUNE
DP-FD-25	Non-FE noise contributions	$<< 1000\ e^-$	High S/N for high reconstruction efficiency.	Engineering calculation and ProtoDUNE
DP-CISC-1	Noise from Instrumentation devices	$\ll 1000\ e^-$	Max noise for 5:1 S/N for a MIP passing near cathode; per SBND and DUNE CE	ProtoDUNE

DP-CISC-2	Max. E field near instrumentation devices	$< 30\,\mathrm{kV/cm}$ ($< 15\,\mathrm{kV/cm}$)	Significantly lower than max field of 30 kV/cm per DUNE HV	3D electrostatic simulation
DP-CISC-3	Precision in electron lifetime	$< 1.4\%$ ($< 1\%$)	Required to accurately reconstruct charge per DUNE-FD Task Force report.	ProtoDUNE and CITF
DP-CISC-4	Range in electron lifetime	0 ms to 10 ms (0 ms to 30 ms) (0 ms to 10 ms (0 ms to 30 ms))	Slightly more than best values so far observed in other detectors.	ProtoDUNE and CITF
DP-CISC-11	Precision: temperature reproducibility	$< 5\,\mathrm{mK}$ ($2\,\mathrm{mK}$)	Allows validating CFD models that predict gradients less than 15 mK.	ProtoDUNE and CITF
DP-CISC-14	Temperature stability	$< 2\,\mathrm{mK}$ at all places and times (Match precision requirement at all places, at all times)	Measures temperature map with sufficient precision for the duration of thermometer operations.	ProtoDUNE
DP-CISC-27	Cold camera coverage	$> 80\%$ of HV surfaces (100%)	Enables detailed inspection of issues near HV surfaces.	Calculated from location, validated in prototypes.
DP-CISC-51	Slow control alarm rate	< 150/day (< 50/day)	Keeps rate low enough to allow response to every alarm.	Detector module; depends on experimental conditions
DP-CISC-52	Total No. of variables	$> 150{,}000$ (150,000 to 200,000)	Scaled from ProtoDUNE	ProtoDUNE and CITF
DP-CISC-54	Archiving rate	0.02 Hz (Broad range 1 Hz to 1 per few min.)	Archiving rate differs by variable, optimized to store important information	ProtoDUNE

4.1.3 Fluid Dynamics Simulation

Proper placement of purity monitors, thermometers, and liquid level monitors within the detector module requires knowing how LAr flows within the cryostat, given its fluid dynamics, heat and mass

Table 4.2: List of specifications for the different CISC subsystems.

Quantity/Parameter	Specification	Goal
Noise from instrumentation devices	$\ll$ 1000 enc	
Max. E field near instrumentation devices	<30 kV/cm	<15 kV/cm
Thermometers (LAr)		
Vertical density of sensors for T-gradient monitors	> 2 sensor/m	> 4 sensors/m
2D horizontal density for bottom individual sensors	1 sensor/5(10) m	1 sensor/3(5) m
Resolution of temperature measurements	< 2 mK	<0.5 mK
Precision: temperature reproducibility	< 5 mK	2 mK
Stability	< 2 mK at all places and times	Match precision requirement at all places/times
Discrepancy between laboratory and *in situ* calibrations for temperature sensors	< 5 mK	< 3 mK
Discrepancy between measured temperature map and CFD simulations in ProtoDUNE-SP	< 5 mK	
Thermometers (GAr)		
Thermometer density (decreases with height)	1 sensor/2-10 cm	1 sensor/1-5 cm
Thermometer coverage	40 cm	60 cm
Resolution of temperature measurements	5 mK	0.5 mK
Precision: temperature reproducibility	100 mK	100 mK
Thermometers (All)		
Reliability	80% (in 18 months)	50% (during 20 years)
Longevity	> 18 months	> 20 years
Level Meters		
Precision (LBNF side)	0.1% over 14 m (14 mm)	
Precision (capacitive level meters, DUNE side)	1 cm	<5 mm
Longevity	20 years	> 20 years
Gas Analyzers		
Operating Range O2	0.2 (air) to 0.1 ppt	
Operating Range H2O	Nom. air to sub ppb; contaminant-dependent	
Operating Range N2	Nominally Air Nom. air to sub ppb; contaminant-dependent	
Precision: 1 sigma at zero	per gas analyzer range	
Detection limit: 3 sigma	Different analyzer modules needed to cover entire range	
Stability	<% of full scale range.	
Longevity	>10 years	

Table 4.3: List of specifications for the different CISC subsystems.

Quantity/Parameter	Specification	Goal
Purity Monitors		
Precision in electron lifetime	<1.4% at 3 ms (<4% at 9 ms)	< 1%
Range in electron lifetime	0 - 10 ms	(0 - 30 ms inline)
Longevity	20 years	> 20 years
Stability	Match precision requirement at all places/times	
Reliability	Daily measurements	Measurements as needed
Pressure Meters (GAr)		
Relative precision (DUNE side)	0.1 mbar	
Absolute precision (DUNE side)	<5 mbar	
Cold cameras		
Coverage	80% of the exterior of HV surfaces	100%
Frames per second	yet to be defined	
Resolution	1 cm on the TPC	yet to be defined
Duty cycle	yet to be defined	
Longevity	> 18 months	> 20 years
Inspection cameras		
Coverage	80% of the TPC	yet to be defined
Frames per second	yet to be defined	
Resolution	2 mm on the TPC	yet to be defined
Heat transfer	no generation of bubbles	
Longevity	> 18 months	> 20 years
Light emitting system		
Radiant flux	> 10 mW/sr	100 mW/sr
Power	< 125 mW/LED	
Wavelength	red/green	IR/white
Longevity	> 18 months (for cold cameras)	> 20 years
cryogenic instrumentation test facility (CITF)		
Dimensions	0.5 to 3 cubic meters	
Temperature stability	±1K	
Turn-Around time	∼9 days	9 days
LAr purity	O2, H2O: low enough to measure drifting electrons of devices under test, ∼ 0.5 ms. N2: ppm for scintillation light tests.	>1.0 ms

Table 4.4: List of specifications for the different CISC subsystems.

Quantity/Parameter	Specification	Goal
Slow Controls		
Alarm rate	<150/day	< 50/day
Total No. of variables	150,000	150,000 - 200,000
Server rack space	2 racks	3 racks
Archiving rate	0.02 Hz	Broad range 1 Hz to 1 per few min.
Near detector status	Beam conditions and detector status	Full beam and detector status

transfer, and distribution of impurity concentrations. Fluid flow is also important in understanding how the positive and negative ion excess created by various sources (e.g., ionization from cosmic rays and ^{36}Ar; ion feedback at the liquid-gas interface in a DP detector) is distributed across the detector as it affects E field uniformity.

Fluid motion within the cryostat is driven primarily by small changes in density caused by thermal gradients within the fluid although pump flow rates and inlet and outlet locations also contribute. Heat sources include exterior heat from the surroundings, interior heat from electronics, and heat flow through the pump inlet. In principle, purity monitors can be placed throughout the cryostat to determine if the argon is pure enough for experimentation. However, some areas inside the cryostat are off limits for such monitors.

To determine the purity of the argon in regions where experimental data is unavailable, CFD simulations can be used to better understand and quantify impurity levels. The overall goal of the CFD simulations is to better understand and predict the fluid (in either liquid or vapor state) motions and the implications for detector performance. The fluid flow behavior can be determined by simulating LAr flow within a detector module using Siemens Star-CCM+[1], a commercially available CFD code. Such a model must properly define the fluid characteristics, solid bodies, and fluid-solid interfaces, as well as provide a way to measure contamination, while still maintaining reasonable computation times. In addition, these fluid dynamics simulations can be compared to available experimental data to assess simulation accuracy and credibility.

Although simulation of the detector module presents challenges, acceptable simplifications can accurately represent the fluid, the interfacing solid bodies, and variations of contaminant concentrations. Because of the magnitude of thermal variation within the cryostat, modeling the LAr is simplified by using constant thermophysical properties, calculating buoyant force with the Boussinesq Model (using a constant density for the fluid with application of a temperature-dependent buoyant force), and a standard shear stress transport turbulence model. Solid bodies that touch the LAr include the cryostat wall, photon detectors, and light reflector foils. The field cage (FC) planes, cathode planes, and grounding grid can be represented by porous bodies. Because impurity concentration and electron lifetime do not affect fluid flow, these variables can be simulated as passive scalars, as is commonly done for smoke released [59] in air or dyes released in liquids.

[1] https://mdx.plm.automation.siemens.com/star-ccm-plus

Discrepancies between real data and simulations may affect detector performance. Simulation results contribute to decisions about where to place sensors and monitors and to the definitions of various calibration quantities. Methods of mitigating such risks include well established convergence criteria, sensitivity studies, and comparison to results of previous CFD simulation work. Moreover, the simulation will be improved with input from temperature measurements and validation tests from ProtoDUNE-SP[2].

Figure 4.2: Distribution of temperature on a plane intersecting ...

This figure will be coming.

.

Figure 4.2 shows an example of the temperature distribution on a plane intersecting an LAr inlet and at a plane halfway between an inlet and an outlet in SP FD. Note the plume of higher temperature LAr between the walls and the outer anode plane assembly (APA) on the inlet plane. The current placement of instrumentation in the cryostat as shown in Figure 4.9 was determined using temperature and impurity distributions from CFD simulations.

The strategy for future CFD simulations begins with validating the CFD model using ProtoDUNE-DP LAr instrumentation data and modeling the FD DP module to derive specifications for instrumentation. We are pursuing a prioritized set of studies to help determine requirements for other systems. We plan to

- review the DUNE DP FD cryogenics system design and verify the current implementation in simulation to ensure that the simulation represents the actual design;
- validate the liquid CFD model using thermometer data from ProtoDUNE-SP because we have no high precision T-gradient thermometers in ProtoDUNE-DP to validate the liquid model;
- model the ProtoDUNE-DP gas regions with the same precision as the FD. The gas model should how to place thermometers in the argon gas and verify the design of the gaseous argon purge system;
- perform a CFD study to determine the feasibility of a wier for DP; this should determine if it can be used to clean the LAr surface before the extraction grid is submerged in the DP module.

4.1.3.1 Validation in ProtoDUNE

Given the HV configuration in ProtoDUNE-DP is more complex than ProtoDUNE-SP (much higher electric potential and no zero field regions on the TPC sides), ProtoDUNE-DP was not in-

[2]Because ProtoDUNE-DP was not instrumented with high-precision thermometers in the liquid phase and because the cryogenics design is the same for single-phase (SP) and DP modules of the DUNE FD, ProtoDUNE-SP data will be used to validate the liquid CFD model.

Table 4.5: CFD input parameters for ProtoDUNE.

Parameter	Value	Comments
Cryostat height	7.878 m	Measured with laser (1 cm error approx.)
LAr surface height	7.406 m	Measured by capacitive level meter (< 1 cm error)
Ullage pressure	1.045 bar	Measured by pressure gauges
LAr surface temperature	87.596 K	Computed using ullage pressure and [60]
LAr inlet temperature	outlet + 0.2 K	Estimated
LAr flow rate per pipe	0.4170025 kg/s	
Heat flux	5.76 W/m^2	This is the heat flux from all four walls as well as the ground
Vapor drawn from the chimneys	5-7 gr/sec	Among all chimneys

strumented with vertical arrays of high precision temperature sensors in the liquid as in ProtoDUNE-SP. These temperature sensors are important elements for validating CFD simulations, but because the cryostat and cryogenics system designs are identical in both the SP and DP far detector modules, temperature data from ProtoDUNE-SP can be used to validate the liquid model for the DP FD. For validating the gas model, data from the vertical array of thermometers installed in the ProtoDUNE-DP will be used.

ProtoDUNE-SP has collected data to validate the CFD using

- static and dynamic T-gradient thermometers,
- individual temperature sensors placed in the return LAr inlets,
- two 2D grids of individual temperature sensors installed below the bottom ground planes and above the top ground planes,
- a string of three purity monitors vertically spaced from near the bottom of the cryostat to just below the LAr surface,
- two pressure sensors (relative and absolute) in the argon gas,
- H_2O, N_2, and O_2 gas analyzers,
- LAr level monitors, and
- standard cryogenic sensors and individual temperature sensors placed around the cryostat on the membrane walls, and recirculation flow rates transducers.

On the other hand, ProtoDUNE-DP has installed the following instrumentation devices to validate CFD:

- two purity monitors, one at the bottom of the cryostat and another 2 m from the bottom;
- two pressure sensors (relative and absolute) in the argon gas;
- vertical array of thermometers in argon gas;
- H_2O, N_2, and O_2 gas analyzers;
- LAr level monitors; and
- standard cryogenic sensors and individual temperature sensors placed around the cryostat on the membrane walls and recirculation flow rates transducers.

The data, which has been logged through the ProtoDUNE-SP slow control system [61], is available for offline analysis.

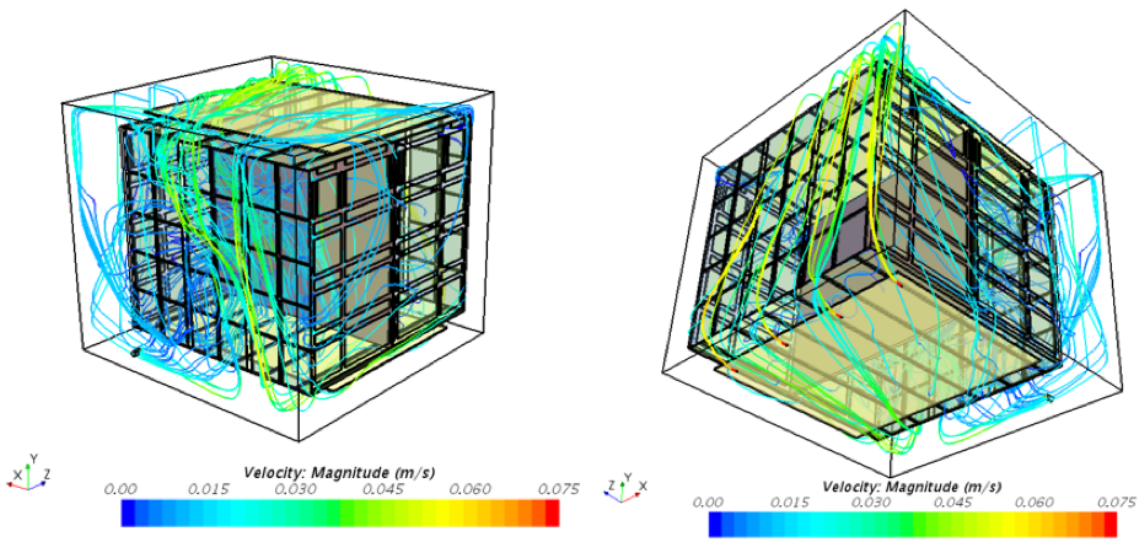

Figure 4.3: Streamlines for LAr flow inside ProtoDUNE-SP.

In parallel, CISC has produced a ProtoDUNE-SP CFD model with input from ProtoDUNE-SP measurements (see Table 4.5). Streamlines[3] from the current simulation (Figure 4.3) show the flow paths from the four cryostat inlets to the outlet. Validating this model requires an iterative process in which several versions of the CFD simulation, using different input parameters, eventually converge to a reasonable agreement with data from instrumentation devices. Preliminary results comparing the vertical temperature profiles already exist. Figure 4.4 shows the fluid temperature measured by the dynamic T-gradient thermometer and compares it to the current ProtoDUNE-SP CFD model, with parameters shown in Table 4.5. The agreement is already quite good.

The CFD reassuringly predicts a reasonable response for more than one set of initial conditions. It is still important to measure the instrumentation response to help establish the validity of the

[3]In fluid mechanics, a streamline is a line that is everywhere tangent to the local velocity vector. For steady flows, a streamline also represents the path that a single particle of the fluid will take from inlet to exit.

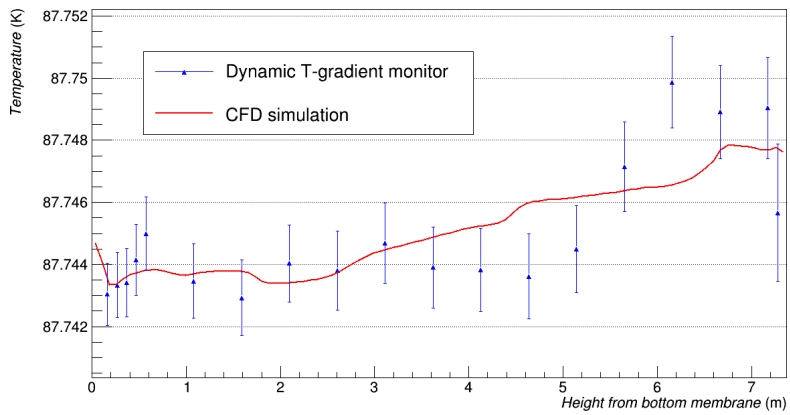

Figure 4.4: Comparison of ProtoDUNE-SP temperature data and CFD simulations.

CFD model. Tests with differing initial conditions have been recently performed (after the beam run), and the analysis of the corresponding data is currently ongoing. Those additional tests include pump and recirculation manipulations such as pump on-off, change of pumping speed, and bypassing filtration, and changing the cryostat pressure set point to a higher (or lower) value[4] to induce changes in pressure for a specified time while monitoring the instrumentation. Any change in pressure changes the temperatures everywhere in the cryostat. Studying the rate of this change, as detected at various heights in the cryostat, might provide interesting constraints on the CFD model.

Once the ProtoDUNE-SP CFD model predicts the fluid temperature in the entire cryostat to a reasonable level under different conditions, this model will be extrapolated to ProtoDUNE-DP to produce maps of impurity levels in the detector module. These can be converted easily into electron lifetime maps, which we will compare to the ProtoDUNE-DP purity monitor data.

4.2 Cryogenic Instrumentation

Instrumentation inside the cryostat must accurately report the condition of the LAr, so we can ensure that it is adequate for operating the TPC. This instrumentation includes purity monitors to check the level of impurity in the argon and provide high-precision electron lifetime measurements, as well as gas analyzers to verify that levels of atmospheric contamination do not drop below certain limits during cryostat purging, cooling, and filling. Temperature sensors deployed in vertical arrays and at the top and bottom of the detector module monitor the cryogenics system operation, providing a detailed 3D temperature map that helps predict LAr purity across the entire cryostat. The cryogenics instrumentation also includes LAr level monitors and a system of internal cameras to help find sparks in the cryostat and to monitor the overall cryostat interior.

The proper placement of purity monitors, thermometers, and liquid-level monitors in the detector module requires understanding LAr fluid dynamics, heat and mass transfer, and distribution of

[4] The HV must be ramped down for this exercise because dropping the pressure too fast might provoke boiling of the LAr near the surface.

impurity concentrations within the cryostat. Both this and coherent analysis of the instrumentation data require CFD simulation results.

ProtoDUNE-SP and ProtoDUNE-DP are testing the performance of all cryogenic instrumentation for the DP module, validating the baseline design. See Section 4.2.8 for more detail.

4.2.1 Purity Monitors

A fundamental requirement of a LAr TPC is that ionization electrons drift over long distances in LAr. Part of the charge is inevitably lost because of electronegative impurities in the liquid. To keep this loss to a minimum, monitoring impurities and purifying the LAr during operation is essential.

A purity monitor is a small ionization chamber used to infer independently the effective free electron lifetime in the LArTPC. It illuminates a cathode with UV light to generate a known electron current, then collects the drifted current at an anode a known distance away. Attenuation of the current is related to the electron lifetime. Electron loss can be parameterized as $N(t) = N(0)e^{-t/\tau}$, where $N(0)$ is the number of electrons generated by ionization, $N(t)$ is the number of electrons after drift time t, and τ is the electron lifetime.

For the DP module, the drift distance is 12 m, and the E field is 500 V cm^{-1}. Given the drift velocity of approximately 1.5 mm µs^{-1} in this field, the time to go from cathode to anode is roughly ∼8 ms [62]. For an LAr TPC signal attenuation, $[N(0)-N(t)]/N(0)$, of 50 % over the entire drift distance, the corresponding electron lifetime is $8\,\mathrm{ms}/[-\ln(0.5)] \simeq 11\,\mathrm{ms}$.

Residual gas analyzers can monitor the gas in the ullage of the tank and would be an obvious choice for analyzing argon gas. Unfortunately, suitable and commercially available mass spectrometers have a detection limit of ∼10 parts per billion (ppb), whereas DUNE requires a sensitivity of parts per trillion (ppt). Therefore, specially constructed and distributed purity monitors will measure LAr purity in all phases of operation. These measurements, along with an accurate CFD model, enable determining LAr purity at all positions throughout the detector module.

Purity monitors also mitigate the risk of LAr contamination. The large scale of the detector modules increases the risk of failing to notice a sudden, unexpected infusion of contaminated LAr back into the cryostat. If this condition were to persist, it could cause irreversible contamination to the LAr and terminate useful data taking. Strategically placed purity monitors mitigate this risk as demonstrated in ProtoDUNE-SP.

Purity monitors are placed inside the cryostat but outside the TPC. They are also placed within the recirculation system outside the cryostat, both in front of and behind the filtration system. Continuous monitoring of the LAr supply lines to the detector module provides a strong line of defense against contamination from sources both in the LAr volume and from components in the recirculation system. Similarly, gas analyzers (described in Section 4.2.5) protect against contaminated gas.

Furthermore, using several purity monitors to measure lifetime with high precision at carefully chosen points provides key input, e.g., vertical gradients in impurity concentrations, for CFD models of the detector module.

Purity monitors were deployed in previous liquid argon time-projection chamber (LArTPC) experiments, i.e., ICARUS, MicroBooNE, and the 35 ton prototype. During the first run of the 35 ton prototype, two of the four purity monitors stopped working during cooldown, and a third operated intermittently. We later found this was due to poor electrical contacts between the resistor chain and the purity monitor. A new design was implemented and successfully tested in the second run.

ProtoDUNE-SP and ProtoDUNE-DP implement purity monitors to measure electron lifetime at different heights. Both use a similar design. The baseline design for the DP FD will be the one used in ProtoDUNE-SP. Figure 4.5 shows the assembly of the ProtoDUNE-SP purity monitors. The design reflects improvements to ensure electric connectivity and improve signals. ProtoDUNE-SP uses a string of purity monitors connected with stainless steel tubes to protect the optic fibers. The purity monitor system at ProtoDUNE-SP measured electron lifetime every hour during commissioning and daily during the beam test. During this time, it alerted us to serious problems twice, first for filter saturation and then because the recirculation pump had stopped. This enabled us to prevent situations that otherwise could have had serious consequences.

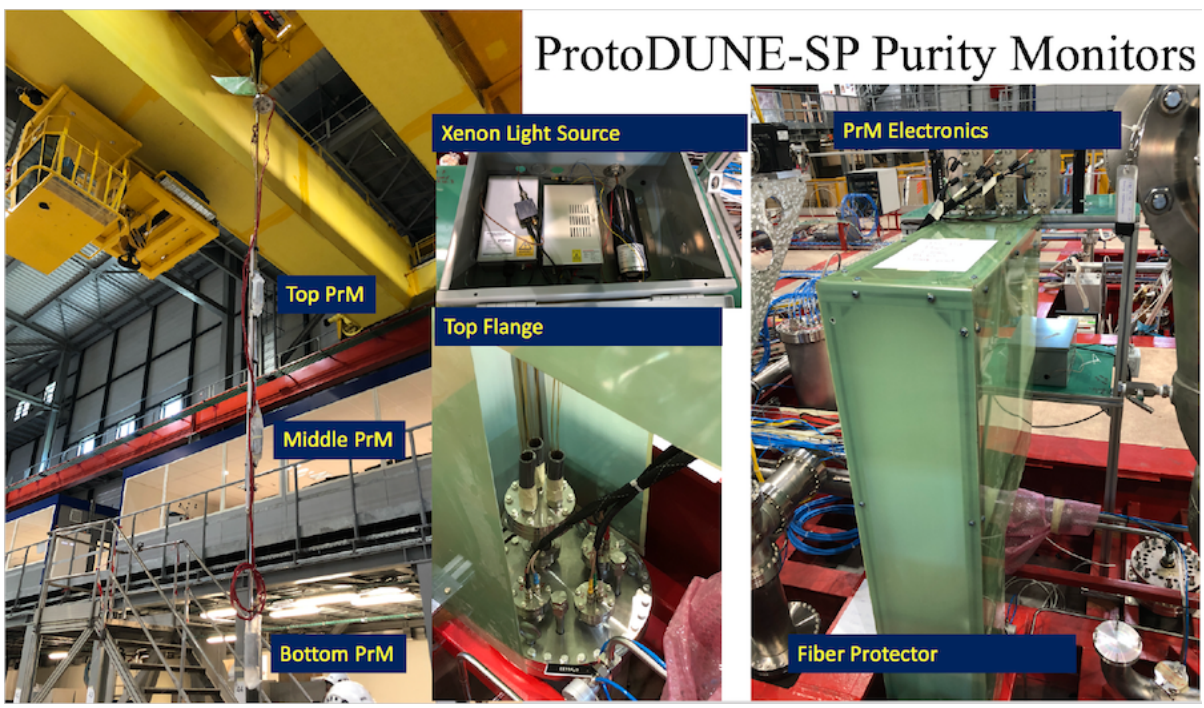

Figure 4.5: The ProtoDUNE-SP purity monitoring system.

During the commissioning and beam test of ProtoDUNE-SP, the purity monitors operated with different high voltages to change electron drift time, ranging from 150 µs to 3 ms. This allowed the ProtoDUNE-SP purity monitors to measure electron lifetime from 35 µs to about 10 ms with high precision, a dynamic range greater than 300. This measurement was also valuable for the ProtoDUNE-SP lifetime calibration. Because purity monitors have much smaller drift volumes than the TPC, they are less affected by the space charge caused by cosmic rays.

A similar operation plan is foreseen for the DP module, with modifications to accommodate the relative positions of the instrumentation port and the purity monitor system and the different geometric relationships between the TPC and cryostat.

ProtoDUNE-SP implements three purity monitors instead of the two deployed in ProtoDUNE-DP. Figure 4.6 shows the ProtoDUNE-SP data taken using its three purity monitors between the commissioning of ProtoDUNE-SP starting in September 2018, to the middle of test beam running, in November 2018.

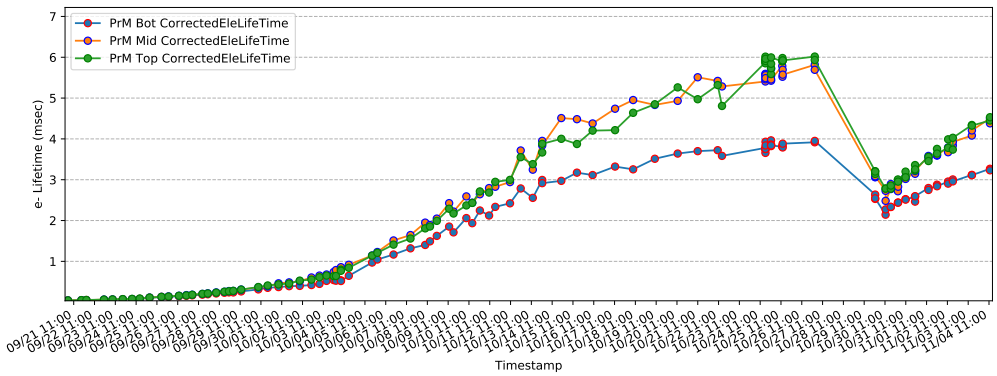

Figure 4.6: The measured electron lifetimes in the three purity monitors as a function of time in ProtoDUNE-SP.

4.2.1.1 Purity Monitor Design

The DP module baseline purity monitor design follows that of the ICARUS experiment (Figure 4.7)[63]. It consists of a double-gridded ion chamber immersed in the LAr volume with four parallel, circular electrodes, a disk holding a photocathode, two grid rings (anode and cathode), and an anode disk. The cathode grid is held at ground potential. The cathode, anode grid, and anode each hold separate bias voltages and are electrically accessible via modified vacuum-grade HV feedthroughs. The anode grid and the field shaping rings are connected to the cathode grid by an internal chain of 50 MΩ resistors to ensure the uniformity of the E fields in the drift regions. A stainless mesh cylinder is used as a Faraday cage to isolate the purity monitor from external electrostatic background.

The purity monitor measures the electron drift lifetime between its anode and cathode. The purity monitor's UV-illuminated photocathode generates electrons via the photoelectric effect. Because electron lifetime in LAr is inversely proportional to the electronegative impurity concentration, the fraction of electrons generated at the cathode that arrives at the anode (Q_A/Q_C) after the electron drift time t gives a measure of the electron lifetime τ: $Q_A/Q_C \sim e^{-t/\tau}$.

Once the electron lifetime becomes much larger than the drift time t, the purity monitor reaches its sensitivity limit. For $\tau >> t$, the anode-to-cathode charge ratio becomes $\sim$ 1. Because the drift time is inversely proportional to the E field, in principle, reducing the field should make it possible to measure lifetimes of any length regardless of the length of the purity monitor. On the

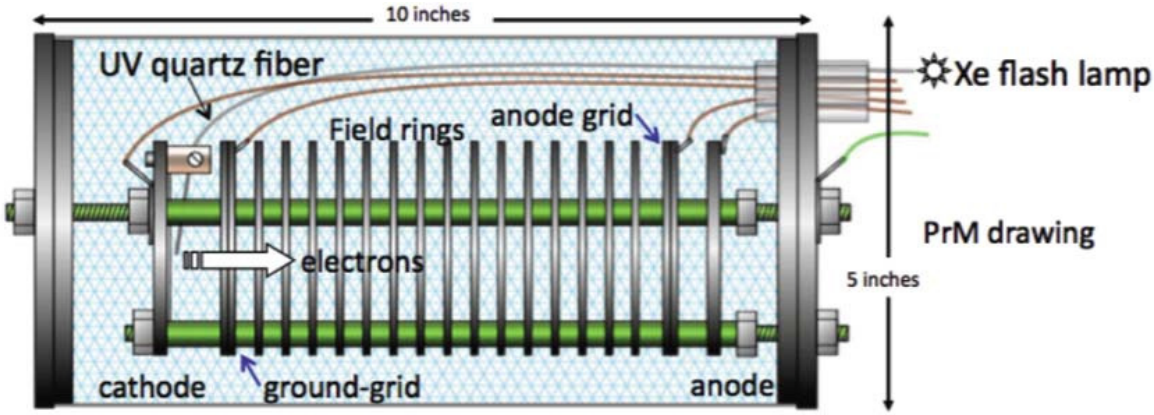

Figure 4.7: Schematic diagram of the basic purity monitor design [63].

other hand, increasing the voltage will shorten the drift time, allowing measurement of a short lifetime when purity is low.

Varying the operational HV on the anode from 250 V to 4000 V in the ProtoDUNE-SP's 24 cm (9.5 inch) long purity monitor allowed us to make the 35 µs to 10 ms electron lifetime measurements.

The electron lifetime of the purest commercial LAr, after the first filtering and during the filling process, is typically longer than 40 µs. However, when the filter starts to saturate, the lifetime decreases to less than 30 µs. To reduce the energy loss due to impurities, the DP module requires an electron lifetime longer than 10 ms. Therefore, purity monitors with different lengths (drift distances) are needed to extend the measurable range to less than 35 µs and more than 10 ms.

The photocathode that produces the photoelectrons is an aluminum plate coated first with 50 Å of titanium followed by 1000 Å of gold; it is attached to the cathode disk. Three photocathodes per purity monitor are implemented in ProtoDUNE-DP, two of silver and one of gold, with each cathode lit by one fiber. The gold cathode is the standard used in ProtoDUNE-SP, but R&D has shown silver emits more photoelectrons. A xenon flash lamp is the light source in the baseline design, although a more reliable and possibly submersible light source, perhaps LED-driven, could replace this in the future. The UV output of the lamp is quite good, approximately $\lambda = 225$ nm, which corresponds closely to the work function of gold (4.9 eV to 5.1 eV). Three UV quartz fibers carry the xenon UV light into the cryostat to illuminate the photocathode. Another quartz fiber delivers the light into a properly biased photodiode outside the cryostat to provide the trigger signal when the lamp flashes.

4.2.1.2 Electronics, DAQ, and Slow Controls Interfacing

The purity monitor electronics and DAQ system consist of front-end (FE) electronics, waveform digitizers, and a DAQ PC. Figure 4.8 illustrates the system.

The baseline design of the FE electronics follows the one used in the 35 ton prototype, LAPD, and MicroBooNE. The cathode and anode signals are fed into two charge amplifiers within the

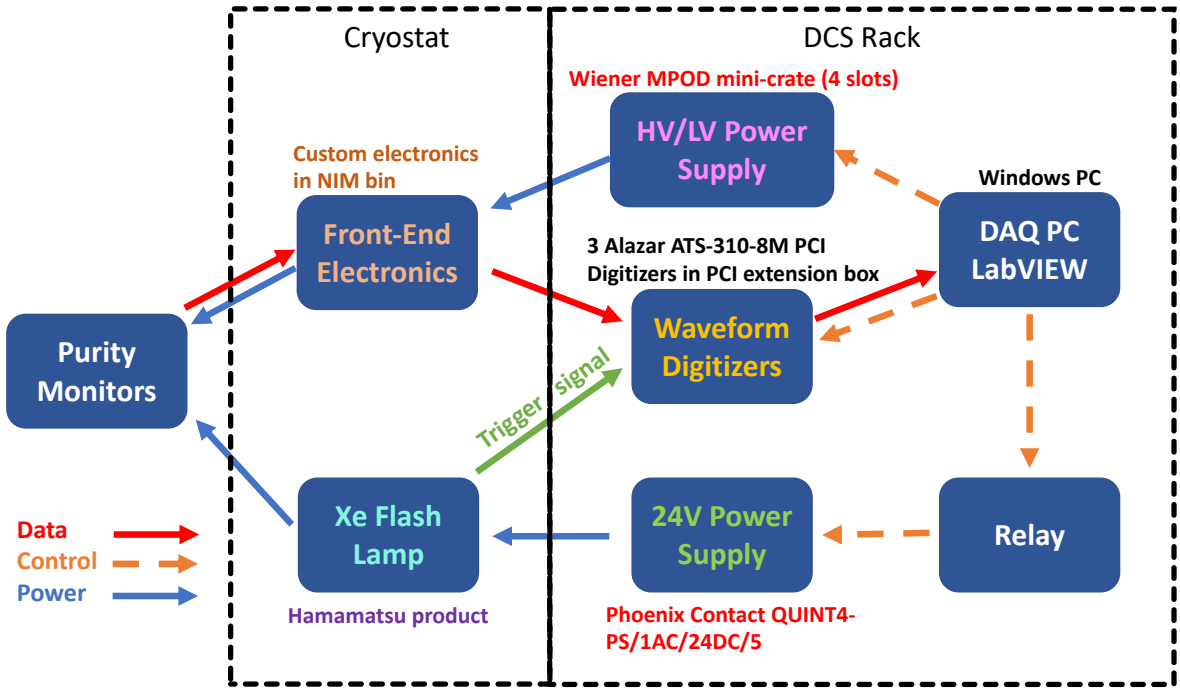

Figure 4.8: Block diagram of the purity monitor system.

purity monitor electronics module. This electronics module includes a HV filter circuit and an amplifier circuit, both shielded by copper plates, to allow the signal and HV to be carried on the same cable and decoupled inside the purity monitor electronics module. A waveform digitizer that interfaces with a DAQ PC records the amplified anode and cathode outputs. The signal and HV cable shields connect to the grounding points of the cryostat and are separated from the electronic ground with a resistor and a capacitor connected in parallel and mitigating ground loops between the cryostat and the electronics racks. Amplified output is transmitted to an AlazarTech ATS310 waveform digitizer[5] containing two input channels, each with 12 bit resolution. Each channel can sample a signal at a rate of $20\,\mathrm{MS\,s^{-1}}$ to $1\,\mathrm{kS\,s^{-1}}$ and store up to 8 MS in memory. One digitizer is used for each purity monitor, and each digitizer interfaces with the DAQ PC across the PCI bus.

A custom LabVIEW[6] application running on the DAQ PC has two functions: it controls the waveform digitizers and the power supplies, and it monitors the signals and key parameters. The application configures the digitizers to set the sampling rate, the number of waveforms to be stored in memory, the pre-trigger data, and a trigger mode. A signal from a photodiode triggered by the xenon flash lamp is fed directly into the digitizer as an external trigger to initiate data acquisition. LabVIEW automatically turns on the xenon flash lamp by powering a relay when data taking begins and then turning it off when finished. The waveforms stored in the digitizers are transferred to the DAQ PC and used to obtain averaged waveforms to reduce any electronic noise in them.

The baseline is estimated by averaging the waveform samples prior to the trigger. This baseline is subtracted from the waveforms prior to calculating peak voltages of the cathode and anode signals.

[5]AlazarTech ATS310™ - 12 bit, 20 MS/s, https://www.alazartech.com/Product/ATS310.
[6]National Instruments, LabVIEW™, http://www.ni.com/en-us.html

The application performs these processes in real time. The application continuously displays the waveforms and important parameters like measured electron lifetime, peak voltages, and drift time in the purity monitors and shows the variation in these parameters over time, thus pointing out effects that might otherwise be missed. Instead of storing the measured parameters, the waveforms and the digitizer configurations are recorded in binary form for offline analysis. HV modules[7] in a WIENER MPOD mini crate[8] supply negative voltages to the cathode and positive voltages to the anode. The LabVIEW application controls and monitors the HV systems through an Ethernet interface.

The xenon flash lamp and the FE electronics are installed close to the purity monitor flange to reduce light loss through the optical fiber and prevent signal loss. Other pieces of equipment that distribute power to these items and collect data from the electronics are mounted in a rack separate from the cryostat. The slow control system communicates with the purity monitor DAQ software and controls the HV and LV power supplies of the purity monitor system. The optical fiber must be placed within 0.5 mm of the photocathode for efficient photoelectron extraction, so little interference with the photon detection system (PDS) is expected. The purity monitors could induce noise in the TPC electronics, in particular via the current surge through a xenon lamp when it is flashed. This source of noise can be controlled by placing the lamp inside its own Faraday cage with proper grounding and shielding. At ProtoDUNE-SP, after careful checks of the grounding, this noise has remained well below the noise generated by other sources.

In the DP module we can make use of triggering to prevent any potential noise from the purity monitor's flash lamp from affecting TPC and PDS signals. The LArTPC trigger rate is a few hertz, and each trigger window is one or a few milliseconds. The pulse from a flash lamp is very short (a microsecond or so, much shorter than the gaps between LArTPC trigger windows). Thus, an LArTPC trigger signal may be sent to a programmable pulse generator, which generates a trigger pulse that does not overlap with LArTPC trigger windows. This trigger pulse is then sent to the external trigger port on the flash lamp HV controller, so the lamp flashes between LArTPC trigger windows. In this way, the electronic and light noises from the flash lamp do not affect data taking at all.

4.2.1.3 Production and Assembly

The CISC consortium will produce the individual purity monitors, test them in a test stand, and confirm that each monitor operates at the required level before assembling them into strings of three monitors that will be mounted in the detector module cryostat using support tubes. The assembly process will follow the methodology developed for ProtoDUNE.

A short version of the string with all purity monitors will be tested in the LAr test facility. The full string will be assembled and shipped to SURF. A vacuum test in a long vacuum tube will be performed on site before inserting the full assembly into the SP module cryostat.

[7] iseg Spezialelektronik GmbH™ high voltage supply systems, https://iseg-hv.com/en.

[8] W-IE-NE-R MPOD™ Universal Low and High Voltage Power Supply System, `http://www.wiener-d.com/`.

4.2.2 Thermometers

As discussed in Section 4.1.3, a detailed 3D temperature map is important in monitoring the cryogenic system for correct functioning and the LAr for uniformity. Given the complexity and size of purity monitors, they can only be installed where there is sufficient space to provide a local measurement of LAr purity. A direct measurement of the LAr purity across the entire cryostat is not feasible, but a sufficiently detailed 3D temperature map based on CFD simulations can predict the purity. The vertical coordinate is especially important because it will relate closely to the LAr recirculation and uniformity. Monitoring the gas phase in the dual-phase technology is also important because the LEM gain calibration depends on gas temperature.

The baseline sensor distribution is shown in Figure 4.9. This baseline distribution will evolve as more information becomes available (precise CFD simulations, better understanding of cryostat ports, installation interfaces with other groups), but the baseline suffices to establish the overall strategy.

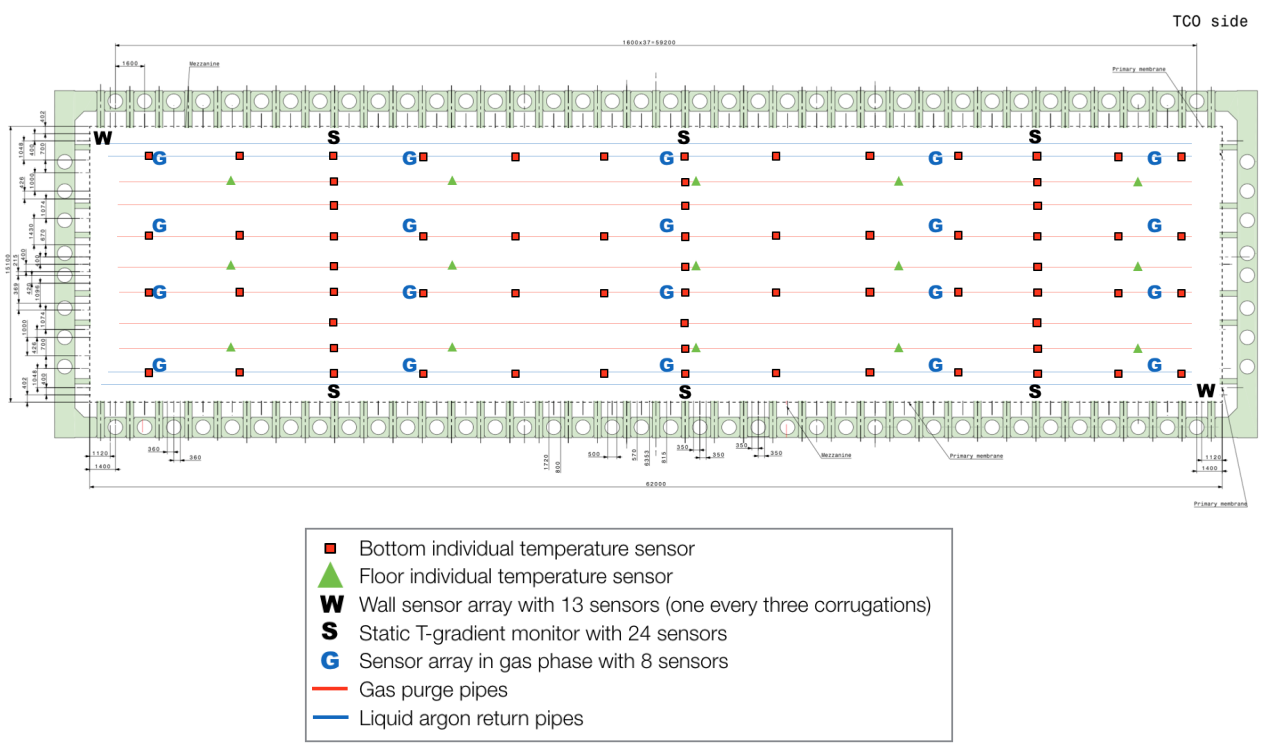

Figure 4.9: Distribution of temperature sensors inside the cryostat.

High-precision temperature sensors will be distributed near the TPC FC walls in two ways: (1) in high density (> 1 sensors/m) vertical arrays (called T-gradient monitors) and (2) in coarser (∼ 1 sensor/5 m) 2D arrays (called individual sensors) at the bottom of the detector module. The temperature map in the gas phase will be measured using several vertical arrays of standard RTDs distributed above the CRPs.

Temperature variations inside the cryostat should be very small (0.02 K for the liquid phase (see Figure 4.2), so sensors must be cross-calibrated to more than 0.005 K. Most sensors will be calibrated in the laboratory before installation. (Installation is described in Section 4.4.6.2.) Cali-

brating sensors before installation is the only option for sensors installed in places where space is limited. Given the precision required and the unknown longevity of the sensors, possibly requiring another calibration after some time, an additional method will be used for one of the T-gradient monitors based on a movable system that can be used to cross calibrate the temperature sensors *in situ*, as described in Section 4.2.2.2.

The baseline designs for all thermometer systems have three elements in common: sensors, cables, and readout system. We plan to use Lake Shore PT100-series[9] platinum sensors with 100 Ω resistance because, in the temperature range 83 K to 92 K, they show high reproducibility of ~ 5 mK and absolute temperature accuracy of 100 mK. Using a four-wire readout greatly reduces issues with lead resistance, any parasitic resistances, connections through the flange, and general electromagnetic noise pick up. Lakeshore PT102 sensors (see Figure 4.13-Right) were used in the 35 ton prototype prototype and ProtoDUNE-SP, giving excellent results. For the inner readout cables, a custom cable made by Axon[10] is the baseline. It consists of four teflon-jacketed copper wires (AWG28), forming two twisted pairs, with a metallic external shield and an outer teflon jacket. The readout system is described in Section 4.2.2.5.

Another set of lower-precision sensors epoxied into the bottom membrane of the cryostat will monitor cryostat filling in the initial stage. Finally, the inner walls and roof of the cryostat will have the same types of sensors to monitor the temperature during cooldown and filling (W sensors in Figure 4.9).

4.2.2.1 Static T-gradient monitors

Several vertical arrays of high-precision temperature sensors cross-calibrated in the laboratory will be installed behind the lateral FCs. The baseline design assumes six arrays with 24 sensors each. Spacing between sensors is 40 cm at the top and bottom and 80 cm in the middle area. As Figure 4.4 shows, a configuration with 24 sensors was appropriate in ProtoDUNE-SP, as it should be in the DP module where the expected total gradient is no larger than in ProtoDUNE-SP (see Figure 4.2). To mitigate the risk of sensor failures, installing two sensors at each position is under consideration.

Sensors will be cross-calibrated in the laboratory using a controlled environment and a high-precision readout system, described in Section 4.2.2.5. The accuracy of the calibration for ProtoDUNE-SP was estimated to be 2.6 mK (see Figure 4.10). Figure 4.11 shows the preliminary results of the analysis of ProtoDUNE-SP static T-gradient monitor data. The temperature profile was computed using both the laboratory calibration and the so-called *in-situ pump-off calibration*, which consists of estimating the offsets between sensors assuming the temperature of LAr in the cryostat is homogeneous when the re-circulation pumps are off. (The validity of this method is demonstrated in Section 4.2.2.2.) The RMS of the difference between both methods is 4.6 mK, slightly more than the value quoted above for the accuracy of laboratory calibration, due to the presence of a few outliers (under investigation) and the imperfect assumption of homogeneous temperature when pumps are off (see Figure 4.15).

[9] Lake Shore Cryotronics™ platinum RTD series, `https://www.lakeshore.com/`.
[10] Axon™ Cable, `http://www.axon-cable.com`.

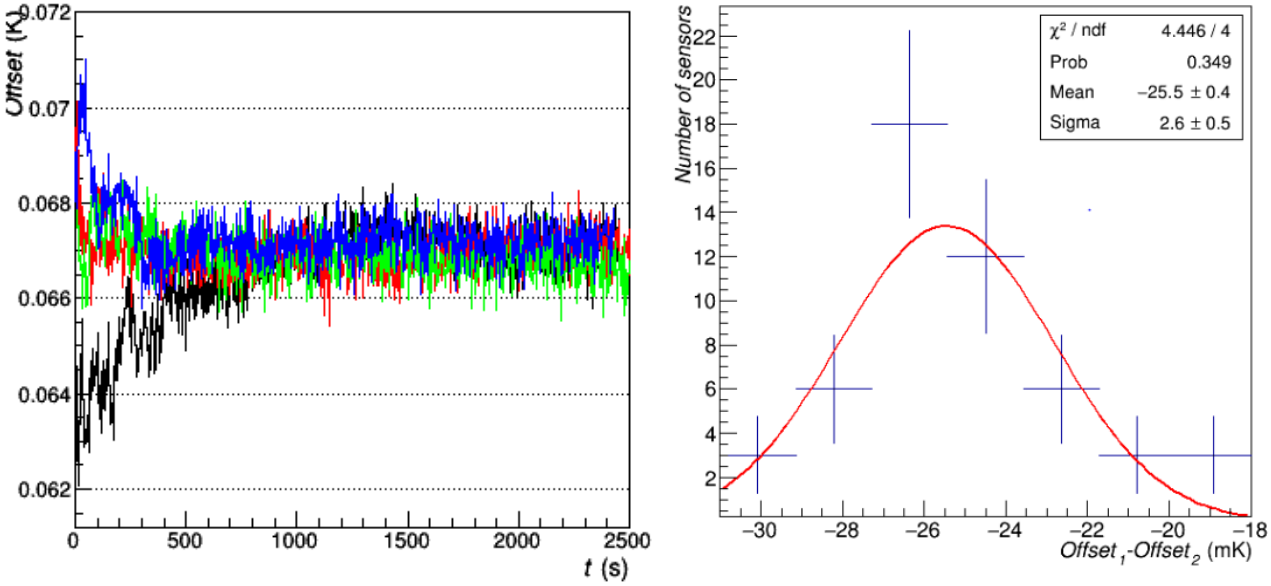

Figure 4.10: Left: Temperature offset between two sensors as a function of time for four independent immersions in LAr. The reproducibility of those sensors, defined as the RMS of the mean offset in the flat region, is $\sim$ 1 mK, The resolution for individual measurements, defined as the RMS of one offset in the flat region, is more than 0.5 mK. Right: Difference between the mean offset obtained with two independent calibration methods for the 51 calibrated sensors. The standard deviation of this distribution is interpreted as precision of the calibration.

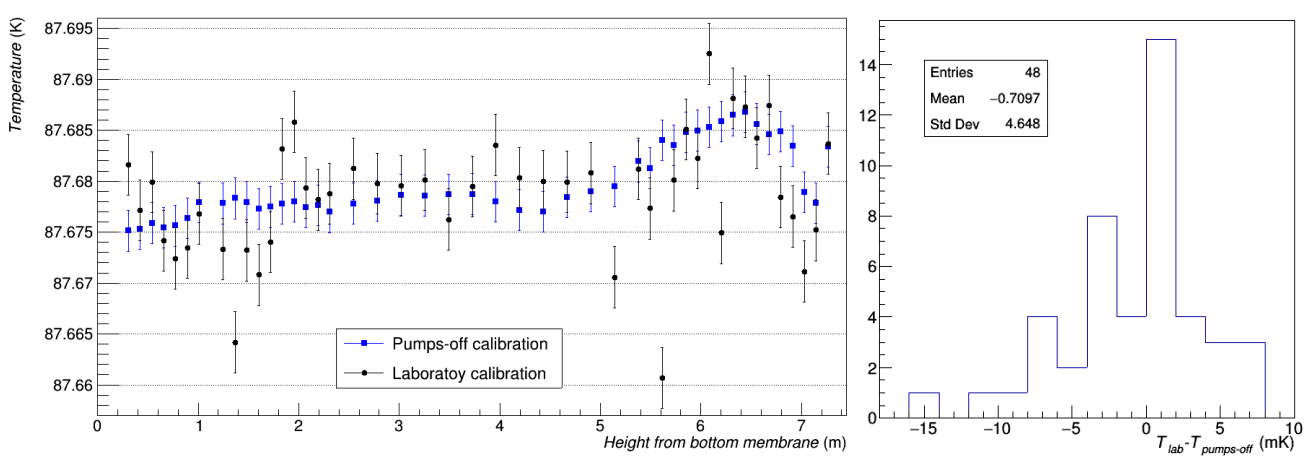

Figure 4.11: Left: Temperature profile as measured by the static T-gradient monitor for two different calibration methods. Right: Distribution of the difference between both methods.

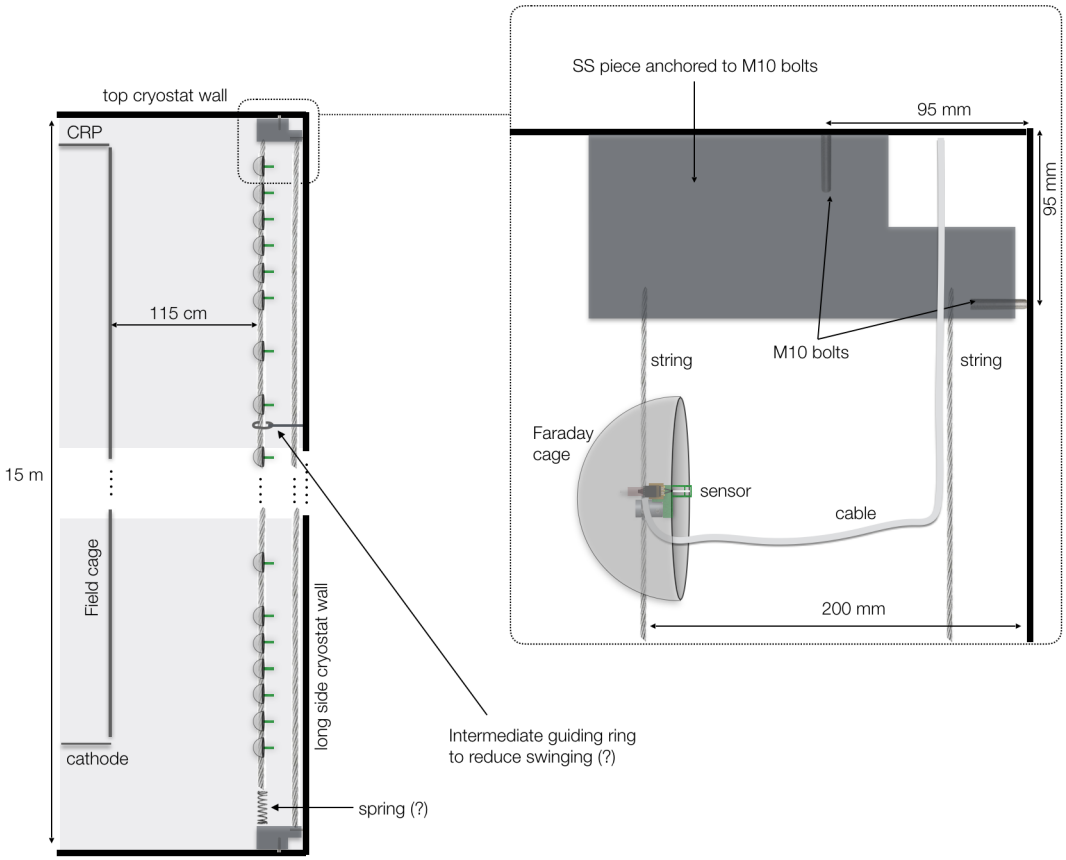

Figure 4.12: Conceptual design of the static T-gradient monitor.

Figure 4.12 shows the baseline mechanical design of the static T-gradient monitor. Two vertical strings are anchored at the top and bottom corners of the cryostat using the available M10 bolts (see Figure 4.13, left). One string routes the cables while the other, separated from the first by 150 mm, supports the temperature sensors and the individual Faraday cages. Given the height of the cryostat, an intermediate anchoring point might be needed to reduce swinging. To reduce the effect of shrinkage in the strings under cryogenic conditions and to guarantee that the same tension is always applied, springs will be made of materials with low coefficients of linear thermal expansion like carbon fiber or invar. A special spring could be also used. A prototype is being built at IFIC, where the full system will be mounted using two dummy cryostat corners.

Figure 4.13, right shows the baseline design of the ($52 \times 15\,\mathrm{mm}^2$) PCB support for temperature sensors with an IDC-4 male connector.

A narrower connector (with two rows of two pins each) is being studied. This alternative design would reduce the width of the PCB assembly and allow more sensors to be calibrated simultaneously. Each four-wire cable from the sensor to the flange will have an IDC-4 female connector on the sensor end; the flange end of the cable will be soldered or crimped to the appropriate connector, whose type and number of pins depend on the final design of the detector support system (DSS) ports that will be used to extract the cables. SUBD-25 connectors were used in ProtoDUNE-SP.

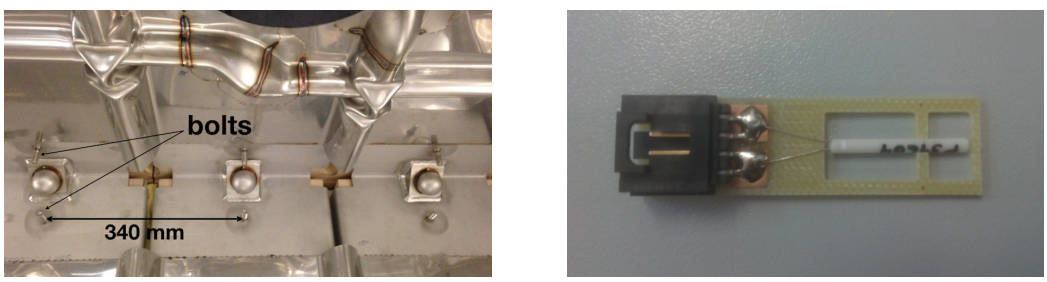

Figure 4.13: Left: bolts at the bottom corner of the cryostat. Right: Lakeshore PT102 sensor mounted on a PCB with an IDC-4 connector.

4.2.2.2 Dynamic T-gradient monitors

Potential differences in sensor readings before and after sensors are installed in a detector module and potential drifts over the lifetime of the module may affect accuracy of the vertical temperature gradient measurement. Thus, to address these concerns, a dynamic temperature monitor can cross-calibrate sensor readings *in situ*. This T-gradient monitor is motorized, allowing vertical movement of the temperature sensor array in the detector module, enabling precise cross-calibration between the sensors *in situ*, as illustrated in Figure 4.14.

Cross-calibrations requires several steps. In step 1, the temperature reading of all sensors is taken at the home (lowest) position of the carrier rod. In step 2, the stepper motor moves the carrier rod up 25 cm. The sensors along the entire carrier rod are positioned 25 cm apart, so when the system moves up 25 cm, each sensor is positioned at the height occupied by another sensor in step 1. Then a second temperature reading is taken. Other than the lowest position, this means two temperature measurements are taken at each location with different sensors. Assuming that the

temperature at each location is stable over the few minutes required to make the measurements, any differences in the temperature readings between the two different sensors would be due to their relative measurement offset. This difference is then calculated for all locations. In step 3, readout differences between pairs of sensors at each location are linked to one another, so each sensor measures the temperature at all heights. In this way, temperature readings from all sensors are cross-calibrated *in situ*, canceling all possible offsets due to electromagnetic noise or any parasitic resistances that may occur despite the four-point connection to the sensors that should cancel most offsets. These measurements are taken with a very stable current source, which ensures high precision of repeated temperature measurements over time. The dynamic T-monitor operates with a stepper-motor, so measurements are delivered with high spatial resolution.

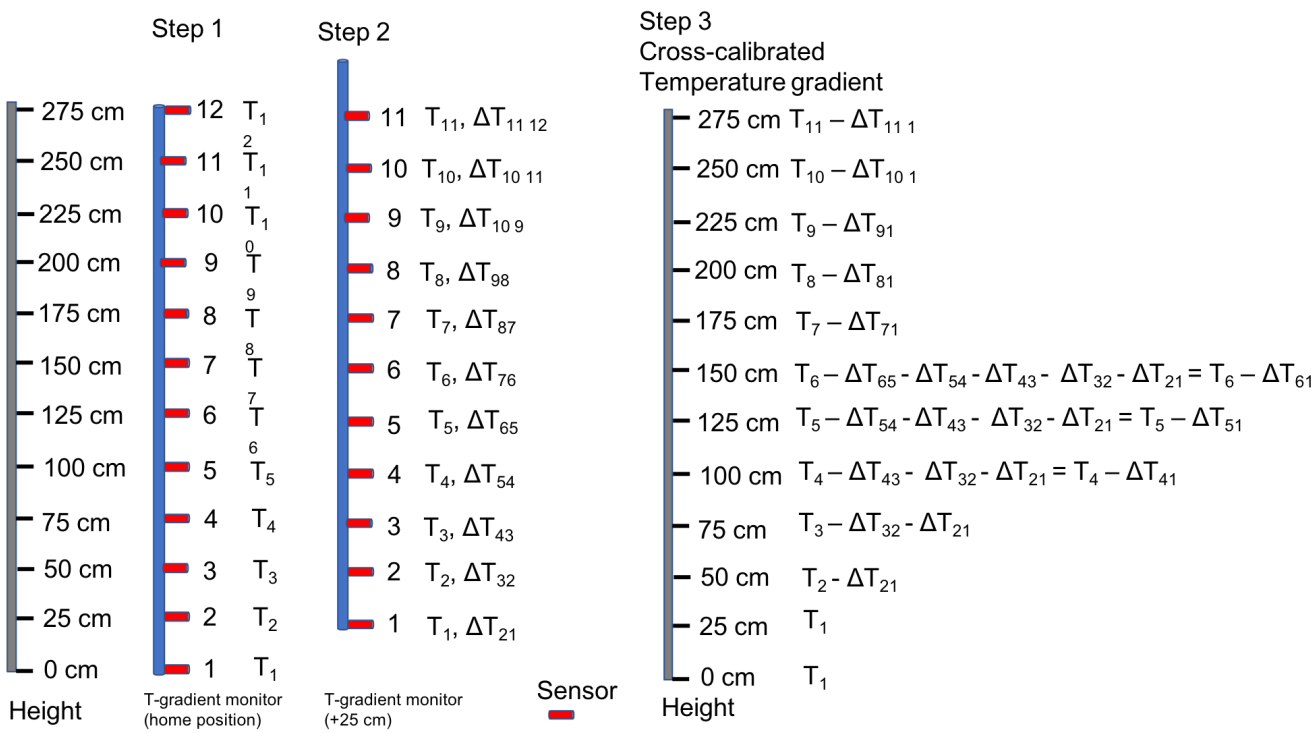

Figure 4.14: In step 1, sensor temperature measurements are taken with the T-gradient monitor in the home position. In step 2, the entire system is moved up 25 cm, and another set of temperature readings is taken by all sensors. Then, the offsets between pairs of sensors are calculated for each position. In step 3, offsets are linked together, providing cross-calibration of all sensors, to obtain the entire vertical temperature gradient measurement for a single sensor (number 1 in this case).

A total of 72 sensors will be installed and spaced 25 cm apart, although at the top and bottom 1 m of the carrier rod, sensor spacing is decreased to 10 cm. With the vertical displacement of the system, every sensor can be moved to the nominal position of at least five other sensors, minimizing any risks associated with sensor failure and providing several points of comparison. The total expected motion range of the carrier rod is 1.35 m.

This procedure was tested in ProtoDUNE-SP, where the system was successfully moved up by a maximum of 51 cm, allowing cross-calibration of all sensors (22 sensors with 10.2 cm spacing at top and bottom and 51 cm in the middle). Figure 4.4 shows the temperature profile after calibration; the smoothness of the profile demonstrates the reliability of the method. An even better figure

of merit is the temperature profile after cross-calibration, when the recirculation pumps are off. Under these conditions, the temperature should be homogeneous except near the surface. This is indeed what Figure 4.15 shows.

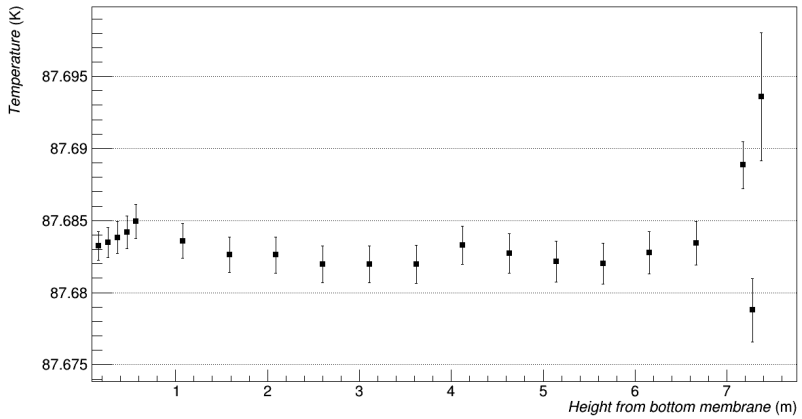

Figure 4.15: Temperature profile as measured by the dynamic T-gradient monitor after cross-calibration when the recirculation pumps are off. Temperature variation is approximately 3 mK except close to the top and the gas phase interface, as expected.

A dynamic T-gradient monitor has three parts: a carrier rod on which sensors are mounted; an enclosure above the cryostat housing space that allows the carrier rod to move vertically 1.5 m over its lowest location; and the motion mechanism. The motion mechanism is a stepper motor connected through a ferrofluidic dynamic seal to a gear and pinion motion mechanism. The sensors have two pins soldered to a PCB. Two wires are individually soldered to the common soldering pad for each pin. A cutout in the PCB around the sensor allows free flow of argon for more accurate temperature readings. Stepper motors typically have very fine steps that allow highly precise positioning of the sensors. Figure 4.16 shows the overall design of the dynamic T-gradient monitor. The enclosure has two parts connected by a six-cross flange. One side of this flange will be used for signal wires, another will be used as a viewing window, and the two other ports will be spares. Figure 4.17, left, shows the PCB mounted on the carrier rod and the sensor mounted on the PCB along with the four point connection to the signal readout wires. Figure 4.17, right, shows the stepper motor mounted on the side of the rod enclosure. The motor remains outside the enclosure, at room temperature, as do its power and control cables.

Figure 4.16: A schematic of the dynamic T-gradient monitor.

4.2.2.3 Individual Temperature Sensors

T-gradient monitors will be complemented by a coarser 2D array (every 5 m) of precision sensors at the bottom of the detector module, as shown in Figure 4.9. These sensors could use the cryogenic pipes as a support structure following the ProtoDUNE-SP design. An alternative design using the support structure for photon detector (PD)s is also under consideration.

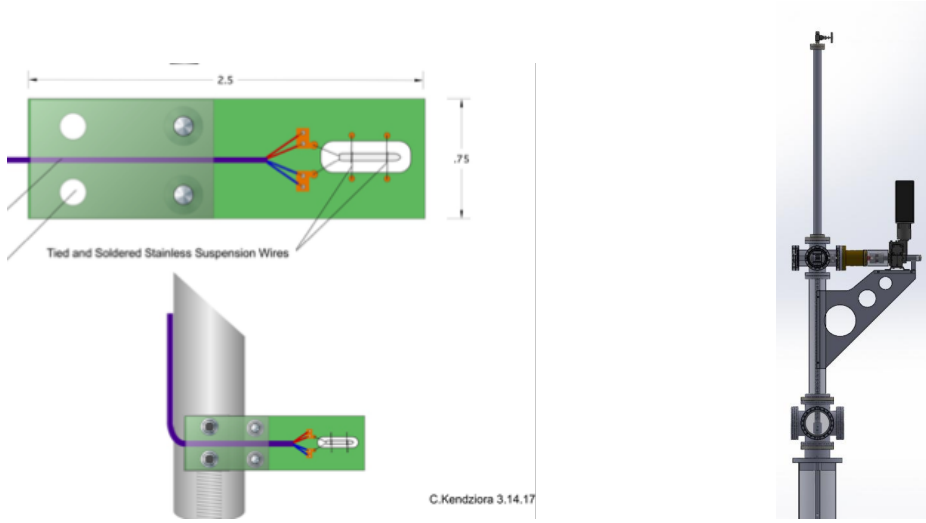

Figure 4.17: Left: Sensor mounted on a PCB board, and PCB board mounted on the rod. Right: The driving mechanism of the dynamic T-gradient monitor consisting of a stepper motor driving the pinion and gear linear motion mechanism.

As in ProtoDUNE-SP, another set of standard sensors will be evenly distributed and epoxied to the bottom membrane. They will detect the presence of LAr when cryostat filling starts. Finally, two vertical arrays of standard sensors will be epoxied to the lateral walls in two opposite vertical corners, spaced 102 cm apart (every three corrugations), to monitor the cryostat membrane temperature during cooldown and filling.

Whereas in ProtoDUNE-SP, cables were routed individually (without touching neighboring cables or any metallic elements) to prevent grounding loops in case the outer Teflon jacket broke, such a failure is very unlikely. Thus, in the detector modules, cables will be routed in bundles, simplifying the design enormously. Cable bundles of several sizes will be configured using custom made Teflon pieces that will be anchored to different cryostat and detector elements to route cables from sensors to the assigned cryostat ports. For sensors at the bottom (on pipes/PDs and floor), cables will be routed towards the bottom horizontal corner of the cryostat using stainless steel split clamps anchored to pipes (successfully prototyped in ProtoDUNE-SP) and from there, to the top of the cryostat using vertical strings (as with static T-gradient monitors). Sensors on the walls will use bolts in the vertical corners for cable routing.

For all individual sensors, PCB sensor support, cables, and connection to the flanges will be the same as for the T-gradient monitors.

4.2.2.4 Vertical arrays in gas phase

The temperature map in the gas is specially important for the dual phase technology. As in ProtoDUNE-DP, the region immediately above (about 40 cm) the CRPs will be instrumented with vertical arrays of temperature sensors. The baseline design foresees for each of these arrays 8 standard RTDs with increasing pitch with height above the CRP, as shown in Figure 4.18 for the device installed in ProtoDUNE-DP. Twenty (20) of these arrays would be distributed throughout

the top of the cryostat. Unlike the liquid, where the temperature gradient is not larger than 10 mK, the temperature in the gas changes very rapidly with height, and a relative precision of 0.1 K is sufficient for those sensors. Thus, standard RTDs with calibration can be used.

Figure 4.18: Vertical array of temperature sensors in ProtoDUNE-DP.

4.2.2.5 Readout system for thermometers

A high-precision and very stable system is required to achieve a readout level of $< 5\,\mathrm{mK}$. The proposed readout system was used in ProtoDUNE-SP and relies on a variant of an existing mass PT100 temperature readout system developed at European Organization for Nuclear Research (CERN) for an LHC experiment; it has already been tested and validated by the collaboration experts. The system has an electronic circuit that includes

- a precise and accurate current source for exciting the temperature sensors measured using the four-wires method;
- a multiplexing circuit connecting the temperature sensor signals and forwarding the selected signal to a single line; and
- a readout system with a high-accuracy voltage signal readout module[11] with 24 bit resolution over a 1 V range.

[11] National Instrument CompactRIO™ device with a signal readout NI9238™ module

This readout system also drives the multiplexing circuit and calculates temperature values. The CompactRIO device is connected to the detector Ethernet network, sending temperature values to the DCS software through a standard OPC-UA driver.

The current mode of operation averages more than 2000 samples taken every second for each sensor. Figure 4.10 shows the system has a resolution higher than 1 mK, the RMS of one of the offsets in the stable region.

4.2.3 Liquid Level Monitoring

The LAr level monitoring system has two goals: basic level sensing when filling and precise level sensing during stable operations. The system also provides information for safety interlocks (e.g. HV). DUNE will use both differential pressure level meters (LBNF scope) and capacitive level meters (DUNE scope). Liquid level meters provide useful information for both cryostat filling and stable operation. Dedicated level meters will be complemented by vertical arrays of temperature sensors (see Section 4.2.2), located at known heights and used to determine the LAr level (they will change temperature dramatically when the cold liquid reaches each of them), and by cameras, which will focus on the LAr surface at all times.

Filling the cryostat with LAr will take several months. During this operation, several systems will monitor the LAr level. The first 5.5 m of LAr will be monitored by cameras and by the vertical arrays of RTDss. Once the liquid reaches the level of the cryogenic pipes going out of the cryostat, the differential pressure between that point and the bottom of the cryostat can be converted to depth using the known density of LAr. Fine tuning the final LAr level require several capacitive level meters at the top of the cryostat; this system comprises several 4 m long capacitive level sensors (with a precision of less than 5 mm) which will be checked against each other. One capacitive level sensor at each of the four corners of the cryostat will provide sufficient redundancy to ensure that no single point of failure compromises the measurement.

During operations, liquid level monitoring has two purposes: monitoring to tune the LAr flow, and monitoring for safety interlocking purposes and for cross checks.

The LAr flow is tuned using two differential pressure level meters, installed as part of the cryogenics system, one on each side of the detector module. They have a precision of 0.1 %, which corresponds to 14 mm at the nominal LAr surface. Cryogenic pressure sensors will be purchased from commercial sources. Installation methods and positions will be determined as part of the cryogenics internal piping plan. The dual phase technology must control the LAr surface at the sub-millimeter level, so fine tuning the LAr level will require two high precision capacitive level meters attached to the inner cryostat membrane at the appropriate height.

For safety interlocking and to cross check measurements with differential pressure level meters the long capacitive level meters will be used.

In addition to these level meters, the CRP will use high precision (less than 1 mm) capacitive level meters attached to the CRP frame to monitor constant CRP alignment to the liquid surface.

These fall under the scope of the CRP consortium and are described in Chapter **??** of this TDR volume.

Figure 4.19 shows the evolution of the ProtoDUNE-SP LAr level over two months as measured by the differential pressure and capacitive level meters.

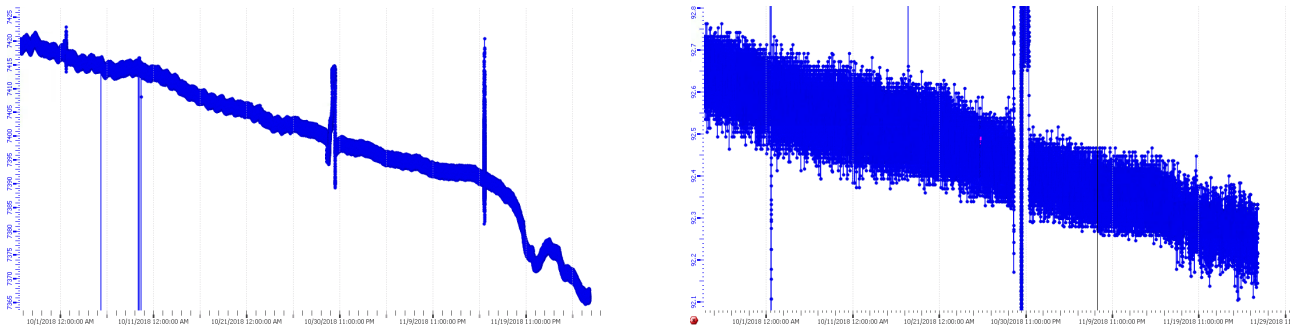

Figure 4.19: Evolution of the ProtoDUNE-SP LAr level over two months. Left: Measured by the capacitive level meter. Right: Measured by the differential pressure level meter. The units in the vertical axis are percentages of the cryostat height (7878 mm).

ProtoDUNE-SP and ProtoDUNE-DP use the same design for differential pressure level meters and will also be used in the far detector SP and DP modules. For the capacitive level meters, ProtoDUNE-SP is using commercial 1.5 m long level meters while ProtoDUNE-DP is using 4 m long level meters custom-built by CERN. For the DUNE FD, we plan to use the longer capacitive level meters custom-built by CERN for both SP and DP modules.

4.2.4 Pressure Meters

Measuring the pressure of argon gas in the DUNE FD is important because it can affect gas density, and consequently, the LEM gain calibration. The accuracy of the pressure sensors should be within at least 0.1% or more of the real value. Moreover, the absolute temperature in the liquid varies with the pressure in the argon gas, so precise measurements of pressure inside the cryostat provides a better picture of temperature gradients and CFD simulations. In ProtoDUNE, pressure values were also used to understand the strain gauge signals installed in the cryostat frame.

Standard industrial pressure sensors can be used for this. For the DUNE FD, the plan is to follow the same design and configuration used in ProtoDUNE-SP and ProtoDUNE-DP. ProtoDUNE uses two types of pressure sensors and a pressure switch as described below:

- A relative pressure sensor (range: 0-400 mbar, precision: 0.01 mbar),
- An absolute pressure sensor (range: 0-1600 mbar, precision: 0.05 mbar),
- A mechanical relative pressure switch adjustable from 50 to 250 mbar.

Both sensors and the pressure switch are installed in a dedicated flange as shown in Figure 4.20

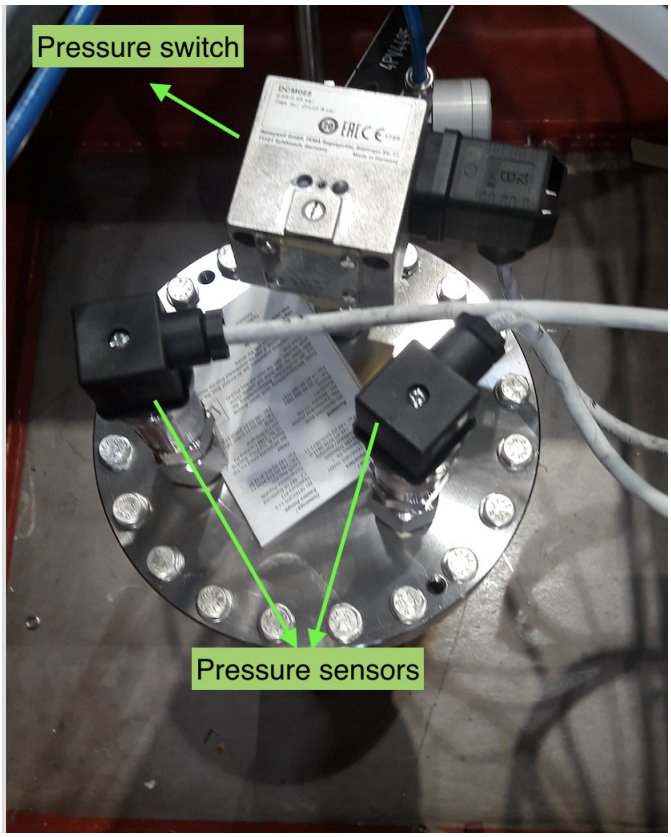

Figure 4.20: Photograph of the pressure sensors installed on a flange in ProtoDUNE-SP.

and are connected directly to a slow controls system PLC circuit. Dedicated analogue inputs are used to read the current values (4 to 20 mA), which are then converted to pressure according to sensor range. Given the much larger size of DUNE FD, this system will be doubled for redundancy: two flanges in opposite cryostat sides will be instrumented with three sensors each.

Further, relative and absolute pressure sensors (with comparatively lower precision) are installed by LBNF that are also recorded by the slow controls system. The availability of two types of sensors from LBNF and CISC provides redundancy, independent measurements, and cross checks.

4.2.5 Gas Analyzers

Gas analyzers are commercially produced modules that measure trace quantities of specific gases contained within a stream of carrier gas. The carrier gas for DUNE is argon, and the trace gases of interest are oxygen (O_2), water (H_2O), and nitrogen (N_2). O_2 and H_2O affect the electron lifetime in LAr and must be kept below 0.1 ppb (O_2 equivalent) while N_2 affects the efficiency of scintillation light production at levels higher than 1 ppm. The argon is sampled from either the argon vapor in the ullage or from the LAr by using small diameter tubing run from the sampling point to the gas analyzer. Typically, the tubing from the sampling points are connected to a switchyard valve assembly used to route the sample points to the desired gas analyzers (see Figure 4.21).

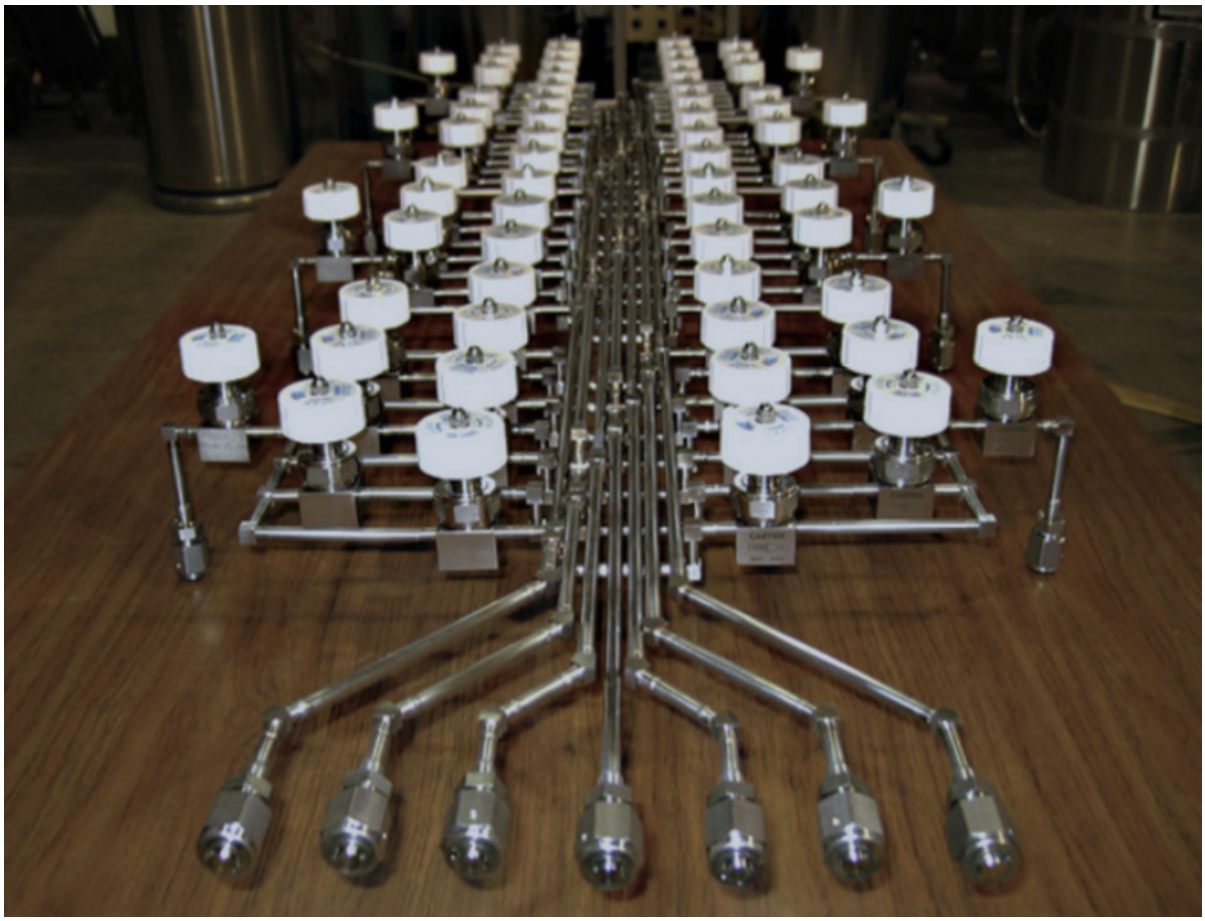

Figure 4.21: A gas analyzer switchyard that routes sample points to the different gas analyzers.

The gas analyzer would be predominantly used during three periods:

1. Once the detector is installed and after the air atmosphere is eliminated from the cryostat to levels low enough to begin cooldown. This purge and gas recirculation process is detailed in Section 4.4.6.3. Figure 4.22 shows the evolution of the N_2, O_2, and H_2O levels from gas analyzer data taken during the purge and recirculation stages of the DUNE 35 ton prototype phase 1 run.

2. Before other means of monitoring impurity levels (e.g., purity monitors or TPC tracks) are sensitive, to track trace O_2 and H_2O contaminants from tens of ppb to hundreds of ppt. Figure 4.23 shows an example plot of O_2 levels at the beginning of LAr purification from one of the later 35 ton prototype HV runs.

3. During cryostat filling to monitor the tanker LAr delivery purity. This tracks the impurity load on the filtration system and rejects any deliveries that do not meet specifications. Likely specifications for delivered LAr are in the 10 ppm range per contaminant.

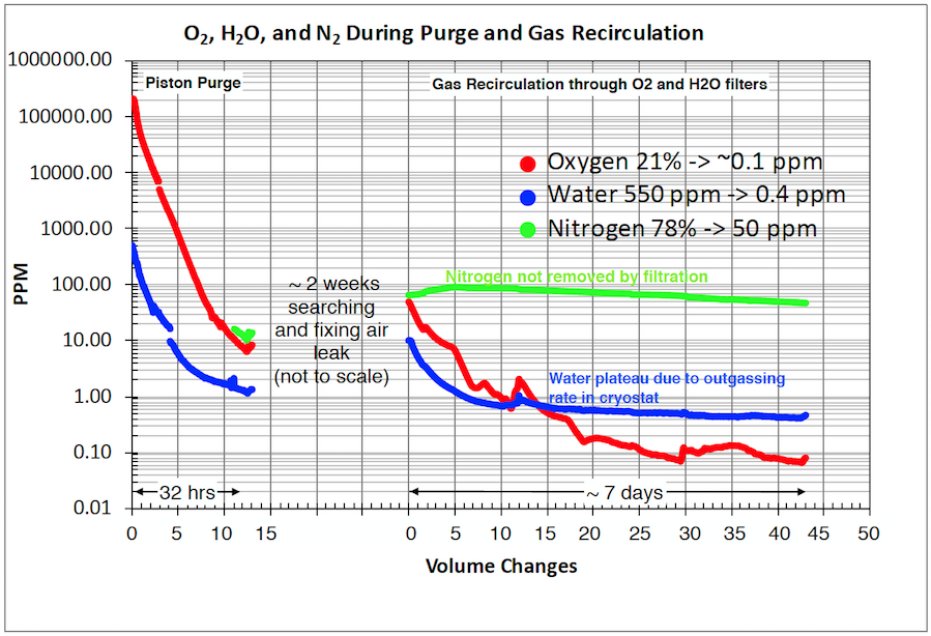

Figure 4.22: Plot of the O_2, H_2O, and N_2 levels during the piston purge and gas recirculation stages of the 35 ton prototype Phase 1 run.

Because the filling and commissioning of different cryostats will occur at different times, sharing the same gas analyzer installation between them should be possible with minimal effect on the operation on other cryostats. The gas analyzer switchyard can easily switch between cryostat source lines. Since any one gas analyzer covers only one contaminant species and a range of 3 to 4 orders of magnitude, several units are needed both for the three contaminant gases and to cover the ranges seen between cryostat closure and the beginning of TPC operations: 20 % to $\lesssim$ 100 ppt for O_2, 80 % to $\lesssim$ 1 ppm for N_2, and $\sim$ 1 % to $\lesssim$ 1 ppb for H_2O. Because the total cost of these analyzers exceeds \$100 k, we want to be able to sample more than a single location or cryostat with the same gas analyzer. At the same time, the tubing run lengths from the sample point should be as short as possible to maintain a timely response for the gas analyzer. This puts some

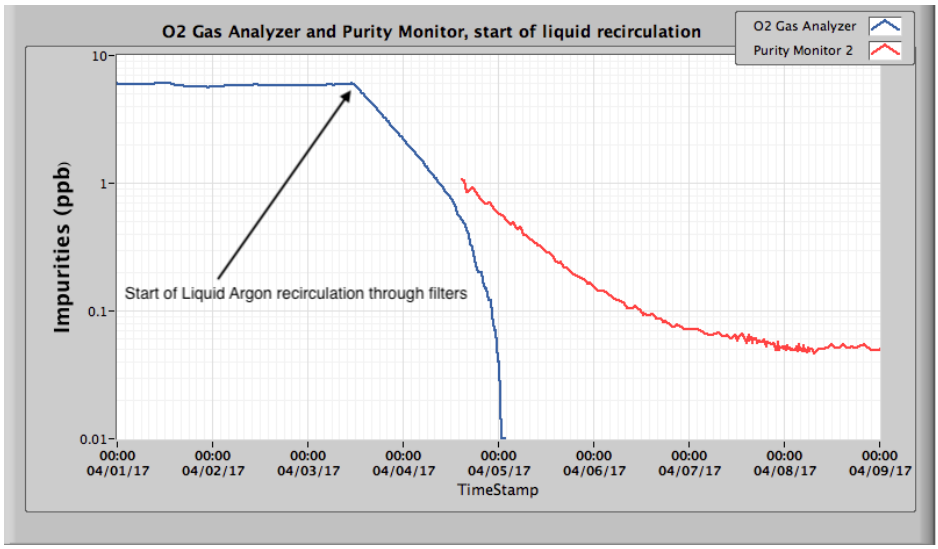

Figure 4.23: O_2 as measured by a precision O_2 analyzer just after the 35 ton prototype cryostat is filled with LAr, continuing with the LAr pump start and beginning of LAr recirculation through the filtration system. As the gas analyzer loses sensitivity, the purity monitor can pick up the impurity measurement. Note that the purity monitor is sensitive to both O_2 and H_2O impurities giving rise to its higher levels of impurity.

constraints on sharing devices because, for example, argon is delivered at the surface, so a separate gas analyzer may be required there.

4.2.6 Cameras

Cameras provide direct visual information about the state of the detector module during critical operations and when damage or unusual conditions are suspected. Cameras in the WA105 DP demonstrator showed spray from cooldown nozzles and the level and state of the LAr as it covered the CRP [64]. A camera was used in the Liquid Argon Purity Demonstrator cryostat[63] to study HV discharges in LAr and in EXO-100 while a TPC was operating [65]. Warm cameras viewing LAr from a distance have been used to observe HV discharges in LAr in fine detail [66]. Cameras are commonly used during calibration source deployment in many experiments (e.g., the KamLAND ultra-clean system [67]).

In DUNE, cameras will verify the stability, straightness, and alignment of the hanging TPC structures during cooldown and filling; ensure that no bubbling occurs near the ground planes (GPs) (SP) or CRPs (DP); inspect the state of movable parts in the detector module (calibration devices, dynamic thermometers); and closely inspect parts of the TPC after any seismic activity or other unanticipated event. For these functions, a set of fixed cold cameras are used; they are permanently mounted at fixed points in the cryostat for use during filling and commissioning. A movable, replaceable warm inspection camera can be deployed through any free instrumentation flange at any time during the life of the experiment.

As this is written, the ProtoDUNE-DP installation is nearing completion, and no validation of

camera operation in ProtoDUNE-DP is yet available. However, eleven cameras were deployed in ProtoDUNE-SP. They successfully provided views of the detector during filling and throughout its operation. The camera designs used in ProtoDUNE will be the basis for the final camera designs used in the DP module.

The following sections describe the design considerations for both cold and warm cameras and the associated lighting system. ProtoDUNE-SP camera system designs and performance are also discussed. The same basic designs can be used for both the SP and DP detector modules.

4.2.6.1 Cryogenic Cameras (Cold)

The fixed cameras monitor the following items during filling:

- positions of corners of CRPs, cathode, FCs, GPs (1 mm resolution),
- relative straightness and alignment of CRPs, cathode, and FCs ($<\sim 1$ mm),
- relative positions of FC profiles and resistive sheaths between super-modules (0.5 mm resolution), and
- the LAr surface, specifically, the presence of bubbling or debris.

One design for the DUNE fixed cameras uses an enclosure similar to the successful EXO-100 design [65], which was also used successfully in the Liquid Argon Purity Demonstrator and ProtoDUNE-SP (see Figure 4.24). A thermocouple in the enclosure allows temperature monitoring and a heating element provides temperature control. SUB-D connectors are used at the cryostat flanges and the camera enclosure for signal, power, and control connections.

An alternative design uses an acrylic enclosure. This design was used successfully in ProtoDUNE-SP (see Figure 4.24, bottom left). All operate successfully, including those at the bottom of the cryostat. Please note that the DUNE FD will be twice as deep as ProtoDUNE, and therefore cameras observing the lowest surfaces of the FC must withstand twice the pressure.

We will continue prototyping and testing to finalize and validate the cold camera design for DUNE, focusing particularly on pressure resistance.

4.2.6.2 Inspection Cameras (Warm)

The inspection cameras are intended to be as versatile as possible. However, the following inspections have been identified as likely uses:

- status of HV feedthrough and cup,

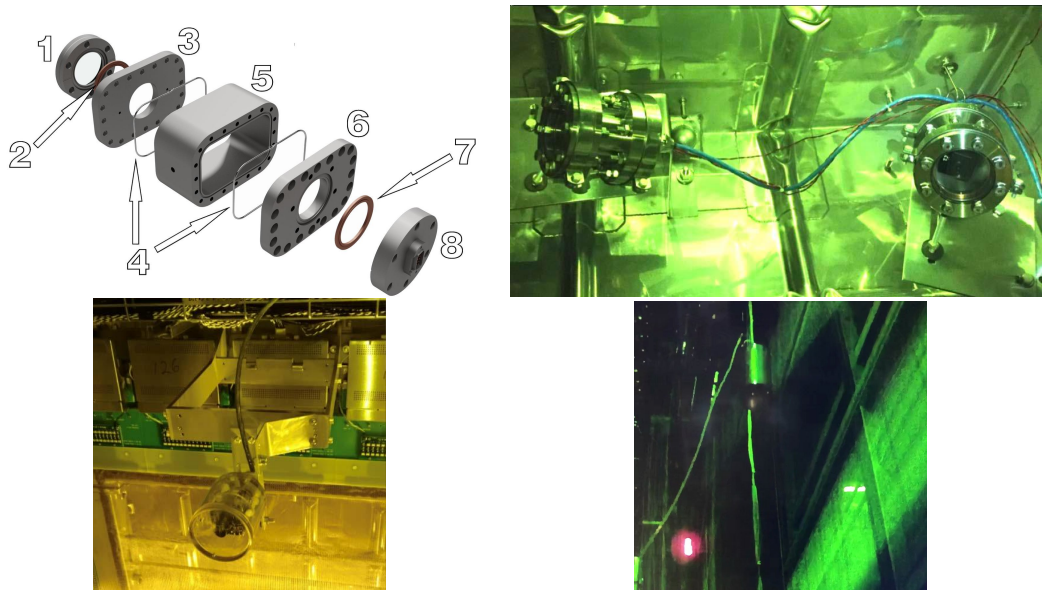

Figure 4.24: Top left: a CAD exploded view of a vacuum-tight camera enclosure suitable for cryogenic applications [65]. (1) quartz window, (2 and 7) copper gasket, (3 and 6) flanges, (4) indium wires, (5) body piece, (8) signal feedthrough. Top right: two of the ProtoDUNE-SP cameras using a stainless steel enclosure. Bottom left: one of the ProtoDUNE-SP cameras using acrylic enclosure. Bottom right: a portion of an image taken with ProtoDUNE-SP camera 105 showing a purity monitor mounted outside the APA on the beam left side. This photo was taken with ProtoDUNE-SP completely filled.

- status and relative position of FC profiles, resistive sheaths between FC super-modules (0.5 mm resolution),
- vertical deployment of calibration sources,
- status of thermometers, especially dynamic thermometers,
- HV discharge, corona, or streamers on HV feedthrough, cup, or FC,
- relative straightness and alignment of CRPs, cathode, and FC (1 mm resolution), and
- gaps between CRP frames (1 mm resolution).

Unlike the fixed cameras, the inspection cameras operate only as long as any inspection; the cameras can be replaced in case of failure. It is also more practical to keep the cameras continuously warmer than −150 °C during deployment; this permits using commercial cameras. For example, cameras of the same model were used successfully to observe discharges in LAr from 120 cm away [66].

The inspection cameras use the same basic enclosure design as cold cameras, but the cameras are mounted on a movable fork, so each camera can be inserted and removed from the cryostat using a design similar to the dynamic temperature probes (see figures 4.25 (left) and 4.17). To avoid contaminating the LAr with air, the entire system is sealed, and the camera can only be deployed

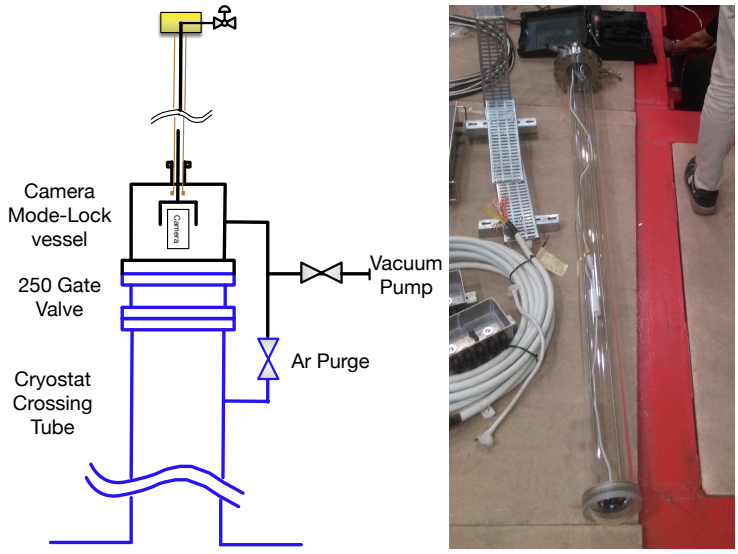

Figure 4.25: Left: An overview of the inspection camera design using a sealed deployment system opening directly into the cryostat. Right: A photograph of the ProtoDUNE-SP warm inspection camera acrylic tube immediately before installation; the acrylic tube is sealed with an acrylic dome at the bottom and can be opened at the top.

through a feedthrough equipped with a gate valve and a purging system, similar to the one used in the vertical axis calibration system at KamLAND [67]. The entire system is purged with pure argon gas before the gate valve is opened.

Motors above the flange allow the fork to be rotated and moved vertically to position the camera. A chain drive system with a motor mounted on the end of the fork allows the camera assembly to tilt, creating a point-tilt mount that can be moved vertically. With the space above the cryostat flanges and the thickness of the cryostat insulation, cameras can be moved vertically up to 1 m inside the cryostat. The motors for rotation and vertical motion are outside the sealed volume, coupled mechanically using ferrofluidic seals, thus reducing any risk of contamination and allowing manual rotation of the vertical drive if the motor fails.

An alternative design was demonstrated in ProtoDUNE-SP. In this design, the warm camera is contained inside a gas-tight acrylic tube inserted into the feedthrough, so a gate valve or a gas-tight rotatable stage is not needed; the warm cameras can thus be removed for servicing or upgrade at any time. Figure 4.25 (right) shows an acrylic tube enclosure and camera immediately before deployment. Three such tubes were installed in ProtoDUNE-SP, and cameras with fisheye lenses were operated successfully. One camera was removed without any evidence of contamination of the LAr.

We will continue prototyping and testing to finalize and validate the inspection camera design for DUNE, focusing particularly on longevity, the ability to replace the camera, and protecting the LAr.

4.2.6.3 Light-emitting system

The light-emitting system uses LEDs to illuminate the parts of the detector module in the camera's field of view with selected wavelengths (IR and visible) that cameras can detect. Performance criteria for the light-emission system include the efficiency with which the cameras can detect the light and the need to avoid adding heat to the cryostat. Very high-efficiency LEDs help reduce heat generation; one 750 nm LED [68] has a specification equivalent to 33 % conversion of electrical input power to light.

While data on how well LEDs perform at cryogenic temperatures is sparse, some studies of NASA projects [69] indicate that LED are more efficient at low temperatures and that emitted wavelengths may change, particularly for blue LEDs. In ProtoDUNE-SP, amber LEDs were observed to emit green light at LAr temperature (see bottom right photo in 4.24). To avoid degradation of wavelength-shifting materials in the PDS, short wavelength LEDs are not used in the FD.

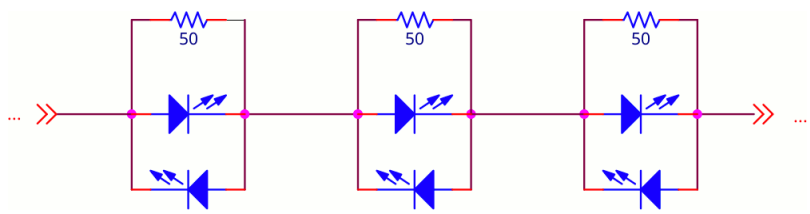

Figure 4.26: Example schematic for LED chain, allowing failure tolerance and two LED illumination spectra.

LEDs are placed in a ring around the outside of each camera, pointing in the same direction as the lens, to illuminate nearby parts of the detector module within the camera's field of view. Commercially available LEDs exist with a range of angular spreads that can match the needs of the cameras without additional optics.

Additionally, chains of LEDs connected in series and driven with a constant-current circuit are used for broad illumination, with each LED paired in parallel with an opposite polarity LED and a resistor (see Figure 4.26). This gives two different wavelengths of illumination using a single chain simply by changing the direction of the drive current and allows continued use of an LED chain even if individual LEDs fail.

4.2.7 Cryogenic Instrumentation Test Facility

The cryogenic instrumentation test facility (CITF) at Fermilab has provided access to small ($<$ 1 ton) to intermediate ($\sim$ 1 ton) volumes of purified TPC-grade LAr, required for any device intended for drifting electrons for millisecond periods.

The PAB facility at Fermilab houses the ICEBERG 3000 liter cryostat that allows fast turnaround for testing of the DUNE cold electronics (CE).

The PAB facility also includes TallBo (450 liter), Blanche (500 liter), and Luke (250 liter) cryostats.

In the recent past, Blanche has been used for HV studies, TallBo for PD studies, and Luke for the material test stand work. These studies have contributed to the design and testing of ProtoDUNE-SP components.

4.2.8 Validation in ProtoDUNE

Design validation and testing of many planned CISC systems for the DUNE DP FD will be done using data from both ProtoDUNE-SP and ProtoDUNE-DP detectors as discussed below.

- **Level Meters:** The same differential pressure level meters that are already validated in ProtoDUNE-SP will be used in DP FD. The same capacitive level meters currently used in ProtoDUNE-DP will be used in the DP FD. These will be validated in the upcoming ProtoDUNE-DP run.

- **Pressure Meters (GAr):** The same high precision pressure sensors which are already validated in ProtoDUNE-SP will be used in DP FD.

- **Gas Analyzers:** The same gas analyzers currently used in ProtoDUNE-SP will be used in DP FD. They have already been validated.

- **Vertical array of thermometers in GAr:** The same design of vertical array of thermometers currently used in ProtoDUNE-DP will be used in DP FD but with different distribution density. This design will be validated with ProtoDUNE-DP data.

- **High precision thermometer arrays in LAr:** The static and dynamic T-gradient thermometers discussed in previous sections are not yet installed in ProtoDUNE-DP, but the plan is to deploy them in the DP FD. Therefore, the validation of these devices will be performed using ProtoDUNE-SP data and can also be tested in future running of ProtoDUNE-DP.

- **Purity monitors:** The purity monitors are being validated at both ProtoDUNE-SP and ProtoDUNE-DP. Currently, ProtoDUNE-SP and ProtoDUNE-DP are using slightly different designs. For the DP FD, the plan is to use the same design as ProtoDUNE-SP along with some improvements such as longer drift purity monitors to increase the range of measured lifetime values. The ProtoDUNE-SP and ProtoDUNE-DP run 2 phase provides opportunities to test improved designs.

- **Cameras:** The various cameras are actively developed in both ProtoDUNE-SP and ProtoDUNE-DP, so the designs will be validated at both the ProtoDUNE-SP and ProtoDUNE-DP. Future improvements can be tested in ProtoDUNE-SP and ProtoDUNE-DP run 2 phase at CERN.

4.3 Slow Controls

The slow controls system collects, archives, and displays data from a broad variety of sources and provides real-time status, alarms, and warnings for detector operators. Slow controls also provides control for items such as HV systems, TPC electronics, and PD systems. Data are acquired via network interfaces. Figure 4.27 shows connections between major parts of the slow controls system and other systems. Hardware, infrastructure, and software are the three main components of the slow controls system.

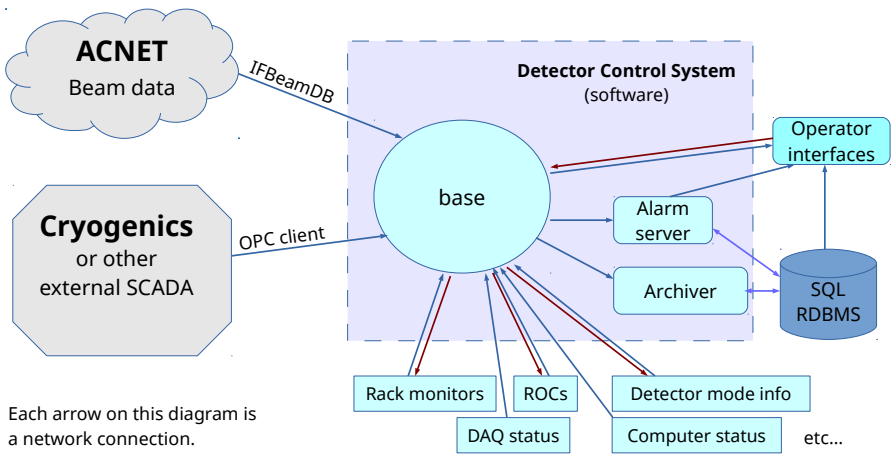

Figure 4.27: Typical slow controls system connections and data flow.

The ProtoDUNE-SP detector control system[61] met its operational requirements fully. Section 4.3.6 provides a short description of the ProtoDUNE-SP slow controls and its performance.

4.3.1 Slow Controls Hardware

Slow controls requires a modest amount of dedicated hardware, mostly for rack monitoring, and a small amount of dedicated network and computing hardware. Slow controls also relies on common infrastructure as described in Section 4.3.2.

4.3.1.1 Dedicated Monitoring Hardware

Every rack (including those in the central utility cavern (CUC)) should have dedicated hardware to monitor rack parameters like rack protection system, rack fans, rack air temperatures, thermal interlocks with power supplies, and any interlock bit status monitoring needed for the racks. For the racks in the CUC server room, this functionality is built into the proposed water cooled racks, much like what is already in place at ProtoDUNE. For the racks on the detector itself, the current plan is to design and install a custom-built 1U rack-mount enclosure containing a single-board computer to control and monitor various rack parameters. Such a system has been successfully

used in MicroBooNE. The design is being improved for the SBND experiment (see Figure 4.28). Other slow controls hardware includes interfacing cables like adapters for communication and debugging and other specialized cables like GPIB or National Instruments cables. The cable requirements must be determined in consultation with other groups once hardware choices for various systems are chosen.

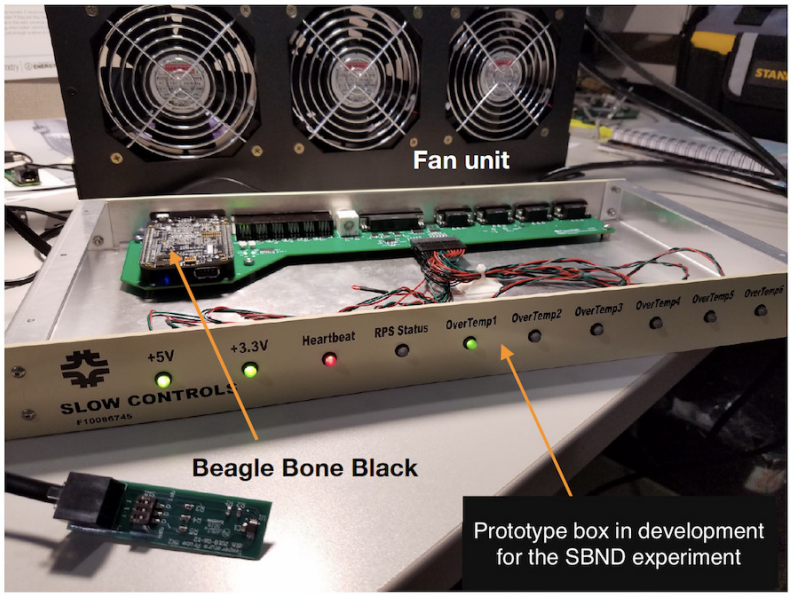

Figure 4.28: Rack monitoring box prototype in development for the short-baseline near detector (SBND) experiment based on the original design from MicroBooNE.

4.3.1.2 Slow Controls Network Hardware

The slow controls data originates from the cryogenic instrumentation and from other systems as listed in Table 4.6. This data is collected by software running on servers (see Section 4.3.1.3) housed in the underground data room in the CUC, where data is archived in a central CISC database. The instrumentation data is transported over conventional network hardware from any sensors located in the cryogenic plant. However, we must remain aware of grounding and noise in readouts in the racks on top of the cryostats. Therefore, each rack on the cryostat has a small network switch that sends any network traffic from that rack to the CUC via a fiber transponder. This is the only network hardware specific to slow controls and will be provided by SURF's general computing infrastructure. The network infrastructure requirements are described in Section 4.3.2.

4.3.1.3 Slow Controls Computing Hardware

Two servers (a primary server and a replicated backup) suitable for the relational database discussed in Section 4.3.3 are located in the CUC data room along with an additional two servers for the FE monitoring interface. These additional servers would cover assembling dynamic CISC monitoring web pages from adjacent databases. Yet another server will be needed to run back-end

I/O. Any special purpose software, such as iFix used by the cryogenics experts, would also run here. One or two additional servers should accommodate these programs. Replicating this setup for each module would make commissioning and independent operation easier, accommodate different module designs (with resulting differences in database tables), and ensure sufficient capacity. These four sets of networking hardware would fit tightly into one rack or very comfortably into two. Using the requirements from CISC, the DAQ consortium will provide the cost estimates for servers and racks.

4.3.2 Slow Controls Infrastructure

The data rate will be in the range of tens of kilobytes per second, given the total number of slow controls quantities and the update rate (see Section 4.3.4), placing minimal demands on local network infrastructure. Network traffic out of SURF to Fermilab will primarily be database calls to the central CISC database, either from monitoring applications or from database replication to the offline version of the CISC database. This traffic requires little bandwidth, so the proposed general purpose links both out of the underground area at SURF and back to Fermilab can accommodate the traffic.

Up to two racks of space and appropriate power and cooling are available in the CUC's DAQ server room for CISC use. This is ample space (see Section 4.3.1.3).

4.3.3 Slow Controls Software

To provide complete monitoring and control of detector subsystems, the slow controls software includes

- the control systems base for input and output operations and defining processing logic, scan conditions, and alarm conditions;
- an alarm server to monitor all channels and send alarm messages to operators;
- a data archiver for automatic sampling and storing values for history tracking; and
- an integrated operator interface providing display panels for controls and monitoring.

In addition, the software must be able to interface indirectly with external systems (e.g., cryogenics control system) and databases (e.g., beam database) to export data into slow controls process variables (or channels) for archiving and status displays. This allows us to integrate displays and warnings into one system for the experiment operators and provides integrated archiving for sampled data in the archived database. As one possibility, an input output controller (IOC) running on a central DAQ server could provide soft channels for these data. Figure 4.27 shows a typical workflow of a slow controls system.

The key features of the software require highly evolved software designed to manage real-time data exchange, scalable to hundreds of thousands of channels sampled at intervals of hours to seconds as needed. The software must be well documented, supported, and reliable. The base software must also allow easy access to any channel by name. The archiver software must allow data storage in an SQL database with adjustable rates and thresholds so data for any channel can be easily retrieved using channel name and time range. Among other key features, the alarm server software must remember the state, support an arbitrary number of clients, and provide logic for delayed alarms and acknowledging alarms. A standard naming convention for channels will be part of the software to help handle large numbers of channels and subsystems.

The ProtoDUNE detector control system software [61] provides a prototype for this required FD slow controls software, as described in Section 4.3.6.

4.3.4 Slow Controls Quantities

The final set of quantities to monitor will ultimately be determined by which subsystems are monitored, documented in appropriate interface control documents , and continually revised based on operational experience. The total number of quantities to monitor is roughly estimated by scaling how much is monitored in ProtoDUNE-DP, approximately 150,000 per FD module. Quantities should update on average no more than once per minute. Transmitting a single update for each channel at that rate translates to a few thousand updates per second, or a few tens of thousands of bytes per second. While this is not a significant load on a network with an efficient slow controls protocol, it would correspond to approximately 1 TB per year if every timestamp and value were stored.

The monitored subsystems include the cryogenic instrumentation described in this chapter, the other detector systems, and relevant infrastructure and external devices. Table 4.6 lists what we can expect from each system.

4.3.5 Local Integration

The local integration of slow controls consists entirely of software and network interfaces with systems outside the scope of the detector module. This includes the following:

- readings from the LBNF-managed external cryogenics systems, for status of pumps, flow rates, inlet, and return temperature and pressure, which are implemented via OPC or a similar SCADA interface ;

- beam status, such as protons-on-target, rate, target steering, and beam pulse timing, which are retrieved via the IFbeam DB ; and

- near detector status, which can be retrieved from a common slow controls database.

Table 4.6: Slow controls quantities.

System	Quantities
Detector cryogenic instrumentation	
Purity monitors	anode and cathode charge, bias voltage and current, flash lamp status, calculated electron lifetime
Thermometers	temperature, position of dynamic thermometers
Liquid level	liquid level
Pressure meters	pressure readings
Gas analyzers	purity level readings
Cameras	camera voltage and current draw, temperature, heater current and voltage, lighting current and voltage
Other detector systems	
Cryogenic internal piping	feedthrough gas purge flow and temperature
HV systems	drift HV voltage and current, end-of-field cage current and bias voltage, electron diverter bias, ground plane currents
TPC electronics	voltage and current to electronics
PD	voltage and current for photodetectors and electronics
DAQ	warm electronics currents and voltages, run status, DAQ buffer sizes, trigger rates, data rates, GPS status, computer and disk health status, other health metrics as defined by DAQ group
CRP / APA	bias voltages and currents
Infrastructure and external systems	
Cryogenics (external)	status of pumps, flow rates, inlet and return temperature and pressure (via OPC or similar SCADA interface)
Beam status	protons on target, rate, target steering, beam pulse timing (via IFBeamDB)
Near detector	near detector run status (through common slow controls database)
Rack power and status	power distribution unit current and voltage, air temperature, fan status if applicable, interlock status
Detector calibration systems	
Laser	laser power, temperature, operation modes, other system status as defined by calibration group
External neutron source	safety interlock status, power supply monitoring, other system status as defined by calibration group
External radioactive source	system status as defined by calibration group

Integration occurs after both the slow controls and non-detector systems are in place. The LBNF-CISC interface is managed by the cryogenics systems working group in CISC (see Section 4.4), which includes members from both CISC and LBNF. The IFbeam DB interface for slow controls is an already well established method used in MicroBooNE, NOνA, and other Fermilab experiments. An internal near detector (ND)/FD working group can be established to coordinate detector status exchange between the near and far sites.

4.3.6 Validation in ProtoDUNE

The ProtoDUNE slow control system has met all requirements for operation of ProtoDUNE-SP[61] and will be used for ProtoDUNE-DP. The requirements for ProtoDUNE are nearly identical to those for the SP module and DP module other than total channel count. Of particular note, the ProtoDUNE slow control system unified a heterogenous set of devices and data sources through several protocols into a single control system (see Figure 4.29). In addition, data were also acquired from external cryogenic and beam systems. The topology and data flow of the system matches the general shape shown in Figure 4.27. In this control system, the unified control system base is WinCC OA [70], a commercial toolkit used extensively at CERN, with device interfaces supported using several standardized interface protocols.

As noted in sections 4.3.3 and 4.3.4, the DP module slow control system will produce massive amounts of data, requiring a sizable database to store the value history and allow efficient data retrieval. Individually adjustable rates and thresholds for each channel are key to keeping this database manageable. The ProtoDUNE-SP operations provided not only a test of these features as implemented in the ProtoDUNE slow control system, but also insight into reasonable values for these archiving parameters for each system.

4.4 Organization and Management

The organization of the CISC consortium is shown in Figure 4.30. The CISC consortium board currently comprises institutional representatives from 19 institutes as shown in Table 4.7. The consortium leader is the spokesperson for the consortium and responsible for the overall scientific program and managing the group. The technical leader of the consortium is responsible for managing the project for the group. Currently, the consortium has five working groups:

Cryogenics Systems: gas analyzers and differential pressure liquid level monitors; CFD simulations.

Argon Instrumentation: purity monitors, thermometers (LAr and GAr), capacitive level meters, pressure meters (GAr), cameras and light emitting system, and cryogenic test facility; feedthroughs; E field simulations; instrumentation precision studies; ProtoDUNE data analysis coordination and validation.

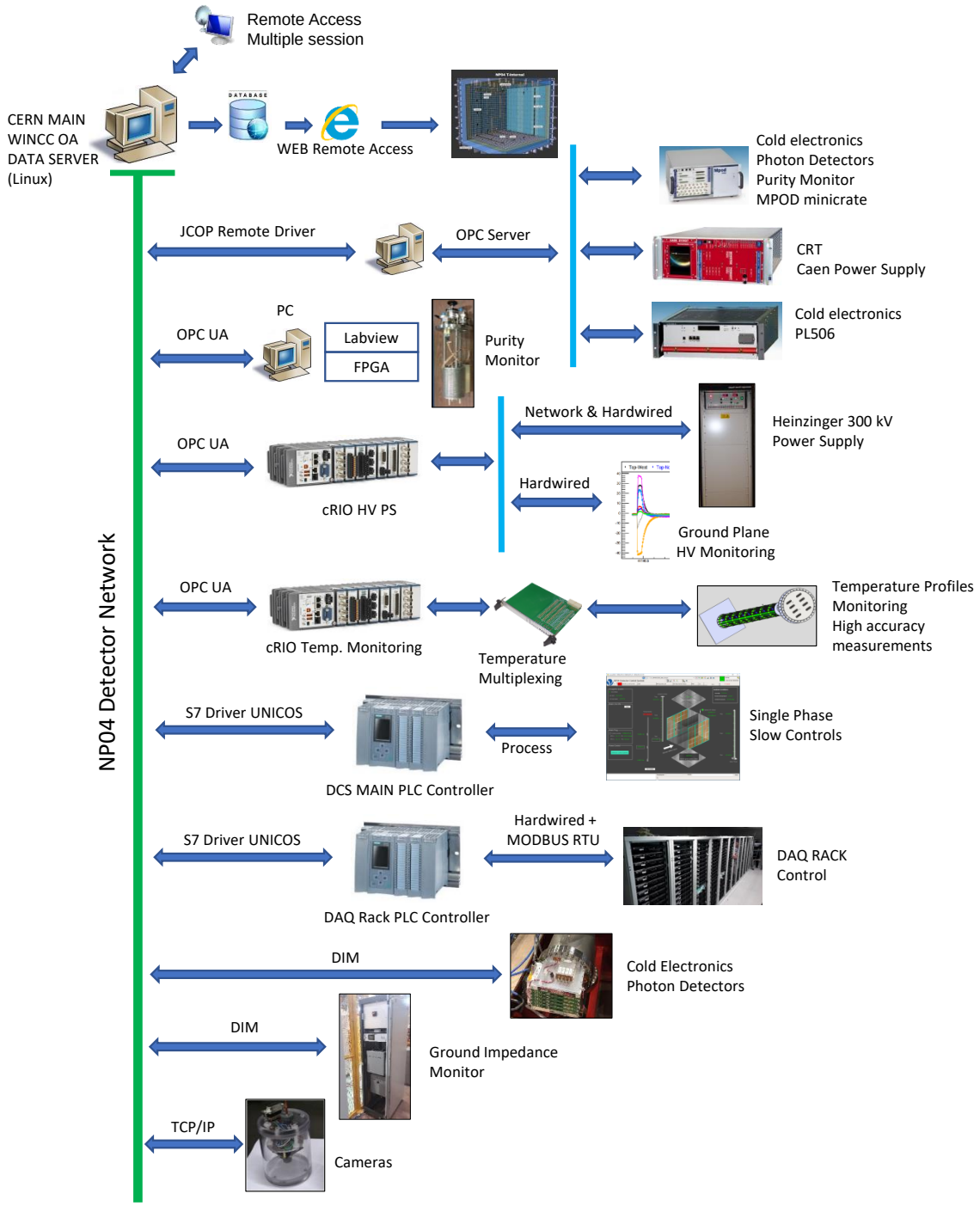

Figure 4.29: Diagram of the ProtoDUNE control system topology as used for ProtoDUNE-SP, from [61].

Slow Controls Base Software and Databases: base I/O software, alarms and archiving databases, and monitoring tools; variable naming conventions and slow controls quantities.

Slow Controls Detector System Interfaces: signal processing software and hardware interfaces (e.g., power supplies); firmware; rack hardware; and infrastructure.

Slow Controls External Interfaces: interfaces with external detector systems (e.g., cryogenics system, beam, facilities, DAQ, near detector status).

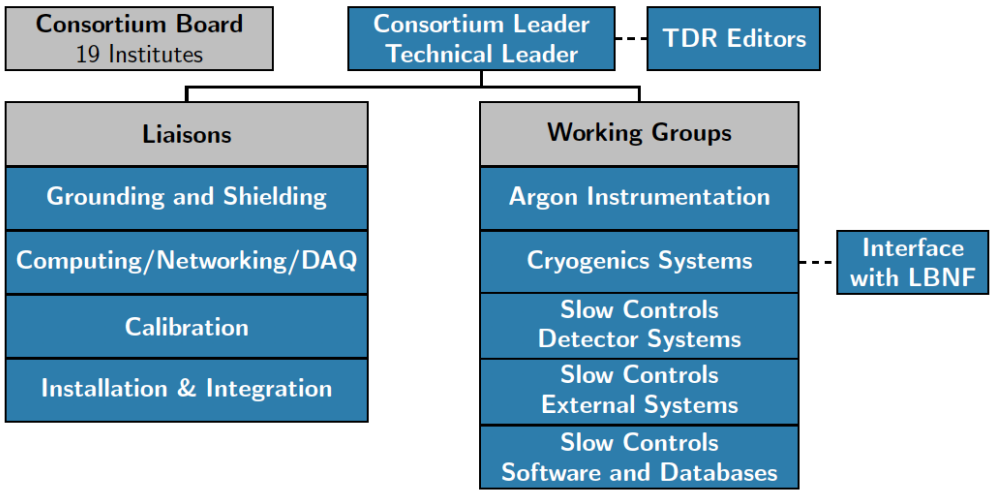

Figure 4.30: CISC Consortium organizational chart.

Moreover, because the CISC consortium broadly interacts with other groups, liaisons have been named (see Figure 4.30). A short-term task force formed in 2017-2018 explored cryogenic modeling for the consortium and corresponding simulation needs. A work plan for CFD simulations for both ProtoDUNE and FD was developed based on input from the task force.

The TDR editors are responsible for the overall editing and delivery of the TDR document. Currently, members from new institutes are added to the consortium with the consensus of the consortium board members following an expression of interest petition from the new institute.

4.4.1 Institutional Responsibilities

The CISC will be a joint effort for SP and DP. A single slow controls system will be implemented to serve both the SP module and the DP module.

Design and installation of cryogenic systems (e.g., gas analyzers, differential pressure liquid level meters) will be coordinated with LBNF and the consortium providing resources and effort; expertise is provided by LBNF. ProtoDUNE-SP and ProtoDUNE-DP designs for argon instrumentation (e.g., purity monitors, pressure meters, thermometers, cameras) will be the basis for FD designs.

Table 4.7: Current CISC Consortium Board Members and their institutional affiliations.

Member Institute	Country
CIEMAT	Spain
Instituto de Fisica Corpuscular (IFIC)	Spain
University of Warwick	UK
University College London (UCL)	UK
Argonne National Lab (ANL)	USA
Brookhaven National Lab (BNL)	USA
University of California, Irvine (UCI)	USA
Drexel University	USA
Fermi National Accelerator Lab (Fermilab)	USA
University of Hawaii	USA
University of Houston	USA
Idaho State University (ISU)	USA
Kansas State University (KSU)	USA
University of Minnesota, Duluth (UMD)	USA
Notre Dame University	USA
South Dakota State University (SDSU)	USA
University of Tennessee at Knoxville (UTK)	USA
Virginia Tech (VT)	USA
Boston University (BU)	USA

Design validation, testing, calibration, and performance will be evaluated using ProtoDUNE-SP and ProtoDUNE-DP data.

Following the conceptual funding model envisioned for the consortium, various responsibilities have been distributed across institutions within the consortium pending final funding decisions. Table 4.8 shows the current institutional responsibilities for primary CISC subsystems. Only lead institutes are listed in the table for a given effort. For physics and simulations studies and for validation using ProtoDUNE, a number of institutes are involved. A detailed list of tasks and institutional responsibilities are presented in [71].

Table 4.8: Institutional responsibilities in the CISC consortium.

CISC Sub-system	Institutional Responsibility
Purity monitors	UCI, Houston, UCL
Static T-gradient monitors	IFIC, CIEMAT
Dynamic T-gradient monitors	Hawaii
Individual sensors	IFIC, CIEMAT
Vertical thermometer arrays (GAr)	TBA
Pressure meters (GAr)	TBA
Readout system for thermometers	IFIC, Hawaii, CIEMAT
Cold cameras	KSU, BNL
Warm cameras	KSU, BNL
Light-emitting system (for cameras)	Drexel
Gas analyzers	FNAL, LBNF
Differential pressure level meters	LBNF
Capacitive level meters	Notre Dame
Cryogenic test facility	FNAL, ANL
CFD simulations	SDSU, ANL
Other simulation & validation studies	Number of Institutes
Slow controls hardware	UMD, UTK, Drexel
Slow controls infrastructure	UMD, UTK
Slow controls base software	KSU, UTK, BU, Drexel, Warwick, UCL, ANL, IFIC
Slow controls signal processing	A number of institutes
Slow controls external interfaces	VT, UTK, UMD

4.4.2 Cost and Labor

Table 4.9 shows the current cost estimates for the CISC subsystems. It also shows the quantity associated with each subsystem and a brief description of what is included in the cost estimate. The cost estimates include only materials and supplies (M&S) and packing and shipping, but not labor and travel costs. Labor costs depend on personnel category (e.g., faculty, student, technician, post-doc, engineer) and vary by region and institution, so costs are quantified using labor hours

needed to fulfill a given task. Table 4.10 provides estimates of labor hours for each subsystem, totaling 95,010 labor hours for all CISC tasks.

Table 4.9: Cost estimates of the different CISC subsystems. All cost estimates include packing and shipping costs.

System	Quantity	Cost (under development)	Description
Purity monitors	10	-	Includes material cost, PC, flanges, mounting structure
Static T-gradient monitors	6	-	Includes cables, sensors and connectors, support structure, flanges
Precision individual temperature sensors	130	-	Includes cables, sensors and connectors, support structure, flanges
Standard individual temperature sensors	35	-	Includes cables, sensors and connectors, support structure, flanges
Dynamic T-gradient monitors	2	-	Includes cables, sensors, motor drive, flanges, sensor holders
Vertical Thermometer Arrays (GAr)	20	-	Includes cables, sensors and connectors, support structure, flanges
Pressure Meters (GAr)	6	-	Includes pressure meters and flanges
Warm cameras	3	-	Includes material cost, computer, argon purge & pressurization system, prototyping & testing
Cold cameras	12	-	Includes material cost, computer, minor jigs & test boards
Light system	15	-	Cost of illuminator and light driver module
Gas analyzers	1	-	Cost of gas analyzers and piping & routing panel
Capacitive level meters	4	-	Cost of level meters and flanges
Cryogenics test facility	1	-	Material cost includes liquid argon costs for years 1 to 5 and minor fixture costs
Slow controls hardware	-	-	Cost of 6 servers, 0.5 rack, 126 rack monitoring boxes, and cables
Slow controls software	-	-	Includes cost of a laptop

4.4.3 Schedule

Table 4.11 shows key construction milestones for the CISC consortium leading to commissioning of the second FD module. CISC construction milestones align with the overall construction milestones of the second FD module (highlighted in orange in the table). The technology design decisions for CISC systems should be made by January 2020 followed by technical design reviews. The production of improved design prototypes (if any) to be deployed at ProtoDUNE-II running should be finished by May 2021 followed by assembly and deployment in ProtoDUNE-II.

Table 4.10: Estimate of labor hours for each category of personnel for different CISC subsystems. For slow controls software, the 884 technician hours comprise 442 hours from information technology professionals and 442 hours from scientific computing professionals.

System	Faculty/Scientist (hours)	Post-doc (hours)	Student (hours)	Engineer (hours)	Technician (hours)	**Total** (hours)
Purity monitors	-	-	-	-	-	-
Static T-gradient monitors	-	-	-	-	-	-
Individual temperature sensors	-	-	-	-	-	-
Dynamic T-gradient monitors	-	-	-	-	-	-
Vertical Thermometer Arrays (GAr)	-	-	-	-	-	-
Pressure Meters (GAr)	-	-	-	-	-	-
Warm cameras	-	-	-	-	-	-
Cold cameras	-	-	-	-	-	-
Light system	-	-	-	-	-	-
Gas analyzers	-	-	-	-	-	-
Capacitive Level meters	-	-	-	-	-	-
Cryogenic test facility	-	-	-	-	-	-
Slow controls hardware	-	-	-	-	-	-
Slow controls software	-	-	-	-	-	-
Physics & simulation	-	-	-	-	-	-

Table 4.11: Key CISC construction schedule milestones leading to commissioning of the second FD module.

Milestone	Date (Month YYYY)
Technology Decision Dates	January 2020
Start of module 0 component production for ProtoDUNE-II	April 2020
Final Design Review Dates	May 2020
Start of ProtoDUNE-SP-II installation	March 2021
End of module 0 component production for ProtoDUNE-II	May 2021
Start of ProtoDUNE-DP-II installation	March 2022
South Dakota Logistics Warehouse available	April 2022
production readiness review (PRR) dates	September 2022
Beneficial occupancy of cavern 1 and CUC	October 2022
Start procurement of CISC hardware	December 2022
CUC counting room accessible	April 2023
Start of production of CISC hardware	April 2023
Top of detector module #1 cryostat accessible	January 2024
End of CISC hardware production	July 2024
Start of detector module #1 TPC installation	August 2024
Top of detector module #2 accessible	January 2025
Start integration of CISC hardware in the cavern	March 2025
Installation of gas analyzers	April 2025
End of detector module #1 TPC installation	May 2025
Installation of support structure for all instrumentation devices	May 2025
Installation of individual sensors, static T-gradient thermometers, and level meters	June 2025
Start of detector module #2 TPC installation	August 2025
All slow controls hardware, infrastructure, & networking installed	February 2026
Slow controls software for I/O, alarms, archiving, displays installed on production systems	May 2026
End of detector module #2 TPC installation	May 2026
Install dynamic T-gradient monitors, cameras, purity monitors	July 2026
Install all feedthroughs for instrumentation devices	July 2026
Install slow control expert interfaces for all systems in time for testing	September 2026
Full slow controls systems commissioned and integrated into remote operations	July 2027

Production of CISC systems for the FD should start in April 2023, followed by assembly of the systems underground in the detector cavern in early 2025. Installation of instrumentation devices will start in April 2025 following the beneficial occupancy of the cryostat. Installing gas analyzers, level meters, individual temperature sensors, static T-gradient thermometers, and support structure for all instrumentation devices will finished before installing TPC, but installing dynamic T-gradient thermometers, purity monitors, and cameras will occur afterward. CISC will work closely with LBNF to coordinate installation of the cryogenic systems and instrumentation devices. For slow controls, the goal is to have the full slow controls system commissioned and integrated into remote operations at least three months before the DP module is ready for operations.

4.4.4 Risks

Tables 4.12, 4.13, and 4.14 list the possible risks identified by the CISC consortium along with corresponding mitigation strategies. The tables list 18 risks at low and medium level. A more detailed list of risks with additional descriptions can be found in [72]. The tables show all risks are medium or low level, mitigated with necessary steps and precautions. Risk#1, where the ProtoDUNE-SP-based designs are inadequate for FD, is important because this requires early validation from ProtoDUNE data so R&D of alternate designs can be timely. With ProtoDUNE-SP data now available, the consortium is focused on validating instrumentation designs.

4.4.5 Interfaces

CISC subsystems interface with all other detector subsystems and could affect the work of all detector consortia, as well as some working groups (physics, software/computing, beam instrumentation), and technical coordination, requiring interactions with all of these entities. We also interact heavily with LBNF beam and cryogenics groups. Detailed descriptions of CISC interfaces are maintained in DUNE DocDB. A brief summary is provided in this section. Table 4.15 lists the IDs of the different DocDB documents as well as their highlights. Descriptions of the interfaces and interactions that affect many systems follow.

Obviously, CISC interacts with the detector consortia because CISC will provide status monitoring of all important detector sub-systems along with controls for some components of the detector. CISC will also consult on selecting different power supplies to ensure monitoring and control can be established with preferred types of communication. Rack space distribution and interaction between slow controls and other modules from other consortia will be managed by technical coordination (TCN) in consultation with those consortia.

If heaters/RTDs are needed on flanges, CISC will specify the heaters/RTDs and will provide the readout/control, while the responsibility for the actual hardware will be discussed with the different groups.

Installing instrumentation devices will interfere with other devices and must be coordinated with the appropriate consortia. On the software side, CISC must define, in coordination with other

Table 4.12: Possible risk scenarios for the CISC consortium along with mitigation strategies. The level of risk is indicated by letters "H", "M", and "L" corresponding to high, medium, and low level risks.

No.	Risk	Risk Level	Mitigation Strategy
1	The baseline design (extrapolated from ProtoDUNEs) for instrumentation devices is not adequate for the FD.	M	This should be detected early on, so R&D on alternative designs can proceed on a reasonable time scale.
2	Potential swinging of long instrumentation devices (T-gradient monitors or purity monitors) due to e.g., misalignment at the top.	L	Add additional intermediate anchoring points (as needed) to prevent swinging.
3	High E field near instrumentation devices could lead to dielectric breakdowns.	L	Instrumentation systems will be placed when possible in regions where the E field should be low (below the grounding grid, above the CRPs, near the lateral cryostat membrane). When this is not possible the appropriate shielding (based on Comsol simulations) will be provided.
4	Light pollution from purity monitors and camera light system could interfere with physics measurements and damage the PDS.	L	Purity monitors and camera systems could be run at specified times and a signal sent to the detector to veto any signals during their operation. For purity monitors, software for light source triggering mechanism will be developed to prevent the flash lamp from operating during photon detector triggering windows.
5	Temperature sensors can induce noise in cold electronics.	M	If noise is discovered before cryostat filling, check all connections, mainly the ones to ground. If noise is discovered after cryostat filling, address the problem at the readout level (e.g., noise filters). If problem persists, connect offending sensors to ground using dummy connectors with all pins grounded.
6	Disagreement between laboratory and *in situ* calibrations for dynamic T-gradient monitor.	M	Understand which of the two calibrations is wrong or has more limitations; improve both methods especially for the laboratory because this is the only way to place sensors in areas where space is restricted.
7	Purity monitor electronics induce noise in cold electronics.	M	Develop software for light source triggering mechanism to prevent operating the purity monitor flash lamp during photon detector data taking. Use Faraday cage to ground the light source.

Table 4.13: Possible risk scenarios for the CISC consortium along with mitigation strategies. The level of risk is indicated by letters "H", "M", and "L" corresponding to high, medium and low level risks. The numbering for listed risks continued from the previous table.

No.	Risk	Risk Level	Mitigation Strategy
8	Discrepancies between measured temperature map and CFD simulations in ProtoDUNE-SP can potentially affect physics because physics relies on simulations to extract various calibration quantities.	L	Improve simulations with more precise input from real measurements (e.g., LAr flows, temperature of incoming LAr, temperature of gaseous argon in the ullage); use a fraction of temperature sensors to predict temperatures in other parts of the cryostat.
9	Difficulty in correlating data from purity monitors and thermometers can affect understanding the behavior of cryogenics system.	L	Understand what aspect (design, drift physics) causes the discrepancy and determine any modifications needed in the design. One option would be to instrument the purity monitors with temperature sensors, so purity and temperature are measured at the same location.
10	During R&D phase, the consortium cannot build a working prototype for cold cameras that meets all requirements & safety. This risk comes about because cold cameras are not operational after time in LAr or perform poorly (e.g., delays, bad resolution)	M	Pursue further R&D: e.g., improve thermal insulation and heaters, use alternative camera models. If problems persist, use cameras at the ullage with the appropriate field of view and lighting, so elements inside LAr can be inspected. Also, recall cold cameras are important for HV diagnosis because not having them may put HV at risk.
11	Cameras can induce HV discharge.	M	Electric field in the camera housing and related anchoring systems must be studied carefully, so proper shielding is used.
12	HV discharge can damage cameras because some cameras will be positioned near HV devices. With proper shielding, this is very unlikely, but some risk remains.	M	The most important cameras should have enough redundancy, so the loss of one camera does not compromise overall performance.
13	Cameras have insufficient light. The attenuation of light in LAr could prevent cameras from seeing objects in the deep regions of the cryostat.	M	Cameras must be tested during the R&D phase under conditions of illumination expected in the actual detector. The cryogenics test facility should have sufficient depth for testing this risk scenario.
14	Cameras may induce noise in cold electronics.	M	Work with the grounding and shielding group to ensure proper grounding.

Table 4.14: Possible risk scenarios for the CISC consortium along with mitigation strategies. The level of risk is indicated by letters "H", "M", and "L" corresponding to high, medium and low level risks. The numbering for listed risks are continued from the previous table.

No.	Risk	Risk Level	Mitigation Strategy
15	Light attenuation in long optic fibers of the purity monitors can cause insufficient intensity to produce enough drift elections for the purity measurement.	M	Test the maximum length of fiber that can be used and optimize accordingly the depth of the bottom purity monitor and the number of fibers to be run.
16	Longevity of purity monitors. The current design could fail if operated for a long time in impure liquid or gaseous argon because of the degradation of the photocathode.	M	Design software deadlock to prevent monitors from running long when low purity is detected. The degradation can be recovered in many ways: 1. by running high frequency/intensity xenon flashes for a few days after purity is recovered, 2. by using RTDs to heat cathode because the primary contamination on a degraded cathode surface is likely to be ice or water from the impurity. The best way to mitigate degradation is to place monitors in line with the cryogenics purification system and have them in valves so they can be maintained over time. This would ensure that the purity of the LAr is always monitored, even if monitors are not directly in the cryostat.
17	Longevity: Gas analyzers and level meters may fail. These are commercial devices with typical warranties of one year from date of purchase.	L	To mitigate this, make provisions for replacement in case of failure or loss of sensitivity.
18	Problems in interfacing hardware devices (e.g., power supplies) with slow controls.	M	Power supplies and other hardware devices that need control/monitoring should be chosen in consultation with slow control experts to ensure the hardware choices have robust control/monitoring at the precision needed.

consortia/groups, the quantities to be monitored/controlled by slow controls and the corresponding alarms, archiving, and GUIs.

Table 4.15: CISC system interface links.

Interfacing System	Description	Linked Reference
CRP	temperature sensors in the gas, cameras, and lights	DocDB 6760 [73]
PDS	PrMs, light emitting system for cameras	DocDB 6781 [47]
TPC Electronics	Noise, Power supply monitoring	DocDB 6784 [15]
HV Systems	shielding, bubble generation by inspection camera, cold camera locations, ground planes	DocDB 6787 [6]
DAQ	Description of CISC data storage, allowing bi-directional communications between DAQ and CISC.	DocDB 6790 [74]
Calibration	multifunctional CISC/CITF ports; space sharing around ports	DocDB 7072 [75]
Physics	Indirect interfaces through calibration, tools to extract data from the slow controls database	DocDB 7099 [76]
Software & Computing	Slow Controls database design and maintenance	DocDB 7126 [77]
Cryogenics	must be designed and implemented. purity monitors, gas analyzers, interlock mechanisms to prevent contamination of LAr	-
Beam	beam status	-
TC Facility	Significant interfaces at multiple levels	DocDB 6991 [78]
TC Installation	Significant interfaces at multiple levels	DocDB 7018 [79]
TC Integration Facility	Significant interfaces at multiple levels	DocDB 7045 [80]

4.4.6 Installation, Integration, and Commissioning

4.4.6.1 Purity Monitors

The purity monitor system will be built in modules, so it can be assembled outside the cryostat leaving few steps to complete inside the cryostat. The assembly itself comes into the cryostat with the individual purity monitors mounted to support tubes and with no HV cables or optical

fibers yet installed. The support tube at the top and bottom of the assembly is then mounted to the brackets inside the cryostat and the brackets attached to the cables trays and/or the detector support structure. At much the same time, the FE electronics and light source can be installed on top of the cryostat, and the electronics and power supplies can be installed in the electronics rack.

Integration begins by running the HV cables and optical fibers to the purity monitors through the top of the cryostat. These cables are attached to the HV feedthroughs with sufficient length to reach each purity monitor inside the cryostat. The cables are run along cable trays through the port reserved for the purity monitor system. Each purity monitor will have three HV cables that connect it to the feedthrough and then further along to the FE electronics. The optical fibers are then run through the special optical fiber feedthrough into the cryostat and guided to the purity monitor system either using the cables trays or guide tubes, depending on which solution is adopted. This should protect fibers from breaking accidentally as the rest of the detector and instrumentation installation continues. The optical fibers are then run inside the purity monitor support tube and to the appropriate purity monitor, terminating the fibers at the photocathode of each monitor while protecting them from breaking near the purity monitor system itself.

Integration continues as the HV cables are connected through the feedthrough to the system FE electronics; then optical fibers are connected to the light source. The cables connecting the FE electronics and the light source to the electronics rack are also run and connected at this time. This allows the system to be turned on and the software to begin testing the various components and connections. Once all connections are confirmed successful, integration with the slow controls system begins, first by establishing communication between the two systems and then transferring data between them to ensure successful exchange of important system parameters and measurements.

Commissioning the purity monitor system is considered official once the cryostat is purged and a gaseous argon atmosphere is present. At this time, the HV for the purity monitors is ramped up without risk of discharge through the air, and the light source turned on. Although the drift electron lifetime in the gaseous argon would be very large and therefore not measurable with the purity monitors themselves, the signal strength at both the cathode and anode will give a good indication of how well the light source generates drift electrons from the photocathode. Comparing the signal strengths at the anode and cathode will indicate whether the electrons successfully drift to the anode.

4.4.6.2 Thermometers

Static T-gradient monitors will be installed after FCs along the long cryostat sides. The profiles are preassembled before they are delivered to SURF. Installation begins by anchoring the support holding the two vertical strings to bolts on the top corner of the cryostat. All cables can then be routed to the assigned cryostat ports. Second, the array is unrolled using a scissor lift, and once at the bottom, it is attached to bolts on the bottom corner of the cryostat. After checking string tension and verticality, cable and sensors supports are checked, and the individual Faraday cages are installed. A precision resistor is plugged into each IDC-4 connector so noise studies can be performed. Sensors will be installed later.

Individual temperature sensors on pipes/PDs[12] and cryostat floor should be installed after PDs and the grounding grid. First, vertical strings for cable routing are installed following a procedure similar to the one described above for the static T-gradient monitors. Next, all cable supports are anchored to pipes/PDs. Then each cable is routed individually starting from the sensor end (with IDC-4 female connector but without the sensor) to the corresponding cryostat port. Once all cables going through the same port have been routed, the cables are cut to the same length, so they can be properly assembled into the corresponding connector(s). To avoid damaging them, sensors are installed later, once all operations at the bottom of the cryostat are complete.

Dynamic T-gradient monitors are installed after the TPC components are in place. Figure 4.16 shows the design of the dynamic T-gradient monitor with its sensor carrier rod, enclosure above the cryostat, and stepper motor. Figure 4.17 shows detailed views of key components. Each monitor comes in several segments with sensors and cabling already in place. Additional slack will be provided at segment joints to make installation easier. Segments of the sensor carrier rod with preattached sensors are fed into the flange one at a time. Each segment, as it is fed into the cryostat, is held at the top with a pin that prevents the segment from sliding all the way in. The next segment is connected at that time to the previous segment. Then the pin is removed, the first segment is pushed down, and the next segment top is held with the pin at the flange. This process is repeated for each segment until the entire sensor carrier rod is in place. Next, the enclosure is installed on top of the flange, starting with the six-way cross at the bottom of the enclosure. (See Figure 4.17, right.) Again, extra cable slack at the top will be provided to ease connection to the D-sub flange and allow the entire system to move vertically. The wires are connected to a D-sub connector on the feedthrough on one side port of the cross. Finally, a crane positions the remainder of the enclosure over the top of the cross. This enclosure includes the mechanism used to move the sensor rod, which is preassembled, with the motor in place, on the side of the enclosure, and the pinion and gear is used to move the sensor inside the enclosure. The pinion is connected to the top of the rod. The enclosure is then connected to top part of the cross, which finishes the installation of the dynamic T-gradient monitor.

Vertical arrays in gas phase, with the baseline design assuming twenty arrays, are each attached to a CRP frame. Thus, they should be installed on the corresponding CRP before being moved into the cryostat. Cables will be routed to the assigned cryostat port using the appropriate elements on the CRP frame.

Commissioning all thermometers will occur in several steps. In the first stage, only cables are installed, so the readout performance and the noise level inside the cryostat is tested with precision resistors. Once sensors are installed, the entire chain is checked again at room temperature. The final commissioning phase takes place during and after cryostat filling.

[12] Actually on PD's support structure

4.4.6.3 Gas Analyzers

The gas analyzers are installed before the piston purge and gas recirculation phases of the cryostat commissioning. They are installed near the tubing switchyard to minimize tubing run length and for convenience when switching the sampling points and gas analyzers. Because each is a standalone module, a single rack with shelves is adequate to house the modules.

For integration, the gas analyzers typically have an analog output (4 mA to 20 mA or 0 V to 10 V), which maps to the input range of the analyzers. They also usually have several relays to indicate the scale they are currently running. These outputs can be connected to the slow controls for readout. However, using a digital readout is preferable because this gives a direct analyzer reading at any scale. Currently, the digital output connections are RS-232, RS-485, USB, and Ethernet. The preferred option is chosen at the time of purchase.

The readout usually responds to a simple set of text query commands. Because of the natural time scales of the gas analyzers and lags in gas delivery times (which depend on the length of the tubing run), sampling every minute is adequate.

The analyzers must be brought online and calibrated before beginning the gas phase of the cryostat commissioning. Calibration varies by module because they differ, but calibration often requires using argon gas with zero contaminants, and argon gas with a known level of the contaminant to check the scale. Contaminants are usually removed with a local inline filter for the first gas sample. This gas phase usually begins with normal air, with the more sensitive analyzers valved off at the switchyard to prevent overloading their inputs (and potentially saturating their detectors). As the argon purge and gas recirculation progress, the various analyzers are valved back in when the contaminant levels reach the upper limits of the analyzer ranges.

4.4.6.4 Liquid Level Monitoring

LBNF will install differential pressure level meters, but the capacitive level meters fall within scope of CISC. The exact number of capacitive level meters is not yet decided. We will need at least four, one for each of the four corners of the cryostat. They will be attached to the M10 bolts in the cryostat corners after the detector is installed. If additional capacitive level meters are needed in the central part of the cryostat, those will be installed after the nearby FC modules, attaching them to the bolts in the top cryostat corner[13]. In all cases, cables will be routed to the appropriate nearby port (not yet assigned).

4.4.6.5 Pressure Meters

CISC will install the pressure meters. Six sensors will be mechanically installed in two dedicated flanges (three sensors each) at opposite sides of the cryostat after the detector is installed. Cables

[13] These level meters must be shorter because no bolts run vertically as they do for the other level meters

will be routed through the dedicated ports assigned for these devices. The pressure signals (absolute and relative) are read and converted to electrical signals corresponding to 4...20 mA range. A twisted pair shielded cable connects the sensors to the slow controls PLC controller using software to convert electrical signals to pressure values.

4.4.6.6 Cameras and light emitting system

Installing fixed cameras is, in principle, simple but involves several interfaces. The enclosure of each camera has exterior threaded holes for mounting the cameras on the cryostat wall, cryogenic internal piping, or DSS. Each enclosure is attached to a gas line to maintain appropriate under-pressure in the fill gas; therefore, an interface with cryogenic internal piping will be necessary. Each camera has a cable (coaxial or optical) for the video signal and a multiconductor cable for power and control. These are run through cable trays to flanges on assigned instrumentation feedthroughs.

The inspection camera is designed to be inserted and removed on any instrumentation feedthrough equipped with a gate valve at any time during operation. Installing the gate valves and purge system for instrumentation feedthroughs falls under cryogenic internal piping.

Fixed lighting sources separate from the cameras are mounted on cryostat wall, cryogenic internal piping, or DSS, and multiconductor cables for power are run through cable trays to flanges on assigned instrumentation feedthroughs.

4.4.6.7 Slow Controls Hardware

Slow controls hardware installation includes several servers, network cables, any specialized cables needed for device communication, and possibly some custom-built hardware for monitoring racks. The installation sequence will be planned with the facilities group and other consortia. The network cables and rack monitoring hardware will be common across many racks and will be installed first as part of the basic rack installation as led by the facilities group. Specialized cables needed for slow controls and servers are installed after the common rack hardware. Selecting and installing these cables will be coordinated with other consortia, and server installation will be coordinated with the DAQ group.

4.4.6.8 Transport, handling, and storage

Most instrumentation devices will be shipped in pieces to SURF via the integration and test facility (ITF) and mounted on site. Instrumentation devices are, in general, small except the support structures for purity monitors and dynamic T-gradient monitors that will cover the entire height of the cryostat. The load on those structures is relatively small ($< 100\,\mathrm{kg}$), so they can be fabricated in sections smaller than 3 m, which can be easily transported to SURF, down the shaft, and through the tunnels. All instrumention devices except the dynamic T-gradient monitors

can be moved into the cryostat without the crane. The dynamic T-gradient monitors, which are introduced into the cryostat from above, require a crane for installing the external enclosure (with preassembled motor, pinion, and gear).

4.4.7 Quality Control

The manufacturer and the institution in charge of device assembly will conduct a series of tests to ensure the equipment can perform its intended function as part of quality control (QC). QC also includes post-fabrication tests and tests run after shipping and installation. For complex systems, the entire system will be tested before shipping. Additional QC procedures can be performed at the CITF and underground after installation.

The planned tests for each subsystem are described below.

4.4.7.1 Purity monitors

The purity monitor system will undergo a series of tests to ensure the system performs as intended. These tests include electronic tests with a pulse generator, mechanical and electrical connectivity tests at cryogenic temperatures in a cryostat, and vacuum tests for short and full assemblies in a dewar and in a long vacuum tube.

The QC tests for FD purity monitors begin with testing individual purity monitors in vacuum after each is fabricated and assembled. This test checks the amplitude of the signal generated by the drift electrons at the cathode and anode to ensure the photocathode can provide sufficient numbers of photoelectrons to measure the signal attenuation with the required precision and the field gradient resistors all work properly to maintain the drift field. A smaller version of the assembly with all purity monitors installed will be tested in the LAr test facility to ensure the full system performs as expected in LAr and to study systematics that may influence the measured lifetime.

Next, the entire system is assembled on the full-length mounting tubes to check connections. Ensuring that all electric and optical connections are operating properly during this test reduces the risk of problems once the full system is assembled and ready for the final test in vacuum. The fully assembled system is placed in the shipping tube, which serves as a vacuum chamber, and tested at SURF before the system is inserted into the cryostat. During insertion, electrical connections are tested continuously with multimeters and electrometers.

4.4.7.2 Thermometers

Static T-gradient thermometers: Static T-gradient monitors undergo three type of tests at the production site before shipping to SURF: a mechanical rigidity test, a calibration of all sensors,

and a test of all electrical cables and connectors. Mechanical rigidity is tested by installing the static T-gradient monitor between two dummy cryostat corners mounted 15 m apart. The tension of the strings is set to match the tension that would occur in a vertical deployment in LAr, and the deflection of the sensor and electrical cable strings is measured and compared to the expected value; this ensures any swinging or deflection of the deployed static T-gradient monitor will be < 5 cm, mitigating any risk of touching the FCs and the cryostat membrane. The laboratory calibration of sensors will be performed as explained in Section 4.2.2. The main concern is reproducibility of results because sensors could change resistance and hence their temperature scale when undergoing successive immersions in LAr. In this case, the calibration procedure itself provides QC because each set of sensors goes through five independent measurements. Sensors with RMS variation outside the requirement (2 mK for ProtoDUNE-SP) are discarded. This calibration also serves as QC for the readout system (similar to the final one) and of the PCB-sensor-connector assembly. Finally, the cable-connector assemblies are tested; sensors must measure the expected values with no additional noise introduced by either cable or connector.

An integrated system test at a LAr test facility on site, which has sufficient linear dimension (>2 m) to test a good portion of the system, would be desirable. This ensures that the system operates in LAr at the required performance level.

The last phase of QC takes place after installation. The verticality of each array is checked, and the tensions in the stainless steel strings adjusted as necessary. Before closing the flange, the entire readout chain is tested. This allows a test of the sensor-connector assembly, the cable-connector assemblies at both ends, and the noise level inside the cryostat. If any sensor presents a problem, it is replaced. If the problem persists, the cable is checked and replaced as needed.

Dynamic T-gradient thermometers: The dynamic T-gradient monitor consists of an array of high-precision temperature sensors mounted on a vertical rod. The rod can move vertically to cross-calibrate the temperature sensors *in situ*. We will use the following tests to ensure that the dynamic T-gradient monitor delivers vertical temperature gradient measurements with a precision of a few mK.

- Before installation, temperature sensors are tested in LN to verify correct operation and to set the baseline calibration for each sensor to the absolutely calibrated reference sensor.
- Warm and cold temperature readings are taken with each sensor after it is mounted on the PCB board and the readout cables are soldered.
- The sensor readout is taken for all sensors after the cold cables are connected to electric feedthroughs on the flange and the warm cables outside of the cryostat are connected to the temperature readout system.
- The stepper motor is tested before and after connecting to the gear and pinion system.
- The fully assembled rod is connected to the pinion and gear and moved with the stepper motor on a high platform many times to verify repeatability, possible offsets, and any uncertainty in positioning. Finally, repeating this test many times will verify the sturdiness of the system.

- The full system is tested after it is installed in the cryostat; both motion and sensor operation are tested by checking sensor readout and vertical motion of the system.

Individual sensors: To address the quality of individual precision sensors, the same method is used as for the static T-gradient monitors . The QC of the sensors is part of the laboratory calibration. After mounting six sensors with their corresponding cables, a SUBD-25 connector is added, and the six sensors tested at room temperature. All sensors must give values within specifications. If any of the sensors present problems, they are replaced. If the problem persists, the cable is checked and replaced as needed.

For standard RTDs to be installed on the cryostat walls, floor, and roof, calibration is not an issue. Any QC required for associated cables and connectors is performed following the same procedure as for precision sensors.

Vertical arrays in gas phase: These thermometers use standard RTDs that require no calibration. Any QC required for associated cables and connectors is performed following the same procedure as for precision sensors. The appropriate QC procedure for the PCB support structure will be elaborated once this is designed.

4.4.7.3 Gas analyzers

The gas analyzers will be guaranteed by the manufacturer. However, once received, the gas analyzer modules are checked for both *zero* and the *span* values using a gas-mixing instrument and two gas cylinders, one having a zero level of the gas analyzer contaminant species and the other cylinder with a known percentage of the contaminant gas. This verifies the proper operation of the gas analyzers. When they are installed at SURF, this process is repeated before commissioning the cryostat. Calibrations must be repeated using manufacturer recommendations over the gas analyzer lifetime.

4.4.7.4 Liquid level monitoring

The manufacturer will provide the QC for the differential pressure level meters; further QC during and after installation is the responsibility of LBNF.

The capacitive sensors will be tested with a modest sample of LAr in the laboratory before they are installed. After installation, they are tested *in situ* using a suitable dielectric in contact with the sensor.

4.4.7.5 Pressure meters

The manufacturer will provide the QC for the pressure meters; CISC will provide further QC during and after installation.

The pressure sensors will be tested with a modest sample of gaseous argon in the laboratory before they are installed. After installation, they are tested *in situ* at atmospheric pressure. The whole pressure readout chain, (including slow controls PLC and WINCC conversion) will also be tested and cross-checked with LBNF pressure sensors.

4.4.7.6 Cameras

Before transport to SURF, each cryogenic camera unit (comprising the enclosure, camera, and internal thermal control and monitoring) is checked for correct operation of all features, for recovery from 87 K non-operating mode, for leakage, and for physical defects. Lighting systems are similarly checked. Operations tests will verify correct current draw, image quality, and temperature readback and control. Each movable inspection camera apparatus is inspected for physical defects and checked for proper mechanical operation before shipping. A checklist is created for each unit, filed electronically in the DUNE logbook, and a hard copy is sent with each unit.

Before installation, each fixed cryogenic camera unit is inspected for physical damage or defects and checked in a cryogenics test facility for correct operation of all features, for recovery from 87 K non-operating mode, and for contamination of the LAr. Lighting systems are similarly checked. Operations tests verify correct current draw, image quality, and temperature readback and control. After installing and connecting the wiring, fixed cameras and lighting are again checked for operation. The movable inspection camera apparatus is inspected for physical defects and, after integration with a camera unit, tested in the facility for proper mechanical and electronic operation and cleanliness before being installed or stored. A checklist will be completed for each QC check and filed electronically in the DUNE logbook.

4.4.7.7 Light-emitting system

The entire light-emitting system is checked before installation to ensure functionality of light emission. Initial testing of the system (see Figure 4.26) begins with measuring the current when low voltage (1 V) is applied to check that the resistive LED failover path is correct. Next, the forward voltage is measured using nominal forward current to check that it is within 10 % of the nominal forward voltage drop of the LED, that all of the LEDs are illuminated, and that each LED is visible over the nominal angular range. If the LEDs are infrared, a video camera with the IR filter removed is used for a visual check. This procedure is then duplicated with the current reversed for LEDs oriented in the opposite direction. Initial tests are performed at room temperature and then repeated in LN. Color shifts in the LEDs are expected and will be noted. A checklist is completed for each QC check and filed electronically in the DUNE logbook.

Room temperature tests are repeated during and immediately after installation to ensure that the system has not been damaged during transportation or installation. Functionality checks of the LEDs are repeated after the cameras are installed in the cryostat.

4.4.7.8 Slow controls hardware

Networking and computing systems will be purchased commercially, requiring quality assurance (QA). The new servers are tested after delivery to confirm they suffered no damage during shipping. The new system is allowed to burn in overnight or for a few days, running a diagnostics suite on a loop to validate the manufacturer's QA process.

The system is shipped directly to SURF where an on site expert boots the systems and does basic configuration. Specific configuration information is pulled over the network, after which others may log in remotely to do the final set up, minimizing the number of people underground.

4.4.8 Safety

Safety is critical during all phases of the CISC project, including R&D, laboratory calibration and testing, mounting tests, and installation. Safety experts review and approve the initial safety planning for all phases as part of the initial design review, as well as before implementation. All documentation of component cleaning, assembly, testing, and installation will include a section on relevant safety concerns and will be reviewed during appropriate pre-production reviews.

Several areas are of particular importance to CISC.

- Hazardous chemicals (e.g., epoxy compounds used to attach sensors to cryostat inner membrane) and cleaning compounds: All chemicals used will be documented at the consortium management level, with a MSDS (material safety data sheet) and approved handling and disposal plans in place.

- Liquid and gaseous cryogens used in calibrating and testing: LN and LAr are used to calibrate and test instrumentation devices. Full hazard analysis plans will be in place at the consortium management level for full module or module component testing that involves cryogens. These safety plans will be reviewed in appropriate pre-production and production reviews.

- High voltage safety: Purity monitors have a voltage of $\sim 2\,\mathrm{kV}$. Fabrication and testing plans will show compliance with local HV safety requirements at any institution or laboratory that conducts testing or operation, and this compliance will be reviewed as part of the standard review process.

- Working at heights: Some fabrication, testing, and installation of CISC devices require working at heights. Both T-gradient monitors and purity monitors, which span the height of the detector, require working at heights exceeding $10\,\mathrm{m}$. Temperature sensors installed near

the top cryostat membrane and cable routing for all instrumentation devices also require working at heights. The appropriate safety procedures, including lift and harness training, will be designed and reviewed.

- Falling objects: all work involving heights has associated risks of falling objects. The corresponding safety procedures, including proper helmet use and a well restricted safety area, will be included in the safety plan.

Glossary

35 ton prototype The 35 ton prototype cryostat and single-phase (SP) detector built at Fermilab before the ProtoDUNE detectors. 168, 170, 174, 186, 187

analog-to-digital converter (ADC) A sampling of a voltage resulting in a discrete integer count corresponding in some way to the input. ix, 54–57, 60, 61, 63–65, 67–69, 74, 75, 78, 119

AISI American Iron and Steel Institute. 22

advanced mezzanine card (AMC) Holds digitizing electronics and lives in Micro Telecommunications Computing Architecture (μTCA) crates. vi, 51, 52, 55–58, 63–65, 68–71, 73–76, 81, 82, 85–87, 231

anode plane assembly (APA) A unit of the SP detector module containing the elements sensitive to ionization in the LAr. It contains two faces each of three planes of wires, and interfaces to the cold electronics and photon detection system. 163, 189, 197

ASIC application-specific integrated circuit. vi, 51, 52, 56–61, 65, 67, 68, 73, 75, 78, 83

Advanced Telecommunications Computing Architecture (ATCA) An advanced computer architecture specification developed for the telecommunications, military, and aerospace industries that incorporates the latest trends high-speed interconnect technologies, next-generation processors, and improved reliability, availability and serviceability. 68

BNL Brookhaven National Laboratory (in Upton, NY). 42

bottom field cage (bottom FC) The horizontal portions of the SP FC on the bottom. 43

CATIROC charge and time integrated readout chip. vi, ix, 57, 65, 67–69, 78

charged current (CC) Refers to an interaction between elementary particles where a charged weak force carrier (W^+ or W^-) is exchanged. 90, 91, 125, 126

European Organization for Nuclear Research (CERN) In French, Organisation européenne pour la recherche nucléaire, derived from Conseil Europ'een pour la Recherche Nuclèaire, the leading particle physics laboratory in Europe and home to the ProtoDUNEs. viii, 33, 34, 40, 42,

43, 84, 136, 137, 181, 183, 192, 198

cold electronics (CE) Refers to readout electronics that operate at cryogenic temperatures. 45, 191

computational fluid dynamics (CFD) High performance computer-assisted modeling of fluid dynamical systems. 145, 155, 157, 162–167, 173, 183, 198, 200, 202, 208

cryogenic instrumentation and slow controls (CISC) A DUNE consortium responsible for the cryogenic instrumentation and slow controls components. 40, 41, 77, 80, 134, 152, 154–157, 165, 172, 184, 192, 194, 195, 198, 200–203, 205–210, 213, 218, 219

cryogenic instrumentation test facility (CITF) A facility at Fermilab with small ($<$ 1 ton) to intermediate ($\sim$ 1 ton) volumes of instrumented, purified TPC-grade LAr, used for testing devices intended for use in DUNE. 155, 161, 191, 210, 215

CMOS Complementary metal-oxide-semiconductor. 58

cathode plane assembly (CPA) The component of the SP detector module that provides the drift HV cathode. 20, 43

charge-parity symmetry violation (CPV) Lack of symmetry in a system before and after charge and parity transformations are applied. 5, 152

charge parity (CP) Product of charge and parity transformations. 5

charge readout (CRO) The system for detecting ionization charge distributions in a DP detector module. vi, vii, 49–52, 54–58, 63, 64, 67, 69, 73, 74, 77–79, 81, 85–87

charge-readout plane (CRP) In the DP technology, a collection of electrodes in a planar arrangement placed at a particular voltage relative to some applied E field such that drifting electrons may be collected and their number and time may be measured. ii, 2, 6, 8, 17, 25, 30, 40, 41, 48–51, 54, 57–62, 76, 77, 81, 82, 84, 156, 173, 180, 182, 183, 187–189, 197, 207, 210, 212

cosmic ray tagger (CRT) Detector external to the TPC designed to tag TPC-traversing cosmic ray particles. 116, 117, 119, 120

CTE coefficient of thermal expansion. 15, 26

Coating, Testing and Storage Facility (CTSF) A facility where the photodetectors of the DP photon detection system (PDS) will be coated, tested and stored.. viii, 98, 132, 133, 135–138, 145, 146, 151

central utility cavern (CUC) The central underground cavern containing utilities such as central cryogenics and other systems, and the underground data center and control room. 47, 79, 86, 149, 193, 194, 205

DAQ primary buffer (primary buffer) The portion of the DAQ front-end fragment that accepts full data stream from the corresponding detector unit and retains it sufficiently long for it to be available to produce a data fragment. 223, 224

DAQ data receiver (DDR) The portion of the DAQ front-end fragment that accepts data from the DAQ front-end readout (FER), emits trigger candidates produced from the input trigger primitives, and forwards the full data stream to the DAQ primary buffer (primary buffer). 224

data selection The process of forming a trigger decision for selecting a subset of detector data for output by the DAQ from the content of the detector data itself. Not to be confused with data selector.. 223

data selector The portion of the DAQ front-end fragment that accepts trigger commands and returns the corresponding data fragment. Not to be confused with data selection.. 223, 224

DAQ front-end readout (FER) The portion of a DAQ front-end fragment that accepts data from the detector electronics and provides it to the front-end computer (FEC).. 223, 224

DAQ front-end fragment The portion of one DAQ partition relating to a single FEC and corresponding to an integral number of detector units. See also data fragment. 223

DAQ partition A cohesive and coherent collection of DAQ hardware and software working together to trigger and read out some portion of one detector module; it consists of an integral number of DAQ front-end fragments. Multiple DAQ partitions may operate simultaneously, but each instance operates independently. 223, 224

data acquisition (DAQ) The data acquisition system accepts data from the detector FE electronics, buffers the data, performs a trigger decision, builds events from the selected data and delivers the result to the offline secondary DAQ buffer. vii, 50–52, 57, 63, 65, 69, 70, 72, 76–79, 81, 82, 84, 105, 108, 133, 134, 139, 156, 170–172, 195, 197, 200, 210, 214

data fragment A block of data read out from a single DAQ front-end fragment that span a contiguous period of time as requested by a trigger command. 223

DCS Distributed Communications System. 182

DUNE detector safety system (DDSS) The system used to manage key aspects of detector safety. 133, 134

detector module The entire DUNE far detector is segmented into four modules, each with a nominal 10 kt fiducial mass. 4, 20, 42, 44, 47, 78, 86, 133, 149, 154–156, 159, 162, 166–168, 172, 173, 177, 179, 180, 182, 187, 188, 191, 196, 205, 229, 230

detector unit A subdetector may be partitioned into a number of similar parts. For example the single-phase TPC subdetector is made up of APA units. 223

secondary DAQ buffer A secondary DAQ buffer holds a small subset of the full rate as selected by a trigger command. This buffer also marks the interface with the DUNE Offline. 223

DP module dual-phase detector module. vi, vii, 2, 5, 6, 8–11, 13, 14, 17, 18, 21, 29, 33–35, 42–44, 46, 48–50, 52, 55–58, 60–62, 65, 69–72, 75, 78, 80, 81, 83, 85, 86, 94, 98, 149, 155, 163, 167, 169, 170, 172, 174, 188, 198, 200, 206

dual-phase (DP) Distinguishes one of the DUNE far detector technologies by the fact that it operates using argon in both gas and liquid phases. vi, vii, 2–4, 6, 8, 11, 15, 18, 24, 25, 34, 40, 42–44, 47, 49, 51, 52, 72, 78, 83, 85, 89, 91, 92, 111–114, 122, 123, 125–128, 132–134, 148, 152, 154, 162–164, 168, 183, 192

detector support system (DSS) The system used to support the SP detector within the cryostat. 177, 214

DUNE Deep Underground Neutrino Experiment. vii, 2, 5, 6, 8, 11, 16, 34, 49, 50, 63, 83, 85, 90, 92, 109, 113, 116, 123, 125, 133, 134, 147–149, 154, 156, 160, 163, 167, 182–184, 186–188, 190–192, 206, 218, 222, 223, 226

electromagnetic interference (EMI) Disturbance generated by an external source that affects an electrical circuit by electromagnetic induction, electrostatic coupling, or conduction. 105

ENC equivalent noise charge. 59

ES&H Environment, Safety and Health. 34

endwall field cage (endwall FC) The vertical portions of the SP FC near the wall. 43

field cage (FC) The component of a LArTPC that contains and shapes the applied E field. vii, viii, 2–4, 8–11, 13–15, 18–21, 24–30, 32–42, 44, 46–48, 94, 95, 101–104, 111–113, 115–117, 125, 127, 133, 134, 137–139, 141, 145, 162, 173, 174, 188, 189, 211, 213, 216

far detector (FD) Refers to the 40 kt fiducial mass DUNE detector to be installed at the far site at SURF in Lead, SD, to be composed of four 10 kt modules. vii, ix, 34, 44, 79, 86, 88–90, 92, 109–112, 116, 121–123, 126, 127, 142, 143, 152, 154, 163, 164, 168, 183, 184, 188, 191, 192, 196, 198, 200, 203, 206, 207, 215, 226

FEA finite element analysis. 21

front-end computer (FEC) The portion of one DAQ partition that hosts the DAQ data receiver (DDR), primary buffer and data selector. It hosts the FER and corresponding portion of the primary buffer.. 223

Fermilab Fermi National Accelerator Laboratory (in Batavia, IL, the Near Site). 84

front-end (FE) The front-end refers a point that is “upstream” of the data flow for a particular subsystem. For example the front-end electronics is where the cold electronics meet the

sense wires of the TPC and the front-end DAQ is where the DAQ meets the output of the electronics. vi, vii, 51, 52, 54–64, 73, 74, 76–78, 80, 81, 83, 84, 86, 87, 107, 108, 133, 134, 170, 172, 194, 211

Fermilab Fermi National Accelerator Laboratory (in Batavia, IL, the Near Site). 34, 43

field programmable gate array (FPGA) An integrated circuit technology that allows the hardware to be reconfigured to execute different algorithms after its manufacture and deployment. 63–65, 67, 68

FRP fiber-reinforced plastic. 8–11, 13–15, 20, 21, 24–27, 29–32, 34–38, 43

full width at half maximum (FWHM) Width of a distribution measured between those points at which the distribution is equal to half of its maximum amplitude. 108

GAr gaseous argon. 198

geometry description markup language (GDML) Application-indepedent geometry description format based on XML. 111

ground grid An electrode that is held to be electrically neutral relative to Earth ground voltage ?? fix def or can we just use gp def?. 8, 11, 14, 21, 22, 24, 25, 30, 33, 37, 39–41, 43, 44, 48, 114, 115, 133

ground plane (GP) An electrode that is held to be electrically neutral relative to Earth ground voltage. 4, 187, 188

add full name (HDPE) add def. 17

HVDB dual-phase HV divider board. 9–11, 14, 24, 29–31, 34–36, 44, 46, 47

HVPS high voltage (HV) power supply. 2, 4, 9, 11, 14, 16, 17, 40, 41, 47

high voltage system (HVS) The detector subsystem that provides the TPC drift field . 13, 15, 37, 40–42, 44, 46, 47

high voltage (HV) Generally describes a voltage applied to drive the motion of free electrons through some media. ix, 2–6, 9–11, 13–20, 22, 25, 26, 29, 30, 32–35, 40–44, 46, 48, 59–61, 95, 99, 100, 102, 104, 105, 107, 114, 131–141, 143–146, 150–152, 154, 156, 157, 163, 166, 169–172, 182, 186–189, 192, 193, 197, 208, 210, 211, 219, 225

ICARUS add def. 17

ICEBERG Integrated Cryostat and Electronics Built for Experimental Research Goals: a new double wall cryostat build at Fermilab and installed in the Proton Assembly Building meant for liquid argon detector R&D and for testing of DUNE detector components. 191

IFbeam Database that stores beamline information indexed by timestamp. 196, 198

IFIC Instituto de Fisica Corpuscular (in Valencia, Spain). 177

integration and test facility (ITF) A facility where various detector components will be tested prior to installation. 214

Joint Project Office (JPO) The office formed from members of the Long-Baseline Neutrino Facility (LBNF) project and DUNE technical coordination (TCN) teams to direct integration and installation of the far detector (FD) modules. Its functions include global project configuration and integration, installation planning and coordination, scheduling, safety assurance, technical review planning and oversight, development of partner agreements, and financial reporting. 42

LabVIEW Laboratory Virtual Instrument Engineering Workbench is a system-design platform and development environment for a visual programming language from National Instruments. 171, 172

LArSoft Liquid Argon Software (LArSoft), a shared base of physics software across LArTPC experiments. 111

liquid argon time-projection chamber (LArTPC) A class of detector technology that forms the basis for the DUNE far detector modules. It typically entails observation of ionization activity by electrical signals and of scintillation by optical signals. 2, 5, 58, 144, 168, 172

liquid argon (LAr) The liquid phase of argon. 5, 6, 13, 18, 20, 21, 44, 48, 50, 84, 88, 91, 108, 110–114, 119, 140–145, 148, 157, 162–167, 182–184, 190, 191, 198, 208, 209

Long-Baseline Neutrino Facility (LBNF) The organizational entity responsible for developing the neutrino beam, the cryostats and cryogenics systems, and the conventional facilities for DUNE. 83, 84, 134, 155, 182, 184, 196, 198, 200, 202, 206, 213, 217, 218, 226, 229

LED Light-emitting diode. vii, 105, 108–110, 132, 144, 191, 218, 219

large electron multiplier (LEM) A micro-pattern detector suitable for use in ultra-pure argon vapor; LEMs consist of copper-clad PCB boards with sub-millimeter-size holes through which electrons undergo amplification. 6, 20, 48, 60, 93, 111, 116, 118, 157, 173, 183

light readout (LRO) The system for detecting scintillation photons in a DP detector module. vi, 49, 51, 52, 55–58, 65, 66, 69, 74, 77–79, 82, 84–87

Least Significant Bit (LSB) The bit with the lowest numerical value in a binary number. 64, 67

LV low voltage. 56, 60, 61, 80, 84, 172

MicroTCA Carrier Hub (MCH) An network switching device. 57, 58, 64, 69, 70, 73, 75, 79, 82, 84

Monte Carlo (MC) Refers to a method of numerical integration that entails the statistical sampling of the integrand function. Forms the basis for some types of detector and physics simulations. vii, 54, 119, 121

mass hierarchy (MH) Describes the separation between the mass squared differences related to the solar and atmospheric neutrino problems. 5

MicroBooNE The LArTPC-based MicroBooNE neutrino oscillation experiment at Fermilab. 194

minimum ionizing particle (MIP) Refers to a momentum traversing some medium such that the particle is losing near the minimum amount of energy per distance traversed. 5, 50, 54, 58, 59, 61, 111

nucleon decay (NDK) The hypothetical, baryon number violating decay of a proton or a bound neutron into lighter particles. vii, 89, 96, 97, 123–126

near detector (ND) Refers to the detector(s) installed close to the neutrino source at Fermilab. 5, 198

Network Time Protocol (NTP) A networking protocol which allows synchronizing of clocks to within a few ms of a time standard on a local network and within a few tens of ms over the Internet.. 71

outer diameter (OD) Outer diameter of a tube.. 48

OPC-UA OPC Unified Architecture is a machine to machine communication protocol for industrial automation developed by the OPC Foundation. OPC stands for Object Linking and Embedding for Process Control. 182

PCB printed circuit board. 11, 77, 177, 179, 180, 216, 217

PCI Peripheral Component Interconnect. 171

ProtoDUNE-DP The DP ProtoDUNE detector. iii, vii, 5, 6, 8–11, 13, 16–18, 20, 30, 33, 34, 39, 42–44, 46, 47, 50, 58, 59, 61, 65, 69, 71, 73, 74, 85, 86, 88, 97–100, 102, 105, 106, 111–113, 115, 116, 121–123, 130, 140, 142, 145, 148, 149, 151, 154, 157, 163, 164, 166–170, 180, 181, 183, 187, 188, 192, 196, 198, 200, 202, 205

ProtoDUNE-SP The SP ProtoDUNE detector. 5, 8, 13, 15, 17, 18, 42–44, 47, 86, 149, 154, 157, 160, 163–170, 172, 174, 177–181, 183, 184, 188–193, 198–200, 202, 205, 206, 208, 216

photon detection system (PDS) The detector subsystem sensitive to light produced in the LAr. vii–ix, 25, 36–38, 40, 41, 49, 51, 78, 82, 84, 88–93, 95–98, 100–102, 108, 109, 111–116, 121–123, 125–127, 129–144, 146–150, 172, 191, 207, 210, 222

photon detector (PD) Refers to the detector elements involved in measurement of number and arrival times of optical photons produced in a detector module. ix, 4, 21, 25, 39, 41, 44, 48,

55, 76, 77, 145–149, 151, 179, 180, 192, 193, 197, 212

photoelectron (PE) An electron ejected from the surface of a material by the photoelectric effect. 107, 119, 123, 124, 127, 129

PLC programmable logic controller. 184, 214, 218

photomultiplier tube (PMT) A device that makes use of the photoelectric effect to produce an electrical signal from the arrival of optical photons. vii, ix, 15, 22, 24, 40, 41, 48, 51, 52, 55, 57, 65, 67, 75, 78, 80–82, 88, 94–102, 104, 105, 107–112, 114–122, 126, 129–146, 149, 151

parts per billion (ppb) A number equal to 10^{-9}. 167

one-pulse-per-second signal (1PPS signal) An electrical signal with a fast rise time and that arrives in real time with a precise period of one second. 75

parts per trillion (ppt) A number equal to 10^{-12}. 167

ProtoDUNE-2 The second run of the ProtoDUNE detector. 39

ProtoDUNE Either of the two DUNE prototype detectors constructed at CERN. One prototype implements SP and the other DP technology. . iv, 42, 163, 164, 172, 183, 188, 193, 196, 198–200, 202, 203, 206, 207, 221

production readiness review (PRR) A project management device by which the production readiness is reviewed. 47, 205

quality assurance (QA) The set of actions taken to provide confidence that quality requirements are fulfilled, and to detect and correct poor results. 9, 31, 32, 43, 73–75, 130, 132, 219, 229

quality control (QC) An aggregate of activities (such as design analysis and inspection for defects) performed to ensure adequate quality in manufactured products. 9, 11, 31, 32, 43, 72–75, 130–133, 136, 145, 148, 215–218

root mean square (RMS) The square root of the arithmetic mean of the squares of a set of values, used as a measure of the typical magnitude of a set of numbers, regardless of their sign.. 91, 97, 112, 116, 117, 157, 174, 182

RTD Cryostat level and temperature monitoring devices. 173, 180–182, 206, 209, 217

S/N signal-to-noise (ratio). 5, 6, 54

SAS A pass-through chamber used to ensure safe transfer of materials, avoiding contamination in both directions. 135

SBND The Short-Baseline Near Detector experiment at Fermilab. 194

signal feedthrough chimney (SFT chimney) In the DP technology, a volume above the cryostat penetration used for a signal feedthrough. vi, vii, 49, 51, 55–59, 61–63, 70, 75–77, 79–84, 87

signal feedthrough (SFT) A cryostat penetration allowing for the passage of cables or other extended parts. vii, 62, 77, 81, 86

safe high voltage (SHV) Type of bayonet mount connector used on coaxial cables that has additional insulation compared to standard BNC and MHV connectots that makes it safer for handling high voltage by preventing accidental contact with the live wire connector in an unmated connector or plug. 131

silicon photomultiplier (SiPM) A solid-state avalanche photodiode sensitive to single photoelectron signals. 55, 109

supernova neutrino burst (SNB) A prompt increase in the flux of low-energy neutrinos emitted in the first few seconds of a core-collapse supernova. It can also refer to a trigger command type that may be due to an SNB, or detector conditions that mimic its interaction signature. vii, 5, 89–92, 96, 97, 125–128, 152

S/N signal over noise ratio. 49

single photoelectron (SPE) A single photoelectron. vii, 107, 108, 112

SP module single-phase detector module. 17, 43, 49, 78, 152, 172, 198, 200

single-phase (SP) Distinguishes one of the DUNE far detector technologies by the fact that it operates using argon in its liquid phase only . 6, 20, 24, 42, 43, 49, 91, 163, 164, 183, 221

subdetector A detector unit of granularity less than one detector module such as the TPC of either a SP or DP module. 223

Sanford Underground Research Facility (SURF) The laboratory in South Dakota where LBNF will be constructed. 31, 32, 35, 75, 76, 84

TallBo A cylindrical cryostat at Fermilab primarily used for developing scintillation light collection technologies for LArTPC detectors. 191

temporary construction opening (TCO) An opening in the side of a cryostat through which detector elements are brought into the cryostat; utilized during construction and installation. 11, 35, 37, 39

technical coordination (TCN) Responsible for overall integration of the detector elements and successful execution of the detector construction project; areas of responsibility include general project oversight, systems engineering, quality assurance (QA) and safety. 42, 206, 226

technical design report (TDR) A formal project document that describes the experiment at a technical level. 5, 42, 152, 183, 200

top field cage (top FC) The horizontal portions of the SP FC on the top. 43

tetra-phenyl butadiene (TPB) A type of wavelength shifting material. viii, 25, 51, 88, 94, 95, 98, 100, 101, 103, 104, 112, 114–116, 132, 136, 137, 140–144, 146, 149

time projection chamber (TPC) The portion of each DUNE detector module that records ionization electrons after they drift away from a cathode through the LAr, and also through gaseous argon in a DP module. The activity is recorded by digitizing the waveforms of current induced on the anode as the distribution of ionization charge passes by or is collected on the electrode. vii, 2, 4–6, 15, 18, 23–25, 27, 29, 33, 48, 49, 51, 55, 59, 72, 78, 81, 83, 85, 89–92, 94, 101, 112–114, 125, 126, 129, 130, 148, 154, 157, 163, 167–169, 172, 173, 187, 191, 193, 206, 212

trigger candidate Summary information derived from the full data stream and representing a contribution toward forming a trigger decision. 230

trigger command Information derived from one or more trigger candidates that directs elements of the detector module to read out a portion of the data stream. 223, 224, 230

trigger decision The process by which trigger candidates are converted into trigger commands. 223, 230

user datagram protocol (UDP) A simple, connectionless Internet protocol that supports data integrity checksums, requires no handshaking, and does not guarantee packet delivery. 79

UHMWPE ultra-high molecular weight polyethylene. 18

underground installation team (UIT) An organizational unit responsible for installation in the underground area at the SURF site. 76, 84, 134

Micro Telecommunications Computing Architecture (μTCA) The computer architecture specification followed by the crates that house charge and light readout electronics in the dual-phase module. 49, 51, 52, 56–58, 61, 64, 65, 68–73, 75–84, 86, 87, 95, 108, 134, 144, 221, 231

VUV vacuum ultra-violet. 100

WA105 DP demonstrator The $3 \times 1 \times 1\,\mathrm{m}^3$ WA105 dual-phase prototype detector at CERN. iii, vi, vii, ix, 4, 5, 50, 60, 61, 63, 70, 71, 77, 84, 85, 88, 100, 102, 108, 111, 113–119, 142, 148, 187

work breakdown structure (WBS) An organizational project management tool by which the tasks to be performed are partitioned in a hierarchical manner. 85, 148

wavelength shifting (WLS) A material or process by which incident photons are absorbed by a material and photons are emitted at a different, typically longer, wavelength. vii, viii, 25, 26, 36–38, 40, 41, 95, 101–104, 111–114, 125, 127, 128, 130, 133, 134, 138, 139, 141–145, 149

WR grandmaster White Rabbit grandmaster. 65, 71, 72, 79, 82

White Rabbit μTCA Carrier Hub (WR-MCH) A card mounted in μTCA crate that recieves time syncronization information and trigger data packets over White Rabbit (WR) network and disributes them to the advanced mezzanine card (AMC) over μTCA backplane. 52, 55–58, 64, 65, 71–73, 75, 79, 81, 87, 231

White Rabbit TimeStamping Node (WR-TSN) A unit on the WR network that timestamps the trigger signals and sends out trigger data packets to White Rabbit μTCA Carrier Hub (WR-MCH). 65, 71

White Rabbit (WR) A component of the timing system that forwards clock signal and time-of-day reference data to the master timing unit. vi, 52, 56, 58, 65, 69–73, 75, 79, 81, 82, 86, 108, 231

References

[1] DOE Office of High Energy Physics, "Mission Need Statement for a Long-Baseline Neutrino Experiment (LBNE)," tech. rep., DOE, 2009. LBNE-doc-6259.

[2] **ICARUS** Collaboration, F. Varanini, "ICARUS detector: present and future," *EPJ Web Conf.* **164** (2017) 07017.

[3] Duchesneau, D. and Gil-Botella, I. and Pietropaolo, F. and Yu, B., "DUNE FD Interface Document: DP Photon Detector to Joint HV," tech. rep., 2018. `https://docs.dunescience.org/cgi-bin/private/ShowDocument?docid=6799&version=2`.

[4] Duchesneau, D. and Pietropaolo, F. and Yu, B., "DUNE FD Interface Document: DP CRP to Joint High Voltage," tech. rep., 2018. `https://docs.dunescience.org/cgi-bin/private/ShowDocument?docid=6754&version=1`.

[5] F. Feyzi, E. James, F. Pietropaolo, T. Shaw, and B. Yu, "DUNE FD Interface Document: SP TPC Electronics to joint DAQ," DUNE doc 6985, 2018. `https://docs.dunescience.org/cgi-bin/private/ShowDocument?docid=6985&asof=2019-7-15`.

[6] A. C. Villanueva *et al.*, "DUNE FD Interface Document: High Voltage to CISC,". `https://docs.dunescience.org/cgi-bin/private/ShowDocument?docid=6787&version=1`.

[7] S. Gollapinni, K. Mahn, and J. Maneira, "DUNE FD Interface Document: Calibration-HV,". `https://docs.dunescience.org/cgi-bin/private/ShowDocument?docid=14005&asof=2019-7-15`.

[8] B. Aimard *et al.*, "A 4 tonne demonstrator for large-scale dual-phase liquid argon time projection chambers," *JINST* **13** no. 11, (2018) P11003, `arXiv:1806.03317 [physics.ins-det]`.

[9] L. Agostino *et al.*, "LBNO-DEMO: Large-scale neutrino detector demonstrators for phased performance assessment in view of a long-baseline oscillation experiment, The LBNO-DEMO - WA105 - Collaboration." CERN-SPSC-2014-013; SPSC-TDR-004, 2014.

[10] S. Blin, S. Callier, S. Conforti Di Lorenzo, F. Dulucq, C. De La Taille, G. Martin-Chassard, and N. Seguin-Moreau, "Performance of CATIROC: ASIC for smart readout of large

photomultiplier arrays," *Journal of Instrumentation* **12** (Mar., 2017) C03041.

[11] J. Wu, "Data Reduction Processes Using FPGA for MicroBooNE Liquid Argon Time Projection Chamber," in *Proceedings, 17th Conference on Computing Applications in Nuclear and Plasma Sciences on Real Time (RT2010): Lisbon, Portugal, May 24-28, 2010*. 2010. http://lss.fnal.gov/cgi-bin/find_paper.pl?conf-10-174.

[12] Autiero, D. and Duchesneau, D. and Hasegawa, T., "DUNE FD Interface Document: DP CRP to DP TPC Electronics," tech. rep., 2018. https://docs.dunescience.org/cgi-bin/private/ShowDocument?docid=6772&version=1.

[13] Duchesneau, D. and Autiero, D. and Gil-Botella, I. and Hasegawa, T., "DUNE FD Interface Document: DP TPC Electronics to DP Photon Detector," tech. rep., 2018. https://docs.dunescience.org/cgi-bin/private/ShowDocument?docid=6772&version=1.

[14] Autiero, D. and Hasegawa, T. and Karagiorgi, G. and Newbold, D., "DUNE FD Interface Document: DP TPC Electronics to Joint DAQ," tech. rep., 2018. https://docs.dunescience.org/cgi-bin/private/ShowDocument?docid=6778&version=1.

[15] D. Autiero *et al.*, "DUNE FD Interface Document: DP TPC Electronics to Joint CISC,". https://docs.dunescience.org/cgi-bin/private/ShowDocument?docid=6784&version=1.

[16] Autiero, D. and Hasegawa, T. and James, E. and Stewart, J., "DUNE FD Interface Document: Installation Interfaces to DP TPC Electronics," tech. rep., 2018. https://docs.dunescience.org/cgi-bin/private/ShowDocument?docid=7009&version=1.

[17] Autiero, D. and Hasegawa, T. and James, E. and Marshak, M., "DUNE FD Interface Document: Integration Facility to DP TPC Electronics," tech. rep., 2018. https://docs.dunescience.org/cgi-bin/private/ShowDocument?docid=7036&version=1.

[18] Autiero, D. and Hasegawa, T. and Gollapinni, S. and Mann, K., "DUNE FD Interface Document: Calibration to DP TPC Electronics," tech. rep., 2018. https://docs.dunescience.org/cgi-bin/private/ShowDocument?docid=7063&version=1.

[19] Autiero, D. and Hasegawa, T. and Worcester, E. and Patterson, R., "DUNE FD Interface Document: DUNE Physics to DP TPC Electronics," tech. rep., 2018. https://docs.dunescience.org/cgi-bin/private/ShowDocument?docid=7090&version=1.

[20] Autiero, D. and Hasegawa, T. and Norman, A. and Schellman, H., "DUNE FD Interface Document: Software and Computing to DP TPC Electronics," tech. rep., 2018. https://docs.dunescience.org/cgi-bin/private/ShowDocument?docid=7117&version=1.

[21] "Om3 fibers." http://shop.fiber24.net/index.php/en/FO-Patch-Cable-OM3-Multi-mode-50-125-m-Duplex-LC-PC-LC-PC/c-OM3-DUPLEX-1TO1/a-FOPC-F2-O3-DX-LCU-LCU.

[22] "Nat-mch." http://www.nateurope.com/products/NAT-MCH.html.

[23] James, E. and Kettell, S., "DUNE Project WBS for the Far Detector," tech. rep., 2018. https://docs.dunescience.org/cgi-bin/private/ShowDocument?docid=5594&version=9.

[24] T. Heindl *et al.*, "The scintillation of liquid argon," *EPL (Europhysics Letters)* **91** no. 6, (2010) 62002. http://stacks.iop.org/0295-5075/91/i=6/a=62002.

[25] T. Lux, "Charge and Light Production in the Charge Readout System of a Dual Phase LAr TPC," arXiv:1812.08700 [physics.ins-det].

[26] R. Francini *et al.*, "Vuv-vis optical characterization of tetraphenyl-butadiene films on glass and specular reflector substrates from room to liquid argon temperature," *Journal of Instrumentation* **8** no. 09, (2013) P09006. http://stacks.iop.org/1748-0221/8/i=09/a=P09006.

[27] R. Acciarri *et al.*, "Design and construction of the microboone detector," *Journal of Instrumentation* **12** no. 02, (2017) P02017. http://stacks.iop.org/1748-0221/12/i=02/a=P02017.

[28] **MiniCLEAN** Collaboration, A. Hime, "The MiniCLEAN Dark Matter Experiment," in *Particles and fields. Proceedings, Meeting of the Division of the American Physical Society, DPF 2011, Providence, USA, August 9-13, 2011*. 2011. arXiv:1110.1005 [physics.ins-det]. https://inspirehep.net/record/930736/files/arXiv:1110.1005.pdf.

[29] "Technical Design Report for large-scale neutrino detectors prototyping and phased performance assessment in view of a long-baseline oscillation experiment," tech. rep., 2014. http://cds.cern.ch/record/1692375/files/arXiv%3A1409.4405.pdf?version=2.

[30] http://www.et-enterprises.com/.

[31] http://www.hzcphotonics.com/en_index.html.

[32] http://www.hamamatsu.com/resources/pdf/etd/LARGE_AREA_PMT_TPMH1286E.pdf.

[33] D. Belver *et al.*, "Cryogenic R5912-20Mod Photomultiplier Tube Characterization for the ProtoDUNE Dual Phase Detector," *JINST* **13** no. 10, (2018) T10006, arXiv:1806.04571 [physics.ins-det].

[34] M. Bonesini *et al.*, "An innovative technique for TPB deposition on convex window photomultiplier tubes," *JINST* **13** no. 12, (2018) P12020, arXiv:1807.07123 [physics.ins-det].

[35] **WA105** Collaboration, L. Zambelli and S. Murphy, "WA105: A large demonstrator of a liquid argon dual phase TPC," *J. Phys. Conf. Ser.* **888** no. 1, (2017) 012202.

[36] https://www.picmg.org/openstandards/microtca/.

[37] **DUNE** Collaboration, C. Cuesta, "Photon detection system for ProtoDUNE dual phase," *JINST* **12** no. 12, (2017) C12048, arXiv:1711.08307 [physics.ins-det].

[38] **MicroBooNE** Collaboration, J. Conrad, B. J. P. Jones, Z. Moss, T. Strauss, and M. Toups, "The Photomultiplier Tube Calibration System of the MicroBooNE Experiment," *JINST* **10** no. 06, (2015) T06001, arXiv:1502.04159 [physics.ins-det].

[39] B. Caccianiga, D. Franco, D. Giugni, P. Lombardi, S. Malvezzi, J. Maneira, G. Manusardi, L. Miramonti, G. Ranucci, and O. Smirnov, "A multiplexed optical-fiber system for the PMT calibration of the Borexino experiment," *Nucl. Instrum. Meth.* **A496** (2003) 353–361.

[40] P. Adamson *et al.*, "The minos light-injection calibration system," *Nucl. Instrum. Meth.* **A492** no. 3, (2002) 325 – 343.

[41] D. Belver *et al.*, "A Light Calibration System for the ProtoDUNE-DP Detector," arXiv:1902.07127 [physics.ins-det].

[42] J. Kapustinsky, R. DeVries, N. DiGiacomo, W. Sondheim, J. Sunier, and H. Coombes, "A fast timing light pulser for scintillation detectors," *Nuclear Instruments and Methods in Physics Research Section A: Accelerators, Spectrometers, Detectors and Associated Equipment* **241** no. 2, (1985) 612 – 613. http://www.sciencedirect.com/science/article/pii/0168900285906229.

[43] **DUNE** Collaboration, B. Abi *et al.*, "The DUNE Far Detector Interim Design Report, Volume 3: Dual-Phase Module," arXiv:1807.10340 [physics.ins-det].

[44] C. Andreopoulos *et al.*, "The GENIE Neutrino Monte Carlo Generator," *Nucl. Instrum. Meth.* **A614** (2010) 87–104, arXiv:0905.2517 [hep-ph].

[45] S. Gardiner, B. Svoboda, C. Grant, and E. Pantic, "MARLEY (Model of Argon Reaction Low Energy Yields)." http://www.marleygen.org/.

[46] Karagiorgi, G. and Newbold, D. and Segreto, E. and Warner, D., "DUNE FD Interface Document: DP Photon Detector to Joint DAQ," tech. rep., 2018. https://docs.dunescience.org/cgi-bin/private/ShowDocument?docid=6802&version=1.

[47] D. Duchesneau, I. Gil-Botella, , S. Gollapinni, and A. Villanueva, "DUNE FD Interface Document: DP Photon Detector to Joint CISC,". https://docs.dunescience.org/cgi-bin/private/ShowDocument?docid=6781&version=1.

[48] Duchesneau, D. and Gil-Botella, I. and Worcester, E. and Patterson, R., "DUNE FD Interface Document: DUNE Physics to DP Photon Detector," tech. rep., 2018. https://docs.dunescience.org/cgi-bin/private/ShowDocument?docid=7087&version=1.

[49] Duchesneau, D. and Gil-Botella, I. and Norman, A. and Schellman, H., "DUNE FD Interface

Document: Software and Computing to DP Photon Detector," tech. rep., 2018. https://docs.dunescience.org/cgi-bin/private/ShowDocument?docid=7114&version=1.

[50] Duchesneau, D. and Gil-Botella, I. and Gollapinni, S. and Mann, K., "DUNE FD Interface Document: Calibration to DP Photon Detector," tech. rep., 2018. https://docs.dunescience.org/cgi-bin/private/ShowDocument?docid=7060&version=1.

[51] Duchesneau, D. and Feyzi, F. and Gil-Botella, I. and James, E. and Shaw, T., "DUNE FD Interface Document: Facility Interfaces to DP Photon Detector," tech. rep., 2018. https://docs.dunescience.org/cgi-bin/private/ShowDocument?docid=6979&version=1.

[52] Duchesneau, D. and Gil-Botella, I. and James, E. and Kettell, S. and Stewart, J., "DUNE FD Interface Document: Installation Interfaces to DP Photon Detector," tech. rep., 2018. https://docs.dunescience.org/cgi-bin/private/ShowDocument?docid=7006&version=1.

[53] J. Asaadi, B. J. P. Jones, A. Tripathi, I. Parmaksiz, H. Sullivan, and Z. G. R. Williams, "Tetraphenyl Butadiene Emanation and Bulk Fluorescence from Wavelength Shifting Coatings in Liquid Argon," arXiv:1804.00011 [physics.ins-det].

[54] **DarkSide** Collaboration, P. Agnes *et al.*, "DarkSide-50 532-day Dark Matter Search with Low-Radioactivity Argon," *Phys. Rev.* **D98** no. 10, (2018) 102006, arXiv:1802.07198 [astro-ph.CO].

[55] **DEAP** Collaboration, R. Ajaj *et al.*, "Search for dark matter with a 231-day exposure of liquid argon using DEAP-3600 at SNOLAB," arXiv:1902.04048 [astro-ph.CO].

[56] B. J. P. Jones, J. K. VanGemert, J. M. Conrad, and A. Pla-Dalmau, "Photodegradation Mechanisms of Tetraphenyl Butadiene Coatings for Liquid Argon Detectors," *JINST* **8** (2013) P01013, arXiv:1211.7150 [physics.ins-det].

[57] **MiniBooNE** Collaboration, S. J. Brice *et al.*, "Photomultiplier tubes in the MiniBooNE experiment," *Nucl. Instrum. Meth.* **A562** (2006) 97–109, arXiv:1005.3525 [physics.ins-det].

[58] D. Duchesneau and Gil-Botella, "DUNE FD WBS: Dual Phase Photon Detector," DUNE doc 5606, LAPP, CIEMAT, 2018. https://docs.dunescience.org/cgi-bin/private/ShowDocument?docid=5606&asof=2019-7-15.

[59] Strons, Ph., and Bailey, J. L., "Flow visualization methods for field test verification of CFD analysis of an ope n gloveport," 2017. https://www.osti.gov/pages/servlets/purl/1402050.

[60] The Liquid Argon Technology @BNL, "Basic properties." https://lar.bnl.gov/properties/basic.html. Accessed Jan. 15, 2019.

[61] A. Kehrli, G. L. Miotto, X. Pons, S. Ravat, and M. J. Rodriguez, "The protoDUNE Single

Phase Detector Control System, in Proceedings of CHEP 2018," tech. rep., 2018. https://docs.dunescience.org/cgi-bin/private/ShowDocument?docid=11098.

[62] W. Walkowiak, "Drift velocity of free electrons in liquid argon," *Nucl. Instrum. Meth.* **A449** (2000) 288–294.

[63] M. Adamowski *et al.*, "The Liquid Argon Purity Demonstrator," *JINST* **9** (2014) P07005, arXiv:1403.7236 [physics.ins-det].

[64] **WA105** Collaboration, S. Murphy, "Status of the WA105-3x1x1 m^3 dual phase prototype," tech. rep., 2017. https://indico.fnal.gov/event/12345/session/1/contribution/5/material/slides/0.pdf.

[65] Delaquis, S. C. and Gornea, R. and Janos, S. and Lüthi, M. and Rudolf von Rohr, C. and Schenk, M. and Vuilleumier, J. -L., "Development of a camera casing suited for cryogenic and vacuum applications," *JINST* **8** (2013) T12001, arXiv:1310.6601 [physics.ins-det].

[66] Auger, M. and Blatter, A. and Ereditato, A. and Goeldi, D. and Janos, S. and Kreslo, I. and Lüthi, M. and Rudolf von Rohr, C. and Strauss, T. and Weber, M. S., "On the Electric Breakdown in Liquid Argon at Centimeter Scale," *JINST* **11** no. 03, (2016) P03017, arXiv:1512.05968 [physics.ins-det].

[67] T. I. Banks *et al.*, "A compact ultra-clean system for deploying radioactive sources inside the KamLAND detector," *Nucl. Instrum. Meth.* **A769** (2015) 88–96, arXiv:1407.0413 [physics.ins-det].

[68] "LUXEON C Color Line (datasheet)." https://www.lumileds.com/uploads/571/DS144-pdf. Accessed: 2018-11-19.

[69] J. Carron, A. Philippon, L. S. How, A. Delbergue, S. Hassanzadeh, D. Cillierre, P. Danto, and M. Boutillier, "Cryogenic characterization of LEDs for space application," *Proc. SPIE, Sixteenth International Conference on Solid State Lighting and LED-based Illumination Systems* **10378** (2017) 20.

[70] Siemens AG, "SIMATIC WinCC open architecture." http:///www.siemens.com/wincc-open-architecture. Accessed: 2018-11-27.

[71] A. C. Villanueva and S. Gollapinni, "DUNE FD WBS: Slow Control," DUNE doc 5609, 2018. https://docs.dunescience.org/cgi-bin/private/ShowDocument?docid=5609&asof=2019-7-15.

[72] S. Gollapinni *et al.*, "DUNE FD Risks: CISC,". https://docs.dunescience.org/cgi-bin/private/ShowDocument?docid=7192&asof=2019-7-15.

[73] A. C. Villanueva *et al.*, "DUNE FD Interface Document: DP CRP to Joint CISC,". https://docs.dunescience.org/cgi-bin/private/ShowDocument?docid=6760&version=1.

[74] A. C. Villanueva *et al.*, "DUNE FD Interface Document: DAQ to CISC,". https://docs.dunescience.org/cgi-bin/private/ShowDocument?docid=6790&version=1.

[75] S. Gollapinni *et al.*, "DUNE FD Interface Document: Calibration to Joint CISC,". https://docs.dunescience.org/cgi-bin/private/ShowDocument?docid=7072&version=1.

[76] S. Gollapinni *et al.*, "DUNE FD Interface Document: DUNE Physics to Joint CISC,". https://docs.dunescience.org/cgi-bin/private/ShowDocument?docid=7099&version=1.

[77] S. Gollapinni *et al.*, "DUNE FD Interface Document: Software and Computing to Joint CISC,". https://docs.dunescience.org/cgi-bin/private/ShowDocument?docid=7126&version=1.

[78] F. Feyzi *et al.*, "DUNE FD Interface Document: Facility Interfaces to Joint CISC,". https://docs.dunescience.org/cgi-bin/private/ShowDocument?docid=6991.

[79] S. Gollapinni *et al.*, "DUNE FD Interface Document: Installation Interfaces to Joint CISC,". https://docs.dunescience.org/cgi-bin/private/ShowDocument?docid=7018&version=1.

[80] S. Gollapinni *et al.*, "DUNE FD Interface Document: Integration Facility to Joint CISC,". https://docs.dunescience.org/cgi-bin/private/ShowDocument?docid=7045&version=1.